

Femtosecond Laser Inscribed Calibration Phantoms for Optical Coherence Tomography

Yang Lu

Doctor of Philosophy

ASTON UNIVERSITY

March 2021

©Yang Lu, 2021

Yang Lu asserts her moral right to be identified as the author of this thesis.

This copy of the thesis has been supplied on condition that anyone who consults it is understood to recognise that its copyright belongs to its author and that no quotation from the thesis and no information derived from it may be published without appropriate permission or acknowledgement.

Aston University
**Femtosecond Laser Inscribed Calibration Phantoms
for Optical Coherence Tomography**

Yang Lu
Doctor of Philosophy
March 2021

The thesis describes work using a femtosecond laser to fabricate high precision microstructures as multipurpose 3D OCT calibration phantoms that can be used to quantitatively characterise and calibrate across different OCT systems. The research has been focused on three areas in developing the OCT calibration phantom - laser power characterisation, fabrication optimisation and novel multipurpose OCT phantom development and phantom application.

For the laser power characterisation process, a detailed in-depth study was performed investigating the correlation between laser power and inscription size. Test phantoms were inscribed with different laser pulse energies. The results showed that with increased laser pulse energy, both the linewidth and the cross-inscription height were increased. The critical power of self-focusing was exceeded when the laser power was around 63% of the total laser average output power. As the non-linear effect caused unexpected control of the inscription size along the axial direction, a laser power range below the self-focusing threshold was selected to inscribe the phantoms which was still enough to extend the design to reach greater depths.

The phantom fabrication optimisation with a layer-by-layer inscription method has allowed inscriptions at a greater depth up to 2mm whilst keeping the inscription size uniform and consistent for all depths. For the inscription method, the laser power was reset at beginning of the inscription for each layer which allowed a customised option to be made to get the desired inscription size that can be kept consistent and uniform for all depths.

In order to address the challenges of inscribing non-planar samples, a series of multipurpose of OCT phantoms were designed and fabricated. A non-planar phantom was initially proposed that comprised of a grid-like pattern inscribed inside a plano-convex lens as the planar side provided a standard non-distorted image and the curved side provided a distorted image which can be used to detect the scanning errors and the post-processing algorithms of the OCT system for distortion correction. However, the grid-like pattern required a highly degree of alignment under the OCT system. Subsequently, a circle-like pattern was proposed to overcome this angular issue with a landmark layer consisting of a series of radial lines inscribed at the top of the test pattern to guide the location.

To investigate the impact of OCT image distortion, a planar phantom was designed and used as a reference to correct the distortion due to the scanning errors caused by the OCT system itself. With a known reference, a phantom-based distortion correction method is possible with the reduction of the scan spacing error by 82% which extends the potential use of the OCT phantoms beyond a qualitative measurement tool.

Keywords: optical coherence tomography (OCT), femtosecond laser inscription, OCT calibration phantom, femtosecond laser direct writing, OCT image distortion correction

Dedicated to my parents and family.

Acknowledgements

First of all, I would like to take the opportunity to thank my supervisor Prof. Kate Sugden for her support, help and encouragement throughout my PhD study. Her knowledge, inspiration and enthusiasm together with so many creative ideas have broadened my horizons. I sincerely appreciate getting her support not only on the academic research but also on the personal skill developments such as PGCert training and Carl Zeiss OCT training.

I would also like to thank my co-supervisor Dr. Vladimir Mezentsev and my mentor Dr. Neil Gordon. Vladimir has shared with me intensive knowledge on femtosecond laser inscription theory and Neil taught me how to operate the Oxford Laser system and teach me how to program. Without their help, this research work would not have progressed as smoothly.

I would specially thank Arden Photonics Ltd. together with Aston University to co-fund my PhD project. Without the financial support, my PhD wouldn't have been possible. I also like to thank Arden Photonics Ltd. to provide internship opportunity to work with them during the PhD study and for financing my accommodation for the 2018 Photonics West conference. I also like to thank SPIE and MKS Instruments to award me a student author grant to attend the 2018 Photonics West conference and SPIE Student Chapter Officer Travel Grant to attend 2020 Photonics West conference.

I would like to thank College of Engineering and Physical Sciences and AIP research institute to support my study and offer the student development funding to attend the conference. I would like to thank Institute of Physics (IOP) to provide a bursary to attend and present at Photon 2018 conference.

I would like to thank my research collaborators: Dr. Izzati Ibrahim, Dr. Benjamin Coldrick, Dr. Antonio Fratini, Dr. Francesco Menduni, Mr. Mala Sadik, Dr. Richard Nock, Dr. Xiao Ai, Prof. Naim Dahnoun, Prof. John Rarity and Prof. David Webb to co-author the conference papers. Having your contribution make the research work more diversified. I would like to thank Dr. Benjamin Coldrick from Optimec Systems, Dr. Christian Broadway from Biomedical Department and Dr. Rebekka Heitmar from Vision Sciences for kindly letting me use your OCT systems for testing the phantoms.

I would like to thank Dr. Elena Turitsyna, Dr. Paul Harper, Dr. Ian Phillips, Mr. Richard Reeves, Dr. Goudarz Poursharif and Dr Panos Doss for teaching opportunities and

support. Thanks to Ms. Swaroopa Mucheli, Dr. Kirill Tokmakov for the research lab support.

I would like to thank Dr. Elena Turtsyna and Prof. Lin Zhang for assessing my first-year qualifying report and viva and other supports during my PhD study. Thanks to Prof. Wenping Cao for being our postgraduate tutor.

I would like to thank the School Administration and Management team (Ms. Helen Yard, Ms. Sandra Mosley, Ms. Catherine Jarrett, Mr. Raymond Timmins, Mr. Stephen Baker and other team members) to help to maintain my student record, annual report and progression, help me booking my flights for the conference travel and provide student letters. Thanks to IT services to solve the technical issues, software update and renew my student card. Thanks to Library services for online support and induction sessions for the copyright and intellectual property information.

I would like to thank Mr. Robert Dean, Mr. Roy Haywood, Mr. Robert Stewart from Oxford Lasers Ltd. and Mr. Anthony Pinal, Mr. Sylvain Dubuc from Amplitude Systemes for technical advice, support and maintenance for the lab equipment.

I would like to thank my colleagues: Ms. Marie Zandi, Ms. Paulami Ray, Dr. Ning Xing, Dr. Anastasiia Vasylychenkova, Ms. Karina Nurlybayeva, Ms. Namita Sahoo, Ms. Gabriella Gardosi, Ms. Shirin Hanaei, Dr. Tingting Zhang, Dr. Changle Wang, Dr. Tom Sun, Mr. Nasir Bello, Mr. Igor Kudelin, Mr. Mala Sadik, Mr. Chengwei Lou, Mr. Sajid Zaki, Mr. Mr. Mahmood Abu-Romoh, Dr. Teerawat Piromjitpong, Dr. Guanhao Du, Dr. Yong Yang, Dr. Amit Yadav, Dr. Syed Abid Ali Shah and more for your support, biscuits and teatime and sharing your knowledge and life experience which make my PhD experience being more joyful. I am really glad to meet such amazing people at Aston.

Finally, I would like to specially thank my parents, my husband and his parents for all the support and love during my PhD study.

List of Contents

ACKNOWLEDGEMENTS	- 4 -
LIST OF CONTENTS	- 6 -
LIST OF TABLES	- 9 -
LIST OF FIGURES	- 10 -
LIST OF ABBREVIATIONS	- 21 -
CHAPTER 1 INTRODUCTION	- 23 -
1.1 Thesis structure	- 28 -
CHAPTER 2 THEORY	- 31 -
2.1 Femtosecond laser-material interactions	- 32 -
2.1.1 Nonlinear excitation mechanisms	- 33 -
2.1.2 Modification regimes	- 37 -
2.2 Experimental considerations	- 39 -
2.2.1 Polarisation	- 40 -
2.2.2 Repetition rate.....	- 41 -
2.2.3 Pulse duration	- 42 -
2.2.4 Writing geometry and aberrations	- 43 -
2.2.5 Self-focusing	- 45 -
2.3 Optical coherence tomography (OCT)	- 46 -
2.3.1 Optical coherence tomography: basic principles.....	- 47 -
2.3.2 OCT systems	- 48 -
2.3.3 Performance parameters of OCT systems.....	- 50 -
2.3.4 OCT image processing	- 55 -
2.4 Chapter conclusions	- 56 -
CHAPTER 3 EXPERIMENTAL SETUP	- 57 -
3.1 Femtosecond laser system	- 58 -
3.1.1 Femtosecond laser.....	- 58 -
3.1.2 Optical components for beam delivery.....	- 60 -
3.2 Phantom design and fabrication workflow	- 63 -
3.3 Sample substrate and material	- 64 -
3.4 Phantom characterisation	- 65 -
3.4.1 Microscope.....	- 65 -
3.4.2 OCT systems	- 66 -
3.5 Quantitative method for sample alignment	- 68 -

3.5.1	Alignment procedure and focus position	- 68 -
3.5.2	Screen-to-ruler method	- 70 -
3.6	Study the existing planar OCT phantom.....	- 73 -
3.6.1	Planar OCT phantom layout.....	- 73 -
3.6.2	Phantom fabrication	- 75 -
3.6.3	Microscope characterisation	- 75 -
3.6.4	OCT systems characterisation	- 84 -
3.7	Chapter conclusions.....	- 87 -
CHAPTER 4 FABRICATION OPTIMISATION.....		- 88 -
4.1	Introduction	- 89 -
4.2	Laser power test pattern design and fabrication	- 89 -
4.3	Laser power test pattern characterisation on the X-Y plane	- 92 -
4.3.1	The correlation between the inscription linewidth and the laser pulse energy at the X-Y plane-	97 -
4.4	Laser power test pattern characterisation on the Y-Z plane.....	- 98 -
4.4.1	The correlation between the inscription size and the laser pulse energy at the Y-Z plane	- 105 -
4.5	Laser power optimisation.....	- 108 -
4.6	Chapter conclusions.....	- 110 -
CHAPTER 5 PLANAR OCT CALIBRATION PHANTOM.....		- 111 -
5.1	Introduction	- 112 -
5.2	Advanced planar phantom design and fabrication.....	- 112 -
5.2.1	Point spread function (PSF) phantom	- 116 -
5.2.2	Sensitivity phantom	- 119 -
5.2.3	Lateral resolution phantom.....	- 122 -
5.2.4	Distortion phantom	- 124 -
5.3	Results and discussions	- 126 -
5.3.1	Point spread function (PSF) phantom	- 126 -
5.3.2	Sensitivity phantom	- 132 -
5.3.3	Lateral resolution phantom.....	- 137 -
5.3.4	Distortion phantom	- 140 -
5.3.5	Further discussions	- 143 -
5.4	Chapter conclusions.....	- 144 -
CHAPTER 6 NON-PLANAR OCT CALIBRATION PHANTOM.....		- 145 -
6.1	Introduction	- 146 -
6.2	Non-planar grid-like OCT phantom	- 147 -
6.2.1	Phantom design and fabrication.....	- 147 -
6.2.2	Results and discussions.....	- 148 -
6.2.3	Further discussions	- 154 -

6.2.4	Section conclusions	- 154 -
6.3	Non-planar circle-like OCT phantom.....	- 155 -
6.3.1	Introduction	- 155 -
6.3.2	Phantom design and fabrication.....	- 156 -
6.3.3	Results and discussions.....	- 157 -
6.3.4	Further discussions	- 162 -
6.3.5	Section conclusions	- 163 -
6.4	Optimised non-planar OCT phantom	- 163 -
6.4.1	Introduction	- 163 -
6.4.2	Phantom design and fabrication.....	- 164 -
6.4.3	Results and discussions.....	- 164 -
6.4.4	Further discussions	- 174 -
6.4.5	Section conclusions	- 174 -
6.5	Inscription from a curved surface	- 175 -
6.6	Chapter conclusions.....	- 178 -
CHAPTER 7 OCT PHANTOM APPLICATION		- 180 -
7.1	Introduction	- 181 -
7.2	Scanning mechanism	- 181 -
7.3	Phantom design and characterisation	- 183 -
7.4	OCT image distortion detection and correction.....	- 185 -
7.4.1	OCT system configuration.....	- 185 -
7.4.2	OCT image analysis	- 186 -
7.4.3	OCT image correction	- 186 -
7.4.4	Discussions	- 191 -
7.5	Conclusions.....	- 191 -
CHAPTER 8 CONCLUSION AND FUTURE WORKS		- 193 -
8.1	Conclusion.....	- 193 -
8.2	Future works.....	- 195 -
REFERENCES		- 197 -
LIST OF PUBLICATIONS.....		- 214 -
APPENDICES		- 215 -
Appendix A.....		- 215 -
Appendix B		- 216 -

List of Tables

Table 2-1. Comparison between different OCT methods.	- 50 -
Table 3-1. Parameters of CNC stages and controller.	- 62 -
Table 3-2. Parameters and comparison of different OCT systems used	- 67 -
Table 3-3. Microscope measurement results of PSF pattern at the top edge.....	- 76 -
Table 3-4. Microscope measurement results of PSF pattern at the bottom edge for all layer depths and layer separations.	- 76 -
Table 3-5. Measurement results of lateral resolution pattern for all layer depths and layer separations.	- 79 -
Table 3-6. Microscope measurement results of grid pattern for all layer depths and layer separations.	- 82 -
Table 3-7. The comparison of the microscope measurement of PSF pattern at the top edge for all layer depths and layer separations between the Person 1 and the Person 2 to show that the measurement difference can be caused by subjective judgement which leads to the measurement errors.	- 83 -
Table 5-1. The parameter settings for the depth, attenuator and the measured values of the laser output power (in mW) and the corresponding energy per pulse (in nJ) at the repetition rate of 100kHz.....	- 115 -
Table 6-1. Microscope measurement (measured in μm) datasheet for the OCT phantom to show the alignment and the flatness of the surface when fabricating the sample.	- 150 -
Table 6-2. OCT system characterization and comparison of OCT systems results-	153 -
Table 6-3. Microscope measurement showing the comparison between the designed values and the measured value for the depth with the inscription linewidth and inscription height measured to show the consistency of the inscription size.	- 171 -

List of Figures

Figure 1-1. Tissue-mimicking phantom presented by Curatolo et al., which the phantom was fabricated from a silicone matrix and titanium dioxide additive by employing a lithographic casting method [18]. This image is [reprinted/reproduced] with permission from [18] © The Optical Society.....	- 25 -
Figure 1-2. A wide-field phantom eye presented by Corcoran et al., which the phantom was designed via using a 3D drawing software and each layer was 3D printed by using photo-polymerisation with sequential row deposition of multiple materials [20]. This image is [reprinted/reproduced] with permission from the publisher [20] under the terms of the Creative Commons CC BY license.....	- 26 -
Figure 1-3. OCT phantom presented by Sandrian et al., which the phantom was fabricated by using the combination of the femtosecond laser inscription and nanoparticle embedded resin where the nanoparticles was firstly added into the resin and then using a femtosecond laser to precisely etch a series of lines in depth with varied pulse energy and the translation speed [22]. This image is [reprinted/reproduced] with permission from the publisher [22].....	- 27 -
Figure 2-1. Schematical diagram showing the photoionisation regimes based on Keldysh's parameter (γ).....	- 35 -
Figure 2-2. Schematic diagram showing the avalanche ionisation process.	- 36 -
Figure 2-3. The schematic diagram showing the writing geometry of the laser beam....	- 43 -
Figure 2-4. The schematic diagram showing the longitudinal writing and the aberration caused by mismatch of the refractive index of two mediums.....	- 44 -
Figure 2-5. Basic OCT system simplified configuration.	- 48 -
Figure 3-1: Schematic diagram of the laser system set-up at a 1026nm central wavelength with a repetition rate of 100kHz and a 100x inscription lens.....	- 58 -
Figure 3-2: Conceptual diagram of the chirped pulse amplification (CPA) technique.-	60 -
Figure 3-3: The correlation between the measured average output laser power (in mW) and the attenuator position (in %).	- 61 -
Figure 3-4: Laser system Z-axis setup including Z-stage opto-mechanical layout includes viewing and machining camera.....	- 62 -
Figure 3-5: Phantom design and fabrication workflow.	- 63 -
Figure 3-6: The refractive index of fused silica at different wavelengths ranging from 200nm to 1500nm based on Malitson's equation [184].	- 65 -

Figure 3-7. A conceptual image showing the pixel size of a 3D OCT image and how it is built from multiple 2D B-scans, which are in turn constructed from 1D A-scans. - 67 -

Figure 3-8. The CCD camera image showing one corner of the substrate which is used for the substrate alignment as a reference point..... - 68 -

Figure 3-9. The CCD camera image showing different focus positions when aligning the substrate where P1 and P2 are two different points showing the focus position. The top left image shows the close to focus position for the P1 and the bottom left image shows the in-focus position for P1. The top right image shows the out of focus position for P2 and the bottom right image shows the in-focus position for P2. - 69 -

Figure 3-10. The CCD camera image showing that a series of small-sized cross shape inscriptions to help to guide when aligning the sample on the fabrication stage. - 70 -

Figure 3-11. A ruler scale printed on a projector paper is used to quantify the alignment process where the printer ruler paper was attached on a PC monitor for guiding the alignment. - 71 -

Figure 3-12. The images showing how to apply this screen-to-ruler method in the alignment process: (a) The image shows the out-of-focus position at the chosen reference point where it is located at 4cm along the X-axis; (b) The image shows the in-focus position at the chosen reference point where it is located at 2cm along the X-axis. - 72 -

Figure 3-13. (a) Planar OCT phantom pattern conceptual layout; (b) Femtosecond laser fabricated planar OCT phantom (previously developed at Aston by Lee et al. [21]); (c) The conceptual images of four test patterns for both the top-view (at the X-Y plane) and the cross-sectional view (at the Y-Z plane) with the index lines/guidelines indicated in red..... - 74 -

Figure 3-14. Microscope measurement of the thinnest linewidth of $1.98\mu\text{m}$ in the sensitivity pattern at the top edge (i.e. the inscription with lowest laser pulse energy of the set energy range)..... - 77 -

Figure 3-15. Microscope measurement of the thicker linewidth of $3.63\mu\text{m}$ in the sensitivity pattern at the bottom edge (i.e. the inscription with higher laser pulse energy). - 78 -

Figure 3-16. Microscope image showing both the index lines (guidelines) and the test lines of the sensitivity pattern as the index lines (guidelines) are used to help the user to locate the test area. - 78 -

Figure 3-17. Microscope image of the line separation measurement of the lateral resolution pattern (Set 1). For Set 1, the line separation between each inscription lines were set to be varied in the range of $1\text{-}10\mu\text{m}$ - 80 -

Figure 3-18. Microscope image of the line separation measurement of the lateral resolution pattern (Set 2). For Set 1, the line separation between each inscription lines were set to be varied in the range of 11-20 μm - 80 -

Figure 3-19. Microscope image of line separation measurement of the lateral resolution pattern (Set 3). For Set 3, the line separation between each inscription lines were set to be varied in the range of 21-30 μm - 81 -

Figure 3-20. Microscope image of line separation measurement of the grid pattern showing the cell size of $\sim 100\mu\text{m} \times 100\mu\text{m}$ and the inscription linewidth of 2.64 μm . - 81 -

Figure 3-21. Microscope images using a 20x objective lens indicating how the focus position was determined for the measurement: (a) when focused on the top of the inscription at 97.791 μm ; (b) when at the in-focus position at 102.816 μm ; (c) when focused on the bottom of the inscription at 108.018 μm - 84 -

Figure 3-22. OCT image of point spread function (PSF) pattern (taken by Optimec is830 system with a central wavelength of 830nm and an axial resolution of 12 μm (in air).- 85 -

-

Figure 3-23. OCT image of sensitivity pattern (taken by Optimec is830 system with a central wavelength of 830nm and an axial resolution of 12 μm (in air). - 86 -

Figure 3-24. OCT image of lateral resolution pattern (taken by Optimec is830 system with a central wavelength of 830nm and an axial resolution of 12 μm (in air). - 86 -

Figure 3-25. OCT image of distortion pattern (taken by Optimec is830 system with a central wavelength of 830nm and an axial resolution of 12 μm (in air). - 87 -

Figure 4-1. The conceptual design for the laser power test pattern showing the design parameters: (a) the view from the X-Y plane with the parameters indicated; (b) a 3D view for the test pattern inside a substrate, where the Y-Z plane showing the cross-sectional image which is how the OCT system usually scans the sample in a 2D scanning mode. - 91 -

Figure 4-2. The microscope image using a 5x objective lens is to inspect the laser energy test pattern, which shows the pair line separation is measured as 20.11 μm , the pair separation is measured 199.73 μm and the separation between pairs is measured as 179.62 μm - 92 -

Figure 4-3. Microscope image using a 20x objective lens shows the inscribed laser power test pattern with the line spacing (measured as 20.76 μm), the pair spacing (measured as 200 μm) and index line annotated in the middle. - 93 -

Figure 4-4. Microscope image using a 20x objective lens showing how the measurement of the inscription linewidth were taken and the measurement points (i.e. 4 measurement points) were selected. In this image, it shows that the linewidth is measured as 5.27 μm for the top pair of inscriptions and 4.94 μm for the bottom pair of inscriptions. - 94 -

Figure 4-5. Microscope images using a 20x objective lens of the first layer of the laser energy test pattern to demonstrate the sample measurement process, where from (a) to (j), it represents the inscription was applied with different laser energy levels, with (a) representing with 5% of the laser power (i.e. 150nJ for energy per pulse at 100kHz), and (j) representing with 100% of laser power (i.e. 3.08μJ for energy per pulse at 100kHz). - 97 -

Figure 4-6. The graph shows the correlation between the linewidth and the laser power based on the microscope measurement data at the X-Y plane at eight different layer depths ranging from 100μm to 1150μm with trend lines and error bars indicated... - 98 -

Figure 4-7. Conceptual diagram for the cross-sectional profile of the laser power test pattern on the Y-Z plane with the parameters indicated. - 99 -

Figure 4-8. The microscope setup for capturing the cross-sectional images..... - 100 -

Figure 4-9. The cross-sectional image of the laser power test pattern by using a 10x objective lens showing a detailed view of the inscription with the measurement of the inscription height (i.e. 40.13μm for 75% of the laser power at ~250μm depth in AD) and the layer separation (i.e. ~219μm) indicated. In this image, it shows the cross-section of the higher energy levels (i.e. 75% - 85% of the total laser power) at top layers (i.e. 250μm - 550μm for the apparent depth from the top surface). The pair separation was measured as 200.94μm. - 101 -

Figure 4-10. The microscope images showing the cross-sectional profile of the laser test pattern using a 5x objective lens: (a) the laser power of 5% - 50% of the total power (i.e. 150nJ - 1.48μJ for energy per pulse); (b) the laser power of 55% - 100% of the total power (i.e. 1.63μJ - 3.08μJ for energy per pulse). - 104 -

Figure 4-11. Summarised line plot diagrams present the correlation between the inscription height and the laser power based on the microscope measurement for all eight layers in the Y-Z plane showing the possible onset of filamentation. Large scale figures are included in Appendix B section for reference..... - 106 -

Figure 4-12. OCT image taken by Optimec is830 SD-OCT system showing the laser power test pattern with a scan size of 4.94mm x 4.55mm with a pixel size of 4.94μm x 8.89μm. The red quadrilateral shape labelled in the image is the ideal laser power range that should be used for the inscription while the green square shape highlighted in the image shows inscriptions that are elongated significantly at this power range, which should be avoided as the inscription shape is distorted..... - 107 -

Figure 4-13. The microscope images using a 5x objective lens show the cross-sectional view of the layer thickness: (a) inscription made with 20% of the laser power with the total inscription depth of ~450μm (in AD); (b) inscription made with 80% of laser power with the layer separation of 150 μm with the total inscription depth of ~1150 μm (in AD);

(c) inscription made with various laser power applied for each layer varied from 20% to 55% with the layer separation of 150 μm so that resulted in the total inscription depth of $\sim 1150 \mu\text{m}$ (in AD)..... - 110 -

Figure 5-1. Femtosecond laser inscribed phantom (based on the previous phantom design developed by Lee et al. [21]) with a greater inscription depth: (a) the front face of the phantom with four patterns indicated; (b) the cross-sectional view for both the current design and the previous design to demonstrate the difference in inscription depth.- 113 -

-

Figure 5-2. Illustration of the previous fabrication process: (a) the inscription writing direction on the X-Z plane for one slice where L1- L8 indicating the layer number at different depths; (b) the writing process for a structure. Note the red arrows signify stage movement between each slice without inscription, black lines signify inscription and green arrows denote stage movement within a slice without inscription. - 115 -

Figure 5-3. Patten design structure of the point spread function (PSF) phantom: (a) the layer pattern on the X-Y plane with index lines and test pattern area indicated; (b) cross-sectional profile of the phantom pattern showing the parameter settings; (c) 3D pattern structure showing every dimension of the pattern. - 118 -

Figure 5-4. Illustration showing the new fabrication method with the writing direction, index lines, and test layer pattern indicated. In the diagram, the black solid line was used to indicate the writing direction and the red dashed line was used to indicate the moving direction. In the real fabrication, 8 layers had been inscribed rather than 4 layers shown in the diagram for the illustration purposes. - 119 -

Figure 5-5. Patten design structure of the sensitivity phantom: (a) the layer pattern showing the first 4 test sets on the X-Y plane with index lines and test pattern area indicated; (b) cross-sectional profile of the phantom pattern of the first 4 test sets showing the parameter settings; (c) 3D pattern structure of the first 4 test sets showing every dimension of the pattern. Please note, there were 6 sets included in the real design and the fabrication. - 121 -

Figure 5-6. Patten design structure of the lateral resolution phantom: (a) the layer pattern showing the first 4 test sets on the X-Y plane with index lines and test pattern area indicated; (b) cross-sectional profile of the phantom pattern of the first 4 test sets showing the parameter settings; (c) 3D pattern structure of the first 4 test sets showing every dimension of the pattern. Please note, there were 10 sets included in the real design and the fabrication. - 124 -

Figure 5-7. Patten design structure of the distortion/grid phantom: (a) the layer pattern showing the grid pattern on the X-Y plane; (b) cross-sectional profile of the phantom

pattern showing the parameter settings; (c) 3D pattern structure showing every dimension of the pattern. - 126 -

Figure 5-8. The microscope image using a 5x objective lens showing the overall pattern of PSF phantom. The line separation of $150.13\mu\text{m}$ is indicated. - 127 -

Figure 5-9. Microscope images using a 20x objective lens showing the linewidth measurement for all eight layers (from (a) to (h)) of the PSF phantom with layer depth and the linewidth indicated. With the varied laser power, the linewidth can be kept consistently for all the layer depths, measured as $2.64\mu\text{m}$ - 128 -

Figure 5-10. The microscope image using a 5x objective lens showing the cross-sectional profile of the PSF phantom: (a) the new phantom design has a larger layer depth of $150\mu\text{m}$ in apparent depth (AD), with the layer separation measured in real depth (RD) as $219.84\mu\text{m}$ and a total inscription depth of $1534.84\mu\text{m}$; (b) the previous phantom design with a smaller layer depth of $50\mu\text{m}$ (in AD), with the layer separation measured in real depth (RD) as $72.39\mu\text{m}$ and a total inscription depth of $508.04\mu\text{m}$ - 129 -

Figure 5-11. OCT images for the point spread function (PSF) phantom showing both (a) the current design with a greater layer separation and (b) the previous design with smaller layer separation in order to make a comparison and present the change in design. Both the OCT images were taken by Optimec is830 SD-OCT system. The measurement values indicated in the image are showing in real depth (RD). - 130 -

Figure 5-12. The OCT image showing the pixel size (labelled in red square) compared with the point size of the PSF phantom. This image also provides a close-up look for the fabrication. - 131 -

Figure 5-13. The microscope images using a 5x objective lens showing the overall pattern of the sensitivity phantom structure: (a) one of the test sets (Set 4); (b) one of the index line sets (Set 4). - 133 -

Figure 5-14. The microscope images using a 20x objective lens showing the linewidth of the inscription: (a) the linewidth of the third energy level pair (i.e. 11.6% of the laser average output power) measured as $1.32\mu\text{m}$; (b) the linewidth of the highest energy level pair (i.e. 100% of the laser average output power) measured as $6.92\mu\text{m}$ - 133 -

Figure 5-15. The microscope image using a 5x objective lens showing the cross-sectional profile of the sensitivity phantom: (a) the phantom design with a larger layer depth ($150\mu\text{m}$ setting for the layer separation) for set 3; (b) the phantom design with a smaller layer depth ($50\mu\text{m}$ setting for the layer separation) for set 3; (c) the phantom design with a larger layer depth ($150\mu\text{m}$ setting for the layer separation) for set 6; (d) the phantom design with a smaller layer depth ($50\mu\text{m}$ setting for the layer separation) for set 6. - 135 -

Figure 5-16. OCT images for the sensitivity phantom showing both (a) the current design with a greater layer separation and (b) the previous design with smaller layer separation in order to make a comparison and present the change in design. Both the OCT images were taken by Optimec is830 SD-OCT system. The measurement values indicated in the image are showing in real depth (RD). - 136 -

Figure 5-17. The microscope image of the lateral resolution phantom using a 5x objective lens shows the overall pattern and the line separation variation for the set 3 and the set 4 of the pattern. - 137 -

Figure 5-18. The microscope image of the lateral resolution phantom using a 20x objective lens to show the line separation variation (i.e. range from 21-30 μ m) for set 3 with the measurement values labelled in the image. - 138 -

Figure 5-19. The microscope image of the lateral resolution phantom using a 5x objective lens to show the cross-sectional view of the pattern structure of set 2 and set 3: (a) the current phantom design with a larger layer depth (150 μ m in AD setting for the layer separation) for both set 2 and set 3 with a total inscription depth of 1534.86 μ m in RD; (b) the previous phantom design with a smaller layer depth (50 μ m in AD setting for the layer separation) for both set 2 and set 3 with a total inscription depth of 508.03 μ m in RD. - 139 -

Figure 5-20. OCT images for the lateral resolution phantom showing both (a) the current design with a greater layer separation and (b) the previous design with smaller layer separation in order to make a comparison and present the change in design. Both OCT images were taken by Optimec is830 SD-OCT system. The measurement values indicated in the image are showing in real depth (RD). - 140 -

Figure 5-21. The microscope image of the distortion/grid phantom using a 5x objective lens to show the overall pattern with the measured cell size of 100.18 μ m x 100.53 μ m, as indicated in the image. - 141 -

Figure 5-22. The microscope image of the distortion/grid phantom using a 20x objective lens to show the detailed pattern with the measured cell size of 100.16 μ m x 100.16 μ m, as indicated in the image. - 141 -

Figure 5-23. The microscope image using a 5x objective lens showing the cross-sectional profile of the distortion/grid phantom: (a) the current phantom design with a larger layer depth (i.e. 150 μ m in AD setting for the layer separation) with the cell size measured as 100.54 μ m, the layer separation measured as 218.76 μ m in RD and a total inscription depth measured as 1534.84 μ m; (b) the previous phantom design with a smaller layer depth (i.e. 50 μ m in AD setting for the layer separation) with the cell size measured as 100.54 μ m, the layer separation measured as 72.39 μ m and a total inscription depth measured as 509.39 μ m. - 142 -

Figure 5-24. OCT images for the distortion/grid phantom showing both (a) the current design with a greater layer separation and (b) the previous design with smaller layer separation in order to make a comparison and present the change in design. Both the OCT images were taken by Optimec is830 SD-OCT system. The measurement values indicated in the image are showing in real depth (RD). - 143 -

Figure 6-1. Conceptual drawings of the OCT phantom pattern: (a) the view from the top; (b) the view from the side..... - 148 -

Figure 6-2. (a) Microscope image using a 5x objective lens from the planar side of the phantom, (b) the OCT phantom grid pattern cell size measurement using a 20x objective lens and giving the cell size of $\sim 100\mu\text{m} \times 100\mu\text{m}$, (c) the view from the curved side of the phantom. - 149 -

Figure 6-3. Microscope measurement points on the plano-convex lens..... - 150 -

Figure 6-4. Comparison of design parameters and measured values from the optical microscope of the OCT phantom design. Measurements are all based on apparent depth (AD)..... - 151 -

Figure 6-5. OCT images obtained from (a) the Optimec is830 system with a scan size of $\sim 12\text{mm} \times 5.6\text{mm}$ and (b) Thorlabs Ganymede SD-OCT system with a scan size of $\sim 4\text{mm} \times 1.9\text{mm}$ for comparison with design parameters and between OCT systems with annotations. - 152 -

Figure 6-6. OCT image taken from the curved side (by using the Thorlabs Ganymede SD-OCT with a central wavelength of 930nm and an axial resolution of $5.8\mu\text{m}$) .. - 153 -

Figure 6-7. OCT image taken from the curved side (by using the Optimec is830 system with a central wavelength of 830 nm and an axial resolution of $12\mu\text{m}$) - 154 -

Figure 6-8. The alignment requirement for the grid-like phantom: (a) Top-view of the grid pattern phantom with red lines indicating aligned scanning position; (b) Top-view of the grid pattern phantom with red lines indicating misaligned scanning position..... - 155 -

Figure 6-9. Conceptual diagram for the non-planar circle-like phantom with the top view and the cross-sectional view showed. - 156 -

Figure 6-10. Phantom design pattern: (a) the pattern initially tested and fabricated in a planar substrate; (b) the pattern fabricated in a curved lens (LA4380, Thorlabs) viewed under an OCT system (Optimec is830 SD-OCT system). - 157 -

Figure 6-11. The comparison of design parameter values and measured values from the microscope measurement of the OCT phantom by using a 20x objective lens. The layer depth is in apparent (measured) depth (AD)..... - 158 -

Figure 6-12. (a) Microscope image using a 5x objective lens taken from the planar side of the phantom; (b) microscope image using a 5x objective lens taken from the curved

side of the phantom; (c) microscope image using a 20x objective lens taken from the planar side at the 5th layer (at 752.485 μm in AD below the planar surface) showing a linewidth of 6.3 μm ; (d) microscope image using a 20x objective lens taken from the planar side at the 7th layer (at 1054.252 μm in AD below the planar surface) showing a linewidth of 6.3 μm - 161 -

Figure 6-13. OCT image taken from the planar surface of the phantom. The scan pattern FOV is 19.00mm x 5.42mm. The scale bar is 500 μm . The value indicated on this image is in real depth as the refractive index is applied. - 162 -

Figure 6-14. OCT image taken from the curved surface of the phantom. The scan pattern FOV size is 19.00mm x 5.42mm. The scale bar is 500 μm - 162 -

Figure 6-15. Femtosecond laser inscribed phantom: (a) the phantom design was initially tested on a planar substrate; (b) the phantom was then inscribed on a non-planar substrate. - 164 -

Figure 6-16. Microscope images using a 5x objective lens showing the landmark layer and the first test pattern layer: (a) the landmark layer viewing from the planar surface; (b) the first test pattern layer viewing from the planar surface with the diameter of the 1st circle measured as 508.8 μm ; (c) the landmark layer viewing from the curved surface; (d) the first test pattern layer viewing from the curved surface with the diameter of the 1st circle measured as 521.44 μm - 167 -

Figure 6-17. The microscope image using a 20x objective lens showing the landmark layer. - 168 -

Figure 6-18. Microscope images using a 20x objective lens showing the linewidth measurement for different depths: (a) the linewidth measured as 2.61 μm for the 1st layer located at depth of 150.603 μm (in AD); (b) the linewidth measured as 2.62 μm for the 2nd layer located at depth of 301.002 μm (in AD); (c) the linewidth measured as 2.59 μm for the 5th layer located at depth of 753.831 μm (in AD); (d) the linewidth measured as 2.64 μm for the 8th layer located at depth of 1204.62 μm (in AD). - 170 -

Figure 6-19. The microscope image showing the cross-sectional view of the circular phantom inscribed in a planar substrate fabricated using the same parameter settings with the inscription height measured. The layer separation was also measured as 219.84 μm (in real depth (RD)) and a circle separation measured as 254.69 μm - 171 -

Figure 6-20. OCT Image taken by Optimec is830 SD-OCT system from both the planar surface (a) and the curved surface (b). The scan size is 19.00mm x 4.55mm and the pixels size is 1900 x 512 pixel. The scale bar is 250 μm . The value indicated is in the real depth as the refractive index of 1.45 (at 830nm wavelength) is applied to the image. ... - 172 -

Figure 6-21. OCT images taken by a commercial OCT system (Carl Zeiss Cirrus HD-OCT): (a) viewing from the planar surface; (b) viewing from the curved surface... - 173 -

Figure 6-22. OCT image taken by Carl Zeiss Cirrus HD-OCT to show the pre-processing algorithm to fit a curve to the phantom..... - 174 -

Figure 6-23. Microscope images using a 5x objective lens showing the inscription from a curved surface: (a) at the centre of the pattern viewing from the planar side with the measurement of the radius of $\sim 254 \pm 1\mu\text{m}$; (b) at the edge of the pattern viewing from the planar side with the measurement of the radius of $\sim 258 \pm 1\mu\text{m}$; (c) at the centre of the pattern viewing from the curved side with the measurement of the radius of $\sim 254 \pm 1\mu\text{m}$; (d) at the edge of the pattern viewing from the curved side with the measurement of the radius of $\sim 254 \pm 1\mu\text{m}$ - 177 -

Figure 6-24. OCT images taken by Optime is830 system showing the inscription from a curved surface: (a) imaging from the planar side; (b) imaging from the curved side. The scan size is 19.00mm x 4.55mm and the pixels size is 1900 x 512 pixel. The scale bar is 250 μm . The value indicated is in the real depth as the refractive index of 1.45 (at 830nm wavelength) is applied to the image..... - 178 -

Figure 7-1. The schematic diagram showing the scanning position using a MEMS mirror. - 182 -

Figure 7-2. Schematic diagram showing the mirror movement for scanning the sample. - 183 -

Figure 7-3. The image showing the phantom fabricated using a femtosecond laser with 8 layers of circular patterns inside the substrate. The landmark layer pattern is highlighted in red. The phantom was designed and fabricated by the thesis author. - 184 -

Figure 7-4. The microscope image showing the inscribed pattern: (a) The overview image taken by the microscope using 5x objective magnification lens; (b) the microscope image showing the circular radius by using a 20x objective magnification lens. This microscope images were captured and measured by the thesis author..... - 184 -

Figure 7-5. Comparison between the designed parameter values and the measured parameter values for the fabrication of the OCT phantom. This graph was plotted by the thesis author. - 185 -

Figure 7-6. The OCT image taken by Optimec is830 SD-OCT systems: (a) the original OCT system; (b) Plot of detected real-time position and ideal true position on the OCT image. The OCT image was captured by Dr. Izzati Ibrahim and Dr. Benjamin Coldrick and analysed by Dr. Izzati Ibrahim with the thesis author's help to understand the phantom parameters..... - 186 -

Figure 7-7. The procedures used for the data collection and analysis for correcting the distortion. - 187 -

Figure 7-8. The plot showing the sinusoidal fitting of a distance between the consecutive points that might be due to the sinusoidal movement of the scanning mirror in projecting the location of the pixels. This graph was plotted by Dr. Izzati Ibrahim. - 188 -

Figure 7-9: Plot of the true position and the detected position on the OCT image. This image was analysed by Dr. Izzati Ibrahim. - 189 -

Figure 7-10. The OCT images showing the comparison between the original image and the transformed corrected image: (a) Image of OCT phantom before correction of scan spacing (RMSE spacing = 3.098) and (b) after correction (RMSE spacing = 1.046). This image was analysed by Dr. Izzati Ibrahim. - 190 -

Figure 7-11: Overlap original image (before correction (in red)) on corrected image (in green). This image was analysed by Dr. Izzati Ibrahim. - 191 -

List of Abbreviations

1D	One dimension
2D	Two dimension
3D	Three dimension
AD	Apparent depth
CCD	Charge-coupled device
CNC	Computer numerical control
CPA	Chirped Pulse Amplification
D	Distortion
dB	Decibel
DIC	Differential interference contrast
DOF	Depth of field
FD-OCT	Fourier domain optical coherence tomography
Fs	Femtosecond (10^{-15} s)
HAL	Tungsten-halogen lamp
HAZ	Heat-affected zone
Hz	Hertz
J	Joule
k	Kilo
LR	Lateral resolution
M	Mega
m	Milli
MEMS	Microelectromechanical systems
MPI	Multiphoton ionisation
n	Nano
NA	Numerical aperture
NIR	Near Infra-Red

ns	Nanosecond (10^{-9} s)
OCT	Optical coherence tomography
p	Pico
PC	Personal computer
PMMA	Polymethyl methacrylate
ps	Picosecond (10^{-12} s)
PSF	Point spread function
PVCP	Polyvinyl chloride-plastisol
RD	Real depth
S	Sensitivity
SB-OCT	Spectrometer-based optical coherence tomography
SD-OCT	Spectral domain optical coherence tomography
SESAM	Semiconductor saturable absorber mirror
SLD	Super luminescent diode
SS-OCT	Swept-source optical coherence tomography
TD-OCT	Time domain optical coherence tomography
TRT	Total retinal thickness
W	Watt
μ	Micro

Chapter 1

Introduction

Optical coherence tomography (OCT), first demonstrated in 1991 by David Huang, is a 3D imaging system which can provide non-invasive high-resolution real-time in-vivo images [1]. It is analogous to the ultrasound scan, although instead of the sound, it utilises the light [1, 2]. OCT techniques and systems have been intensively used in areas such as ophthalmology to help in the diagnosis of the retinal diseases [2-4] and dermatology for the diagnosis of skin diseases [5-7].

With the unique resolution range (i.e. 1-15 μ m) and penetration depth (i.e. 2-3mm) benefits offered by OCT imaging systems [2], enabling a deeper penetration depth compared with confocal microscopes and a higher resolution than ultrasound, which makes the OCT technique very unique for optical imaging as it can optimise both the scanning depth and imaging resolution [8]. Besides, OCT can be performed with no need to have physical contact to the sample or tissue, which provides a possible solution to scan especially when the standard biopsy is hazardous or impossible [2]. Potentially, OCT can also be considered using as a surgical guiding device as it provides a real-time 3D imaging [2], which has been proven to be a very useful tool for medical diagnosis and clinical management [2].

Currently, there is no standard available to be used to calibrate and compare the performance between different OCT systems used across the world. An optical device (so called OCT phantom) that can be used as a calibration tool and acting as a 3D optical ruler is therefore needed and to act as a reference point among different OCT systems.

An OCT phantom can be used to assess various performances of the OCT system such as point spread function (PSF), resolution, sensitivity, distortion and being able to qualitatively and quantitatively measure the system. It is useful and important when

developing the OCT system and validate a new built OCT system as well as comparing across different OCT systems.

A widely used 1951 USAF resolution testing target is used for the microscope optical resolution testing but it is only a two-dimensional (2D) test device. For the OCT system, as it can provide a depth profile of the sample, a 2D test target will no longer satisfy the needs as it fails to provide the depth information. Hence, a three-dimensional (3D) test device is needed for the purpose of the OCT system calibration.

To date, there have been various research works investigating OCT phantom fabrication. Several methods of fabricating OCT phantoms are presented and reviewed. The rationale behind the creation of an OCT phantom is that a universally accepted standard is required to assess, calibrate and compare different OCT systems [9-13].

Tomlins et al. created a PSF phantom by doping a clear epoxy resin with a low density of nanoparticles (i.e. mono-dispersed silica micro-spheres) [14]. The theory asserts that it can be used to characterise both the axial and lateral resolution with PSF widths of less than $7\mu\text{m}$ by using $1\mu\text{m}$ spheres [14]. However, it has been mentioned that the limited access to the raw data hinder widespread adoption [14]. Similarly, Agrawal et al. created a PSF phantom by embedding nanoparticles (i.e. gold-silica nanoshells) into an optically transparent medium, with resultant phantoms exhibiting a sub-micrometre spatial resolution [15]. However, the results exhibited some uncertainty due to the occasional aggregation of the particles and also the imperfections of the silicone [15].

Compared with those methods mentioned previously, Bykov et al. presented a different way for making OCT phantoms. The process involves making a skin phantom by using polyvinyl chloride-plastisol (PVCP) with titanium dioxide (TiO_2) powder and light-absorbing plastic ink used to introduce the scattering to the phantom [16]. However, the durability and the accuracy of the phantom is questionable, as the process involves estimated optical properties [16].

Kennedy et al. demonstrated a method to create a novel tissue-mimicking biocompatible phantom based on a fibrin matrix made of the mixture of fibrinogen and thrombin [17]. It has a short fabrication time (e.g. 30 minutes) [17] compared with other phantoms. However, further investigation on the scattering properties of such phantoms is needed due to the variability in measurement results shown by OCT systems [17].

Similarly, Curatolo et al. presented tissue-mimicking phantoms (shown in Figure 1-1) fabricated from a silicone matrix and titanium dioxide additive by employing a

lithographic casting method [18]. In this study, two phantoms were fabricated: one has no scattering elements; and one with scattering elements for comparison [18]. However, the fabrication procedure requires carefully manufactured frames and the lifetime is expected to be approximately 2 years [18].

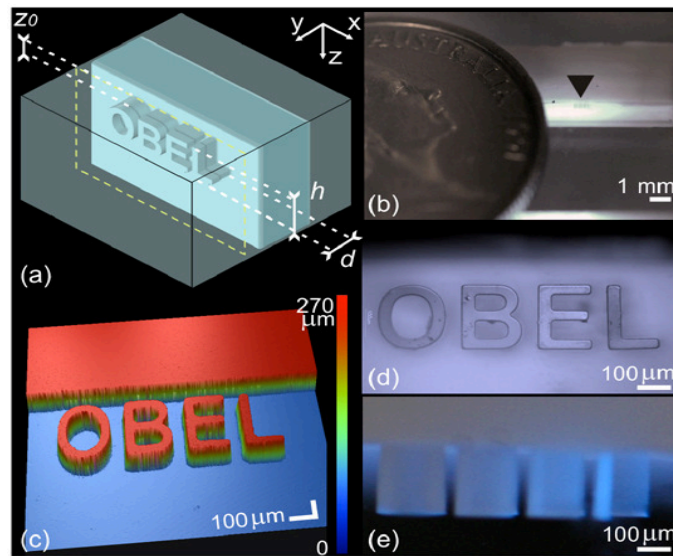


Figure 1-1. Tissue-mimicking phantom presented by Curatolo et al., which the phantom was fabricated from a silicone matrix and titanium dioxide additive by employing a lithographic casting method [18]. This image is [reprinted/reproduced] with permission from [18] © The Optical Society.

A retina-simulating phantom was created by Baxi et al. with a fabrication process involving layer-by-layer spin coating of nanoparticle embedded silicon which was finished with a laser micro-etching procedure [19]. Measurement results have shown that there is a disagreement presented on the measurement of the total retinal thickness (TRT) and there is an obvious discrepancy on the measurement of the profilometry [19].

Corcoran et al. fabricated a wide-field phantom eye (shown in Figure 1-2) by employing 3D printing technology [20]. It is designed via 3D drawing software and each layer is 3D printed by using photo-polymerisation with sequential row deposition of multiple materials before UV curing [20]. The measurement results show that both the resolution and accuracy of 3D printing are not sufficient when measuring the low transverse resolution as the phantom shows an irregular surface at larger field angles [20]. This study has shown an innovative method of fabricating OCT phantoms by using 3D printing technology.

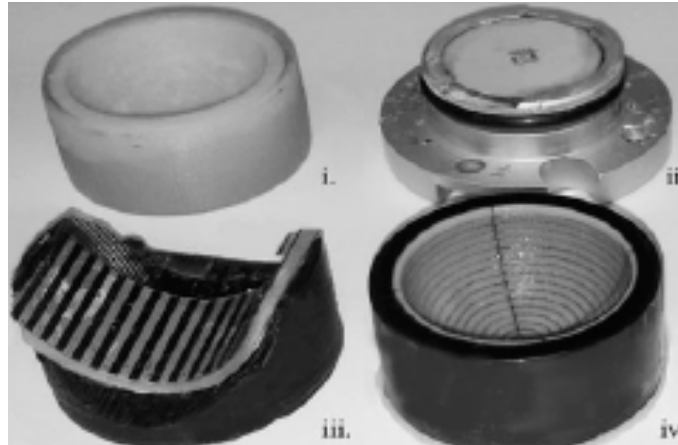


Figure 1-2. A wide-field phantom eye presented by Corcoran et al., which the phantom was designed via using a 3D drawing software and each layer was 3D printed by using photopolymerisation with sequential row deposition of multiple materials [20]. This image is [reprinted/reproduced] with permission from the publisher [20] under the terms of the Creative Commons CC BY license.

It can be noticed that all of these methods require multiple steps in the fabrication process. Moreover, the stability, accuracy and lifetime of OCT phantoms are still challenging to the adoption of phantoms as a comparison and calibration tool.

An innovative method using femtosecond laser micro-inscription techniques to fabricate test phantoms has been explored by Tomlins et al [9]. In this study, a PSF phantom was created on a clear fused silica substrate which consisted of a regular series of line defects with different pulse energies and depths. The phantoms were utilised to evaluate the visibility under an OCT system [9]. This method enables the accurate positioning of the defects and it shows the possibility of a highly repeatable fabrication process [9].

The use of the femtosecond laser micro-inscription techniques has been further investigated by numerous researchers. Lee et al. inscribed four unique patterns (including PSF, sensitivity, lateral resolution and distortion) on fused silica substrate to measure various the parameters of an OCT system [21]. Quantitative methods still needed further development in order to measure the performances of the OCT system [21]. Sandrian et al. demonstrated a method using the combination of the femtosecond laser inscription and nanoparticle embedded resin to fabricate the phantom (shown in Figure 1-3) [22] where the sample was precisely etched using a femtosecond laser with a series of lines in depth inscribed with varied pulse energy and translation speed after the nanoparticles were added into the resin. However, the phantom was limited in terms of the inscription depth [22].

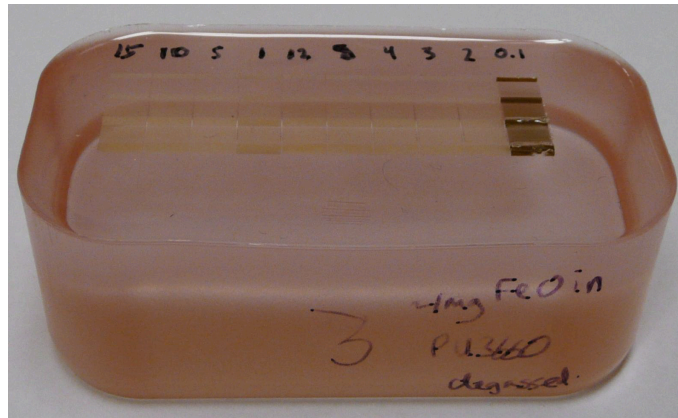


Figure 1-3. OCT phantom presented by Sandrian et al., which the phantom was fabricated by using the combination of the femtosecond laser inscription and nanoparticle embedded resin where the nanoparticles were firstly added into the resin and then using a femtosecond laser to precisely etch a series of lines in depth with varied pulse energy and the translation speed [22]. This image is [reprinted/reproduced] with permission from the publisher [22].

Different methods of making OCT phantoms have been reviewed. It can be seen that nanoparticle embedded methods have disadvantages in terms of the consistency and stability in the phantom fabrication process. Moreover, the accuracy of using phantoms to test OCT systems is still questionable. However, the use of femtosecond laser inscription on a transparent media (i.e. fused silica substrate) has shown a highly repeatable method to accurately reproduce the phantom. Hence, it is a potential area for research and will be discussed in further detail in the next section.

The rationale for this project is based on the fact that there is currently no standard used to calibrate or compare the performance of an OCT system. As the previous literature [10, 21, 22] showed the femtosecond laser direct writing process enable a highly repeatable and accurate fabrication process, it leads to the main research question of this project to further research how femtosecond laser machining techniques can be utilised in the creation of OCT calibration phantoms and whether these artefacts can fulfil the purposes that can be used to calibrate and assess the performance of different OCT systems. Therefore, the aim of this work is to design novel OCT calibration phantoms using the femtosecond laser inscription process that the phantom can be used to quantitatively characterise and calibrate across different OCT systems.

To enable to reach the aim, the following objectives need to be fulfilled. First of all, a further investigation on femtosecond laser fabrication process is needed to understand how the phantom to be made and to optimise the current fabrication process. Secondly, as the existing phantom cannot fully fulfil the purpose as a multi-purposed calibration phantom, such as not being able to detect the image distortion and validate the post-

processing algorithms and an inability to test a broad range of OCT systems with differing axial and lateral resolutions, the second objective for this project is to continue previous work to develop new novel calibration phantoms that can fulfil those purposes.

Moreover, the third objective is to focus on the non-planar phantom development as the OCT image distortion caused by the nature of the curvature structures needs to be further investigated and a solution will benefit the accuracy of the OCT system. Potentially, with using the phantom, a quantitative method on how to correct the image distortion can be presented. In addition to this missing technology, there is also the potential for such work to generate impact via the process of commercialisation to benefit to those OCT end users.

1.1 Thesis structure

Here presents the thesis structure and brief summary addressing each individual chapter with published conference and journal papers highlighted.

Chapter 2 This chapter presents the fundamental background theory behind the research work and critically reviews and evaluates previous work to explore possible directions for the research work on the development of OCT phantoms. First of all, the physical mechanism of the femtosecond laser and material interaction are presented. Secondly, the experimental considerations (i.e. polarisation, repetition rate, pulse duration, writing geometry, aberrations and self-focusing) are investigated. Thirdly, OCT basic principles are introduced, and different OCT systems and techniques are compared. Key performance parameters of the OCT system and the issue of the image distortion are highlighted.

Chapter 3 This chapter presents the details and specifications of the experimental equipment and processes used for OCT phantom design, fabrication, characterisation and calibration in this thesis. Firstly, the femtosecond laser system and the experimental setup are presented, which includes a description of the laser head and optical components along the beam delivery path in the system. Secondly, the workflow of the phantom design and fabrication are described. Thirdly, the phantom substrate and material considerations are introduced and studied. Moreover, a detailed description of the sample alignment procedure when placing the substrate on the fabrication stage is given. After the laser fabrication process, phantom characterisation using a microscope and OCT systems is described. Finally, a study of the existing planar phantom, including

the parameter settings, the fabrication process and characterisation process are investigated.

Chapter 4 This chapter presents the research work for the study on the laser power and the fabrication optimisation. The chapter starts with a brief introduction to discuss the current issue and further improvements that needed on the fabrication process optimisation. Then, the design and fabrication of a laser power test pattern are described, which is used for the laser power study. Furthermore, a detailed study is presented on investigating the correlation between the laser pulse energy and the inscription size which includes the inscription linewidth study on the X-Y plane and the inscription height study on the Y-Z plane. The findings from those studies directly contribute to standardisation and optimisation of the phantom fabrication process. Finally, the fabrication optimisation implemented on a revised design is presented to verify the findings.

Chapter 5 This chapter presents work on the planar OCT calibration phantom development. Firstly, a new fabrication method is introduced that is designed to optimise the fabrication process. After discussing the fabrication approach, characterisation of the new phantom design is presented which include both the microscope characterisation and the OCT system characterisation. A detailed side-by-side comparison is made between the previous design and the new optimised design to show the improvement.

Chapter 6 This chapter presents the research work on the development of a novel non-planar OCT calibration phantom, which includes two published conference papers on the first two non-planar OCT phantoms that were proposed to be used as a potential multipurpose OCT system calibration tool. The first non-planar phantom was fabricated and reported in 2018 at Photonics West conference, where the design was based on a grid pattern to test the image distortion and was the first phantom demonstrated in a non-planar (i.e. plano-convex) lens to prove the idea that a curved phantom can be used as a self-referencing and comparison tool for OCT systems. The second non-planar phantom was designed, fabricated and reported in 2020 at Photonics West conference, which addressed alignment issues seen with the initial phantom due to the grid patterns requiring a high level of alignment to the nearest 90° angle. The third non-planar phantom was an upgraded version based on the same pattern design but with the layer energy setting refined so that the inscription would show the consistency on layer thicknesses for every single layer, and it also reduce the effect of the laser beam filamentation. In addition, the results of an inscription attempted from the curved surface

are given to illustrate the fabrication challenges with non-planar substrates and the resulting distortion caused by the curvature of the lens.

Chapter 7 This chapter presents the OCT phantom application for detecting OCT system scanning errors and provides a phantom-based method to correct the distortion caused by such errors. The scanning mechanism of the OCT system is briefly introduced. The phantom design, fabrication and characterisation are then presented. The image analysis and correction methods are described to indicate the use of the OCT phantom to detect the system scanning error and acting as a reference point to correct the image.

Chapter 8 This chapter concludes the thesis and highlights the key findings. It also proposes future works which covers potential directions and areas to expand this research work further.

Chapter 2

Theory

This chapter presents the fundamental background theory behind the research work and critically reviews and evaluates previous work to explore possible directions for the research work on the development of OCT phantoms. Firstly, the physical mechanism of the femtosecond laser and material interaction are presented (Section 2.1). Secondly, the experimental considerations (Section 2.2) (i.e. polarisation, repetition rate, pulse duration, writing geometry, aberrations and self-focusing) are investigated. Thirdly, in Section 2.3, OCT basic principles are introduced, and different OCT systems and techniques are compared. Key performance parameters of the OCT system and the issue of the image distortion are highlighted.

2.1 Femtosecond laser-material interactions

Femtosecond lasers enables ultra-high precise and versatile three-dimensional (3D) micro/nano-structures to be fabricated inside of materials [23] due to its unique characteristics of ultrashort pulse width ($\sim 10^{-15}$ s) and extremely high peak intensity ($> 10^{14}$ W/cm²) [24-26] irradiating with tightly focused laser beam. In recent years, femtosecond lasers have gained intensive interest and been widely used for fabricating photonic devices for applications including material processing [27, 28], waveguides [29-31], optical data storage [32-34], microfluidics [35, 36], lab-on-a-chip [24, 37, 38] and laser surgery [39, 40] within transparent materials [27] such as glasses [29, 41], crystals [42-44] and polymers [45, 46]. After the femtosecond laser irradiation, various highly localised microstructures have been formed such as permanent refractive index changes and micro-voids [41] within the focal volume in a spatially selective manner [26].

Femtosecond laser machining has been rapidly developed since it was firstly demonstrated in fused silica in 1994 [47] and metal films in 1995 [48]. In 1994, Du et al. investigated the laser-induced breakdown threshold in transparent materials (i.e. fused silica (SiO₂)) using 780nm laser pulses over a wide range of pulse widths from 7ns to 150fs, which the experimental data was strongly agreed with the impact ionisation theory [47]. Moreover, the experimental results showed that precise control of the interaction region can be achieved due to the generated plasma by using ultrashort pulses remained localised during breakdown which can benefit for material processing and medical laser applications [47].

In 1995, Pronko et al. demonstrated the capability that the femtosecond laser can create very small features over nanosecond pulses due to the minimised effect of thermal diffusion by using ultrashort pulses to reduce the heat-affected zone (HAZ) formation [26, 48, 49]. The paper presented laser ablated holes in metal films (i.e. gold and silver films) that had a diameter of 300nm located at depth of 52nm which had been created by using a 200fs, 800nm femtosecond laser. The smallest hole diameter was around 10% of the spot size, this compared favourably to those produced by nanosecond pulses where the smallest diameter was around 60% of the spot size [48].

In 1996, Davis et al. created the first 3D waveguide using an 120fs, 810nm femtosecond laser on various glasses [29]. The sample structures were directly inscribed by translating the stage either parallel or perpendicular to the incident laser beam and positive refractive index changes that were restricted to the region at the focal point of the laser were observed [29]. In the meantime, Glezer et al. demonstrated the use of a

780nm, 100fs femtosecond laser to produce localised sub-micrometre structures for 3D optical data storage in transparent materials without affecting the surface [32]. Both research works demonstrated the potential to fabricate complex 3D structures inside transparent bulk glasses by using tightly focused femtosecond pulses through a microscope objective.

2.1.1 Nonlinear excitation mechanisms

In non-metallic materials, electrons are strongly bounded to the lattice in the valence band. A direct single photon linear absorption cannot be achieved due to the lack of energy to exceed the bandgap energy to the conduction band for transparent dielectric materials. Therefore, to promote an electron from the valence band, nonlinear absorption processes are required [50]. When the laser intensity is high enough and tightly focused inside the material, a nonlinear absorption process can occur to modify the material within the focal volume without causing absorption at the surface [27]. The nonlinear excitation mechanisms include two classes – photoionisation and avalanche ionisation. The nonlinear ionisation process includes the following steps. First of all, the nonlinear photoionisation that initially generate free electrons, which includes two regimes that are multiphoton ionisation [51] and tunnelling ionisation [52]. With free electrons provided by photoionisation, through the avalanche ionisation [53] process, the density of the free electron grows. Once enough energy is absorbed, a plasma is formed therefore leads to the modification in the material due to the deposition of the energy.

2.1.1.1 Photoionisation

Photoionisation refers to the process that direct excitation of electrons by using the laser field [50] so that free electrons can be promoted from the valence band to the conduction band. There are two regimes of photoionisation – multiphoton ionisation and tunnelling ionisation which depends on the laser frequency and intensity [54].

Tunnelling ionisation

In tunnelling ionisation regime, the nonlinear ionisation is typically dominated by lower laser frequency and strong laser fields [50, 54]. It happens when the strong electric field of the laser suppress the Coulomb potential well to enable the bound electrons to tunnel out and become free [50, 54].

Multiphoton ionisation

In the multiphoton ionisation regime, the nonlinear ionisation is typically dominated by high laser frequencies (but still below that required for single photon absorption) [50, 54], where simultaneous absorption happens as multiple photons are absorbed by one electron in the valence band [50]. Both the material bandgap energy and the laser wavelength can affect the number of photons that are needed to be equal or greater than the bandgap of the chosen material [55]. The relationship between the bandgap energy of the material and the number of photons can be expressed in Equation 2-1 [54, 56].

$$k\hbar\omega \geq E_{bg}$$

Equation 2-1

where k represents the number of photons, \hbar represents Planck's constant, ω represents the frequency of the incident laser, $\hbar\omega$ is the single photon energy and E_{bg} represents the bandgap energy of the material [54]. The minimum k number of photons are required. In fused silica, the bandgap energy is 9eV [50, 55] while the single photon energy is around 1.5eV (at 800nm wavelength). Therefore, k is 6 for number of photons required to free one electron [57].

There is a transition as an intermediate regime between the tunnelling ionisation and the multiphoton ionisation that was expressed by Keldysh's parameter (γ) [52, 54, 58, 59]. The Keldysh's parameter (γ) is defined in Equation 2-2.

$$\gamma = \frac{\omega}{e} \sqrt{\frac{m c n \varepsilon_0 E_{bg}}{I}}$$

Equation 2-2

where γ represents the Keldysh's parameter, ω represents the frequency of incident laser, e represents the charge of the electron, m represents the effective mass, c represents the speed of light, n represents the refractive index of the material, ε_0 is the permittivity of free space, I represents the laser intensity at the focus and E_{bg} represents the bandgap energy of the material [54].

The occurrence of photoinisation mechanisms based on Keldysh's parameter is described by the schematic diagram shown in Figure 2-1. When $\gamma < 1.5$, the tunnelling ionisation dominates the nonlinear absorption process. However, when $\gamma > 1.5$, the multiphoton ionisation dominates the nonlinear absorption process. When $\gamma \approx 1.5$, the

intermediate regime, both the tunnelling ionisation and multiphoton ionisation involved in the nonlinear absorption process. Therefore, Keldysh's parameter (γ) enables both regimes to be included into one theoretical framework [58].

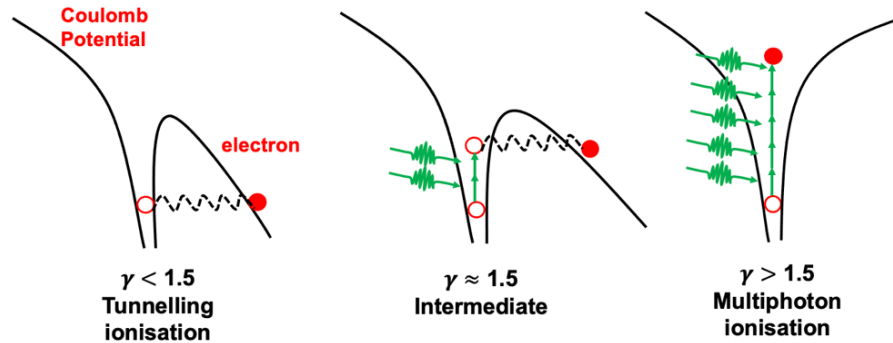


Figure 2-1. Schematic diagram showing the photoionisation regimes based on Keldysh's parameter (γ).

The photoionisation rate for the multiphoton ionisation strongly depends on the laser intensity [54, 56] and can be expressed as function of laser intensity [57] in Equation 2-3.

$$P(I)_{MPI} = \sigma_k I^k$$

Equation 2-3

where σ_k represents the multiphoton absorption coefficient for absorbing k photons and I represents the intensity of incident laser [54, 60].

2.1.1.2 Avalanche ionisation

Avalanche ionisation occurs with free carrier absorption followed by impact ionisation [54, 58] with the schematic diagram shown in Figure 2-2. When free electrons are available in the conduction band of the material, they are treated as seed electrons for avalanche process that can be either provided easily by ionised impurity or defect states through thermal excitation, or by carriers excited through photonisation (i.e. tunnelling ionisation or multiphoton ionisation) [54]. The available electron in the conduction band can linearly absorb several laser photons sequentially until gaining enough energy to exceed the conduction band minimum by more than the bandgap energy that enables to move to higher energy states in the conduction band [54]. The energetic electron can then impact ionise another electron from the valence band resulting in two electrons near

the conduction band being freed at minimum [54, 60]. With further free-carrier absorption and impact ionisation from these two electrons, more electrons can be ionised from valence band. The process is repeated with the presence of the laser fields leading to the density of the electrons growing exponentially [50]. The electron density grows until the plasma frequency is resonant with the laser frequency (i.e. the critical density) leading to the reflection or absorption of the laser energy [27, 54]. A rate equation for the electron density growth in the conduction band is given by Equation 2-4 [54].

$$\frac{dN}{dt} = \eta N = \alpha I N$$

Equation 2-4

where N represents the density of the electrons, η represents the avalanche ionisation rate, α represents the avalanche ionisation coefficient and I represents the laser intensity. As the avalanche rate linearly correlates with the laser intensity, therefore $\eta = \alpha I$ [61]. However, it has been proved that only 200fs and above pulse widths can largely contribute into the impact ionisation process as this gives enough time for electron density grow exponentially [62]. The femtosecond laser used for the experiments presented in this thesis has a pulse width around 500fs, which results in the avalanche ionisation mainly dominating the material modification process.

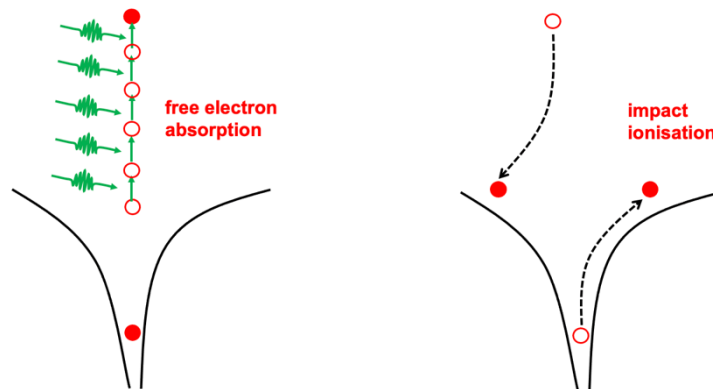


Figure 2-2. Schematic diagram showing the avalanche ionisation process.

As a result of the nonlinear excitation mechanism, the deposited energy is transferred from laser radiation fields to the electrons and then transferred to the lattice to heat up the material [50, 58]. As the time scale of the energy transfer is much shorter than the thermal diffusion time, it leads to a permanent structural modification in the material [54]. The dynamics of energy transfer strongly depends on the input laser pulse duration [58]. For a femtosecond laser, the timescale for nonlinear absorption is much shorter than the

timescale for the energy transfer in the material, therefore the nonlinear absorption and the heating process can be treated separately [50, 61]. With the advantages provided by ultrafast pulses (i.e. femtosecond laser pulses), the optical breakdown intensity can be achieved with less energy deposited in the material so that it leads to a more precise ablation or material modification [54].

2.1.2 Modification regimes

Depending on the laser pulse energies, there are three types of material modifications can be produced in the bulk of transparent materials using the femtosecond laser direct writing technique including homogenous modification associated with smooth refractive index change [30], birefringent refractive index change [63, 64] and void formation [50, 58, 65]. The modification is strongly dependent on the laser pulse duration and the laser energy [65, 66] but also other experimental parameters such as repetition rate, focusing numerical aperture (NA), laser wavelength, polarisation and material properties [67]. However, in fused silica, those three types of modification can be simply observed by only changing the laser energy [68].

2.1.2.1 Smooth refractive index change

With lower pulse energies that are higher than the material damage threshold, material modification associated with either positive or negative refractive index change can occur at the focal point of the laser beam depending on the material properties. This regime benefits the fabrication for optical waveguide since it can ensure a smooth and uniform refractive index change [69]. Refractive index changes on order of 10^{-3} can be typically observed in fused silica irradiated by femtosecond laser pulses [65, 70-73]. Different models and hypotheses were proposed for explaining the isotropic refractive index change, although exact mechanisms are still not fully understood [58]. However, possible causes for inducing the smooth refractive index change can be explained by contributions of the following models or hypotheses [50] – thermal effects such as melting [74, 75], stress-induced changes [76, 77], colour centre formation [72, 78-80], and structural change such as densification [74, 81-84].

Miura et al. investigated the permanent photo-written optical waveguide formation on various types of glasses by using femtosecond laser pulses at 800nm with 120fs pulse width that the visible laser damages only showed in the laser focused region inside of material [30]. The mechanisms for inducing the positive refractive index changes were believed to be due to various phenomena such as the local densifying, colour centre

formation and thermal effects such as melting [30]. Itoh et al. also observed a higher refractive index change in fused silica that can be attributed to thermal related effects as localised melting and rapid quenching of the glass [68]. Chan et al. used a tightly focused 800nm, 130fs laser at 1kHz repetition rate to modify inside the glass, the results of which showed that from the increased density that the mechanisms were induction of a localised plasma followed by micro-explosion inside the glass [74]. When the energy transferred into the lattice from the electron plasma formed through nonlinear multiphoton absorption and the avalanche ionisation process, a very localised high temperature generated and pressure leading in shock wave and densification [74].

Hirao and Miura presented the results of writing round-elliptical damage lines by using 810nm, 120fs laser with 200kHz mode locked pulses that suggested the positive change in refractive index can be related to local densification and defect generation [85]. Saliminia et al. discussed the mechanisms of refractive index change based on the fabrication of waveguides using a 1.5 μ m infrared femtosecond laser at 1kHz repetition rate [86]. However, the results indicated that colour centre formation may not play a crucial role in the refractive index change as colour centres were completely erased after annealing at 400°C [86].

Therefore, the smooth refractive index change caused by not only one effect but the contribution of multiple effects (i.e. thermal effects, colour centre formation and densification). Contributions from those effects to induce the refractive index change will vary depending on the material properties and the laser properties.

2.1.2.2 Birefringent refractive index change

Birefringent refractive index changes are associated with the formation of periodic nanostructures. It occurs when using higher laser pulse energies than that required for the smooth refractive index change but lower for void formation. The formation of nanostructures is strongly dependent on the polarisation of the incident laser pulse train [58]. Sudrie et al. firstly reported that a birefringent refractive index change can be observed in fused silica [87]. Shimotsuma et al. observed that periodic self-organised grating structures sized around 20nm that aligned perpendicularly to the laser polarisation direction were formed after irradiating the femtosecond laser beam inside fused silica [64]. The structural modification phenomenon was interpreted as the interference between the laser field and the electric field of free electron plasma wave in the material [58, 64].

Similarly, Wang et al. presented the self-organised nanograting with a spatial period of 200-300nm in fused silica that perpendicularly oriented to the polarisation of the laser pulse [88]. The results provide further evidence that a strong connection is presented between the nanograting and the multiple ionisation channels [88]. The use of this modification regime can benefit the fabrication of microchannels for microfluidic devices [65, 89].

2.1.2.3 Void creation

With extremely high intensities that exceed the ablation threshold of the material, a shock wave is generated that accompanies the energy transfer from free electron plasma to the lattice, which can lead to micro-exploration and void formation at the focal volume [50, 58, 68]. The shock wave carries highly excited, vaporised material out of the focal volume into the surrounding materials [68]. As the micro-exploration occurs within the material, it results into a less dense or hollow core (termed as void) surrounded by material with a higher density [50, 68]. The void formation can benefit and exploit for 3D optical memory storage [32, 33], fibre Bragg gratings [90] and photonic devices [91]. The use of the void formation can also benefit the fabrication of OCT calibration phantom [10, 21, 22, 92, 93] by using high pulse energies to create micrometre size modification in fused silica.

2.2 Experimental considerations

Direct laser writing is a novel method based on using ultra-short laser pulses [94, 95] which is employed by the laser system and is used for all the experiments presented in this thesis. Fused silica is the only material used for all experiments undertaken in this work. As mentioned earlier, induced refractive index changes occur due to the non-linear multiphoton absorption processes [94] and take place when ultrashort (i.e. femtosecond) laser pulses are focused into the bulk of a transparent material (e.g. glass) [94]. Ehrt et al. presented a way to use a direct laser writing technique on various glass materials [94]. Different types of glasses have been studied and written by a 800nm femtosecond laser with 50fs pulses at a repetition rate of 1kHz [94]. The study concluded that the induced refractive index is heavily dependent on both the laser writing conditions (e.g. wavelength, pulse energy, pulse duration, repetition rate) and the material composition and structure [94]. Similarly, Dmitriev et al. also demonstrated a novel single-step method of using femtosecond laser with laser pulses at 800nm central wavelength, a maximum pulse energy of 5nJ and a pulse duration of 100fs at a repetition rate of 80MHz

to directly write of arrays of metallic (Au) and semiconductor (Si) nanoparticles [96]. Femtosecond laser direct writing in transparent materials enables highly precise and high-quality 3D micro/microfabrication which shows great potential for numerous applications [97].

In the following section, a number of key parameters and effects (i.e. polarisation, repetition rate, pulse duration, writing directions, self-focusing and spherical aberrations) that play crucial roles in the process of the laser-material interaction are discussed.

2.2.1 Polarisation

Polarisation can significantly affect the energy absorption process, which is polarisation-dependent, such that it affects the changes in structures and properties caused by the irradiating incident laser beam [67, 82]. Little et al. presented that the polarisation of incident laser irradiation between linear polarisation and the circular polarisation can result in a refractive index contrast of up to two times difference [98]. It concluded that the difference was caused by different nonlinear photoionisation rates of fused silica, with the circular polarisation exhibiting higher photoionisation rates than the linearly polarised laser beams [98].

Moreover, Liu et al. reported that the difference in the damage threshold of fused silica for linear and circular polarisations. For a $NA > 0.4$, the damage threshold for the circular polarised beam was higher than that for the linear polarised beam, however when $NA < 0.4$, the damage threshold for the linear polarised beam was higher than that for circular polarised beam [99]. It was suggested that the reason might be caused by different damage processes so that there is laser induced damage for the high NA but the self-focusing induced breakdown at low NA [99].

Gaudfrin et al. showed that the effect caused by polarisation to the ablated volume was that a linear polarised beam led to a higher absorption cross section than the circular polarised beam, which makes the linear polarisation state more efficient [100]. However, the experimental setting was also associated with a change to the pulse-to-pulse delay which the researchers concluded that the effect of polarisation on ablated volume is delay-dependent. Nanostructures, such as nanogratings, are shown to be strongly polarisation-dependent [64, 65, 101]. The formed nanogratings are self-ordered and periodic that orientated perpendicularly to the electric vector of a linearly polarised laser beam [65, 67, 102].

The polarisation of the femtosecond laser system used for all fabrication related work presented in this thesis is circularly polarised. The circular polarisation has been shown to be less sensitive to the writing direction which allows the laser to inscribe any path in 3D without requiring continuous alignment for the electric field and magnetic field as required for the linear polarisation [60, 65].

2.2.2 Repetition rate

Repetition rate is one of the most important parameters and it is highly influential on the performance of the femtosecond laser inscription process depending on the repetition rate regimes [67]. At low to moderate repetition rates (i.e. 1-200kHz), the time between the laser pulses are relatively long to allow the thermal diffusion extend to quite a large area outside of the focal volume, therefore an increase in laser pulse energy leads to larger microstructure formation [67, 103, 104]. At high repetition rates (i.e. 0.5-2MHz), as the time between laser pulses has become much shorter than the thermal diffusion rate, hundreds of pulses accumulate to heat up the focal volume therefore there is heat accumulation constituting a point source of heat [50, 67, 104].

Bovatssek et al. studied the effect of the repetition rate on transparent materials (i.e. glass) [105]. The work found that a high repetition rate would result a point-like heat source, due to the nonlinear absorption of tightly focused femtosecond pulses [105]. It stated that a low repetition rate limited the linear welding speed while a high repetition rate can lead to thermal energy accumulated in the focal region [105].

Similarly, Rasakanthan et al. also studied the effect of the repetition rate along with other parameters to fabricate the OCT artefact [10]. In this study, three different femtosecond lasers with different repetition rates (i.e. 11MHz for the high repetition rate laser system, 1kHz and 100kHz for two low repetition rate laser systems respectively) were used to perform tests on different types of transparent materials (i.e. fused silica, PMMA and doped BK-7) [10]. It concluded that the microstructures produced by low repetition rate systems in fused silica and PMMA were more visible under the OCT system than the waveguide-like structures produced by high repetition rate system [10]. The high repetition system was capable of producing more symmetrical and homogeneous structures. However, at lower repetition rates, the structure written in PMMA tended to be more symmetric than in fused silica where the difference may be caused by the material properties [10].

The femtosecond laser system used has variable repetition rates ranging from 1kHz to 100kHz with the maximum of 100kHz repetition rate was used for the laser setting to fabricate inside pure fused silica substrate. Thermal diffusion dominated for the structure modification.

2.2.3 Pulse duration

Pulse duration is another important parameter that needs to be considered when using the femtosecond laser writing process as the damage threshold has been shown to be pulse duration dependent [67]. The relationship between the pulse duration, peak power and pulse energy can be simply represented as shown in Equation 2-5. When the laser pulse energy is fixed, changes in pulse duration can directly affect the peak power so that an increase in pulse duration leads to a decrease in peak power.

$$\text{Peak power (Watts)} = \frac{\text{Laser pulse energy (Joules)}}{\text{Pulse duration (seconds)}}$$

Equation 2-5

Sun et al. demonstrated the nonlinear propagation of a single focused femtosecond laser pulse in fused silica to be pulse duration dependent at fixed incident laser pulse energies, in which the peak electron plasma density differs with different pulse durations (the pulse duration was varied from 50fs to 1600fs in this experiment) [106]. The results showed that the peak electron plasma density when at a relatively low pulse energy firstly increased with increasing pulse duration and then decreased, this was due to the avalanche ionisation acting differently at different pulse durations [106].

Stuart et al. investigated laser-induced damage in dielectrics with different pulses ranging from 140fs to 1ns [107]. The results showed that a strong deviation had been observed from the long-pulse (i.e. pulses shorter than 20ps) and the damage threshold continues to decrease with decreasing pulses in the range of 0.1 to 20ps [107]. For the ultra-short pulses (i.e. pulses less than 30fs), the multi-photon ionisation on its own accumulated enough density to cause damage [107]. This study provided a good foundation for using the femtosecond laser with short pulses to control the damage area. Hantovsky et al. demonstrated the effect of the pulse duration to the fabrication by varying the pulse duration at a range of 40-450fs and the results showed that when the pulse duration decreases, the pulse energy threshold increases [63].

The pulse duration for the experiments presented in this thesis was fixed around 500fs, therefore, the peak power varied with the incident laser pulse energy by adjusting the laser attenuator.

2.2.4 Writing geometry and aberrations

The writing direction and the chosen focusing objective lens can significantly affect the structure modification inside the material. There are two main writing geometries used for the translation of the computer-controlled XYZ stage – longitudinal and transverse writing direction. In longitudinal writing, the laser beam is parallel to the propagation of the incident laser beam which either towards to or away from the beam [69]. While in transverse writing, the laser beam is perpendicular/orthogonal to the propagation of the laser beam [69]. The schematic diagram for showing the laser writing direction is shown in Figure 2-3.

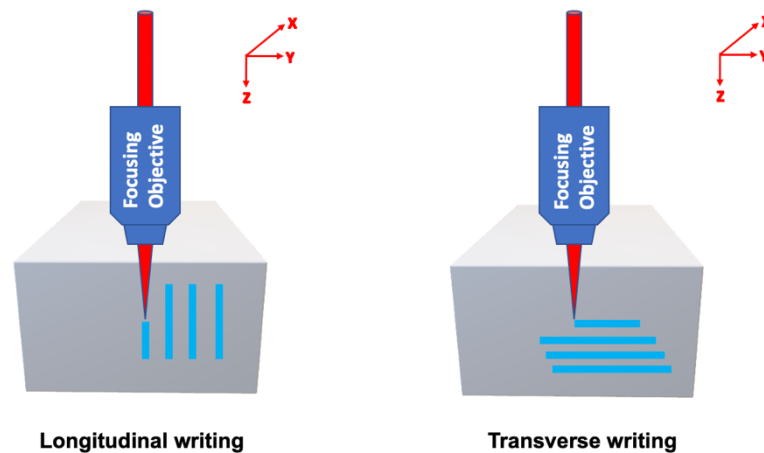


Figure 2-3. The schematic diagram showing the writing geometry of the laser beam.

In longitudinal writing, the resulting structures tend to be cylindrically symmetric due to the transverse symmetry in the Gaussian intensity profile of the laser beam [69]. However, the inscription length can be limited due to the working distance of the chosen objective lens [69]. To address this limitation, a low numerical aperture (NA) focusing lens is beneficial to extend the inscription length with higher laser powers to reach the optical breakdown threshold [69, 108]. However, when the peak power is relatively high, nonlinear effects (i.e. filamentation and self-channelling) will appear which can lead to an elongated structure in the axial direction [69, 108]. Another issue is caused by the spherical aberration, which can significantly distort the structure [109]. A spherical aberration happens when light goes through different mediums due to the mismatch of

the refractive index, which is depth dependent. This can become more severe for high NA objectives (0.4 or above) that distort the focal volume with an axial elongation of the focus which therefore leads to a distortion in refractive index change [110, 111]. A schematic diagram is used to show the focusing geometry for the longitudinal writing and focusing aberrations presented in Figure 2-4. When the significant depth is reached, the focusing geometry is distorted and elongates the focal volume that spreads the longitudinal intensity [108] and lowers the axial energy density [109]. The axial stretching increases with the focusing depth and causes a decrease in peak intensity and a modulation in the axial intensity profile [109, 112]. Therefore, without using adaptive optics to correct the aberration [109], the results are compromised by choosing a high NA objective lens which can produce small structures over a limited depth or choosing a lower NA objective lens which can produce larger structures with a greater depth [113].

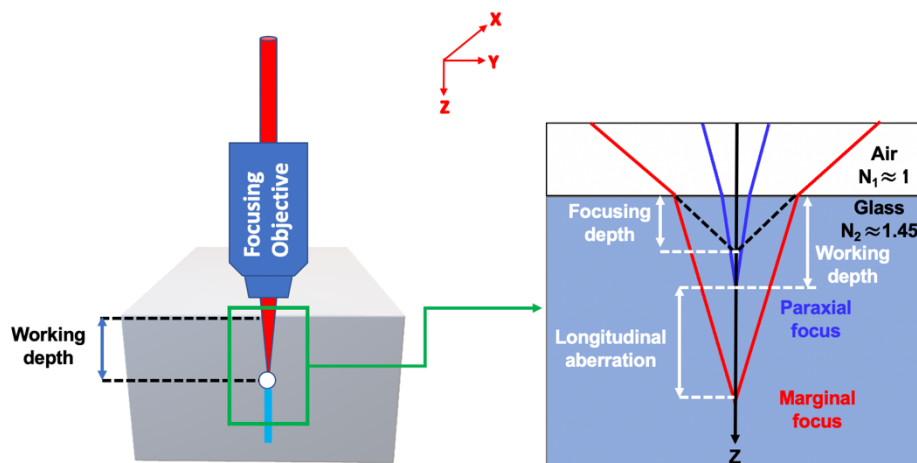


Figure 2-4. The schematic diagram showing the longitudinal writing and the aberration caused by mismatch of the refractive index of two media.

In transverse writing, however, as the sample is scanned perpendicular to the incident beam, the working distance no longer limits the writing length, this is generally used for the fabricated structures presented in this thesis [69]. However, the cross-sectional area of the inscribed structure can be asymmetric or elliptical [110] due to the ratio between depth of focus and the spot size [69]. The waist radius (w_0) for the diffraction-limited minimum (i.e. 1/2 of the spot size) for a collimated Gaussian beam focused in a dielectric can be defined in Equation 2-6 [69].

$$w_0 = \frac{M^2 \lambda}{\pi NA}$$

Equation 2-6

where M^2 is the Gaussian beam propagation factor which is used to quantify the laser beam quality [114], λ is the laser wavelength and NA is the numerical aperture of the focusing objective lens [69].

The Rayleigh range (z_0) (i.e. 1/2 of the depth of focus) inside a transparent material of refractive index n is defined as shown in Equation 2-7 [69].

$$z_0 = \frac{nM^2\lambda}{\pi NA^2}$$

Equation 2-7

Therefore, the ratio between the depth of focus ($2z_0$) and the spot size ($2w_0$) can be therefore represented by Equation 2-8 for a given focal volume asymmetry of the structure cross-section.

$$\frac{2z_0}{2w_0} = \frac{n}{NA}$$

Equation 2-8

where n is the refractive index of the material and NA is the numerical aperture of the focusing objective lens. It can be seen that the NA of the focusing objective lens plays a significant role. This asymmetry results in elliptical structures. In this thesis, the transverse writing was mainly used for the structure writing, and longitudinal aberration is observed when inscribing at greater depths.

2.2.5 Self-focusing

The high peak power of the laser can induce nonlinear propagation effects (i.e. Kerr self-focusing) that can significantly distort the laser beam profile and peak intensity [54], which can cause laser pulse to collapse into a filament [27]. The spatially varying refractive index in a dielectric can be created by the spatially varying intensity of a Gaussian laser beam [69]. This nonlinear refractive index (n_2), also known as Kerr non-linearity, is positive in most of materials, where the highest laser intensity is at the centre of the beam compared to the wings [54].

This variation (Δn) in refractive index acts as a focusing lens (i.e. Kerr lens) inside of the material which the strength of the self-focusing lens is dependent on the laser pulse intensity (I) [67, 69] given by Equation 2-9.

$$n = n_0 + \Delta n = n_0 + n_2 I$$

Equation 2-9

where n is the total refractive index of the material, n_0 is the linear refractive index, n_2 is the non-linear refractive index, I is laser pulse intensity and Δn is the variation of the refractive index [115]. Although the refractive index variation depends on the peak intensity, the self-focusing strength is dependent on the laser peak power solely [54]. If the peak power exceeds the critical power for self-focusing (P_{cr}), the laser pulse can be predicted to collapse [54, 116]. The critical power (P_{cr}) for self-focusing of a Gaussian beam can be calculated based on the Equation 2-10 [117-119].

$$P_{cr} = \frac{3.77\lambda^2}{8\pi n_0 n_2}$$

Equation 2-10

where λ is the laser wavelength, n_0 is the linear refractive index and n_2 is the non-linear refractive index. However, as the laser beam self-focuses, it can induce the nonlinear excitation to form a free electron plasma which has a negative refractive index acting as a diverging lens causes de-focusing of the laser beam [54]. Therefore, a balance between self-focusing and de-focusing leads to the filamentation that elongates the structure along the axial direction over a given length when the peak power is around the critical power for self-focusing [67, 115, 118, 120, 121].

For the femtosecond laser used for the work presented in this thesis, the femtosecond laser has a central wavelength (λ) of 1026nm, the fused silica substrate used to fabricate the OCT phantoms has an n_0 of 1.45 (at $\lambda = 1026\text{nm}$), n_2 is $2.9 \times 10^{-16} \text{ cm}^2/\text{W}$ [122], therefore, the critical power for self-focusing is around 3.75MW, which the corresponding pulse energy for the pulse duration of ~500fs is around 1.875 μJ . Therefore, for a precise control of the inscription size, a laser pulse energy below the threshold should be selected with a high NA employed to ensure the enough peak intensity can be reached below the self-focusing threshold for nonlinear absorption process [60].

2.3 Optical coherence tomography (OCT)

Since 1991 with the first OCT system demonstrated by Huang et al. [1], optical coherence tomography (OCT) technique has been developed rapidly and been extensively used for biomedical/medical and clinical applications [123] such as helping diagnose and assess the treatment of retinal diseases [3, 124-126] and other

applications such as dimensional metrology [127, 128] and contactless material characterisation [129-131]. OCT can provide a 3D non-invasive, high resolution, cross-sectional in-vivo image of the internal microstructures in materials and biological systems by scanning the backscattered or back reflected light [1, 2, 132]. OCT performs the way that is analogous to ultrasound echo imaging technique [133], which provides a 2D cross-sectional image of optical scattering from internal tissue microstructures [1].

2.3.1 Optical coherence tomography: basic principles

The underlying principle of the OCT technique is utilising the low-coherence interferometry [1], and it is responsible for the high resolution of which OCT systems exhibit. The high velocity of light and the resolution limitations of time measurement technologies (i.e. measuring the round trip time from the source, to the sample and back again) prohibit direct measurement techniques [134]. However, for OCT technique, the coherent property of the light enables a direct measurement on the tissue microstructure determining on the echo time delay (i.e. time of flight delay) between the reflective boundaries and the backscattering from the sample [1, 2]. The core of the OCT system is a Michelson Interferometer with a low-coherence light source [134].

Figure 2-5 shows the simplified configuration [1, 134] of a basic OCT system configuration. A light source emits light that passes through a beam splitter which divides the incident light into two optical paths. One optical path goes to the moving reference arm and the other goes to the sample arm. The returns from the sample and reference mirror constructively or destructively interfere at the beam splitter, dependent upon their time delay and magnitude of the reflected light [134]. The output of the OCT system, which is essentially a Michelson interferometer monitored by a detector [135].

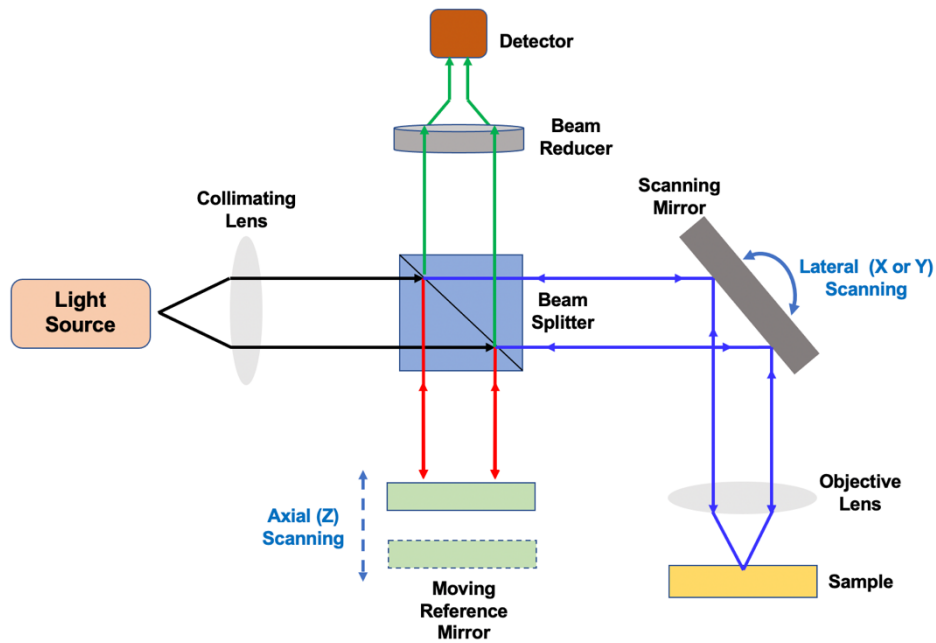


Figure 2-5. Basic OCT system simplified configuration.

A single depth of profile (i.e. A-scan) can be obtained by completing one trip along the reference arm [136]. A 2D OCT image or B-scan can be obtained by scanning at incremental steps [137] or multiple longitudinal locations [1] of the sample which is a series of A-scans. A 3D OCT image can be obtained by having multiple depth scans with the beam propagating at two orthogonal directions which is a series of B-scans [138].

2.3.2 OCT systems

There are two main OCT methods: time domain OCT (TD-OCT) and spectral domain OCT (SD-OCT). The SD-OCT can be implemented in two ways which are Fourier domain OCT (FD-OCT) and swept source OCT (SS-OCT).

2.3.2.1 Time domain OCT (TD-OCT)

Time-domain OCT (TD-OCT) is the most fundamental OCT system based on a detection technique that use a low-coherent light source and a reference arm [136]. A TD-OCT system outputs reflectivity depth profiles (i.e. A-scan) [137] by measuring the echo time delay and intensity of the light reflected or backscattered from the sample [1, 134]. When the reference mirror moved to a certain position, the corresponding pattern can only be obtained when the same distance that light travels to the reference arm is equal to the distance that light reflected back from the inside of the sample [136]. Therefore, when the reference mirror moving along the reference arm, the interference pattern can be

generated from the backscattering of the sample of the sample arm [136]. By this way, the dependence on depth of the intensity of light backscattered from inside of the sample can be measured [136].

However, for TD-OCT system, the light echoes or the variation of interference can only be detected when the optical path difference (OPD) is less than the coherence length of the light source (C_l) [139]. The optical path difference is defined as $OPD = |\text{Object path length} - \text{reference path length}|$ [139]. The coherence length of the light source is determined by the spectral bandwidth. The condition of $C_l < OPD$ has to be met for the sample scanning [139]. When $OPD = 0$, the maximum inference can be obtained for each depth of the sample [139].

2.3.2.2 Spectral domain OCT (SD-OCT)

Spectral-domain OCT (SD-OCT) is the most commercially used OCT technique presently. It can be implemented in two ways which are Fourier-domain (FD-OCT) and swept-source OCT (SS-OCT) [137]. The SD-OCT method eliminates the needs of depth of scanning by mechanically moving the reference mirror that the TD-OCT requires [139]. Previous studies [4, 135, 140] have shown that SD-OCT systems have a considerable sensitivity advantage [141] compared with TD-OCT systems due to their higher acquisition rates [142] and deeper penetration features [137]. In addition to this, the SD-OCT technique enables systems to capture higher resolution images [4, 137, 143, 144].

Fourier-domain OCT (FD-OCT), also known as spectrometer-based OCT (SB-OCT) was initially demonstrated by Fercher in 1995 [145] and the firstly commercial OCT available system was introduced in 2006 [3]. It is different from the TD-OCT in that the detector in this system is changed to a high-speed spectrometer and that the reference arm is fixed [137, 138]. Unlike TD-OCT where the light echoes are detected from sequentially moving the reference mirror, in FD-OCT all the spectral components captured at the same time as the light echoes come from all axial depths and are detected as modulations in the spectrum [136]. The spectrometer consists of a prism or diffraction grating with a photodetector array [139]. The detected signal is then converted to the time domain by applying Fourier transformation to obtain the depth profile of the sample [138].

Swept-source OCT (SS-OCT) is essentially employing same fundamental approach as SD-OCT, however, the broadband source is replaced with tuneable frequency swept narrowband laser source which emits various frequencies sequentially in time [3] and a conventional photodetector instead of a spectrometer is used to the monitor the output

[139]. The response of the interferometer at each wavelength can be determined and the same Fourier transformation performed. It can obtain the fastest acquisition scan rate with sufficient image quality for deeper tissue [3, 139, 140].

2.3.2.3 Comparison of OCT methods

The main parameters and features for the TD-OCT, FD-OCT/SB-OCT and SS-OCT methods been reviewed and are summarised in Table 2-1 for comparison [139].

OCT system parameters	TD-OCT	FD-OCT/SB-OCT	SS-OCT
Light source	Broadband light source	Broadband light source	Tuned narrowband laser source
Detector	Photodetector	Spectrometer	Photodetector
Axial resolution depends on	Optical source bandwidth	Optical source bandwidth	Tuned bandwidth
Acquisition line rate	16kHz [139]	~300kHz [139]	~5MHz [140]

Table 2-1. Comparison between different OCT methods.

2.3.3 Performance parameters of OCT systems

Performance parameters of OCT systems enable a better understanding of the needs for designing and fabricating an OCT calibration phantom. Previous studies [21, 146] have shown that quantitative methods need further development to assess the performance of various OCT systems. In this section, three key performance parameters of the OCT system which are resolution, point spread function (PSF), sensitivity are reviewed.

2.3.3.1 Resolution

Resolution (i.e. axial resolution and transverse resolution) is one of main performance parameters of the OCT system. For a typical OCT system, the coherence length of the light source determines the depth resolution (i.e. axial resolution), which is inversely proportional to its spectral bandwidth [136, 138], hence the utilisation of a broadband

light source benefits the axial resolution [134]. When a spectral distribution of a light source is Gaussian, the axial resolution (Δz) (i.e. depth resolution) of the OCT system can be determined by Equation 2-11.

$$\Delta z = 0.44 \frac{\lambda^2}{\Delta \lambda}$$

Equation 2-11

where λ is the central wavelength of the light source, Δz and $\Delta \lambda$ is the axial resolution and the bandwidth of the light source respectively [2]. Therefore, to achieve a high axial resolution, broadband light sources are required [2, 136]. The micron or submicron range of the resolution can be achieved by employing a very large spectral band light source such as femtosecond pulsed lasers or white light sources [136]. To date, the axial resolution of conventional OCT systems used in Ophthalmology is reported to be 5-20 μm [147]. For ultrahigh-resolution OCT systems, a much higher axial resolution range was reported as 1-2 μm [148-151].

However, the transverse resolution (Δx) (i.e. lateral resolution) is independent on the depth resolution (Δz) (i.e. axial resolution), which is determined by the minimum spot size of the focusing beam that inversely proportional to the numerical aperture (NA) of the focusing lens [2, 136] represented in Equation 2-12.

$$\Delta x = \frac{4\lambda}{\pi} \left(\frac{f}{d} \right) = 1.27 \left(\frac{\lambda}{NA} \right)$$

Equation 2-12

where λ is the central wavelength of the light source, d is the spot size of the focusing beam, f is the focal length of the focusing lens and NA is the numerical aperture of the focusing lens. Lateral resolution is limited by the diffraction limit [152], which is independent from the axial resolution so that the system can be optimised for lateral scanning [138] without affecting the axial resolution [2]. A high transverse resolution can be achieved by employing a high NA focusing lens. The transverse resolution (Δx) is also related to the depth of field (DOF) with the correlation given by Equation 2-13 [2].

$$DOF = \frac{\pi \Delta x^2}{2\lambda}$$

Equation 2-13

As increasing of the transvers resolution (i.e. smaller Δx), the DOF will be decreased. With using a high NA focusing lens, the transverse resolution will increase, however, the DOF will be decreased. In contrast, a low NA focusing lens leads to a larger beam size at the focal point as the transverse resolution decreased with a larger DOF. Most commercial OCT systems performs with a lower NA focusing lens which ensures a larger DOF of the order of millimetres (i.e. $\sim 20\text{-}30\mu\text{m}$) [153, 154] can be obtained which is longer than the coherent length of the light source [136].

2.3.3.2 Point spread function (PSF)

The spatial resolution of the OCT system can be also treated as a point spread function (PSF) when the object is infinitesimally small [152]. When the object size is much smaller than the OCT resolution that can be treated as a delta function, a direct measurement of PSF becomes possible [155].

The final OCT image $I(x, y, z)$ is a convolution of the system PSF $\Gamma(x, y, z)$ and the object being imaged $H(x, y, z)$, which can be represented in Equation 2-14:

$$\begin{aligned} I(x, y, z) &= \Gamma(x, y, z) \otimes H(x, y, z) \\ &= \iiint_{-\infty}^{\infty} \Gamma(\chi, \xi, \zeta) H(x - \chi, y - \xi, z - \zeta) d\chi d\xi d\zeta \end{aligned}$$

Equation 2-14

A Dirac delta function, also called the unit impulse function, denoted as $\delta(x)$, which have a value of zero everywhere except at the origin [156], represented in Equation 2-15.

$$\delta(x) = \begin{cases} \infty, & x = 0 \\ 0, & \text{otherwise} \end{cases}$$

Equation 2-15

It has an important property is that the integral for the delta function is always equal to 1 [156] given in Equation 2-16.

$$\int_{-\infty}^{\infty} \delta(x) dx = 1$$

Equation 2-16

When the cross-section of the object is smaller than the resolution of the OCT system, it can approximately be treated as a 2D PSF of the system [60]. Therefore, by using this property of the delta function, a direct measurement of PSF of the OCT system becomes possible.

However, when the object size is larger than the OCT system, a deconvolution must be used to obtain the PSF. Tomlins et al. suggested that well-characterised larger particles can be used and de-convolved from the known shape of the OCT signal to obtain the PSF [155]. Therefore, the needs of the OCT phantom which is well-characterised with a known shape is necessary for the PSF measurement of the OCT system.

2.3.3.3 Sensitivity

The sensitivity of the OCT system is the minimum reflectivity required to achieve a signal-to-noise ratio (SNR) of 1, defined as the ratio of the signal intensity from the sample to the standard deviation of image background intensity with no sample presented [138, 146, 157] and it is an important parameter to evaluate the performance of an OCT system. The detector used for the measurement can be either a CCD camera or a silicon photodiode [146]. The SNR can be calculated as [135, 146]:

$$SNR = \left(\frac{I_{sample}}{\sigma_{background}} \right)^2$$

Equation 2-17

which can be represented in decibels (dB) [146] as:

$$SNR (dB) = 20 \log \left(\frac{I_{sample}}{\sigma_{background}} \right)$$

Equation 2-18

where I_{sample} is the signal intensity detected by the detector of the OCT system, $\sigma_{background}$ is the standard deviation of the background intensity with no sample presented [146]. The ratio needs to be squared in order to convert the intensity value to the power values [146].

The measurement of OCT sensitivity has been reported in previous literature. Leitgeb et al. [135] demonstrated a method to measure the sensitivity of the OCT system to compare the performance between the FD-OCT and the TD-OCT systems by using two mirrors with known reflectivity. One mirror was placed at the reference arm and another

mirror placing together with neutral density filters at the sample arm. Therefore, the signal intensity at different reflectivity levels can be measured with a neutral density filter [135, 146]. To accurately calculate the SNR, the expression from Equation 2-18 needs to be adjusted to:

$$SNR (dB) = 20 \log \left(\frac{I_{sample}}{\sigma_{background}} \right) - 10 \log (R_{sample} T_{ND}^2)$$

Equation 2-19

where R_{sample} is the reflectivity of the mirror, T_{ND} is the transmittance of the neutral density filter for attenuating the signal [146].

Another way to measure the sensitivity of the OCT system is using a well-characterised phantom which allows a direct measurement. Agrawal et al. presented methods to assess the sensitivity of OCT systems by using phantom-based methods which can provide directly visualised measurement of the system [146]. One phantom-based method was using a femtosecond laser inscribing the phantom presented by Lee et al. [21] (it has been commercialised by Arden Photonics Ltd., UK [146]) that uses a series of lines inscribed with different laser pulse energies. Another phantom-based method was the microsphere suspension phantoms that is comprised of various silica microspheres that have a mean diameter of $1.57\mu\text{m}$ [146]. The results indicated that the phantom-based methods could fill an important role for the sensitivity assessment which can provide a spot-check through simple visualisation of the signal level of the OCT system [146].

As the sensitivity of the OCT system determined by the minimum signal intensity, the signal intensity is associated with the reflectivity of the sample which is correlated with the refractive index of the medium. According to Fresnel equations, the reflectivity can be represented as:

$$R = \left| \frac{n_1 - n_2}{n_1 + n_2} \right|^2$$

Equation 2-20

where n_1 and n_2 represent the refractive index of two mediums. For a fused silica material with the refractive index of 1.5, the reflectivity is 4% when the incident light goes through the air ($n_1 = 1$) into the material ($n_2 = 1.5$). Therefore, by using the structures with different refractive indices, the sensitivity level of the OCT system can be

determined. Those structures with varied refractive indices can be inscribed by the femtosecond laser with varying the laser power or the writing speed [158].

2.3.4 OCT image processing

2.3.4.1 OCT image acquisition

The acquisition rate and the image quality are very essential to the OCT system as it is employed as medical scanning equipment. Eye movement remains an issue when doing the OCT scanning [159]. Previously, work has been conducted by researchers on the reconstruction and restoration of the OCT images [160, 161]. Other works [162-167] have focused on improving the acquisition technique of the OCT system.

Lebed et al. demonstrated a method which can speed up the image acquisition rate to reduce the scan time and improve the image quality by using Compressive Sampling (CS) [168]. It can recover/reconstruct a full 3D image based on a subset of the acquired data [168]. Differently, Su et al. presented an automated 3D image processing method with a high accuracy and subpixel resolution by using ridge detection algorithms [169]. This method enables the system to handle large amounts of data and this method can preserve the original data as it does not apply any filtering techniques [169].

Recently, Munro et al. developed a full wave model of the OCT image formation to overcome the limitations of existing models based on Maxwell's equations in three dimensions [170]. However, the experimental results acquired by the OCT system showed a noticeable difference to the simulated result due to various reasons (i.e. significant scattering coefficient variations), although the main features seems to be consistent [170].

2.3.4.2 OCT image distortion

The OCT image distortion is one of issues presented caused by different factors such as the nature of curvature structures, scanning procedures [171]. Podoleanu et al. quantified the distortions by using two quantities – a lateral and an axial error [171]. However, this method was based on the assumption of simplified and homogeneous tissue. Hence, the method would be more useful in longitudinal OCT imaging [171].

Similarly, Westphal et al. described a quantitative method to correct for OCT image distortion caused by refraction, scanning geometries and nonlinearities based on Fermat's principle [172]. The method can correct the distortion down to 10-20 μ m [172].

However, this method may have limits on detecting smooth interfaces as it is sensitive to position noise of the detected interface[172].

Ortiz et al. developed a numerical method for 3D OCT image distortion caused by the refraction on anterior segment [173]. The method implemented is based on a 2D Ray tracing method that applies Snell's law [173]. Through the comparison of corrected (simulated) values and the nominal values, the discrepancy is less than 1% in all surfaces [173]. Diaz et al. conducted a series of work on the one step geometric calibration method for geometrical distortion correction [174-176]. A landmark based OCT calibration model has been created and the distortion can be corrected by matching the known landmarks [176].

2.4 Chapter conclusions

This section has reviewed the background theory of the femtosecond laser micro-inscription process. Key parameters of the femtosecond laser have been investigated for experimental considerations. In order to have a well-controlled structure, such parameters needed to be well studied, controlled and defined. Moreover, the direct laser writing process heavily depends on these parameters. Moreover, the basic principles for OCT systems with different OCT methods have been presented. Performance parameters of OCT systems highlight the needs of the OCT phantom that can satisfy the OCT system requirements and solve the potential image distortion issues so that the correct image can be obtained.

Chapter 3

Experimental setup

This chapter presents the details and specifications of the experimental equipment and processes used for OCT phantom design, fabrication, characterisation and calibration in this thesis. Firstly, the femtosecond laser system and the experimental setup (Section 3.1) are presented, which includes a description of the laser head and optical components along the beam delivery path in the system. Secondly, the workflow of the phantom design and fabrication are described (Section 3.2). Thirdly, the phantom substrate and material considerations (Section 3.3) are introduced and studied. Moreover, a detailed description of the sample alignment procedure (Section 3.4) when placing the substrate on the fabrication stage is given. After the laser fabrication process, phantom characterisation using a microscope and OCT systems (Section 3.5) is described. Finally, a study of the existing planar phantom (Section 3.6), including the parameter settings, the fabrication process and characterisation process are investigated.

3.1 Femtosecond laser system

A femtosecond laser micromachining system (built by Oxford Lasers, UK) is used to fabricate the phantoms. The system consists of a laser unit, optical components located on the optical path, an on-axis camera, a microscope observation lens and an inscription lens, with a CNC stage equipped with a goniometer underneath to allow for accurate position adjustment of the blank silica substrates and other materials.

3.1.1 Femtosecond laser

The system contains a mode-locked femtosecond laser (Amplitude Systemes s-Pulse HP) that uses Ytterbium as the active laser medium which consists of a pulsed diode pumped solid state laser. An Ytterbium doped crystal can be directly pumped, which enables a high efficiency, that is capable of generating femtosecond pulses with a high average power. The laser has a central wavelength of 1026nm with a variable repetition rate ranged from 1kHz to 100kHz. The pulse duration remains fixed around 485fs at 1kHz and 500fs at 100kHz. The maximum average output power measured at the laser head was 1.23W at 1kHz and 3.86W at 100kHz [177]. The laser system layout is shown in Figure 3-1.

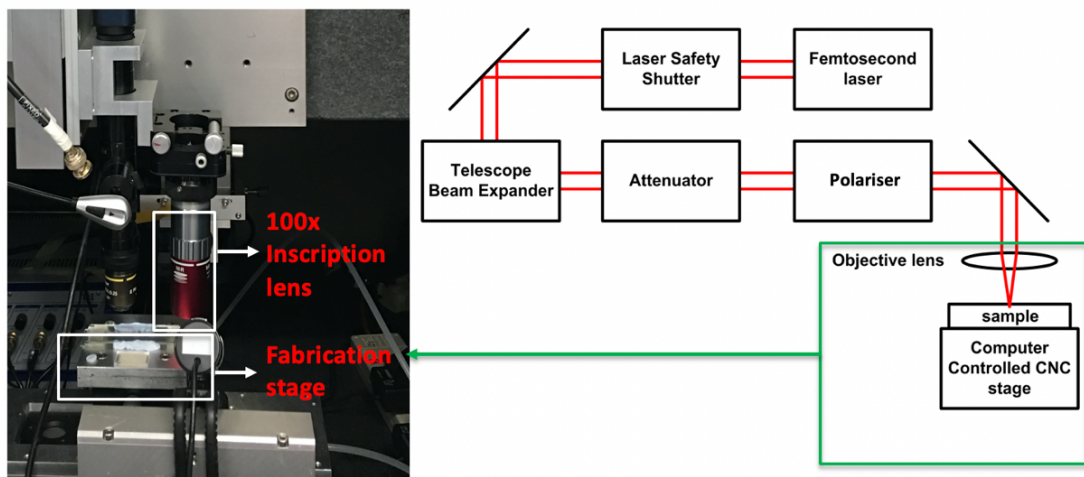


Figure 3-1: Schematic diagram of the laser system set-up at a 1026nm central wavelength with a repetition rate of 100kHz and a 100x inscription lens.

3.1.1.1 Chirped pulse amplification (CPA) technique

As the peak power is inversely proportional to the pulse duration, the direct amplification of a femtosecond pulse will lead to damage in the amplifier before reaching the desired energy level. Therefore, the chirped pulse amplification (CPA) technique is applied to remove the limitation of the peak power laser pulse amplification which can lead to optical damage to the gain medium caused by the nonlinear process (i.e. self-focussing) but enable efficient amplification of femtosecond pulses.

The CPA technique was initially introduced in 1960 for increasing the average power for radar systems [178] and was adapted to amplify short laser pulse in 1985 [179]. There are four stages contained in the CPA technique (shown in Figure 3-2). The first stage is to use an integrated laser oscillator that uses the soliton mode-locking technique [180], therefore a series of low energy with a high repetition rate femtosecond laser pulse are emitted [180]. A Ytterbium doped crystal is used as laser gain media which has a large fluorescence bandwidth to sustain ultrashort pulse duration [181] achieved by using a solid-state nonlinear mirror which is also known as a semiconductor saturable absorber mirror (SESAM) [182]. Soliton mode-locking technique enables a stable balance between the dispersion and Kerr nonlinearity in the resonator [183].

The second stage of the process utilises a pulse stretcher to stretch the femtosecond pulse. This is done by using two diffraction gratings so that each spectral component of the laser pulse experiences a different optical path length resulting in a pulse which is temporally stretched to a much longer duration and then chirped spectrally at the output of the stretcher. The third stage is to amplify the laser pulse to a high energy level by using a regenerative amplifier which consists of a laser resonator. After stretching the laser pulses, each temporally stretched low peak power pulse is trapped by a Pockels cell switching module and amplified to a desired energy level by completing multiple round trips through the gain medium in an optical resonator. The amplified pulse is then switched out by using the same Pockels cell switch. A Faraday rotator is used to send the pulse out to the pulse compressor. The final stage is to use a pulse compressor to recover the pulse duration back to its initial status. A dispersive compressor consisting of a pair of diffraction grating removes the chirp and temporally compresses the pulse to the input pulse duration. Then the amplified laser pulse with ultrashort duration is delivered out of the laser head.

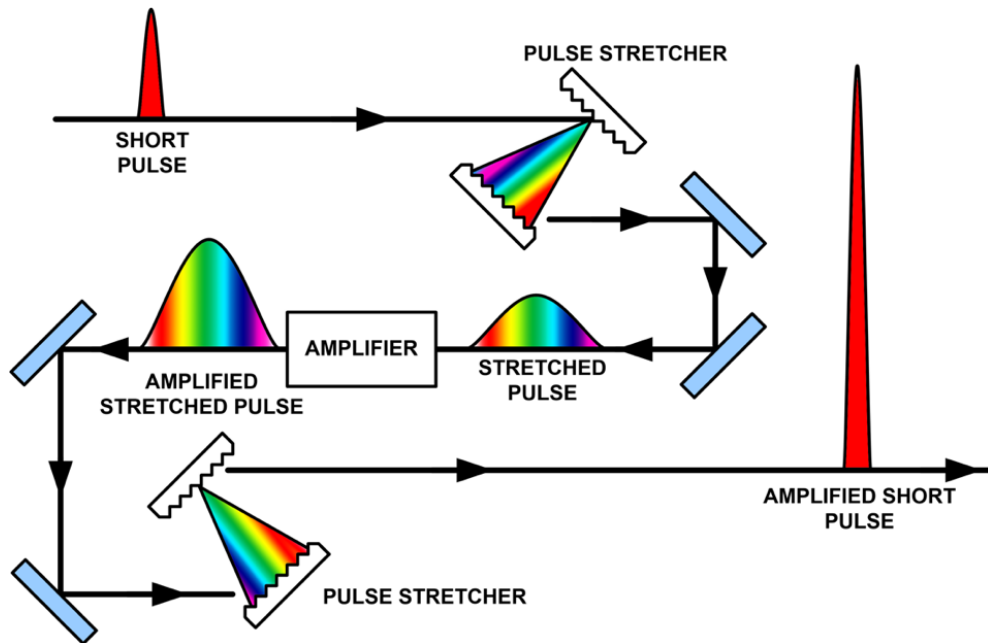


Figure 3-2: Conceptual diagram of the chirped pulse amplification (CPA) technique.

3.1.2 Optical components for beam delivery

The laser beam is confined through the beam delivery elements which contain a safety shutter, dielectric turning mirrors, the beam expander, laser attenuator and the polariser on the beam path before it exits to the z-axis where the focussing optics are located. The dielectric turning mirrors located on the beam path are incident at a 45-degree angle and specially coated for broadband near-infrared laser operation [180]. The beam expander, located before the beam entering into the attenuator and the machining lens, is used to vary the size of the beam and minimise the beam divergence so that to reduce the risk of damaging the any optical components [180]. The beam expander is used to vary the focus spot size so that it allows a precise control of the size of the laser beam [177]. To achieve this, a pair of plano-concave and plano-convex singlets with different focal lengths are used [180]. By expanding the beam by 2x or 4x, a pair of -50mm plano-concave and +100mm plano-convex or a pair of -50mm plano-concave and +200mm plano-convex can be used respectively [180].

The laser attenuator controls the laser energy in a linearised mode and it operated by a motorised half waveplate and thin film polariser pair [180]. The laser attenuator can be controlled by using a software or a customised program. It can be proportionally adjusted between 0% to 100% of the total output power, which means that 0% represents that the minimum transmission so that no laser beam can be emitted and 100% represents that the attenuator is fully open so that the maximum transmission can be allowed to go

through. This is illustrated in Figure 3-3 where the laser output power has been measured with an optical power meter (Coherent FieldMax II) at the fabrication stage (i.e. after the laser beam passes the machining lens, a 100x objective lens), a measurement of the average output power (in mW) versus the attenuator position (in %). Then the laser beam is circularly polarised by using a quarter waveplate directly after the beam exits from the attenuator [180].

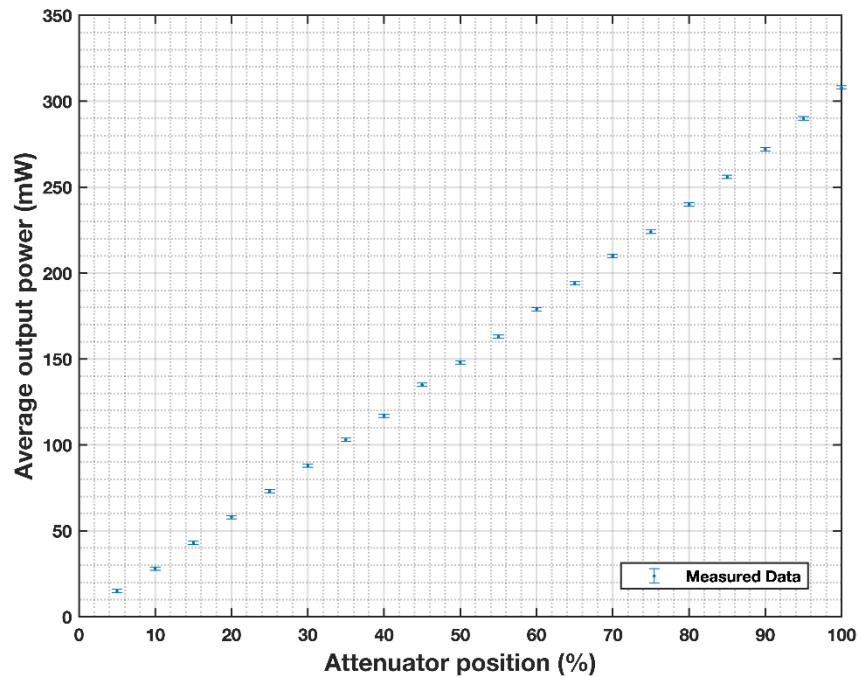


Figure 3-3: The correlation between the measured average output laser power (in mW) and the attenuator position (in %).

The Z-axis shown in Figure 3-4, it includes an on-line camera, vertical off-axis viewing lens and the machining lens which can be controlled by computer software. The inscription lens has a magnification of 100x (Mititoyo M Plan Apo NIR Series) with a numerical aperture (NA) of 0.5, working distance of 12mm and a focal length of +2mm which results in a laser spot size of approximately 2 μ m at the focal point.

The sample was secured to an aluminium plate which was mounted on a software-based motion control multi-axis stage (Aerotech ABL1000). A goniometer located underneath allows for precise manual position and angle control of the sample in the initial alignment process.

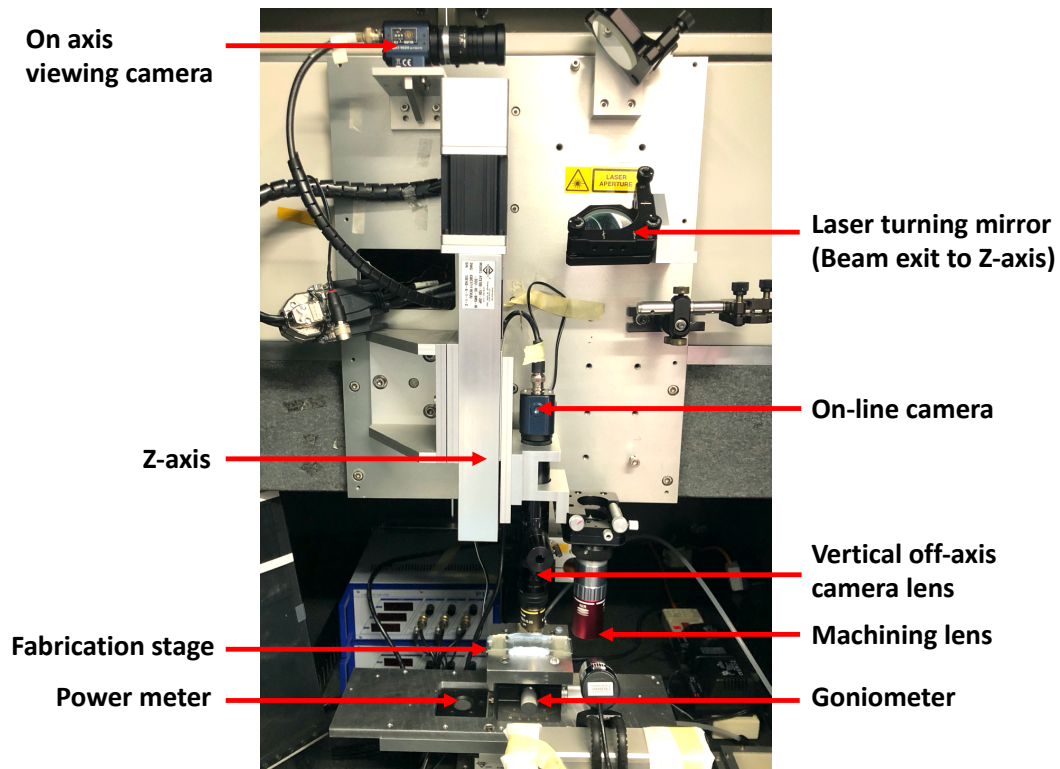


Figure 3-4: Laser system Z-axis setup including Z-stage opto-mechanical layout includes viewing and machining camera.

The multi-axis stage is controlled by a high accuracy and high-resolution computer numerical control (CNC) motion controller (Aerotech A3200) through a computer software package (NView). The parameters of the CNC stages and controller are listed in Table 3-1.

Axis name	X	Y	Z	ZZ
Motor type	Linear	Linear	Servo	Linear
Bearing type	Air	Air	Mechanical	Mechanical
Resolution	1nm	1nm	1 μ m	2nm
Travel	150mm	150mm	100mm	4mm
Accuracy	+/-500nm	+/-200nm	+/-3 μ m	+/-200nm
Repeatability	+/- 50nm	+/- 50nm	+/-1 μ m	+/- 50nm
Speed (max)	300mm/s	300mm/s	>50mm/s	50mm/s

Table 3-1. Parameters of CNC stages and controller.

X-axis and Y-axis are air bearing stages, while Z-axis and ZZ-axis are mechanical stages. Both X-axis and Y-axis can be precisely adjusted through goniometer during the alignment. The ZZ-axis is the machining lens axis, which is together mounted with the viewing lens along the Z-axis.

3.2 Phantom design and fabrication workflow

There were six steps involved in fabricating and validating a phantom as presented in Figure 3-5.

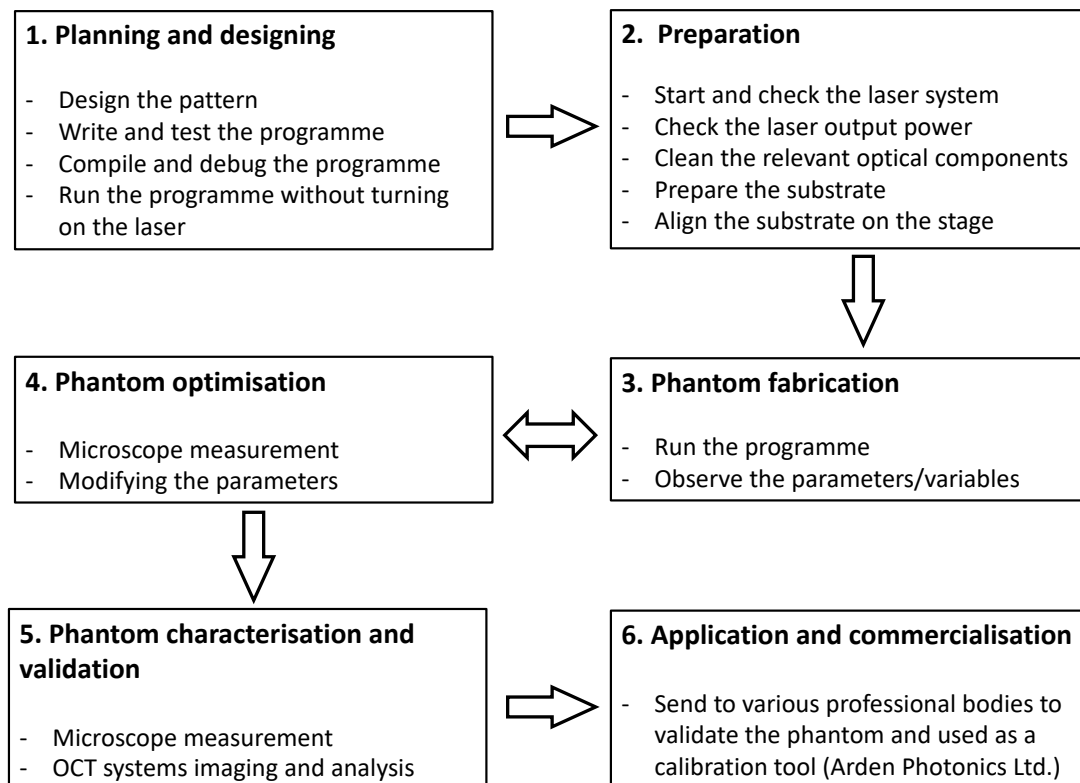


Figure 3-5: Phantom design and fabrication workflow.

The preparation process involves first checking the laser system (such as chiller, air compressor, oscilloscope and the computer-controlled shutter). After switching on the laser system, the laser output power is measured using an optical power meter. Subsequent to this, the relevant optical components (i.e. inscription lens, viewing lens) are then inspected and carefully cleaned. The sample substrate can then be carefully cleaned and aligned on the CNC fabrication stage.

The phantom fabrication and optimisation process involves running and modifying the program and observing the resultant inscribed sample under the microscope numerous times until a phantom has been fabricated which matches the intended design. Typically,

this will require optimisation of the design parameters such as the writing speed, moving/translation speed, laser pulse energy (i.e. by adjusting the attenuator position through the program) and layer separation.

For the phantom characterisation and validation process, both microscope and OCT system are used to measure and characterise the phantom. The microscope measurement is typically used as a reference and OCT images are analysed and compared with the microscope images, which also reflects back to the original parameter settings used in the program.

Finally, for the phantom application, the phantoms are sent to different professional bodies (who have either a research-based OCT system or commercial OCT system used for clinical diagnosis) whom measured the samples and provided feedback on the phantom's suitability.

3.3 Sample substrate and material

The material used for fabrication under the femtosecond laser system is mainly fused silica, as it is one of optimal materials to be used under most OCT systems. Fused silica is a widely used material which is transparent across a wide wavelength range and also exhibits high mechanical, thermal and chemical stability with low cost [98]. The standard phantoms are made in planar substrates of dimensions 30mm×25mm×2mm (Ibsen Photonics, Denmark). However, the thickness of the substrate used in the study was roughly around 2mm with a variation of 0.04-0.08mm. A detailed measurement of the substrate thickness variations as measured by a precision micrometre is listed in Appendix A. For the plano-convex lens (LA4380, Thorlabs), the sample material is made of fused silica. It has a diameter of 25mm, a radius of curvature of 46mm, central thickness of 3.8mm and an edge thickness of 2.0mm.

The refractive index of fused silica is dependent on the wavelength [184], data for the wavelength range of 200nm – 1500nm, based on Malitson's equation, is shown in Figure 3-6. This wavelength variation of refractive index is important for both the design and calibration of the phantoms.

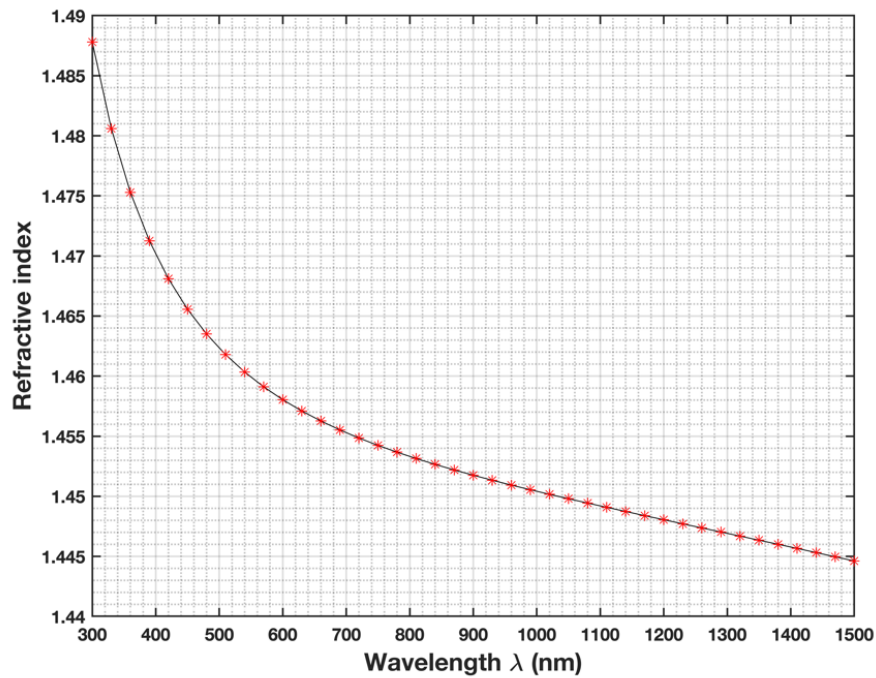


Figure 3-6: The refractive index of fused silica at different wavelengths ranging from 200nm to 1500nm based on Malitson's equation [184].

3.4 Phantom characterisation

3.4.1 Microscope

After fabrication, a bright-field transmitted light with differential interference contrast (DIC) microscope (Axioscope 2 MOT Plus, Zeiss) was used for the characterisation of the samples. The illumination lamp is a HAL100 (Tungsten-halogen lamp), which is dimmable and can be adjusted to different colour temperatures, up to 3200K. For the phantom characterisation, both 5x and 20x objective lenses were used for the measurement. The 5x objective lens gives a larger field of view and the 20x objective lens is used for the detailed measurements such as the layer depth and the linewidth. No colour filter or polariser was used for the phantom characterisation. The microscope is connected with a computer where the software (AxioVision 4.8) is used for the camera and measurement settings, live microscope image capture with the measurement tool is used to measure the inscription parameters.

In the software, there are few settings needed to be configured before the measurement can take place. The camera used on the microscope is 'AxioCam HR' with a setting of both 'RGB' colour space and '1300 x 1300 standard colour' selected for the image under the 'frame' section. By using the microscope to measure the sample, the 'manual' mode

is used so that the depth (Z-axis) can be manually set to 0 μ m, with a scaling unit of micrometres (μ m). Under the 'microscope' section, different objective lenses are available to be selected and activated. To measure the distance on the acquired image, there is 'distance measure' function under the 'measure' section on the toolbar that can be used.

3.4.2 OCT systems

Optical coherence tomography (OCT) system is an imaging technique that used to provide an in vivo high resolution 3D cross-sectional imaging of a transparent medium [2] with a penetration depth of 1-3mm [185]. Two different research spectral-domain OCT (SD-OCT) systems (Optimec is830 and Thorlabs Ganymede) and one commercial SD-OCT system (Carl Zeiss Cirrus HD-OCT 5000) were used for the characterisation and validation of the OCT phantoms. The Thorlabs Ganymede series SD-OCT system has a higher resolution, and it is used to see smaller details. It has a central wavelength of 930nm, an axial resolution of 5.8 μ m (air) and a lateral resolution of 8 μ m, allowing for more accurate measurement results. The Carl Zeiss Cirrus HD-OCT 5000 is an SD-OCT system which has a central wavelength of 840nm with an A-scan depth of 2mm in tissue, an axial resolution of 5 μ m (in tissue) and a lateral resolution of 15 μ m [186, 187]. It has a scan size of 15.5mm x 5.8mm [186].

The Optimec is830 system (Optimec Systems Limited, Malvern, UK) is a customised OCT-based inspection instrument with a central wavelength of 830nm [154]. It is mainly used to inspect the curvature and characterise contact lenses [154]. The system has an axial resolution of 12 μ m (air) and a lateral resolution of 30 μ m [154]. It is designed to see large areas with a measurement volume of 20 x 20 x 6 mm [154]. In this system, a super luminescent diode (SLD) is used as a light source and it is split between the reference arm and the sample arm by using a fibre coupler [154]. For the scanning system, a microelectromechanical scanning system (MEMS) is employed to scan across the sample [154]. A spectrometer is used to analyse the return combined signals from the reference arm and the sample [154]. The cross-sectional image (B-scan) of the sample consisted a series of A-scan (i.e. 1024 A-scans for some measurements presented in this thesis) laterally with each A-scan containing 512 depth positions, which produces 1024 x 512 pixels for each image [154]. Essentially, an A-scan is a 1D measurement on the Z-axis, a B-scan is a series of A-scans along the X-axis to form a 2D image and a C-scan is multiple B-scans (slices) put together to form a 3D image. A conceptual image

is used to show the scan size of a B-scan of 1024 x 512 pixels and a volumetric 3D C-scan of 1024 x 512 x 512 pixels is presented in Figure 3-7.

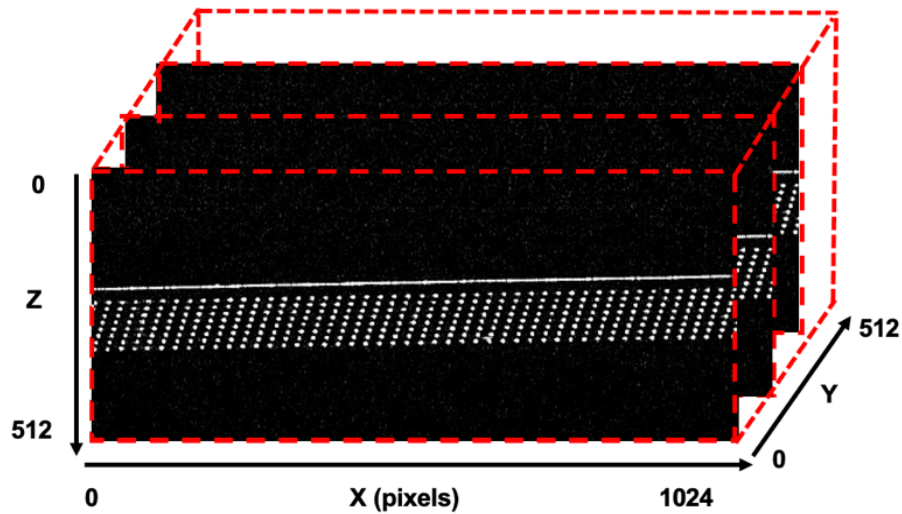


Figure 3-7. A conceptual image showing the pixel size of a 3D OCT image and how it is built from multiple 2D B-scans, which are in turn constructed from 1D A-scans.

These three OCT systems have different properties for comparison and were used to validate the phantom performance. The details of those OCT systems are listed in Table 3-2.

OCT system	Optimec is830	Thorlabs Ganymede Series	Carl Zeiss Cirrus HD-OCT 5000
Type	SD-OCT	SD-OCT	SD-OCT
Central wavelength	830nm	930nm	840nm
Axial resolution	12 μ m (air)	5.8 μ m (air)	5 μ m (tissue)
Lateral resolution	30 μ m	8 μ m	15 μ m

Table 3-2. Parameters and comparison of different OCT systems used.

3.5 Quantitative method for sample alignment

3.5.1 Alignment procedure and focus position

A high degree of alignment is required for the fabrication process. The alignment process usually involves subjective judgements on the focus position and a manual adjustment to flatten the stage and to true the sample with respect to the stage. The corners of the substrate (a typical sample is shown in Figure 3-8) are used for the alignment.

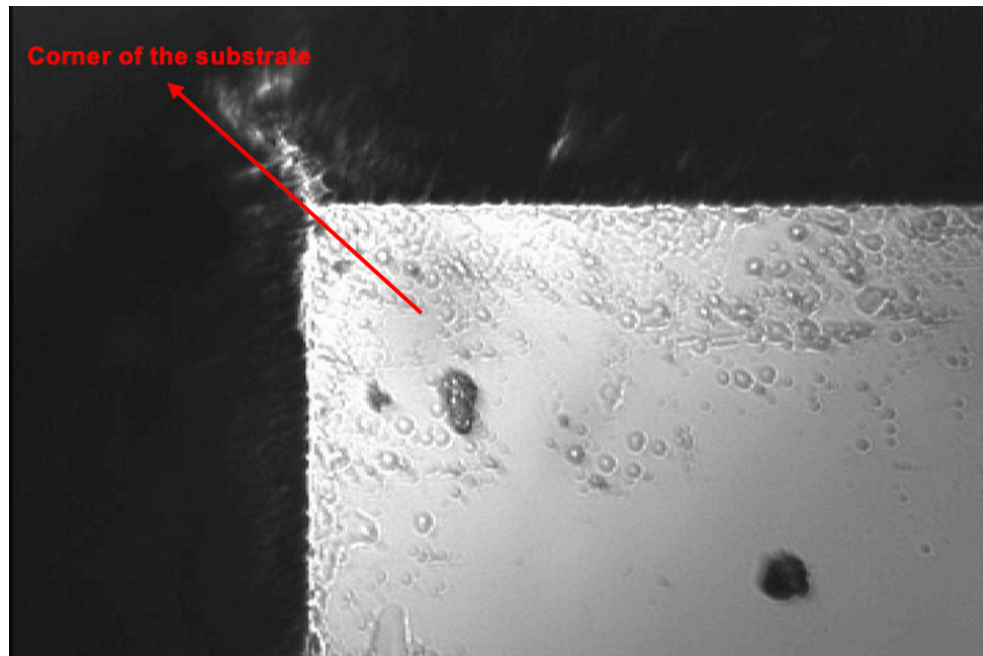


Figure 3-8. The CCD camera image showing one corner of the substrate which is used for the substrate alignment as a reference point.

The difficulty of this process is that judgement of the focus point can be problematic due to the imperfection of the materials shown in Figure 3-9. It can be seen that in this image for example at the P1 focus location, the focus position can be difficult to decide between the close to focus position and in focus position. For the P2 focus location shown in Figure 3-9, it shows a comparison between the out of focus position and in focus position which can be easily distinguished. However, as moving closer to the focus position, it becomes very difficult to determine the most focused position where the inaccuracy of the alignment can be introduced due to the subjective judgement. Moreover, this can also cause inaccuracies in setting the focal position as those imperfections which are typically used to set the focus position might not be located at the surface of the material.

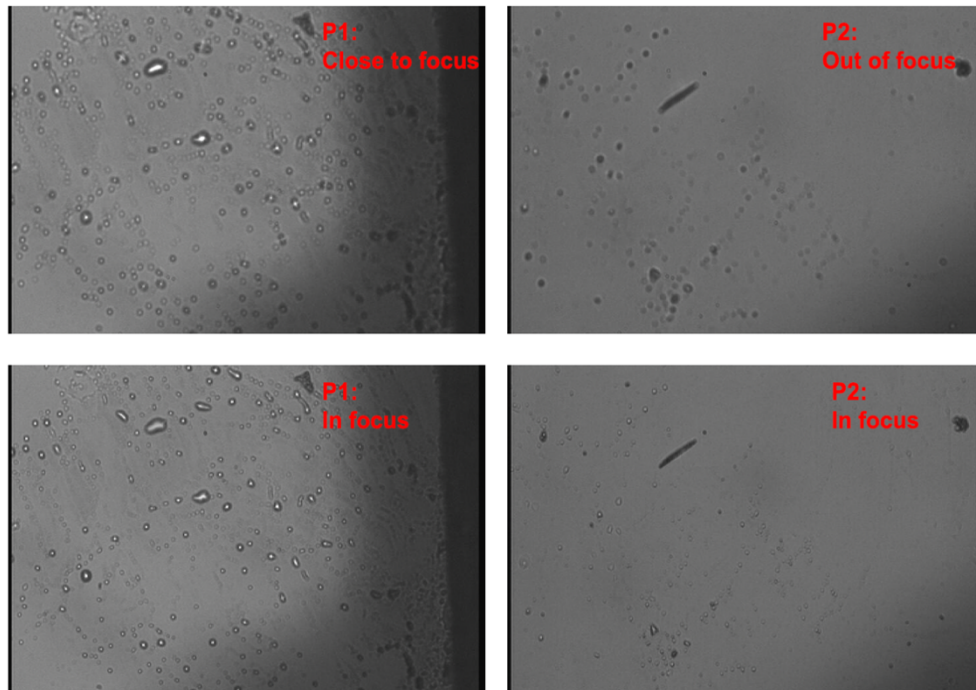


Figure 3-9. The CCD camera image showing different focus positions when aligning the substrate where P1 and P2 are two different points showing the focus position. The top left image shows the close to focus position for the P1 and the bottom left image shows the in-focus position for P1. The top right image shows the out of focus position for P2 and the bottom right image shows the in-focus position for P2.

One improvement that has been implemented by using an inscription program is to create a series of small sized inscriptions at different depths. The program writes five cross patterns with a $15\mu\text{m}$ Z-axis layer separation, with the bottom layer being $30\mu\text{m}$ below the believed surface position. An example of such an inscription is shown in Figure 3-10, where all five depth layers are visible. A central cross is inscribed at a bigger size (i.e. 2 times larger than other cross inscriptions) to indicate the believed surface or $0\mu\text{m}$ layer. Ideally, if the sample is aligned at the ideal focus position, there should only be three crosses seen (i.e. crosses inscribed at $-30\mu\text{m}$, $-15\mu\text{m}$ and $0\mu\text{m}$) as the remaining two crosses (i.e. crosses inscribed at $+15\mu\text{m}$ and $+30\mu\text{m}$) won't get inscribed as it will be above the surface of the substrate. Here in Figure 3-10, there are five crosses inscribed which means that the sample was aligned below the surface by at least $30\mu\text{m}$ which also means that the stage is too close to the inscription lens.

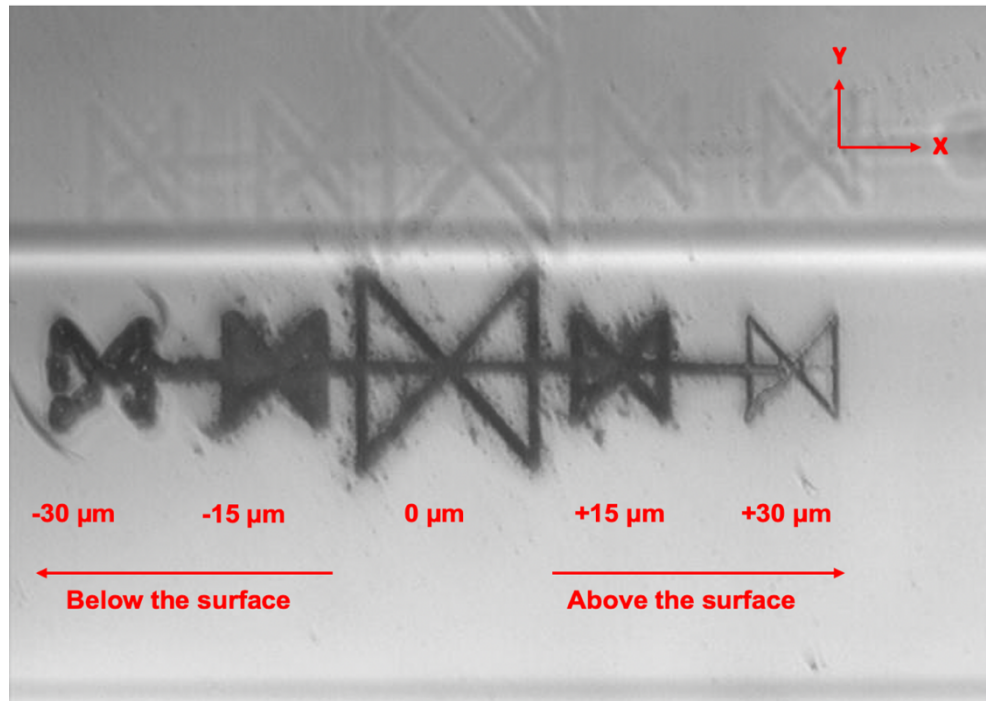


Figure 3-10. The CCD camera image showing that a series of small-sized cross shape inscriptions to help to guide when aligning the sample on the fabrication stage.

Once the surface is located, the software-controlled stage is used to adjust half of the distance through the software-based stage controller and the other half needs to be manually adjusted by using the goniometer. However, this presents a challenge as this manual adjustment is heavily dependent on the subjective decision for the focus point. Experimentally, this error has been observed to cause a focus point setting error of $20\mu\text{m}$ or more. Therefore, in order to increase the alignment accuracy, a quantitative method is needed to overcome this challenge.

3.5.2 Screen-to-ruler method

A screen-to-ruler method was therefore proposed, developed and used to assist the alignment to be more precise. With this method, the accuracy for the alignment can be controlled to within $\pm 5\mu\text{m}$. To be more specific, when adjusting the stage manually via the goniometer, the movement can be either on X-axis or Y-axis. Here, a ruler scale printed on acetate (clear plastic 'paper') was attached to the inspection microscope viewing monitor on the femtosecond laser setup (shown in Figure 3-11). When the stage is rotated around the X and Y axis manually via the goniometer, this method can record the exact distance the sample has moved based on the ruler scaling until the image becomes clear (i.e. in focus position).

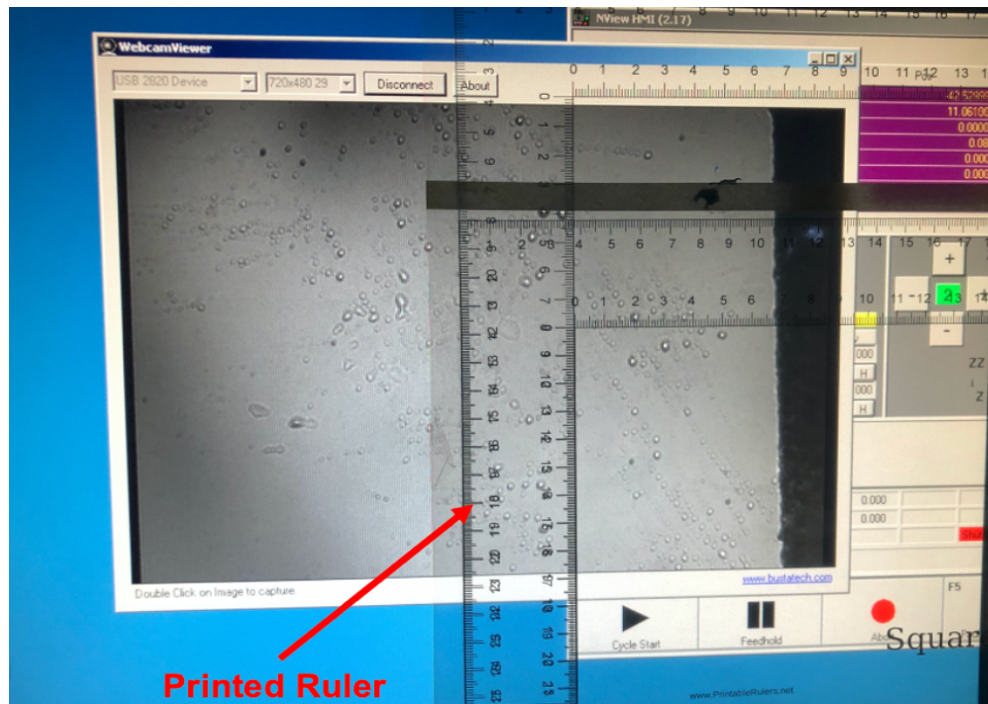
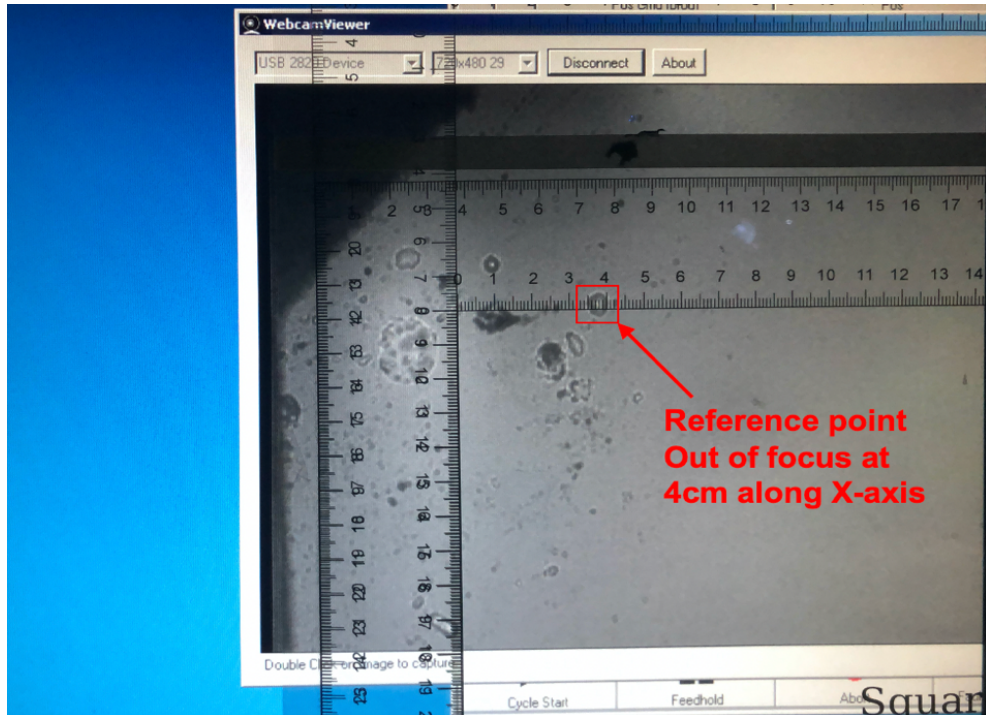
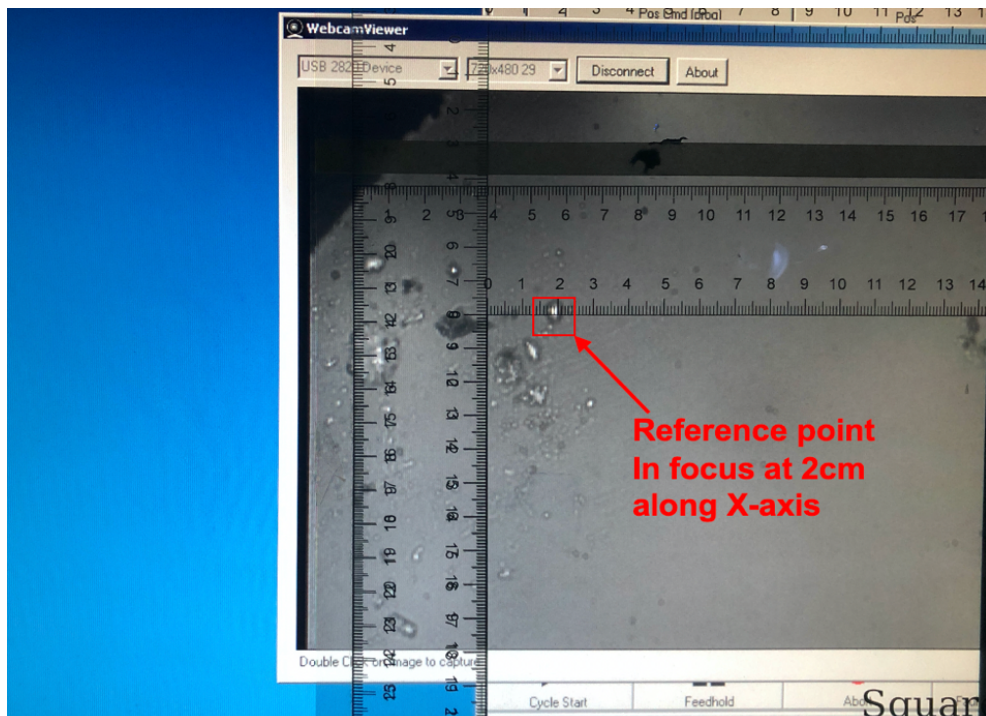


Figure 3-11. A ruler scale printed on a projector paper is used to quantify the alignment process where the printer ruler paper was attached on a PC monitor for guiding the alignment.

An example shown in Figure 3-12 is used to demonstrate how this method works. It can be seen from Figure 3-12(a), it shows an out of focus position at the chosen reference point which is at 4cm along the X-axis of the ruler. By adjusting the goniometer, this blurry reference point becomes clear as shown in Figure 3-12(b), where along the X-axis of the ruler, it is now at the 2cm position. Therefore, a 2cm apparent movement has been made manually by rotating the sample along the X-axis. Then the inscription program mentioned earlier is needed to verify the focus point. Finally, after several tries, a certain relationship between the goniometer movement and the ruler distance can be confirmed. By using this method, it enables a high degree of alignment which can also be traced back to the previous step even if a mistake has been made. It can quantitatively and qualitatively improve the alignment process.



(a)



(b)

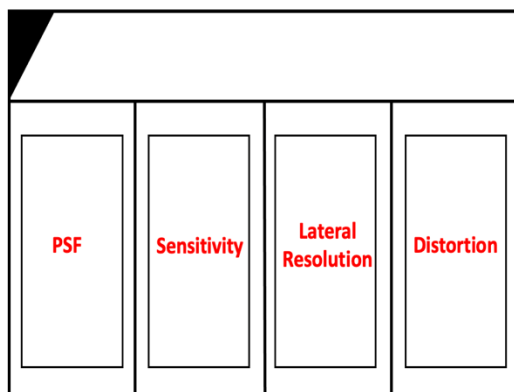
Figure 3-12. The images showing how to apply this screen-to-ruler method in the alignment process: (a) The image shows the out-of-focus position at the chosen reference point where it is located at 4cm along the X-axis; (b) The image shows the in-focus position at the chosen reference point where it is located at 2cm along the X-axis.

3.6 Study the existing planar OCT phantom

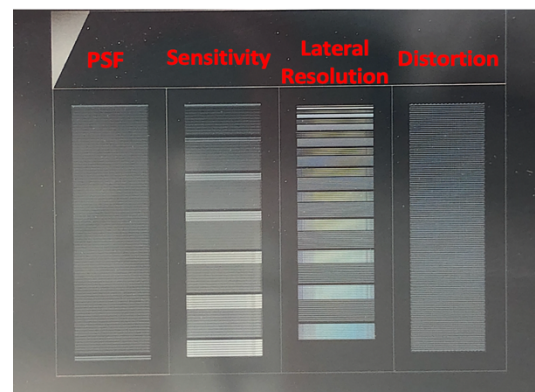
3.6.1 Planar OCT phantom layout

In the original planar OCT phantom, four patterns were designed to be used for measuring differing performances of the OCT systems, which are the point spread function (PSF), sensitivity (S), lateral resolution (LR) and distortion/grid (D). Each pattern has 8 layers in total to test for such parameters across various depths in the material. This design has been previously developed [21] by Lee et al. at Aston University.

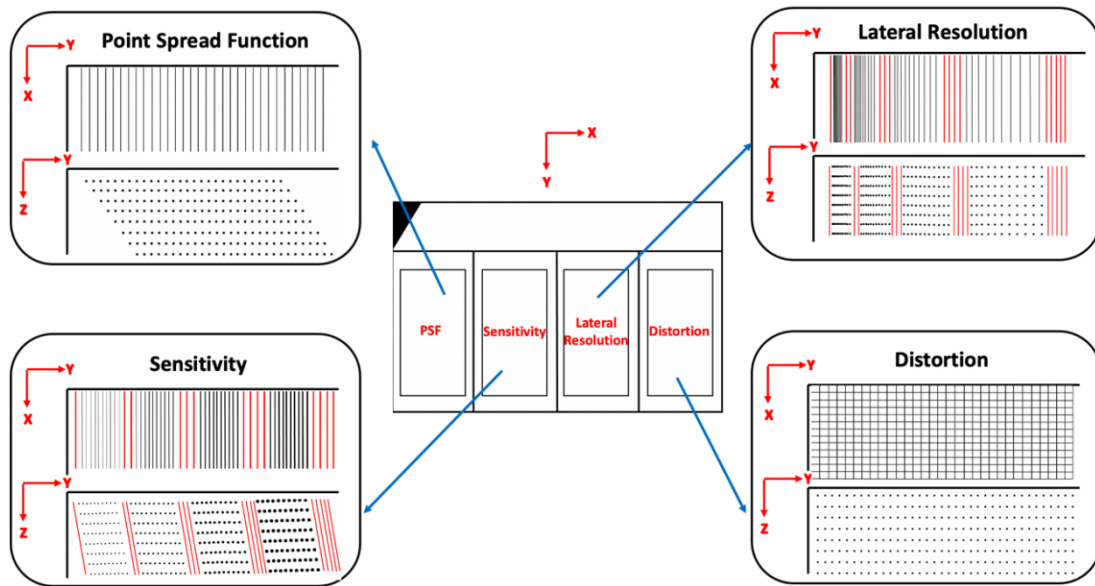
The purpose of this study presented in this section was to learn the fabrication process and understand the challenges involved in the characterisation and validation process in detail. The design is shown in Figure 3-13(a) and the fabricated OCT phantom using previous fabrication method and design is shown in Figure 3-13 (b), and the top-view at the X-Y plane and the cross-sectional view at the Y-Z plane conceptual images are presented in Figure 3-13 (c).



(a)



(b)



(c)

Figure 3-13. (a) Planar OCT phantom pattern conceptual layout; (b) Femtosecond laser fabricated planar OCT phantom (previously developed at Aston by Lee et al. [21]); (c) The conceptual images of four test patterns for both the top-view (at the X-Y plane) and the cross-sectional view (at the Y-Z plane) with the index lines/guidelines indicated in red.

A PSF pattern is used to measure the spatial resolution of an OCT system. It is the first pattern shown in Figure 3-13 (b) from the left. All lines are spaced at the same distance and inscribed with fixed pulse energy. The first layer was set to be approximately $100\mu\text{m}$ (in apparent depth (AD)) below the surface and the subsequent layer separation was set to be $50\mu\text{m}$ (in AD). There were 110 lines plus 3 index lines with a line separation of $150\mu\text{m}$ and a layer offset of $25\mu\text{m}$.

The sensitivity pattern is designed to detect the smallest intensity signal that the system can capture. It is the second pattern shown in Figure 3-13 (b) from the left. The pattern consists of 6 sets of lines with 5 pairs in each set (i.e. 30 pairs in total) separated with guidelines. Each pair was set at different energy levels varied in a range of 30%-39% of the attenuator position which was set in the fabrication program. There was an even increase (i.e. 0.3%) in the energy level from pair to pair.

The lateral resolution pattern is designed to enable quick qualitative checks of an OCT system's resolution, i.e. the smallest line spacing that the system can resolve [21]. It is the third pattern shown in Figure 3-13 (b) from the left. It consisted of 10 sets of lines with the line separation varying from $1\text{-}100\mu\text{m}$, with the line separation being gradually increased. Each set contained 11-line separations with varying line spacing at a step of $1\mu\text{m}$, for example, the line spacing for the set 1 varies from $1\text{-}10\mu\text{m}$, for the set 2 varies

from 11-20 μm and for the set 3 varies 21-30 μm separately. Guidelines located among each set are used to distinguish the valid test area. There was no layer offset for this pattern, hence all lower layers are aligned with layers above.

The grid pattern is typically used to detect the system distortion, as distortion will apply some level of transformation on the grid structure. It is the fourth pattern shown in Figure 3-13 (b) from the left. The cell size of the grid pattern was set to be 100 μm x 100 μm and there was no layer offset for this pattern. Each layer is essentially the same at different Z heights.

3.6.2 Phantom fabrication

The inscription lens used to fabricate the phantom was 100x objective lens (Mitutoyo M Plan Apo NIR) with a NA of 0.5, 100kHz for the repetition rate and the writing speed was set to 10mm/s. The laser power was set to 35% of the maximum attenuator position (i.e. 1.03 μJ for energy per pulse) to fabricate PSF, lateral resolution (LR) and distortion (D) patterns. The sensitivity pattern is inscribed by using different energy levels varying from 30% to 39% of the total output power (i.e. 880nJ-1.142 μJ for energy per pulse). To avoid scattering from pre-written lines, the inscription process is always started from the lowest layer. This process enabled each layer to be clearly inscribed without the light path being influenced by prior inscriptions.

3.6.3 Microscope characterisation

Before performing pattern measurements, an initial test was to measure the depth of planar substrate by focusing on pen marks on the top and the bottom of the substrate. The apparent depth (AD) of the top of the substrate was measured as -2025.108 μm and the apparent depth (AD) of the bottom of the substrate was measured as -622.251 μm . Therefore, the thickness of the substrate (in AD) can be calculated as the difference between the top surface and the bottom surface of the substrate which was $\Delta = 2025.108 - 622.251 = 1402.857\mu\text{m}$. The refractive index of 1.461 at the wavelength of 532nm was used to calculate the real depth (RD) from the apparent depth (AD). Hence, the real depth (RD) of the substrate can be calculated by $1402.857 \times 1.461 = 2049.574\mu\text{m} = 2.049\text{mm}$, which showed an agreement to the substrate thickness of 2mm, in which a batch of substrates was mechanically measured by a precision micrometre as shown in Appendix A. There is a slight difference in refractive index due to various imaging systems having different central wavelengths (i.e. the range of 532nm -1030nm), hence a slight difference in the refractive index, with it ranging from 1.450 to 1.461.

3.6.3.1 Point spread function (PSF) pattern

The first pattern evaluated was the point spread function (PSF), with the measurement starting from the top layer. The top edge and the bottom edge were selected to measure and to be compared for the reference. The results were obtained by focusing the line on each layer. The measurement results are shown in Table 3-3 and Table 3-4 at below.

20x microscope objective used to measure the PSF pattern (top edge)

	1 st pattern (AD) (μm)	AD difference (μm)	1 st pattern (RD) (μm)	RD difference (μm)
Surface	31.732		43.360	
D1	139.026	107.294	203.117	156.757
D2	197.472	58.446	288.507	85.390
D3	249.849	52.377	365.029	76.523
D4	300.186	50.337	438.572	73.542
D5	346.545	46.359	506.302	67.730
D6	397.698	51.153	581.037	74.735
D7	448.443	50.745	655.175	74.138
D8	498.882	50.439	728.867	73.691
Average		51.408		75.107

Table 3-3. Microscope measurement results of PSF pattern at the top edge.

20x microscope objective used to measure the PSF pattern (bottom edge)

	1 st pattern (AD) (μm)	AD difference (μm)	1 st pattern (RD) (μm)	RD difference (μm)
Surface	83.181		121.527	
D1	184.212	101.031	269.134	147.606
D2	235.365	51.153	343.868	74.735
D3	287.997	52.632	420.764	76.895
D4	348.942	60.945	509.804	89.041
D5	397.902	48.960	581.335	71.531
D6	443.445	45.543	647.873	66.538
D7	492.996	49.551	720.267	72.394
D8	547.179	54.183	799.429	79.161
Average		51.852		75.756

Table 3-4. Microscope measurement results of PSF pattern at the bottom edge for all layer depths and layer separations.

By averaging the results for 8 layers, the apparent depth (AD) of the top edge was approximately 51.4 μm and the real depth (RD) of the top edge is approximately 75.1 μm . The apparent depth of the bottom edge is approximately 51.8 μm and the real depth of the bottom edge is approximately 75.7 μm . The results agree to previous work. The top

edge and the bottom edge have a very minor difference which is $\Delta = 75.7 - 75.1 = 0.6\mu\text{m}$, however, under the scale of micrometre (μm), this difference would be negligible for an OCT system to be detected and also the subjective judgment can lead to the measurement error.

3.6.3.2 Sensitivity pattern

In this pattern design, pairs of lines are inscribed with the same pulse energy so that they are two identical lines in a pair. Different pairs are inscribed with different laser pulse energy. There are 30 energy pairs in total. The thinnest linewidth is around $1.98\mu\text{m}$ (shown in Figure 3-14) and the thicker linewidth is around $3.63\mu\text{m}$ (shown in Figure 3-15). The line separation is $150\mu\text{m}$ and the layer offset is $25\mu\text{m}$.

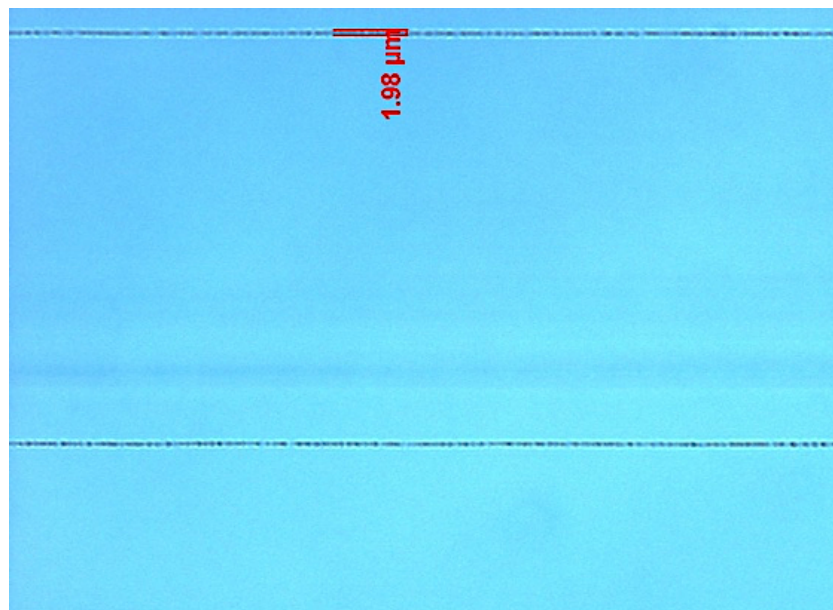


Figure 3-14. Microscope measurement of the thinnest linewidth of $1.98\mu\text{m}$ in the sensitivity pattern at the top edge (i.e. the inscription with lowest laser pulse energy of the set energy range).

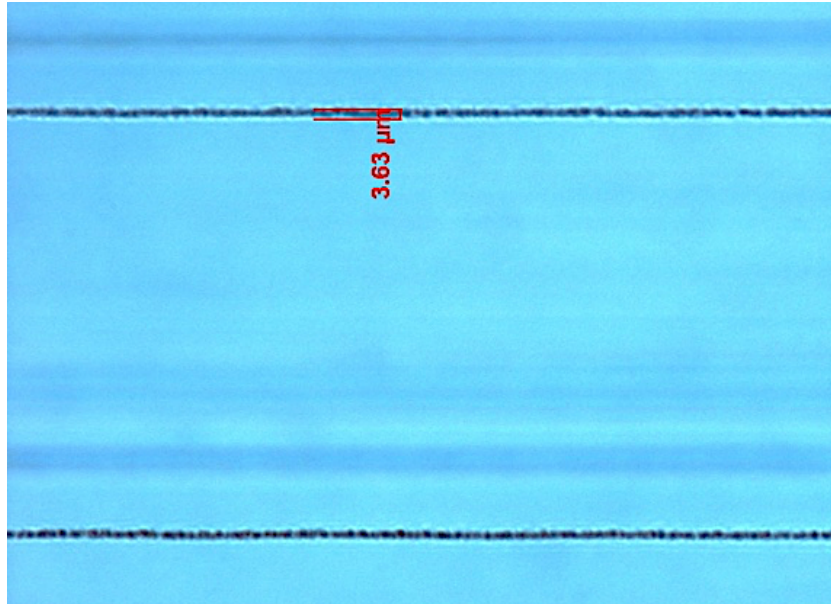


Figure 3-15. Microscope measurement of the thicker linewidth of 3.63 μ m in the sensitivity pattern at the bottom edge (i.e. the inscription with higher laser pulse energy).

For the sensitivity pattern, the guideline is used to help the user to locate the test area. The set n will be located between n and $n+1$ index line. In Figure 3-16, it can be seen that it is quite easy to distinguish the area of the test lines and the index lines/guidelines.

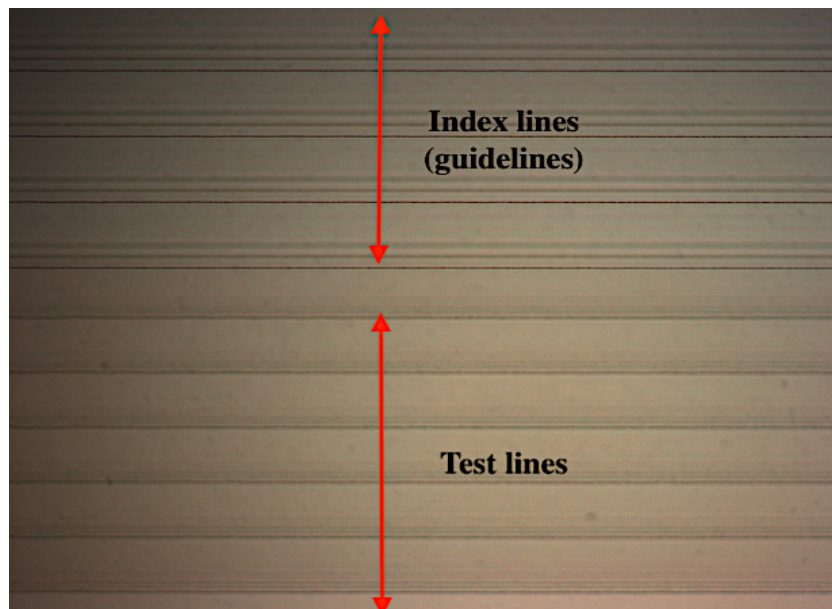


Figure 3-16. Microscope image showing both the index lines (guidelines) and the test lines of the sensitivity pattern as the index lines (guidelines) are used to help the user to locate the test area.

3.6.3.3 Lateral resolution pattern

According to the microscope, the measurements of the apparent depth (AD) for each layer has also conducted and analysed. The layer distance keeps at around 51 μm (in AD) or 75 μm (in RD). The measurement results are shown in Table 3-5.

20x microscope objective used to measure the lateral resolution pattern

	1st pattern (AD) (μm)	AD difference (μm)	1st pattern (RD) (μm)	RD difference (μm)
Surface	0		0	
D1	104.244	104.244	152.300	152.300
D2	159.273	55.029	232.698	80.397
D3	209.610	50.337	306.240	73.542
D4	258.927	49.317	378.292	72.052
D5	308.040	49.113	450.046	71.754
D6	357.459	49.419	522.248	72.201
D7	418.149	60.690	610.916	88.668
D8	462.774	44.625	676.113	65.197
Average		51.219		74.830

Table 3-5. Measurement results of lateral resolution pattern for all layer depths and layer separations.

Figure 3-17 - Figure 3-19 show the microscope measurement of the line separation for first three sets of the lateral resolution pattern. It can be seen that Figure 3-17 shows that the line separation is varying in the range of 1-10 μm for the first set. Figure 3-18 shows that the line separation is varying in the range of 11-20 μm for the second set and Figure 3-19 shows that the line separation is varying in the range of 21-30 μm for the third set.

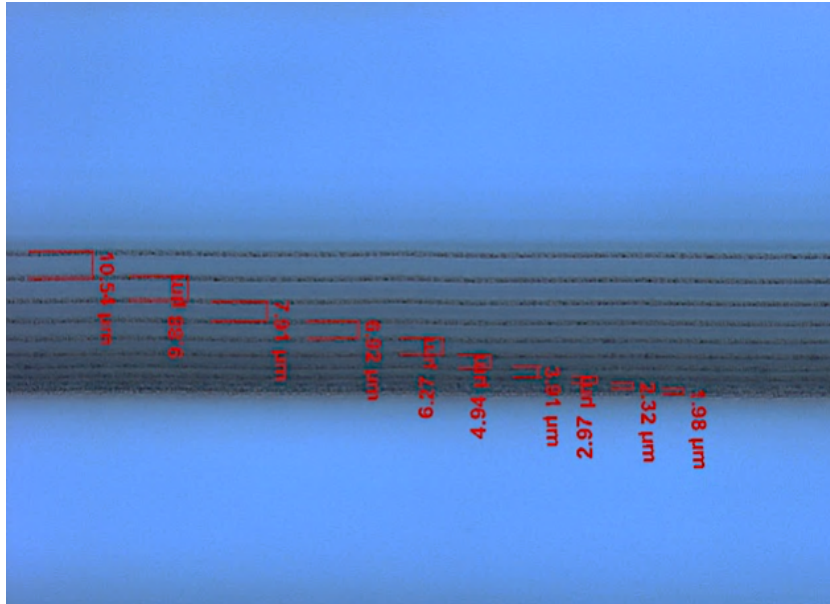


Figure 3-17. Microscope image of the line separation measurement of the lateral resolution pattern (Set 1). For Set 1, the line separation between each inscription lines were set to be varied in the range of 1-10 μ m.

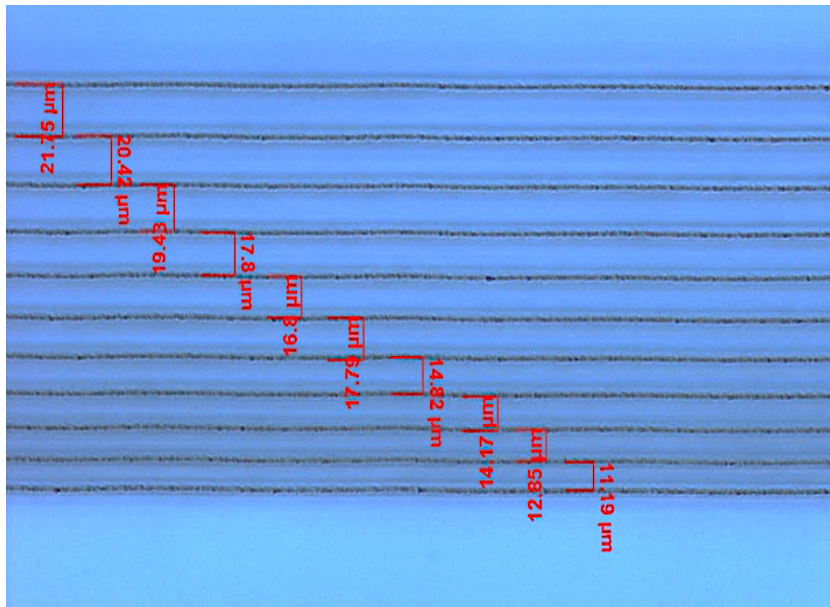


Figure 3-18. Microscope image of the line separation measurement of the lateral resolution pattern (Set 2). For Set 1, the line separation between each inscription lines were set to be varied in the range of 11-20 μ m.

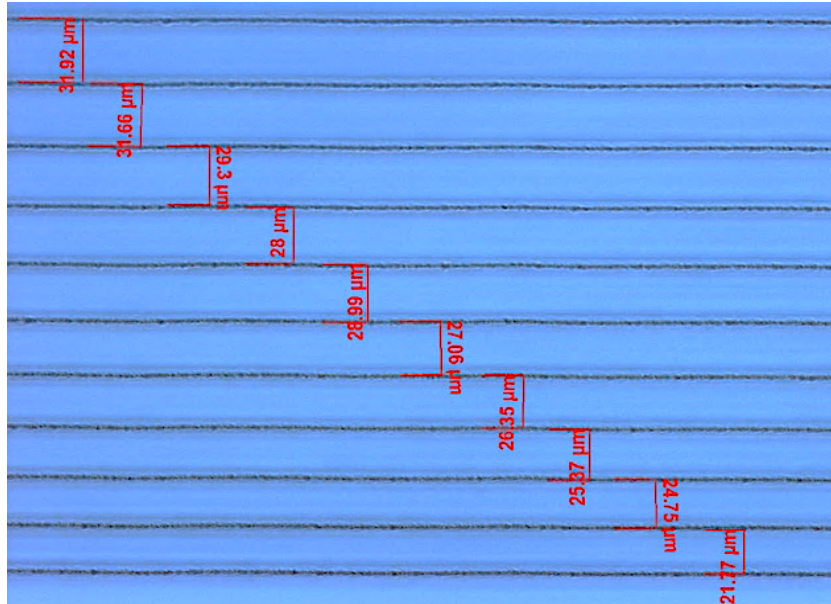


Figure 3-19. Microscope image of line separation measurement of the lateral resolution pattern (Set 3). For Set 3, the line separation between each inscription lines were set to be varied in the range of 21-30 μ m.

3.6.3.4 Distortion/grid pattern

The cubic size of the grid pattern was set to be 100 μ m x 100 μ m shown in Figure 3-20 and it has 8 layers in total. The thickness of each line is around 2.64 μ m. The pattern is mainly used for the distortion detection of the OCT system.

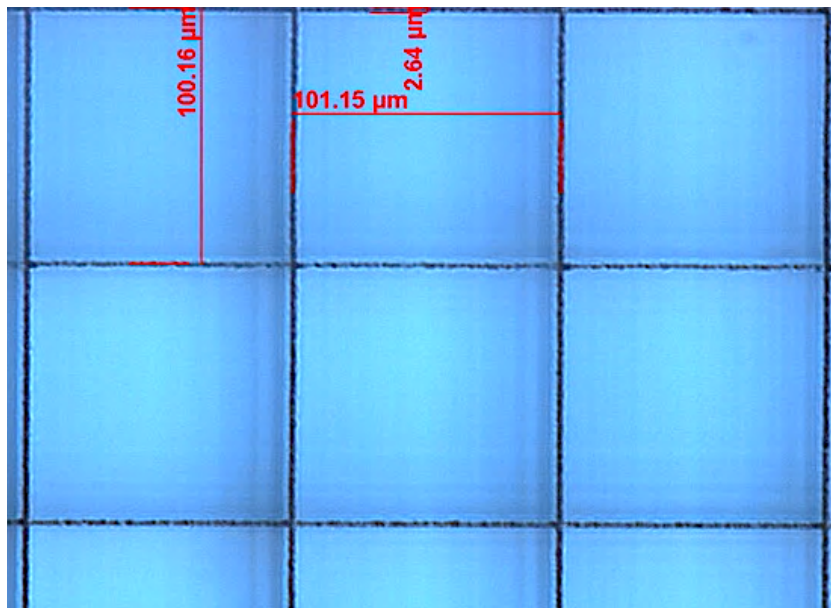


Figure 3-20. Microscope image of line separation measurement of the grid pattern showing the cell size of ~100 μ m x 100 μ m and the inscription linewidth of 2.64 μ m.

Under the microscope, the layer distance for 8 layers has been measured and analysed, shown in Table 3-6 below. However, it was noticed that the real depth difference between each layer is approximately 72 μm , which is 3 μm different from the other patterns. This difference could be caused by the subjective judgment for the focusing point of the microscope when measuring the sample.

20x microscope objective used to measure the Grid pattern				
	1st pattern (AD) (μm)	AD difference (μm)	1st pattern (RD) (μm)	RD difference (μm)
Surface	0		0	
D1	110.925	110.925	162.061	162.061
D2	161.925	51.000	236.572	74.511
D3	213.180	51.255	311.456	74.884
D4	262.344	49.164	383.285	71.829
D5	314.415	52.071	459.360	76.076
D6	363.477	49.062	531.040	71.680
D7	412.488	49.011	602.645	71.605
D8	456.501	44.013	666.948	64.303
Average		49.368		72.127

Table 3-6. Microscope measurement results of grid pattern for all layer depths and layer separations.

3.6.3.5 Measurement error

It should be noted that the measurement results can be subjective when using the manual focus of the microscope. According to the Table 3-7 at below, there are slight differences in the measurement on the same sample based on two different persons' measurements. It can be seen that the subjective judgment could cause the measurement difference as shown in some measurements which can result in up to 7 μm difference. For example, for the measurement of layer separation of D3, the person 1 measured and reported as 52.377 μm but the person 2 measured and reported as 46.92 μm .

Moreover, the surface of the substrate can also cause difference as the person 1 result showing as 107.294 μm while the person 2 result showing as 103.428 μm , which presents almost a 4 μm measurement difference. By minimising the measurement errors, an average of the multiple tests can be used. After taking the average, the AD difference become $\Delta = 51.772 - 51.408 = 0.364\mu\text{m}$ and for the corresponding RD difference become $\Delta = 75.639 - 75.107 = 0.532\mu\text{m}$.

Person 1:**20x microscope objective used to measure the PSF pattern (top edge)**

	1st pattern (AD) (μm)	AD difference (μm)	1st pattern (RD) (μm)	RD difference (μm)
Surface	31.732		46.360	
D1	139.026	107.294	203.117	156.757
D2	197.472	58.446	288.507	85.390
D3	249.849	52.377	365.029	76.523
D4	300.186	50.337	438.572	73.542
D5	346.545	46.359	506.302	67.73
D6	397.698	51.153	581.037	74.735
D7	448.443	50.745	655.175	74.138
D8	498.882	50.439	728.867	73.691
Average		51.408		75.107

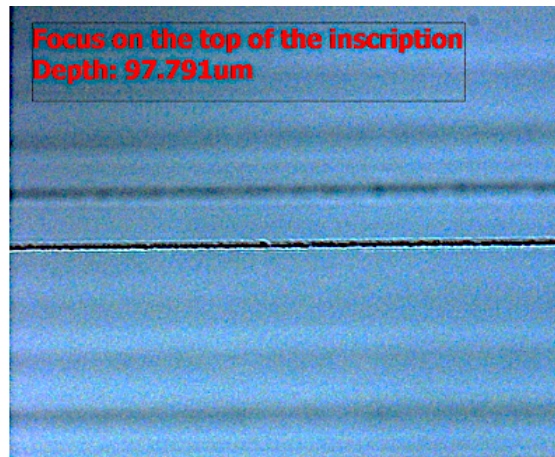
Person 2:**20x microscope objective used to measure the PSF pattern (top edge)**

	1st pattern (AD) (μm)	AD difference (μm)	1st pattern (RD) (μm)	RD difference (μm)
Surface	33.762		49.326	
D1	137.190	103.428	200.435	151.108
D2	194.361	57.171	283.961	83.527
D3	241.281	46.920	352.512	68.550
D4	293.454	52.173	428.736	76.225
D5	345.372	51.918	504.588	75.852
D6	395.097	49.725	577.237	72.648
D7	445.179	50.082	650.407	73.170
D8	499.596	54.417	729.910	79.503
Average		51.772		75.639

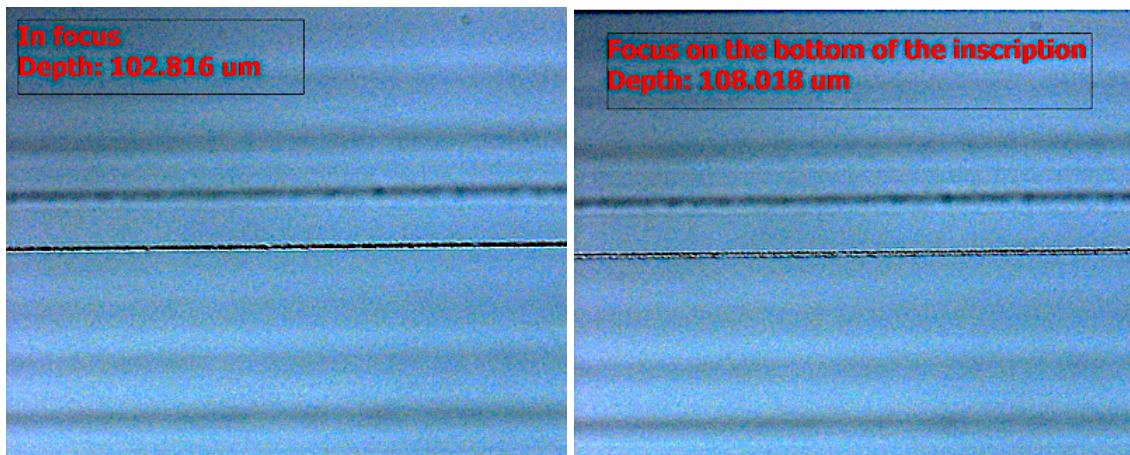
Table 3-7. The comparison of the microscope measurement of PSF pattern at the top edge for all layer depths and layer separations between the Person 1 and the Person 2 to show that the measurement difference can be caused by subjective judgement which leads to the measurement errors.

In Figure 3-21, three different positions were selected to show how much the differences in depth can be at different focus positions. Figure 3-21(a) shows if focused on the top of the inscription, the depth was measured as $97.791\mu\text{m}$, at this point, the image was not completely focused as it still blurred at the edge of the inscription. Figure 3-21(b) shows if focused on the middle of the inscription, which was treated at the focus position for the measurement, the depth was measured as $102.816\mu\text{m}$. Figure 3-21(c) shows if focused on the bottom of the inscription, the depth was measured as $108.018\mu\text{m}$. It is

noticeable that from the top of the inscription to the bottom of the inscription, there is around $10.227\mu\text{m}$ distance, by having such span, that is where the measurement error comes from. However, by having multiple times of the measurement, an average measurement value is used to minimise the measurement error caused by the subjective judgement.



(a)



(b)

(c)

Figure 3-21. Microscope images using a 20x objective lens indicating how the focus position was determined for the measurement: (a) when focused on the top of the inscription at $97.791\mu\text{m}$; (b) when at the in-focus position at $102.816\mu\text{m}$; (c) when focused on the bottom of the inscription at $108.018\mu\text{m}$.

3.6.4 OCT systems characterisation

3.6.4.1 Point spread function (PSF) pattern

The OCT image shown in Figure 3-22 was taken using the Optimec is830 system. It can be seen that the index lines are located at two ends of the pattern. The layer separation

is $76.4\mu\text{m}$ (in real depth (RD)) which closely matches the value measured by the microscope of $75.7\mu\text{m}$. The line separation is $\sim 152.8\mu\text{m}$ which is really close to the designed value of $150\mu\text{m}$.

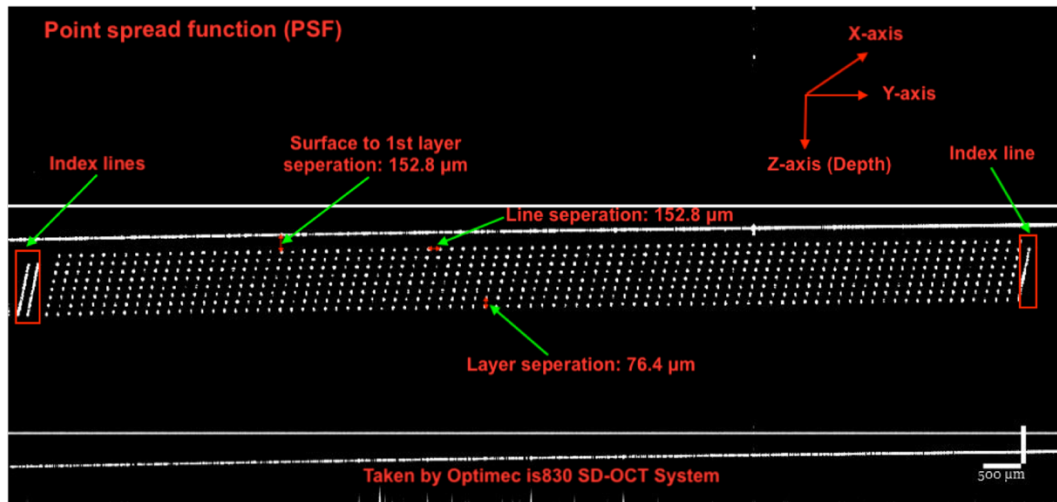


Figure 3-22. OCT image of point spread function (PSF) pattern (taken by Optimec is830 system with a central wavelength of 830nm and an axial resolution of $12\mu\text{m}$ (in air)).

3.6.4.2 Sensitivity pattern

The second pattern on the OCT phantom is the sensitivity pattern. It can be seen from the Figure 3-23 that there are totally 6 sets separated by index lines/guidelines. There are 5 pairs in a set, therefore 30 pairs in total. Each pair has different energy level varied at a range of the power (i.e. 30%-39%) so that there are 30 different energy levels. Therefore, for set 1, the energy level varies from 30% to 31.2% with an incremental difference of $\sim 0.3\%$ for each pair. For the set 2, the energy level varies from 31.6% to 32.8%. The layer separation is around $72.3\mu\text{m}$ which matches the theoretical value which is set to $50\mu\text{m}$ in apparent depth (AD) or $73.05\mu\text{m}$ in real depth (RD). The line separation is around $150.1\mu\text{m}$ which also matches closely to the theoretical value which is set to $150\mu\text{m}$.

Set 1 and 2 show missing lines at the bottom of the image illustrating the sensitivity limit of the measurement system. By comparing scans at a later date, the user can gain reassurance that the sensitivity of the system has not decreased due to misalignment.

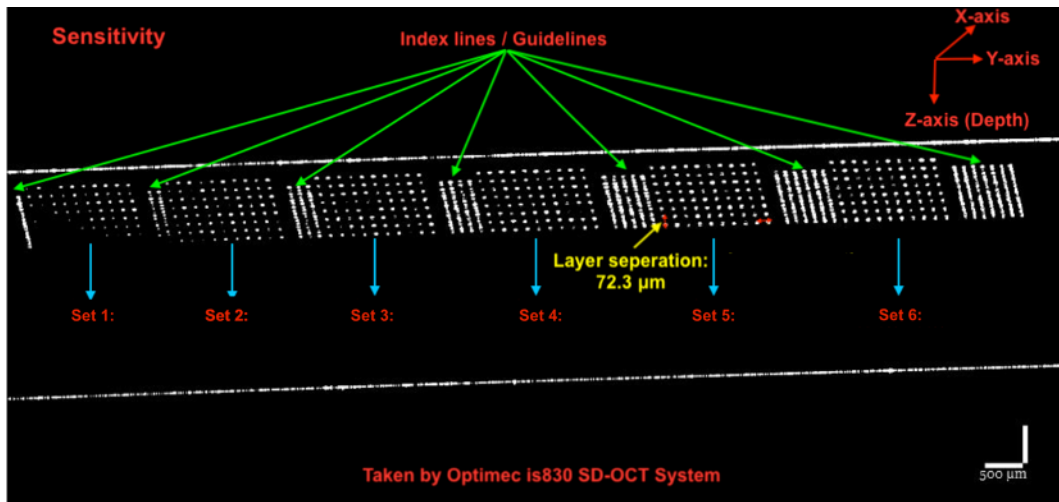


Figure 3-23. OCT image of sensitivity pattern (taken by Optimec is830 system with a central wavelength of 830nm and an axial resolution of 12μm (in air)).

3.6.4.3 Lateral resolution pattern

The lateral resolution pattern shown in Figure 3-24 has 10 sets with each set having 11 lines. The line separation varied from 1-100μm with 1μm increments. The line separation is around 91.2μm which matches to the designed value which is around 91μm. The layer separation is around 76.2μm which matches to the microscope measurement value of 74.8μm.

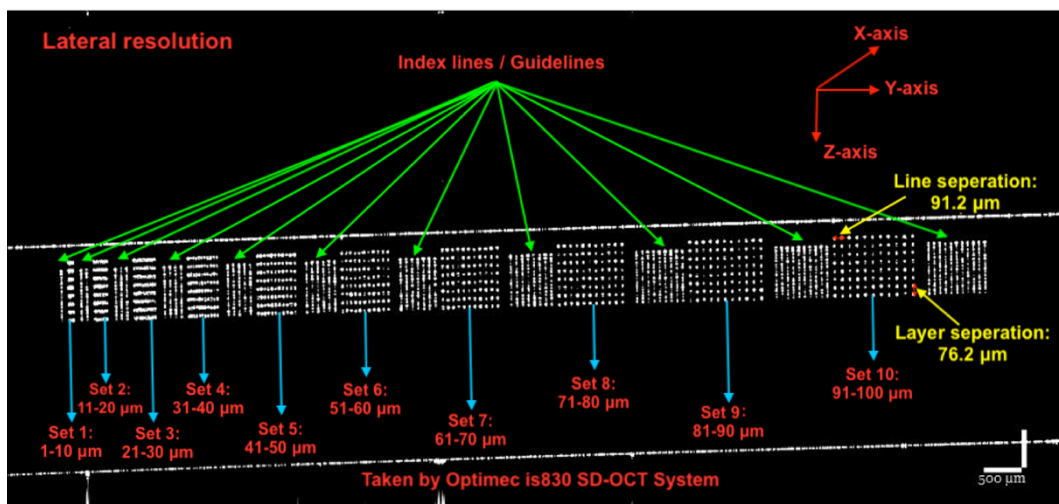


Figure 3-24. OCT image of lateral resolution pattern (taken by Optimec is830 system with a central wavelength of 830nm and an axial resolution of 12μm (in air)).

3.6.4.4 Distortion/grid pattern

The distortion/grid pattern shown in Figure 3-25 has a cell size of $100.3\mu\text{m}$ which matches closely to the theoretical value of $100\mu\text{m}$. It has a layer separation of $\sim 72.6\mu\text{m}$ which matches the microscope measurement result of $72.1\mu\text{m}$.

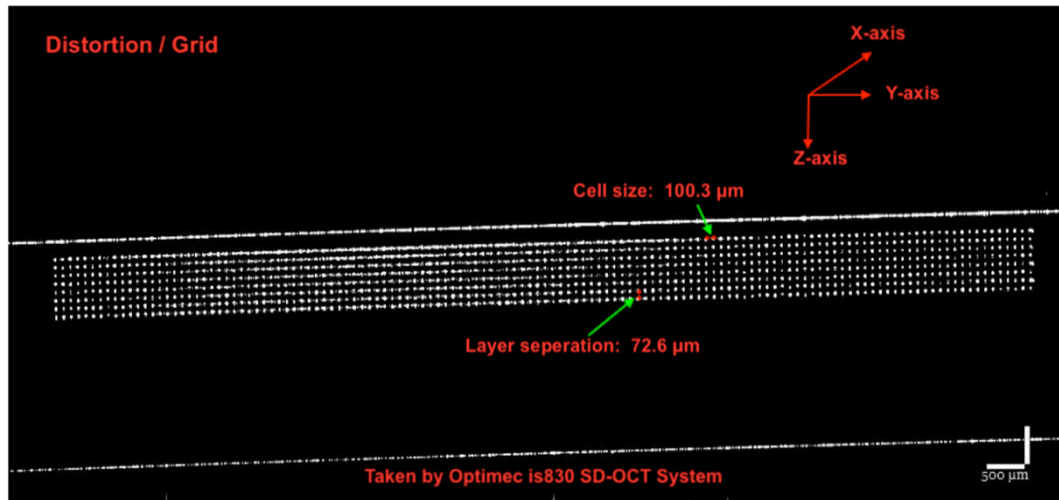


Figure 3-25. OCT image of distortion pattern (taken by Optimec is830 system with a central wavelength of 830nm and an axial resolution of $12\mu\text{m}$ (in air)).

3.7 Chapter conclusions

In conclusion, this chapter presented the specifications and operating performance of the femtosecond laser system used to fabricate the phantom with the following section describing the phantom design and fabrication workflow. The sample substrate and material has also been introduced. The quantitative method used to improve the alignment accuracy has been demonstrated as an alignment process can be time-consuming and the flatness of the substrate can affect the fabrication results significantly. The equipment used for the phantom characterisation has then been introduced. A detailed study of the existing OCT phantom previously developed at Aston has been presented with the measurement error discussed.

Chapter 4

Fabrication optimisation

This chapter presents the research work for the study on the laser power and the fabrication optimisation. The chapter starts with a brief introduction presented in Section 4.1 to discuss the current issue and further improvements that needed on the fabrication process optimisation. Section 4.2 demonstrates the design and fabrication of a laser power test pattern which is used for the laser power study. A detailed study focused on investigating the correlation between the laser pulse energy and the inscription size which is the inscription linewidth study on the X-Y plane presented in Section 4.3 and the inscription height study on the Y-Z plane presented in Section 4.4. The findings from those studies directly contribute to standardisation and optimisation of the phantom fabrication process. Section 4.5 discusses the fabrication optimisation implemented on a revised design to verify the findings.

4.1 Introduction

Femtosecond laser direct writing is a laser-based method that enables a highly accurate fabrication process and finish inside of the material. One of the most challenging aspects of the femtosecond laser inscription is that it is difficult to keep the size of inscription consistent at different depths inside of the material. This is due to inducing the nonlinear Kerr effect of the laser beam self-focusing when the power is exceeding the critical power value [188] and the depth dependent spherical aberration. However, it is extremely important when fabricating optical calibration devices such as OCT phantoms as the inscription size is directly affected by the laser pulse energy applied. Therefore, a comprehensive study was needed on the correlation between the laser pulse energy and the inscription size so that the appropriate laser pulse energy can be applied to obtain the same size of the inscription at various depths with minimising the self-focussing effect,

In this section, the correlation between the laser pulse energy and the inscription size is investigated and quantitatively analysed. The femtosecond laser direct writing technique was used to fabricate test patterns which were characterised with an optical microscope and an OCT system. Here, the inscription size is not only investigated in the X-Y plane (i.e. the inscription linewidth) and also in the Y-Z plane which is the cross-sectional image of the test pattern (i.e. the inscription height) which is the same perspective that viewing under an OCT system. The findings of this study benefit the further development of the new phantoms shown in this thesis.

4.2 Laser power test pattern design and fabrication

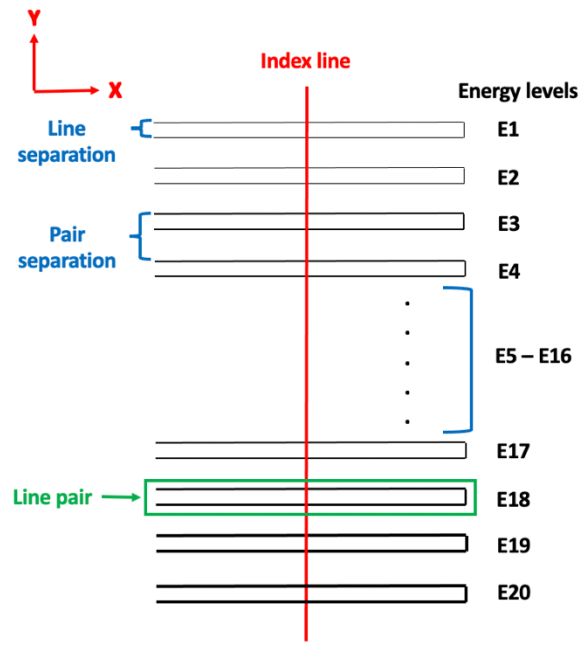
The previous research findings show that the laser energy can heavily affect the laser induced modification [189, 190]. In order to study and analyse how the variation of the laser pulse energy can affect the inscription size, a test pattern was designed that covers the full power range of the laser system. The laser power test pattern was designed and written as a CNC program, which in the program, the laser power was set to start from 5% to 100% of the total average output power with a step of 5% of the total average output power increase from pair to pair. The output power was measured from 15mW to 308mW, which corresponds to a pulse energy from 150nJ to 3.08 μ J per pulse at the repetition rate of 100kHz and a pulse width of ~500fs. The average laser output power was measured by an optical laser power metre before this test pattern was fabricated as

part of the preparation work. The substrate used was planar fused silica with a dimension of 30mm x 25mm x 2mm (Ibsen Photonics, Denmark).

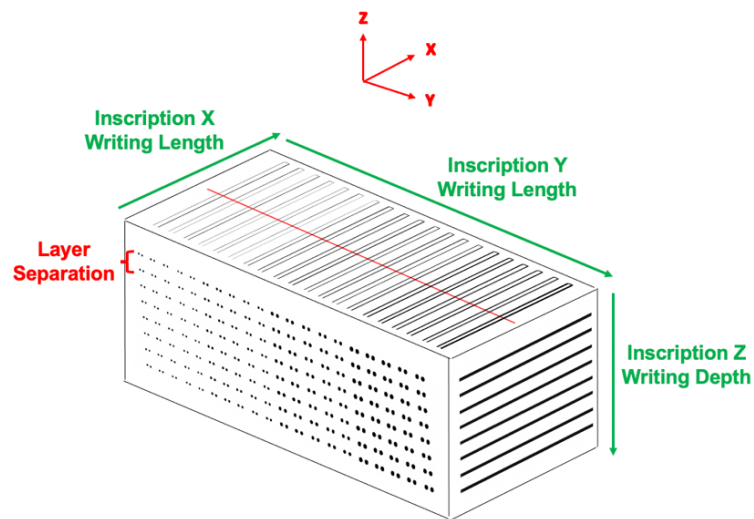
The pattern was inscribed within the substrate with the top pattern layer located at 100 μ m (in apparent depth (AD)) below the front surface. There were eight layers in total inscribed and the same pattern was inscribed to all the layers located at various depths. For the parameter settings, the layer separation was set to 150 μ m (in AD) and the total inscription depth was around 1150 μ m (in AD). Each layer pattern shown in Figure 4-1(a) consisted of 20 energy pairs, which started from 5% for the first energy pair, and then 10%, 15%, 20% with a step of 5% increase for following pairs and then the 100% of the total average output power was used for the last pair.

The index line which was located in the middle was inscribed with 100% of the laser power vertically so that it could be easily recognised and distinguished. Each energy pair included two lines which were inscribed with same pulse energy with the writing directions of +X direction and -X direction along the X-axis, which was set to 20 μ m apart between each line and there was 200 μ m apart between each pair. There was a 25 μ m layer offset between each layer to reduce the back scattering.

A 3D conceptual design diagram was showed in Figure 4-1(b) to illustrate the idea that how the overall test pattern looks like inside a substrate with the cross-sectional slice indicated to present the depth information of the pattern. It can be seen that on the Y-Z plane shows the cross-sectional image which is how the OCT system usually scans the sample in a 2D scanning mode.



(a)



(b)

Figure 4-1. The conceptual design for the laser power test pattern showing the design parameters: (a) the view from the X-Y plane with the parameters indicated; (b) a 3D view for the test pattern inside a substrate, where the Y-Z plane showing the cross-sectional image which is how the OCT system usually scans the sample in a 2D scanning mode.

For the fabrication method, the substrate was carefully cleaned and aligned on the fabrication stage to ensure its flatness of the surface. The CNC program was compiled and executed by using the NView software. The fabrication was started from the most bottom layer (i.e. at the depth of 1150 μm (in AD) from the front surface) to avoid any scattering caused by any pre-written inscription. As the stage moved downwards, the

successive layer patterns were inscribed layer by layer. The test pattern was inscribed layer by layer as the pattern consisted of multiple laser energy pairs with each pair had different laser pulse energy applied.

Moreover, an index line was inscribed in the middle for each pattern layer for a position reference. It is useful when quantifying the inscription under the microscope as it can help to improve the consistency of the measurement position. The total laser fabrication process took around 10 minutes to fabricate this test pattern.

4.3 Laser power test pattern characterisation on the X-Y plane

After the fabrication, the sample was then characterised by using an optical microscope and validating by OCT systems after the characterisation. For the microscope images, both a 5x objective and a 20x objective lens were used to inspect and characterise the inscription on the X-Y plane. In Figure 4-2, a 5x objective lens was used to inspect the sample and provide an overview of the pattern structure. The separation between pairs, the pair separation and the line separation in a pair have been measured, which are in good agreement with the designed parameters. It can be used to demonstrate how accuracy and smooth finish by using a femtosecond laser for the fabrication.

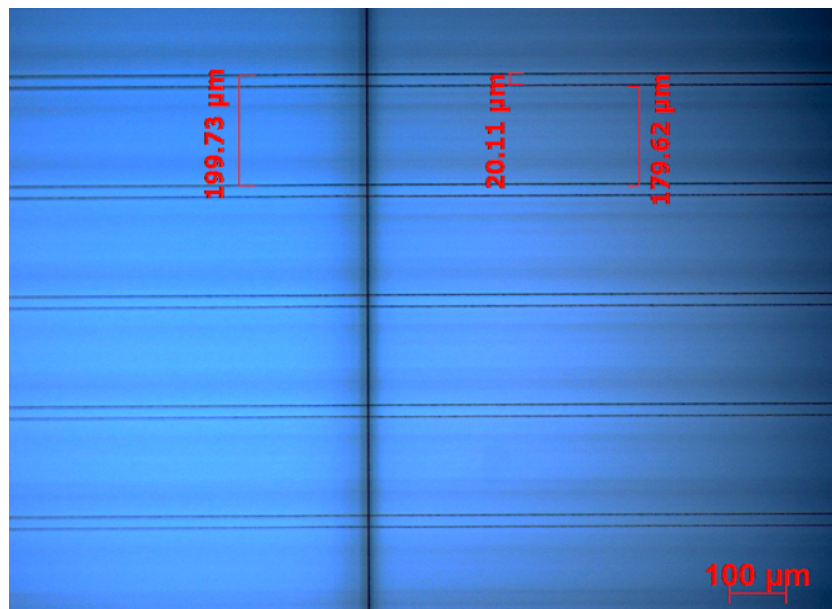


Figure 4-2. The microscope image using a 5x objective lens is to inspect the laser energy test pattern, which shows the pair line separation is measured as 20.11 μm , the pair separation is measured 199.73 μm and the separation between pairs is measured as 179.62 μm .

In Figure 4-3, a 20x objective lens was used and the microscope image shows that the real measurement of the laser power test pattern that matches to the design parameters

settings. It can be seen that the line-to-line separation in a pair was measured as $\sim 20.76\mu\text{m}$ and the line pair to line pair separation as $200\mu\text{m}$. The pair edge to edge separation was measured as $\sim 180.37\mu\text{m}$. At here, it has around $1\mu\text{m}$ measurement error existed, which was due to the variation on the exact measurement position. However, based on the real measurements of the inscription, it matched to the design parameters setting in the fabrication CNC program, which can also demonstrate the accuracy of the fabrication process by using a femtosecond laser direct writing technique.

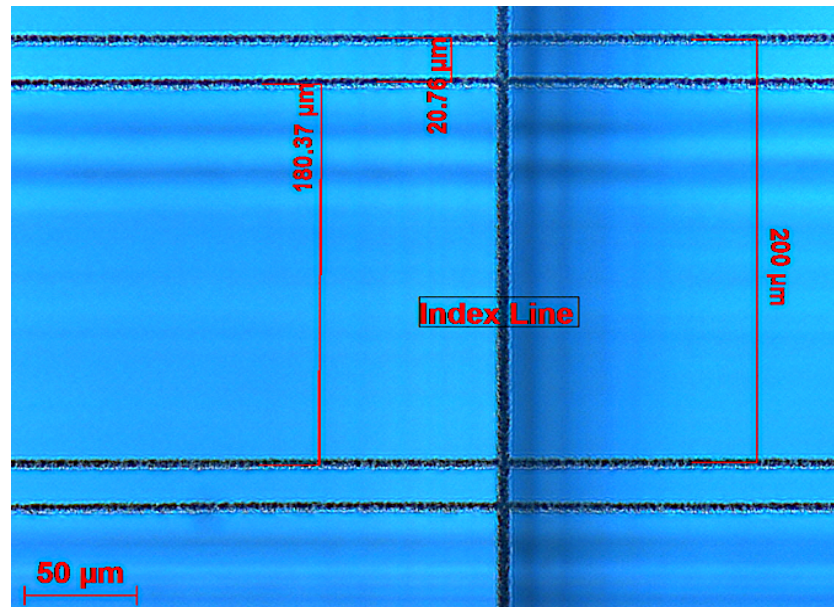


Figure 4-3. Microscope image using a 20x objective lens shows the inscribed laser power test pattern with the line spacing (measured as $20.76\mu\text{m}$), the pair spacing (measured as $200\mu\text{m}$) and index line annotated in the middle.

For the study on the inscription linewidth, a full set of measurement of the linewidth (i.e. the line thickness) on the X-Y plane was carried out with findings presented at the following section. For the measurement position, it involved with subjective judgements on where should be the most focused position along the depth (i.e. the Z-axis) and also where should be used as the measured position along the line. With regard to the determination of the focus position along the depth, for the measurement of the inscription dimension, the measurements involved multiple in and out movements to determine the focus position. It can be difficult sometimes when examining the inscription which is fairly small (i.e. less than $2\mu\text{m}$ for the line thickness). In order to keep the consistency of the measurement position on the inscription, a vertical index line located in the centre of the inscription was used. The measurement points were selected around the index line.

To ensure the accuracy for the measurement on the linewidth, once confirmed with the in-focus position, multiple points were chosen from both sides of the index line and on both lines inside a pair presented in Figure 4-4, so that an average of the measurement values was taken into account to the final readings if the readings were slightly different. This allowed a series of lines in the test pattern was inspected and measured, so that a set of data was generated and analysed for the correlation between the laser energy and the linewidth.

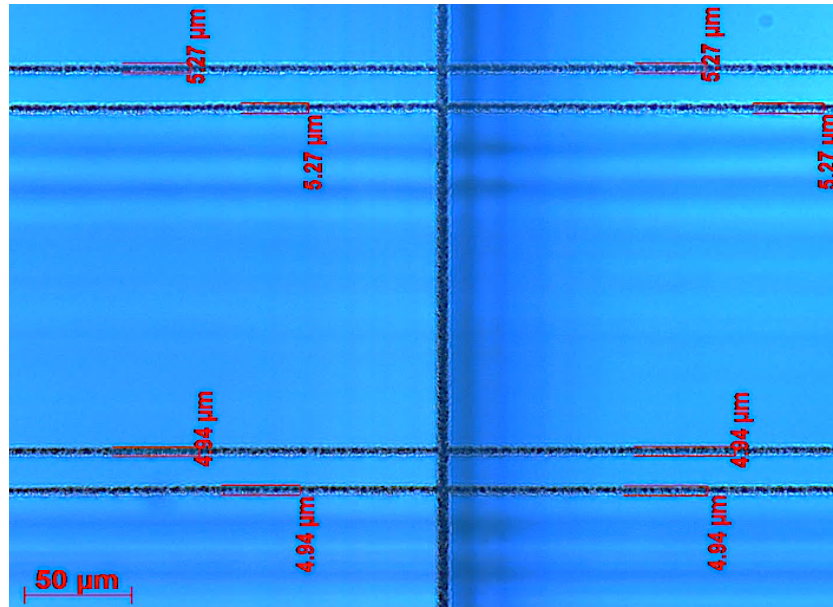
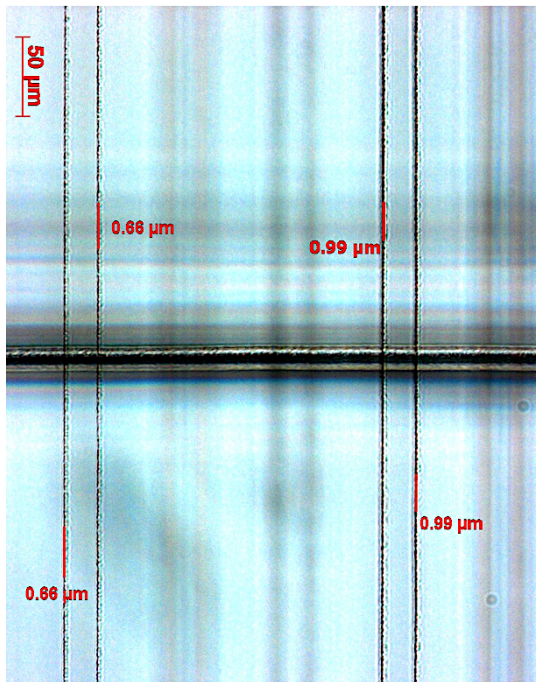


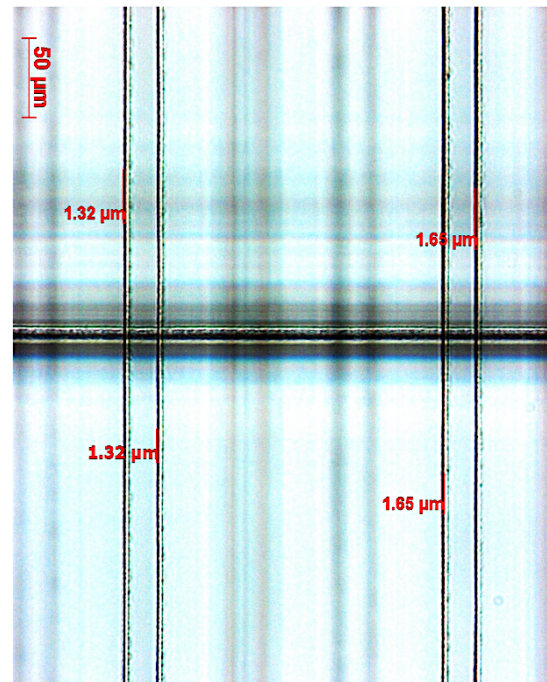
Figure 4-4. Microscope image using a 20x objective lens showing how the measurement of the inscription linewidth were taken and the measurement points (i.e. 4 measurement points) were selected. In this image, it shows that the linewidth is measured as 5.27μm for the top pair of inscriptions and 4.94μm for the bottom pair of inscriptions.

In order to get a full dataset of the linewidth on the X-Y plane, 160 pairs of inscription lines with different energy levels were inscribed and measured, with 20 measurements for each layer. In total, there were 8 layers of test patterns included in this test pattern structure. Here presented in Figure 4-5, the first layer of the test pattern located at 100μm below the front surface was presented to demonstrate how the measurement process was carried out. From Figure 4-5 (a) to (j), it presents the inscription applied with different laser energy levels. In each image, it contains two energy levels with a 5% step. For Figure 4-5 (a), a 5% of the output power (the lower pair of the lines in the image) was used to inscribe, which produced a 0.66μm linewidth and 10% of the output power (the upper pair of the inscription lines in the image) was used to inscribe, which produced a 0.99μm linewidth. The measurement data from microscope images shown in Figure 4-5, confirms that with the increase in the laser pulse energy applied, the linewidth of the inscription increased to a maximum of 100% of the output power was applied, resulting

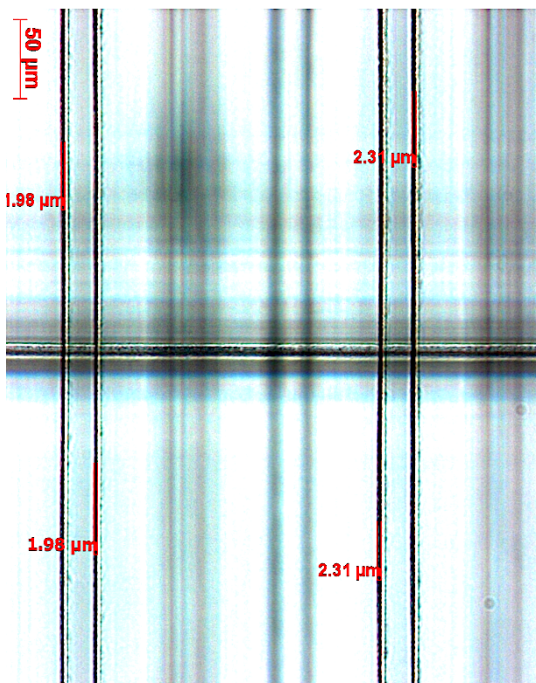
in a linewidth of $6.92\mu\text{m}$ (Figure 4-5(j)). This variation needs to be considered in the design parameters of the fabrication.



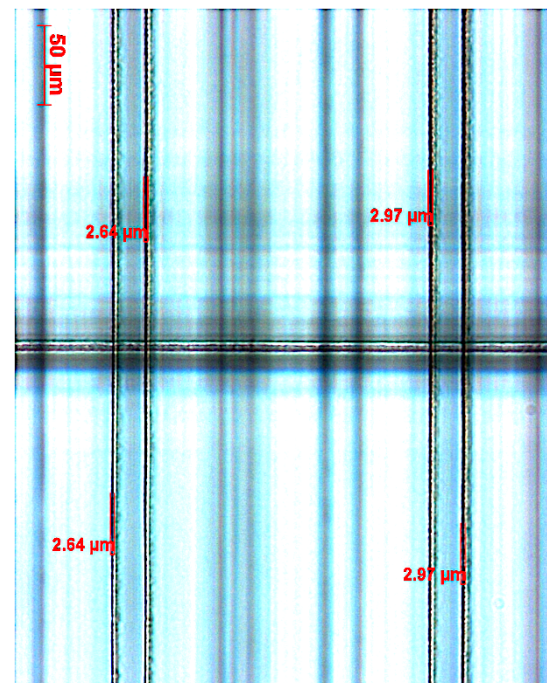
(a) 5% (left): 150nJ; 10% (right): 280nJ



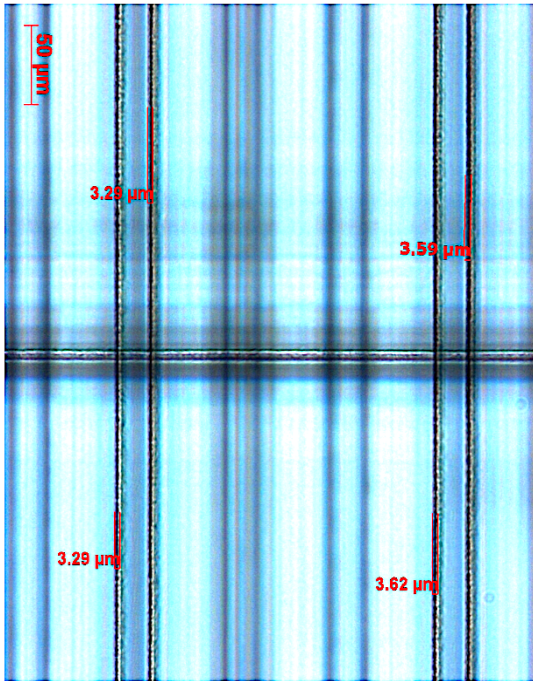
(b) 15% (left): 430nJ; 20% (right): 580nJ



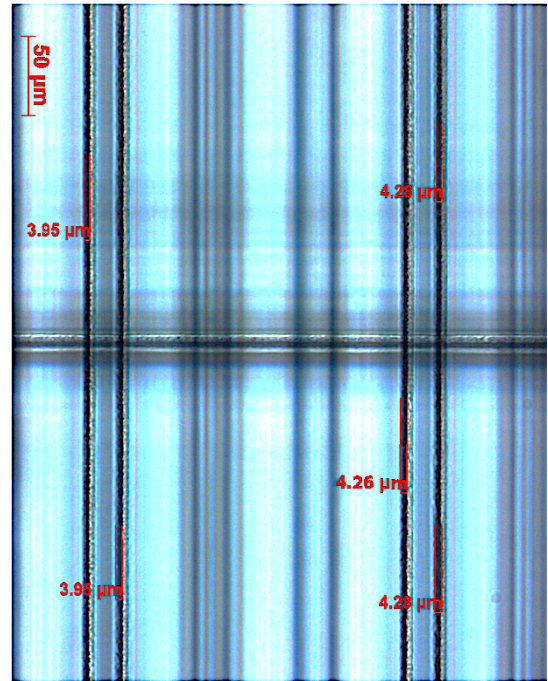
(c) 25% (left): 730nJ; 30% (right): 880nJ



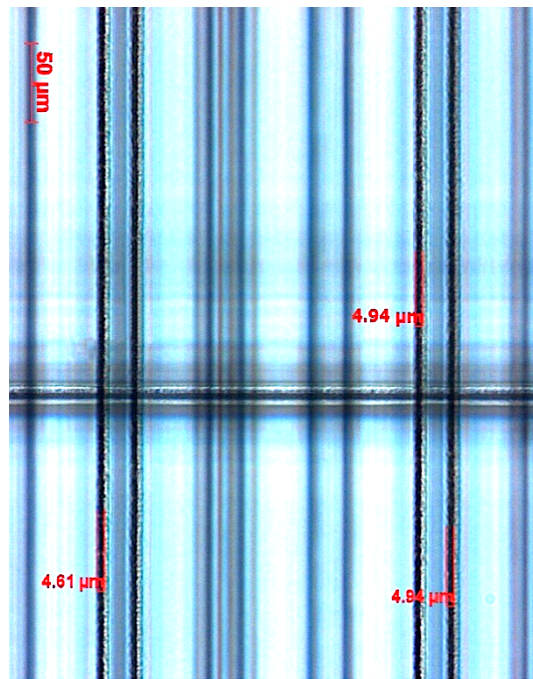
(d) 35% (left): 1.03μJ; 40% (right): 1.17μJ



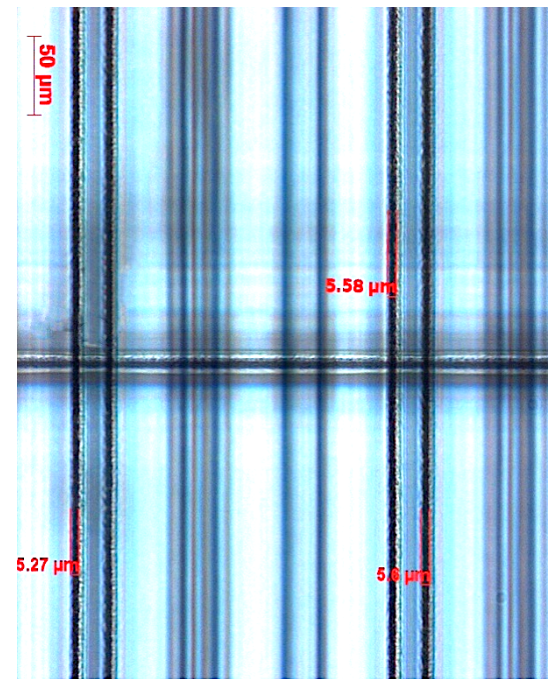
(e) 45% (left): 1.35 μ J; 50% (right): 1.48 μ J



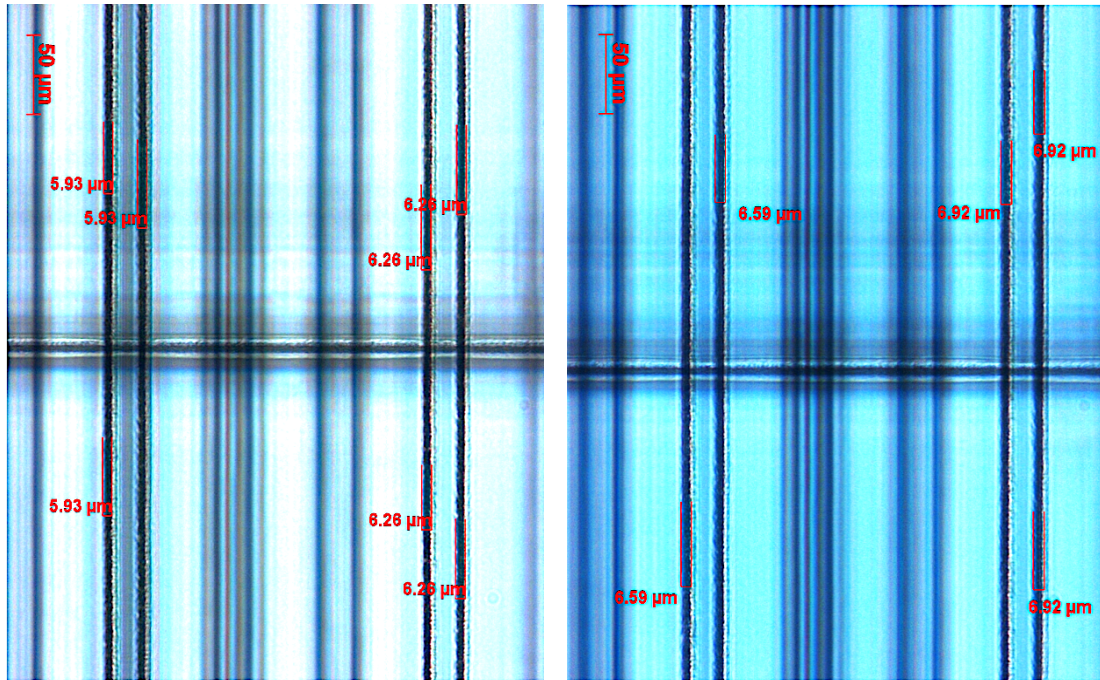
(f) 55% (left): 1.63 μ J; 60% (right): 1.79 μ J



(g) 65% (left): 1.94 μ J; 70% (right): 2.1 μ J



(h) 75% (left): 2.24 μ J; 80% (right): 2.4 μ J



(i) 85% (left): 2.56 μ J; 90% (right): 2.72 μ J (j) 95% (left): 2.9 μ J; 100% (right): 3.08 μ J

Figure 4-5. Microscope images using a 20x objective lens of the first layer of the laser energy test pattern to demonstrate the sample measurement process, where from (a) to (j), it represents the inscription was applied with different laser energy levels, with (a) representing with 5% of the laser power (i.e. 150nJ for energy per pulse at 100kHz), and (j) representing with 100% of laser power (i.e. 3.08 μ J for energy per pulse at 100kHz).

4.3.1 The correlation between the inscription linewidth and the laser pulse energy at the X-Y plane

The correlation between the laser pulse energy and the linewidth can be further investigated through data analysis. The measurement data was plotted with a trendline fitted as shown in Figure 4-6. It can be seen that this data strongly correlates with a linear trend line. From this graph, a lot of information can be gained and used for understanding the correlation between the linewidth and the laser pulse energy. It can be used as a calibration look up table to determine the correct laser energy level that can be used to get the expected linewidth at the required depth and vice versa.

Moreover, to keep the consistency of the linewidth for various depth, the graph can be used to find out what the laser energy should be used for each depth. For example, if a 3 μ m is a desired inscription linewidth for every depth, from the graph, the average laser power in percentage of the total power should be used for the depth of \sim 100 μ m is around 40%, then for the depth of \sim 250 μ m is around 45%, then for the depth of \sim 400 μ m is around 50%, and so on. It can also be used to predict if a fixed laser pulse energy is applied to every depth of the inscription, what the linewidth can be gained. For this, a

vertical line can be drawn at the corresponding laser power in Figure 4-6. For instance, if 30% of the laser power is set to use for all the inscription, it can be seen that different linewidth size will be produced at different depths such as at the depth of $\sim 100\mu\text{m}$, around $2.6\mu\text{m}$ linewidth can be achieved and at the depth of $\sim 700\mu\text{m}$, only around $1\mu\text{m}$ linewidth can be reached.

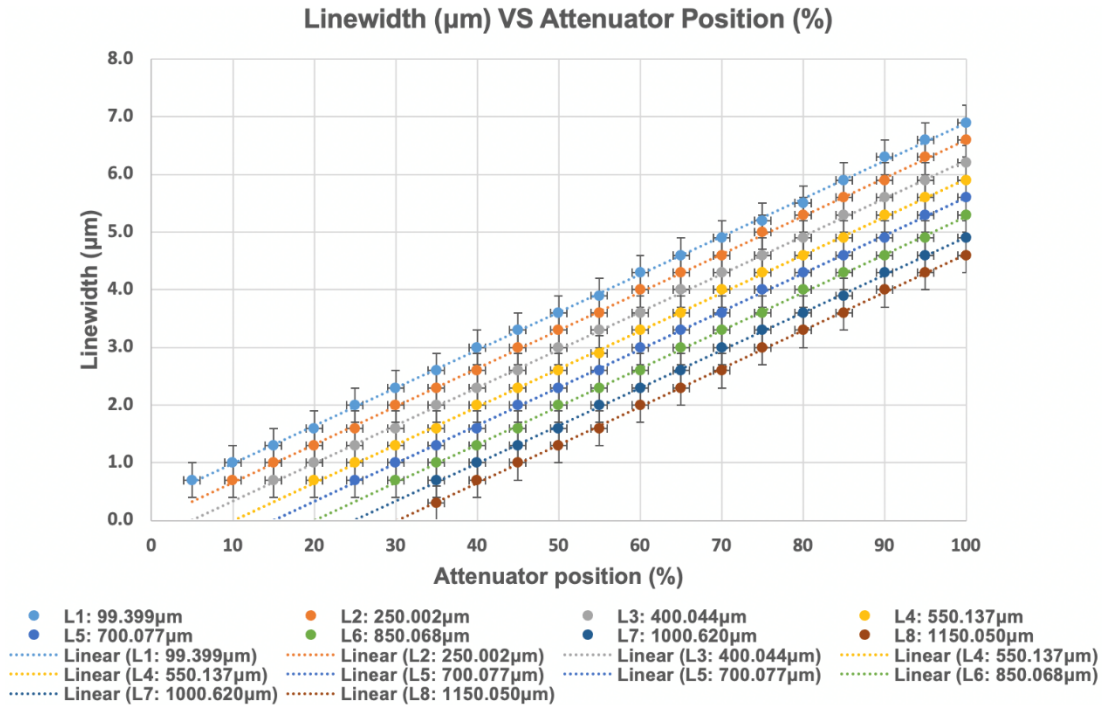


Figure 4-6. The graph shows the correlation between the linewidth and the laser power based on the microscope measurement data at the X-Y plane at eight different layer depths ranging from $100\mu\text{m}$ to $1150\mu\text{m}$ with trend lines and error bars indicated.

Previously, the control of the laser power had only been considered the X-Y plane and the power variation with depth had been ignored. This is not ideal for optimisation the fabrication. What also became apparent was that measuring the linewidth in the X-Y plane does not provide any cross-sectional information about the dimensions of the line in the Z-axis, which will be therefore discussed in the next section.

4.4 Laser power test pattern characterisation on the Y-Z plane

This section presents the research on the investigation of the correlation between the laser pulse energy and the inscription height along the Z-axis (i.e. the Y-Z plane). Filamentation and spherical aberration can be damaging to the precision of the fabrication as they distort the axial focus. However, as this cannot be observed on the X-Y plane, a further study was required to understand the full 3D dependence on the

laser power and the depth in the Y-Z plane due to the spherical aberration and the self-focusing.

The same laser power test pattern was used for the captured images of the cross-sectional profiles under both the microscope and the OCT system. Both a 5x objective lens and 10x objective lens were used for viewing the sample and capturing the images under the microscope which a 5x objective lens provided a broad view and a 10x objective lens provided more detailed look on the inscription. A conceptual drawing of the cross-section of the laser power test pattern is shown in Figure 4-7 so that it can easily distinguish each plane which is referred in this section. The Y-Z plane provides the information on the inscription height.

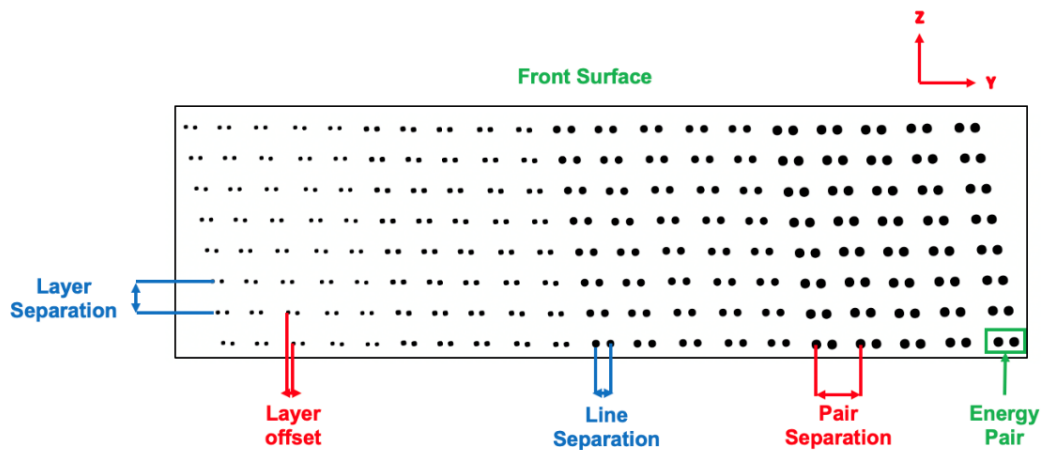


Figure 4-7. Conceptual diagram for the cross-sectional profile of the laser power test pattern on the Y-Z plane with the parameters indicated.

To obtain the cross-sectional images, the sample has to be placed upright by turning 90 degrees so that the side of the substrate can be viewed under the microscope. However, there was one issue presented when doing this way as the height of the substrate exceeded the distance between the stage and the objective lens.

There were two options to overcome this limitation. The first option was cut the substrate into smaller piece so that the substrate height can meet the focal length requirement. However, this option is time consuming for preparing the sample. It could also cause damage to the pattern, such as cracks when cutting the glass and also the flatness and the smoothness of the surface which can affect the accuracy of the measurement results.

The second option is to attach the sample substrate to another heavier objective by using a thin layer double-sided tape so that the cross-sectional area can be showed. This option allowed the sample to be located within the illumination hole of the stage and

allowed certain lenses to be used for imaging the lines. In this section, all the images and measurements were using this option presented in Figure 4-8.

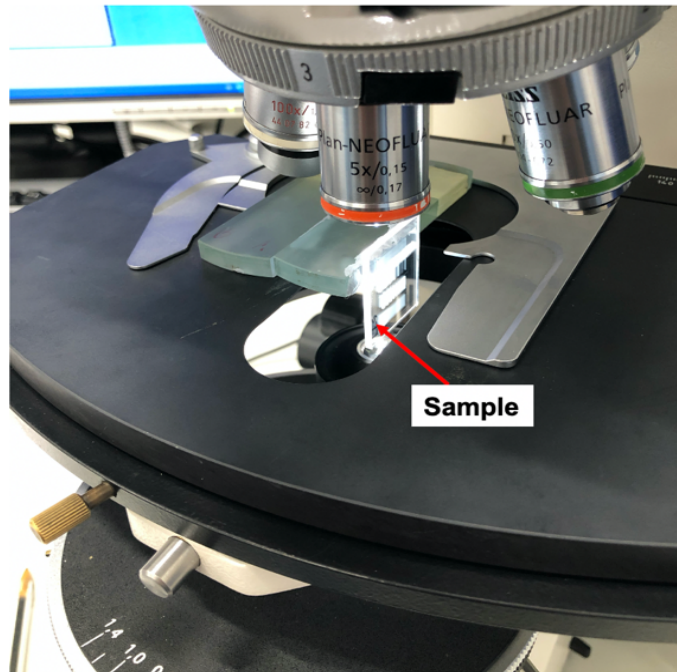


Figure 4-8. The microscope setup for capturing the cross-sectional images.

After the microscope setup, a 5x objective lens was firstly used to focus and inspect for a general overview and then a 10x objective lens was used to gain a closer detailed look. By viewing the sample cross-sectionally, the real depth of the layer separation can be then measured, which also can be used to work out the refractive index of the microscope and the wavelength of the light source used. It can be seen from Figure 4-9, the measurement of the inscribed line height for E15 (i.e. 75% of the total laser power so that $2.24\mu\text{J}$ energy per pulse at 100kHz) was $40.13\mu\text{m}$ and the inscription height for E16 (i.e. 80% of the total laser power so that $2.4\mu\text{J}$ energy per pulse at 100kHz) was $41.1\mu\text{m}$ at the apparent depth of $\sim 250\mu\text{m}$.

For the layer separation, three measurements were taken which had an average value of $219.13\mu\text{m}$. The setting parameter of the layer separation was set to $150\mu\text{m}$ in apparent depth (AD) in the program. Therefore, the refractive index can be calculated through the relationship between the apparent depth (AD) and the real depth (RD), which yields the refractive index of $219.13\mu\text{m}/150\mu\text{m}=1.461$. Referring to the refractive index curve of the fused silica based on the dispersion equation derived by Malitson [184] presented in Section 3.3, the corresponding wavelength for the refractive index of 1.461 can be determined as 525nm. This allows the wavelength of the imaging system can be determined based on the design parameters and the experimental data even its unknow

beforehand. Moreover, by viewing the inscription cross-sectionally, it can provide information about how the laser power can affect the dimensions of the inscription lines.

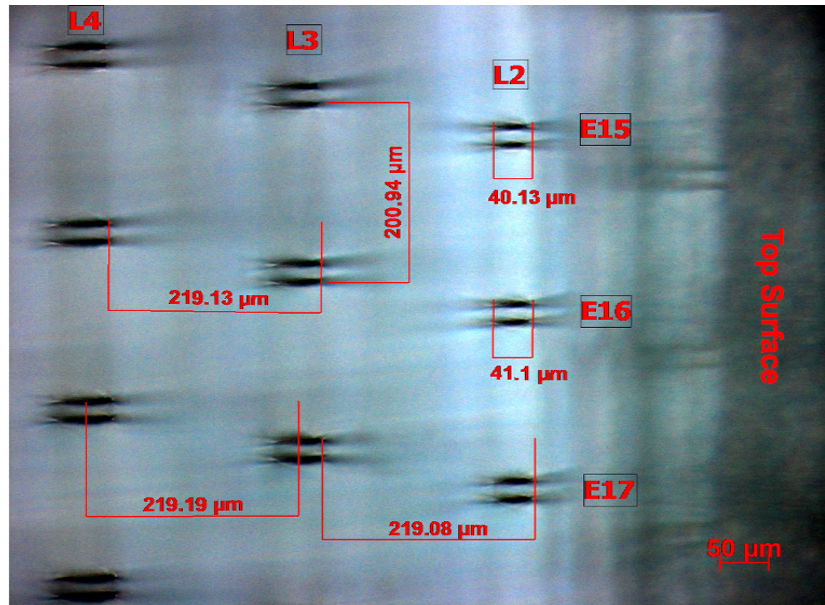


Figure 4-9. The cross-sectional image of the laser power test pattern by using a 10x objective lens showing a detailed view of the inscription with the measurement of the inscription height (i.e. $40.13\mu\text{m}$ for 75% of the laser power at $\sim 250\mu\text{m}$ depth in AD) and the layer separation (i.e. $\sim 219\mu\text{m}$) indicated. In this image, it shows the cross-section of the higher energy levels (i.e. 75% - 85% of the total laser power) at top layers (i.e. $250\mu\text{m}$ - $550\mu\text{m}$ for the apparent depth from the top surface). The pair separation was measured as $200.94\mu\text{m}$.

A detailed cross-sectional image of the test pattern is presented in Figure 4-10, which includes the whole range of the laser energy levels and all the inscription layer patterns with the measurement value indicated at bottom of each inscription image. From Figure 4-5 and Figure 4-10, it can be seen clearly that when increasing the laser power, both the inscription linewidth and the inscription height is increased. However, unlike the linewidth observed in the X-Y plane which seems to have a linear trend, the cross-sectional images for measuring the inscription height shows non-linear trends.















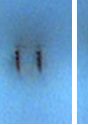

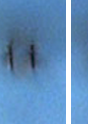




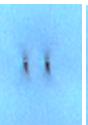
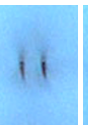
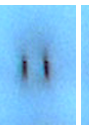


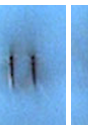







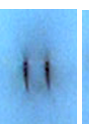
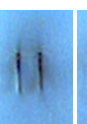
















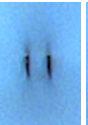












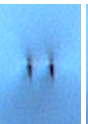




As the inscription moves to large depths, a critical issue for the fabrication can be caused by spherical aberration [111]. With the peak power intensity varied with the depth along the axial direction, when it is close to the real focal point (i.e, for the depth of $\sim 100\mu\text{m}$), the fabrication is hardly affected by the spherical aberration as at this depth that axial focal remains undistorted [110].

However, it can be seen in Figure 4-10 that at a deeper depth (i.e. the depth beyond $250\mu\text{m}$), the elongation of the inscription becomes more apparent due to the extended dimension of the writing focus [110, 111]. Moreover, it can be seen that when the pulse

energy increases [70], the inscription height increases which is still close or around to the geometrical focus [118]. This trend continues until a certain depth is reached, where the inscription tends to become smaller at deeper depths beyond which is probably due to the peak intensity degradation as a result of a rapid peak intensity reduction and severe focal distortion [111]. With the power loss when travelling to a deeper depth, a higher energy level is required to sustain a similar level for the refractive index modification [110]. Therefore, there is a shift to a higher energy level for deeper depths.

Moreover, self-focusing is another issue when inscribing the structure with a higher pulse energy which can distort the inscription structure. In theory, self-focusing can only happen when the critical power of self-focusing is exceeded. The critical power for fused silica at the wavelength of 1026nm is about 3.75MW [117, 118]. For a laser with a 500fs pulse duration, the critical power of the self-focusing for the pulse energy is calculated as 1.877 μ J. According to the theoretical calculation, the critical power of the self-focusing should be exceeded if the pulse energy above 1.877 μ J, which corresponds to ~63% of the laser average output power.

In Figure 4-10, when the laser power increases to 65% or above, significant changes in inscription dimension can be seen with the presence of the filamentation phenomena, which is suspected to be caused by the self-focusing [118] associated with multiple filaments which is probably due to the refocusing of the laser beam of the self-focusing effect [191]. When the pulse energy is sufficiently high, self-focusing of the laser beam become observable and it can be repeatably seen until the intensity significantly decreases [192].

Power (%)	5%	10%	15%	20%	25%	30%	35%	40%	45%	50%
Energy (nJ)	150	280	430	580	730	880	1030	1170	1350	1480
99.399 μ m										
Height (μ m)	10.72	14.75	17.43	18.77	20.11	21.45	22.79	24.12	26.81	
250.002 μ m										
Height (μ m)		12.06	16.09	20.11	21.45	22.79	24.13	25.47	29.49	
400.044 μ m										
Height (μ m)	8.04	14.75	21.45	22.8	24.13	28.15	32.17	33.40		
550.137 μ m										
Height (μ m)			9.38	16.09	17.43	18.77	30.83	40.12	44.24	
700.077 μ m										
Height (μ m)				6.70	13.40	17.43	22.79	24.13	45.58	
850.068 μ m										
Height (μ m)					12.06	16.09	18.77	21.45	28.15	
1000.62 μ m										
Height (μ m)						10.72	17.43	20.11	25.47	
1150.05 μ m										
Height (μ m)							9.38	12.06	17.43	20.11

(a)

Power (%)	55%	60%	65%	70%	75%	80%	85%	90%	95%	100%
Energy (nJ)	1630	1790	1940	2100	2240	2400	2560	2720	2900	3080
99.399 μ m										
Height (μ m)	29.49	30.83	33.51	36.23	38.82	40.21	41.55	42.76	44.24	46.95
250.002 μ m										
Height (μ m)	32.17	32.17	34.85	38.87	40.21	41.55	42.84	44.25	45.59	49.72
400.044 μ m										
Height (μ m)	34.83	40.13	42.9	44.24	45.59	46.95	49.70	54.96	56.30	58.98
550.137 μ m										
Height (μ m)	45.61	48.26	49.60	50.94	52.21	53.62	56.30	61.66	62.98	64.39
700.077 μ m										
Height (μ m)	48.26	52.28	57.63	58.93	59.08	60.23	61.66	72.46	73.73	75.07
850.068 μ m										
Height (μ m)	32.17	34.85	58.98	67.04	76.41	77.80	78.01	79.10	81.74	84.59
1000.62 μ m										
Height (μ m)	30.85	32.01	36.19	40.21	68.36	80.43	81.76	83.16	85.79	96.54
1150.05 μ m										
Height (μ m)	21.45	29.51	34.85	37.41	45.63	49.60	65.62	91.15	101.88	104.56

(b)

Figure 4-10. The microscope images showing the cross-sectional profile of the laser test pattern using a 5x objective lens: (a) the laser power of 5% - 50% of the total power (i.e. 150nJ - 1.48 μ J for energy per pulse); (b) the laser power of 55% - 100% of the total power (i.e. 1.63 μ J - 3.08 μ J for energy per pulse).

4.4.1 The correlation between the inscription size and the laser pulse energy at the Y-Z plane

In order to understand the correlation between the inscription size and the laser pulse energy in the Y-Z plane, a line plot diagram for each layer was generated and shown in Figure 4-11. For the first layer pattern inscribed at the depth of $\sim 100\mu\text{m}$, the trend for the inscription height is similar to that seen for the linewidth and shows a gradually linear increase with laser power. However, as shown in Figure 4-10 and Figure 4-11 between the inscription height inscribed at 10% which measured $10.72\mu\text{m}$ and for the 100% which measured as $46.95\mu\text{m}$ results in a ratio of four. A similar trend shows for the second layer which the inscription is located at $\sim 250\mu\text{m}$.

From the inscription depths of $\sim 400\mu\text{m}$ and $\sim 550\mu\text{m}$, there is a rapid change in inscription size, due to the distance to the surface becoming larger. This results in spherical aberration affecting to the axial focus to a much greater level as the focal point is moving away from the optimal focus point of the laser beam.

At higher energy levels, as the critical power of self-focusing is exceeded, the filamentation, presented as an elongated water-drop like shape, appears with the spherical aberration, this results in the laser inscription becoming more elongated. The most dramatic changes happen at deeper depths from $\sim 850\mu\text{m}$. It can be seen that a significant increase in inscription size happens at 65% of the laser power for the depth of $\sim 850\mu\text{m}$, at 75% of the laser power for the depth of $\sim 1000\mu\text{m}$ and at 80% of the laser power for the depth of $\sim 1150\mu\text{m}$. Therefore, there is a shift to a higher laser power for deeper depth for the onset of filamentation where the inscription shape is elongated along the depth significantly which results from the combined effect from both the spherical aberration and the self-focusing.

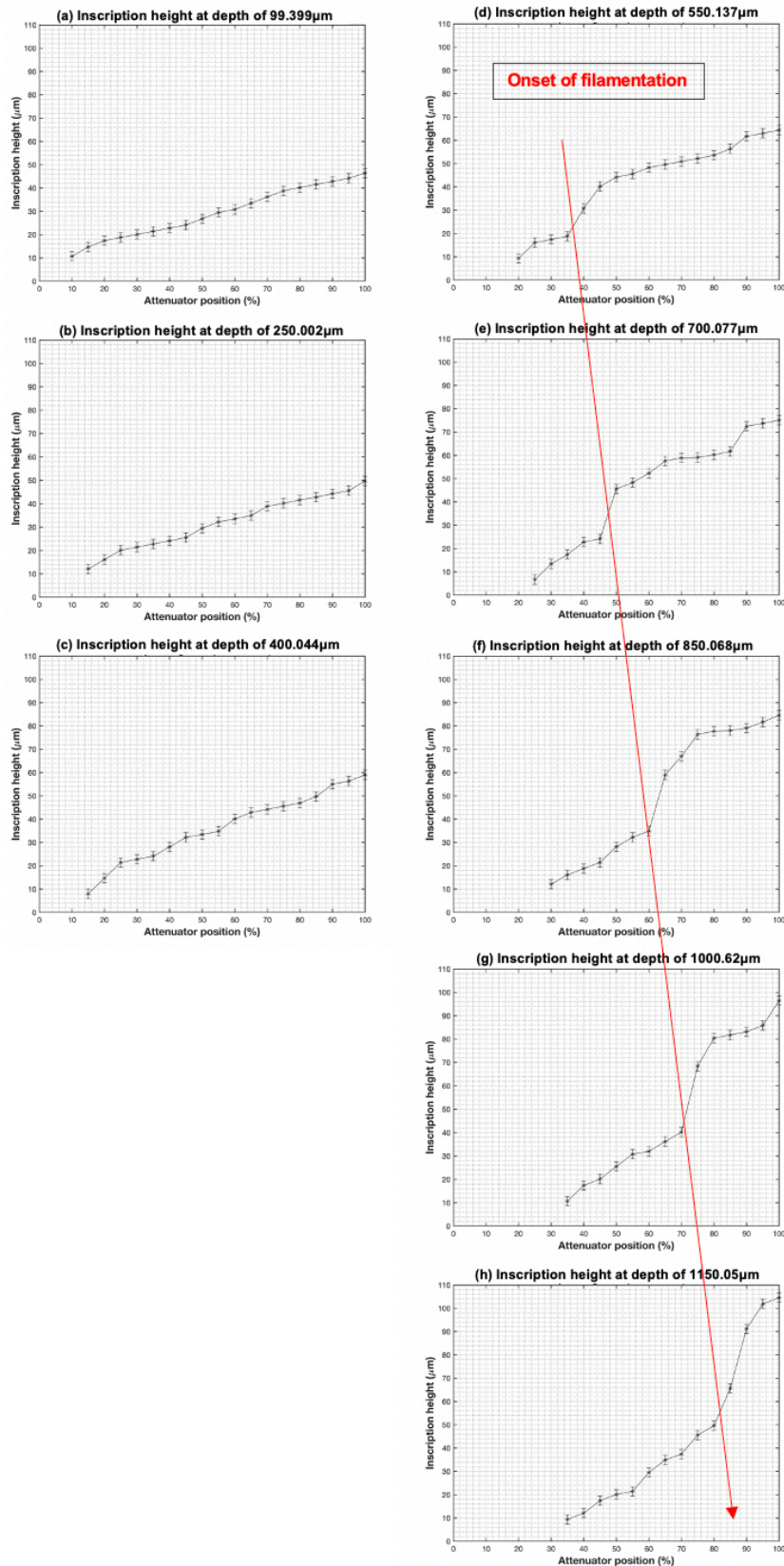


Figure 4-11. Summarised line plot diagrams present the correlation between the inscription height and the laser power based on the microscope measurement for all eight layers in the Y-Z plane showing the possible onset of filamentation. Large scale figures are included in Appendix B section for reference.

An OCT image shown in Figure 4-12 illustrates the laser power test pattern under an OCT system (Optimec is830 OCT system). It can be seen that the inscription size tends to become larger when the laser power increased. However, at deeper depths with a higher pulse energy (i.e. above 60% of the laser power), the shape of the inscriptions is getting elongated to a water drop shape caused by the spherical aberration and the self-focusing that distorts the axial focus, therefore a higher pulse energy above the self-focusing critical power should be avoided.

Ideally, the power range should be selected below the self-focusing critical power, which is around 63% of the total laser power for the laser system used. Moreover, in order to keep a consistent inscription size, the laser energy pulse for different depths should be adapted and varied so that a similar size of the inscription can be maintained at all the inscription depths.

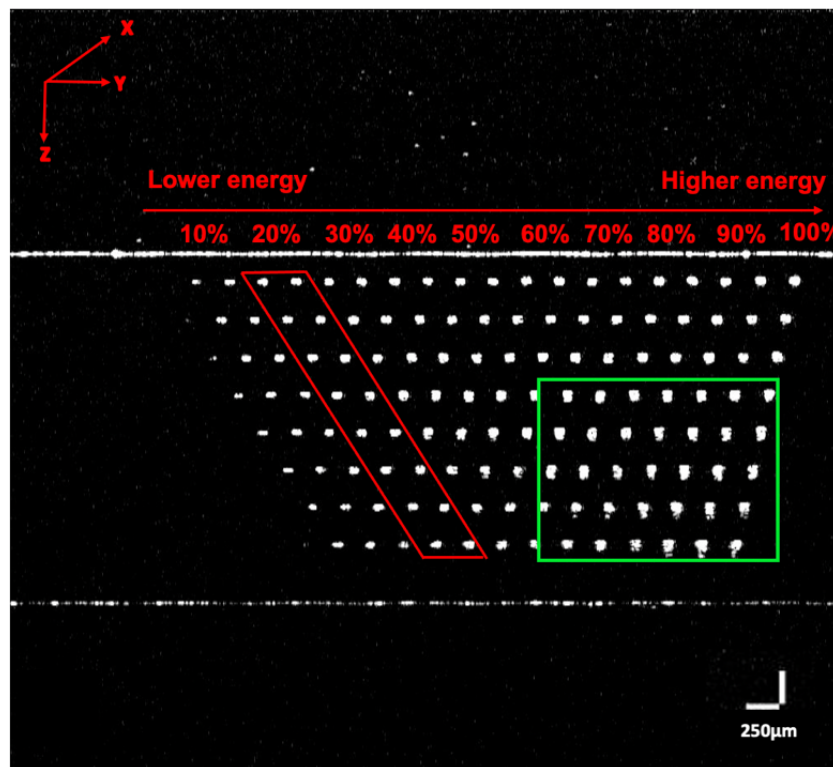


Figure 4-12. OCT image taken by Optimec is830 SD-OCT system showing the laser power test pattern with a scan size of 4.94mm x 4.55mm with a pixel size of 4.94 μ m x 8.89 μ m. The red quadrilateral shape labelled in the image is the ideal laser power range that should be used for the inscription while the green square shape highlighted in the image shows inscriptions that are elongated significantly at this power range, which should be avoided as the inscription shape is distorted.

4.5 Laser power optimisation

By imaging the cross-sectional profile of the layer thickness on the X-Z plane, useful information on the inscription size variation affected by the laser power can be obtained. This also demonstrates the reason why changing the laser pulse energy is necessary at different depths. However, the cross-sectional profile only allows for the closest line of the inscription layer set which means either the first line of a layer set (i.e. the inscription fabricated with the lowest pulse energy) or the last line of the layer set (i.e. the inscription fabricated with the highest pulse energy) of the test pattern can be viewed. Here, the last line of the layer set was chosen as it can show more information on the elongation of the inscription as the pulse energy far exceeded the critical power for the self-focusing.

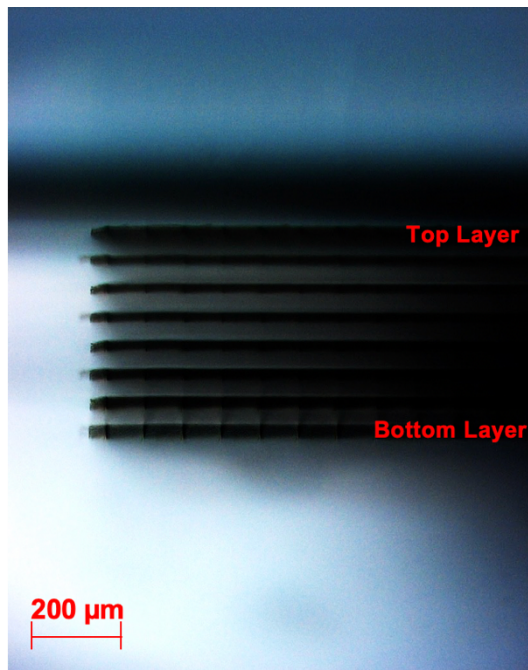
From Figure 4-13(a) to Figure 4-13(c), different laser settings are used to illustrate the inscription size variations. Figure 4-13(a) shows the microscope image using a 5x objective lens to present the cross-sectional view of the laser power test pattern that used 20% of the laser power with a smaller layer separation of 50 μ m setting among layers. When the lower level of laser power was used (i.e. 20% of the total average output power) at shallower depths (i.e. 450 μ m depth in AD), the layer thickness seems to be quite consistent with little or no elongation.

Figure 4-13(b) shows the microscope image of the cross-sectional view of the phantom structure that used 80% of the laser power for all layers but with a larger layer separation of 150 μ m. It can be seen from this image that as the laser pulse energy has been increased, the layer thickness become thicker compared with Figure 4-13(a). With the depth increased at higher pulse energy, the elongation of the inscription increased significantly. Therefore, if a deeper layer inscription is desired, the same laser pulse energy applied to every depth would not be feasible as the elongation of the inscription caused by both spherical aberration and self-focusing which would heavily affect the inscription dimension as the axial focus is distorted.

Therefore, in order to optimise the fabrication and to minimise those distorted effect caused by Kerr-induced self-focusing at higher energy levels above the self-focusing critical power and the spherical aberration at greater depths, a range of the energy levels were selected with the fabrication method optimised based on the study presented in previous sections (Section 4.3 & Section 4.4) so that at each depth, a different laser energy level can be applied to maintain the same inscription dimension and compensate the power loss at the deeper depth without exceeding the critical power to induce the self-focusing and minimise the spherical aberration.

The optimal range of the laser power was set to 20%-55% to generate a linewidth around $2\pm 0.6\mu\text{m}$, where $0.6\mu\text{m}$ is not an inscription width variation range but the measurement error (discussed in Section 3.6.3.5). These optimal results for the laser power were used for the later phantom fabrication presented in the latter chapters.

In Figure 4-13(c), the microscope image shows the inscription with a larger layer separation of $150\mu\text{m}$ that used the optimised fabrication method, which it can be seen that the layer thickness is more consistent and uniform at all depths of inscription.



(a)

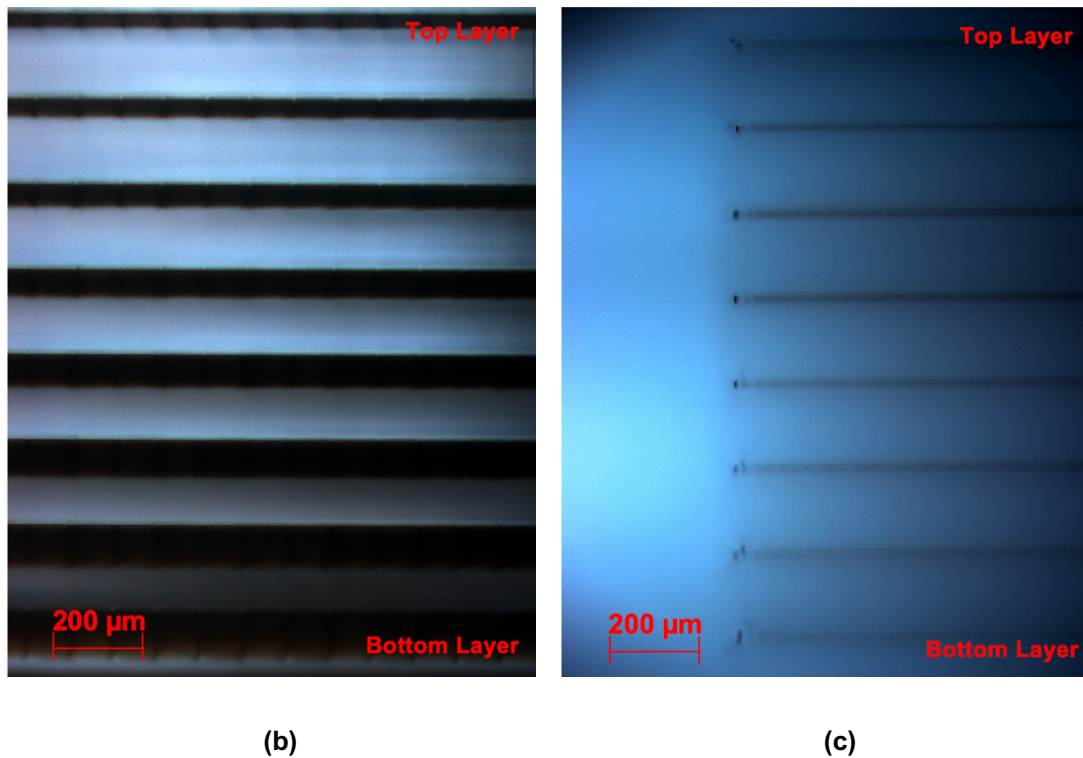


Figure 4-13. The microscope images using a 5x objective lens show the cross-sectional view of the layer thickness: (a) inscription made with 20% of the laser power with the total inscription depth of $\sim 450\mu\text{m}$ (in AD); (b) inscription made with 80% of laser power with the layer separation of $150\mu\text{m}$ with the total inscription depth of $\sim 1150\mu\text{m}$ (in AD); (c) inscription made with various laser power applied for each layer varied from 20% to 55% with the layer separation of $150\mu\text{m}$ so that resulted in the total inscription depth of $\sim 1150\mu\text{m}$ (in AD).

4.6 Chapter conclusions

In this chapter, a detailed study to investigate the correlation between the laser power and the inscription size. As the inscription is a 3D structure, all three dimensions have been studied. The correlation between the inscription linewidth and the laser power at the X-Y plane showed as a linear relationship. However, when viewing the inscription structure cross-sectionally, all the inscriptions can be seen, the inscription size has been individually examined so that to be quantitatively analysed. Finally, after a series of studies on the laser power and the inscription size, an optimal range of laser powers has been selected with the fabrication method revised so that at every single depth, different laser energy level can be applied. It has then been shown through further fabrication of samples to give a consistent and uniform size of inscription.

Chapter 5

Planar OCT calibration phantom

This chapter presents work on the planar OCT calibration phantom development. A new fabrication method (Section 5.2) is introduced that is designed to optimise the fabrication process. After discussing the fabrication approach, characterisation of the new phantom design is presented (Section 5.3) which includes both the microscope characterisation and the OCT system characterisation. A detailed side-by-side comparison is made between the previous design and the new optimised design to show the improvement.

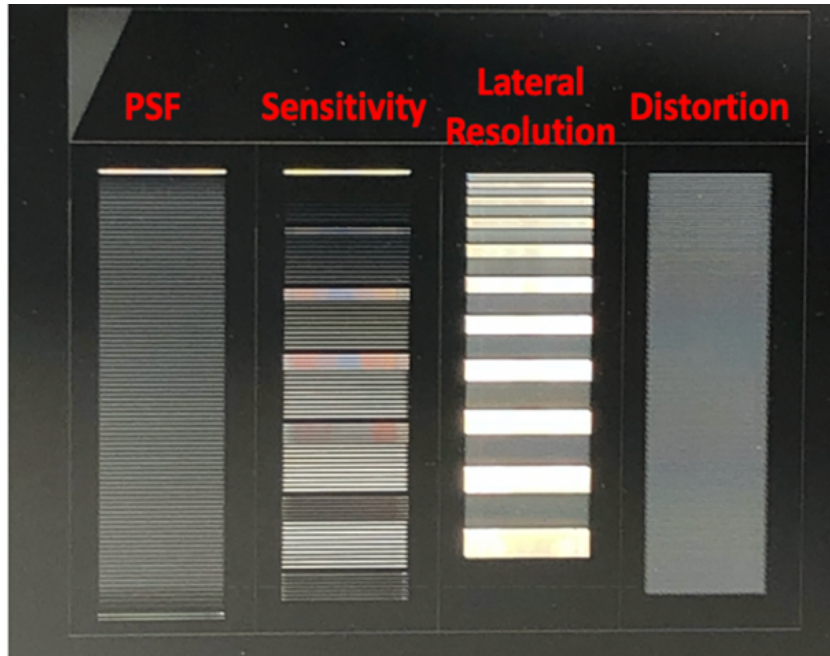
5.1 Introduction

Through the detailed study of the previous existing femtosecond laser inscribed planar OCT phantom developed by Lee et al. [21], limitations in the fabrication method are evident when inscribing at a deeper depths inside of the material. The existing software design was optimised for inscription speed but only allowed the same laser pulse energy to be applied to all the depths. When extending the design to inscribe at a greater depth, a higher laser pulse energy is required to inscribe visible lines. An additional complication is that beyond a certain laser pulse energy self-focusing of the laser beam starts appearing. This causes the resulting inscription to be elongated with the presence of the spherical aberration when the inscription depth is increased, which can significantly affect the fabrication quality. It is important that the inscription size should keep consistent and uniform throughout the phantom. To achieve this, a new fabrication routine was developed, which allows various levels of the laser pulse energy to be applied according to the inscription depth so that a consistent inscription size can be achieved even when inscribing at a greater depth with a higher laser power.

In this section, the femtosecond laser direct writing technique was used to inscribe the phantom structure in planar fused silica substrate. An optical microscope and an OCT system were used to characterise and validate the OCT phantom. Although the patterns look similar to that presented in chapter 3, all of them required re-coding to meet the requirements of both additional depth and consistency of inscription size. These were achieved by varying the pulse energy at each layer to minimum the self-focussing of the laser beam. This improvement enabled the optimisation of the fabrication process on the phantom.

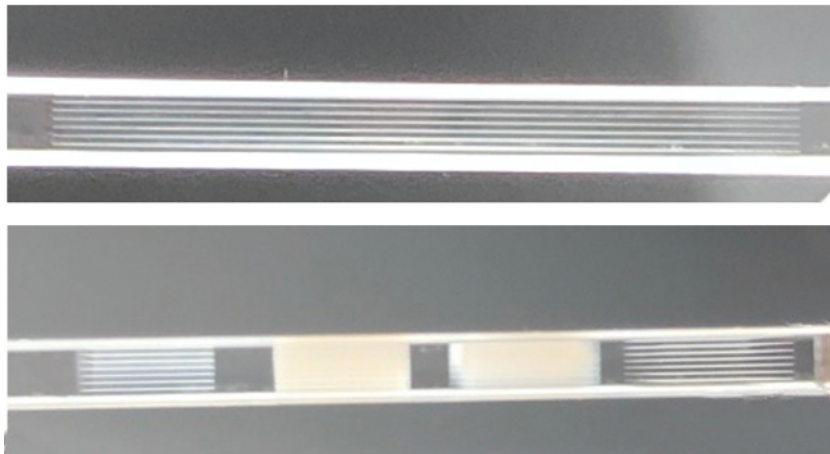
5.2 Advanced planar phantom design and fabrication

The advanced phantom design shown in Figure 5-1 is extended in depth from the previous phantom design [21] (refer to Section 3.6) and includes: point spread function (PSF), sensitivity (S), lateral resolution (LR) and distortion (D) grid phantom patterns. These patterns can fulfil the general requirement for assessing the various performances of being a standard calibration phantom. However, the previous inscription approach would only allow one pulse energy level to be used for all depths. With the laser power increased to reach greater depths, it will result in filamentation caused by the self-focussing of the laser beam with the linewidths varied with depth.

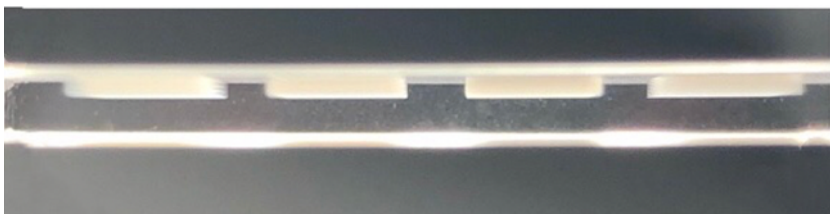


(a)

Cross-sectional view of the new design



Cross-sectional view of the previous design



(b)

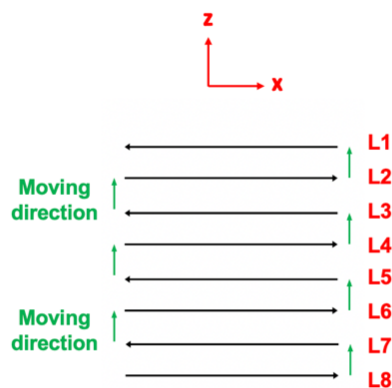
Figure 5-1. Femtosecond laser inscribed phantom (based on the previous phantom design developed by Lee et al. [21]) with a greater inscription depth: (a) the front face of the phantom with four patterns indicated; (b) the cross-sectional view for both the current design and the previous design to demonstrate the difference in inscription depth.

The previous fabrication method (used to fabricate the phantom presented in Section 3.6) was ideal for the inscription at smaller depths (i.e. inscribed at the maximum depth of $450\mu\text{m}$ (in AD) which is approximately $657\mu\text{m}$ (in RD)) shown in Figure 5-1(b). However, most of the OCT system have the penetration depth of 1 to 3mm [185] and consequently a deeper depth inscription will benefit most OCT users. The thickness of the planar substrate is 2mm, therefore, the main purpose of this work was to see whether patterns reaching the maximum depth with a minimum of self-focusing could be achieved.

The parameters of the laser pulse energy in this chapter were based on the findings presented in Chapter 4 and the results shown in Figure 4-10. The same fused silica substrates with a dimension of 30mm x 25mm x 2mm (Ibsen Photonics, Denmark) were used to fabricate the phantom.

As with the previous approach, the laser inscription always started from the bottom layer to the top layers so that to avoid the scattering from the pre-written structures. However, the previous fabrication method writes in a slice-by-slice manner which means that for a slice of inscription, the laser starts from the bottom layer and writes a line, and then moves towards to the top until all 8 lines are written so that a slice is completed (shown in Figure 5-2(a)), then it moves to the next slice, and this process is repeated until the completion of the pattern. This has the benefit of a time optimised inscription as it minimises movement on the X and Y axes.

However, if the energy needs to be changes for each layer this approach becomes problematic because changing the energy is a relatively slow process and would become a dominant factor in the inscription speed. The diagrams shown in Figure 5-2 describe this vertical inscription process further. Therefore, a new fabrication approach is needed to enable various pulse energies applied at different depths. The fabrication process will be presented individually in the following section for each phantom pattern.



(a)

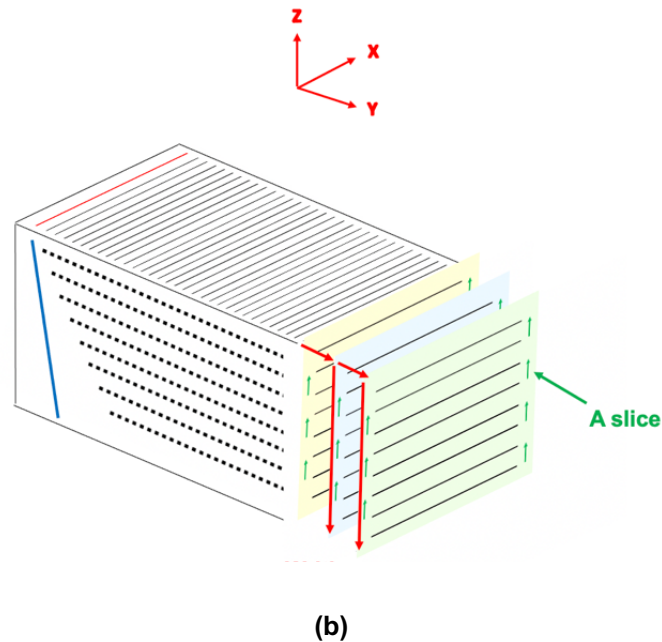


Figure 5-2. Illustration of the previous fabrication process: (a) the inscription writing direction on the X-Z plane for one slice where L1- L8 indicating the layer number at different depths; (b) the writing process for a structure. Note the red arrows signify stage movement between each slice without inscription, black lines signify inscription and green arrows denote stage movement within a slice without inscription.

All four phantom patterns have eight pattern layers inscribed inside the fused silica substrate. All the pattern structures were inscribed at a speed of 10mm/s. The repetition rate for the laser system was set to 100kHz. The inscription lens used was the 100x Mititoyo M Plan Apo NIR objective. There was a layer separation of 150 μ m (in AD) setting between layers with the first layer located at 100 μ m (in AD) underneath of the front surface of the substrate. For the index lines, there was 75 μ m setting for the index line separation. There was 100 μ m for the separation between the index line and the test pattern. The laser energy and the depth settings were listed in Table 5-1 at below.

Layer Number	Depth (μ m)	Attenuator position (%)	Average power (mW)	Pulse energy (nJ)
D1	100	20	58	580
D2	250	25	73	730
D3	400	30	88	880
D4	550	35	103	1030
D5	700	40	117	1170
D6	850	45	135	1350
D7	1000	50	148	1480
D8	1150	55	163	1630

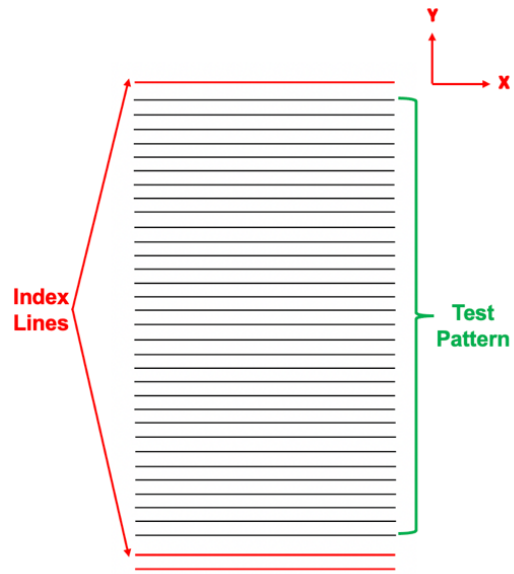
Table 5-1. The parameter settings for the depth, attenuator and the measured values of the laser output power (in mW) and the corresponding energy per pulse (in nJ) at the repetition rate of 100kHz.

For the PSF, lateral resolution (LR) and grid/distortion patterns, the laser pulse energy was set as per Table 5.1 for the corresponding depth. For example, for the depth of 100 μm (in AD), the attenuator was set to 20% so that 580nJ energy per pulse was applied to that depth. The energy range of 20% - 55% of the total average output power was based on the findings (presented in Chapter 4) on the correlation between the linewidth, the inscription height and the laser pulse energy such that the inscription size can be kept as a similar size. Moreover, a low pulse energy was preferred to avoid any distortion effects caused by spherical aberration and self-focusing. For the PSF and the sensitivity pattern, a layer offset of 25 μm was set in this pattern to reduce the effect caused by the multiple backscattering from other layers when measuring under the OCT system [21]. All the index lines were inscribed at the same pulse energy with the maximum power so that it can be easily recognised and used to guide the location.

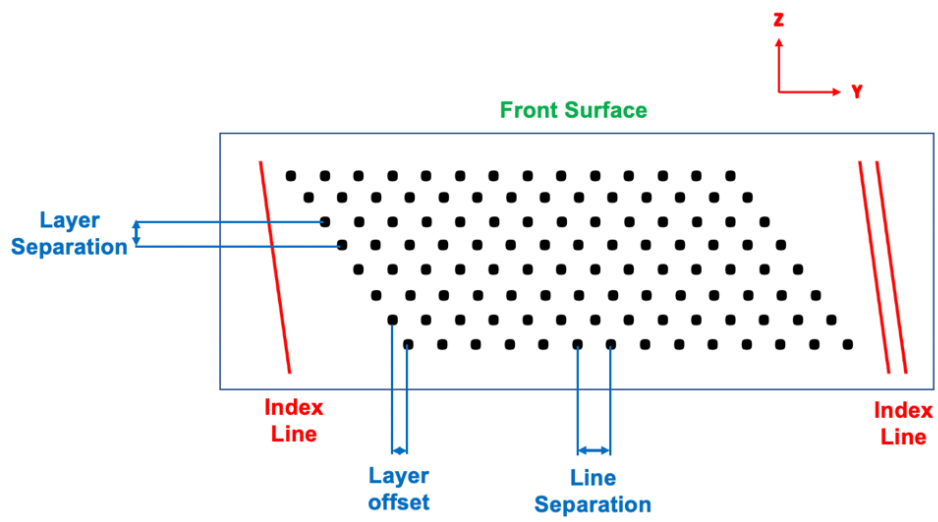
5.2.1 Point spread function (PSF) phantom

The point spread function (PSF) phantom was designed to assess the spatial resolution of the OCT system, which is a fundamental parameter of the system imaging quality [193]. If the structure size is much smaller than the resolution of the OCT system, the PSF of the system can be directly determined [14] [177]. To enable this, the previous research pointed out that the target point size should be less than 15% of the full width at half maximum (FWHM) of the OCT light source when considering the design and the fabrication for the PSF phantom [14].

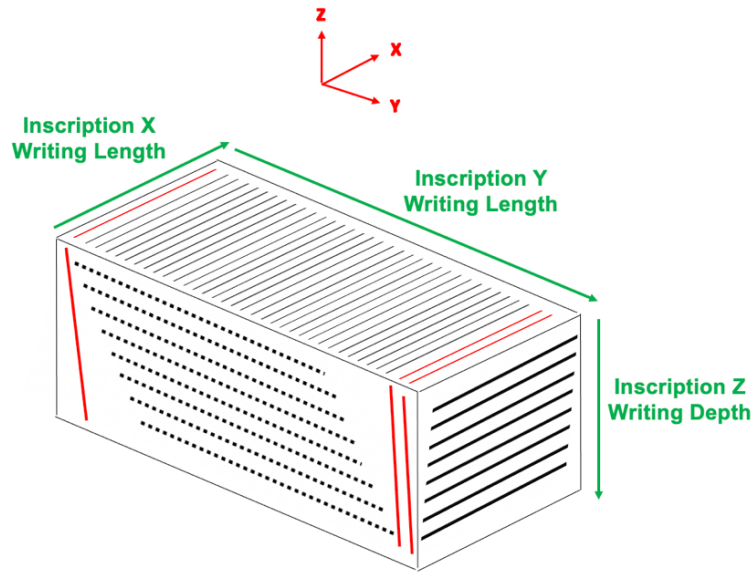
The phantom structure consists of a series of lines which have a line separation of 150 μm and there are 3 index lines located at both ends of the pattern on the X-Y plane at each layer. The number of lines is dependent upon the inscription area (i.e. the substrate size) which can be customised to set for the pattern size in the design and the space for the line separation. For this design, it was around 90 test lines inscribed plus 3 index lines. The phantom pattern structure is presented in Figure 5-3, with a detailed cross-sectional profile of the phantom pattern structure showing the parameter settings in Figure 5-3(b). The layer separation was set to 150 μm (in AD) and there was 25 μm layer offset set in this structure. The pulse energy used to inscribe each layer was presented in Table 5-1.



(a)



(b)



(c)

Figure 5-3. Patten design structure of the point spread function (PSF) phantom: (a) the layer pattern on the X-Y plane with index lines and test pattern area indicated; (b) cross-sectional profile of the phantom pattern showing the parameter settings; (c) 3D pattern structure showing every dimension of the pattern.

For the layer-by-layer method, illustrated in Figure 5-4, the top index line was inscribed for all layers, then the stage moved to the bottom line so that the bottom layer pattern would be inscribed. When each of the series of lines for the test pattern was completed, the stage then moved to the next layer up and then repeat the process for the line inscription until all the 8 layers were inscribed. After that, the stage would move to the bottom layer to inscribe the index lines at the end. The reason for inscribing the index lines individually was that in order to show as a solid line at the cross-sectional profile, the index line section needed to be inscribed more densely with very small layer separations so that all of series of lines overlap together vertically to form an inscribed layer, therefore, under the OCT system, it would always show as a solid line wherever the scan position is selected.

By using the layer-by-layer method, it takes a longer time compared with the slice-by-slice method as the stage needs to move back to the start position for each layer. However, the layer-by-layer method allows the pulse energy levels to be varied at different depths as every layer would be a fresh start and the machine would have enough time to reset to a new energy level.

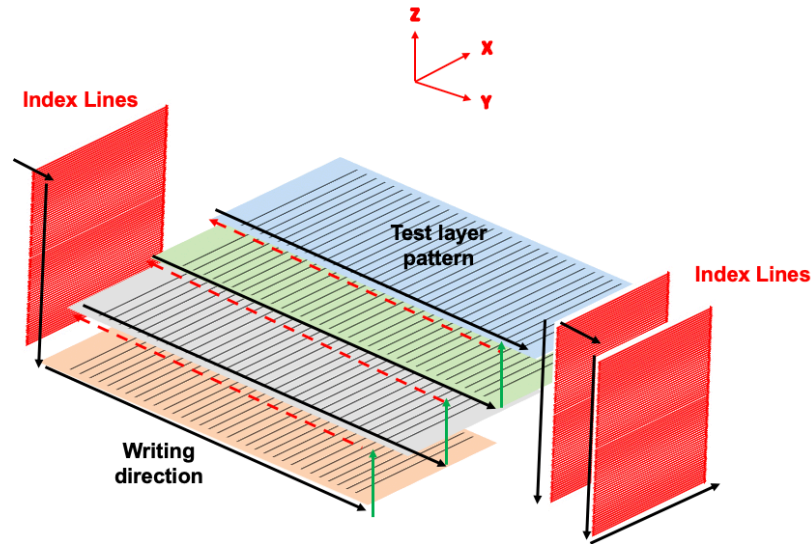


Figure 5-4. Illustration showing the new fabrication method with the writing direction, index lines, and test layer pattern indicated. In the diagram, the black solid line was used to indicate the writing direction and the red dashed line was used to indicate the moving direction. In the real fabrication, 8 layers had been inscribed rather than 4 layers shown in the diagram for the illustration purposes.

5.2.2 Sensitivity phantom

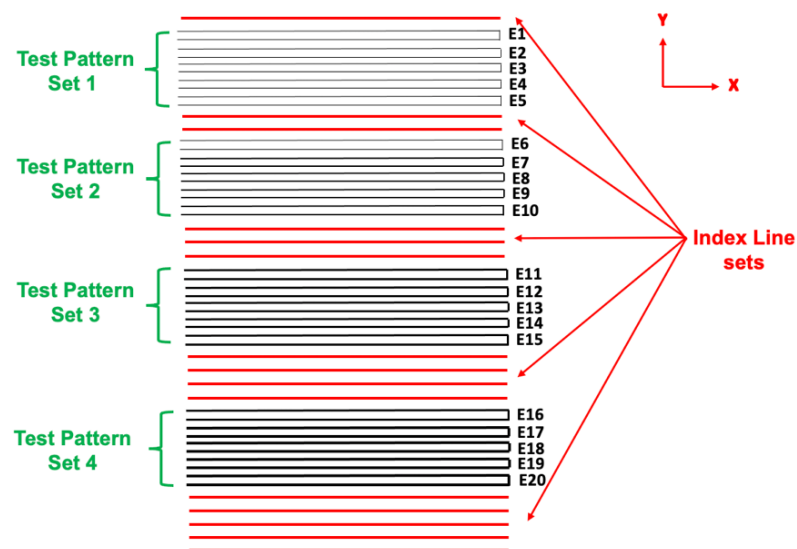
The sensitivity phantom was designed to assess the sensitivity of the OCT system that is a measure of the minimum reflectivity that an OCT system can detect [146]. At each pattern layer, it consists of a series of line pairs inscribed with different energy levels starting from a lower pulse energy to a higher pulse energy at each layer shown in Figure 5-5(a). For this phantom, the lowest energy level was set to 5% of the total average output power (i.e. 150nJ for the energy per pulse) and the highest energy level was set to 100% of the total average output power (i.e. 3.08 μ J for the energy per pulse). There were 6 sets included with 5 pairs of lines in each set, therefore, there were 30 pairs of lines inscribed with different energy levels for the pattern with a step of \sim 3.276% added on the next pair of lines starting from the lowest energy level which was 5%.

There were index lines located between each set. The number of index lines was used to guide the location of the test pattern. The set n was located between the n index line set and $n+1$ index line set. For example, set 3 was located between the index line set of 3 lines and the index line set of 4 lines. The cross-sectional profile of the phantom pattern and the 3D conceptual diagram of the sensitivity pattern are presented in Figure 5-5(b) and (c). For the sensitivity pattern, the laser energy level variation is the same for every layer. However, the layer separation was increased to 150 μ m compared with the

previous phantom design which was set to 50 μ m. Moreover, the previous design only set a small range of laser energy variation such as 30%-39% for the studied phantom presented in Section 3.6.

For the fabrication of this specific phantom, both the slice-by-slice method and the layer-by-layer method can be used as this phantom was not affected by the variation of the layer energy. However, the slightly slower layer-by-layer method has been developed and employed to satisfy the specific needs and allow more dynamic requirements.

When using the slice-by-slice method, the first index line group was inscribed firstly and followed by the first set of the energy test pattern for all eight layers inscribed and then moved to the second index line group and then the second set of the test pattern for all the layers. The process was repeated until the last set of the test pattern inscribed followed by the index line group. When using the layer-by-layer method, it involved a two-stage process as the index line and the test pattern were inscribed separately. First of all, all the test pattern layers were inscribed starting from the bottom layer to the top layer. Between the test set, there was enough space left for the index lines to be inscribed afterwards. The fabrication process for this phantom takes a bit longer (approximately an additional 10 minutes) as the stage needs to be moved back to inscribe the index line separately.



(a)

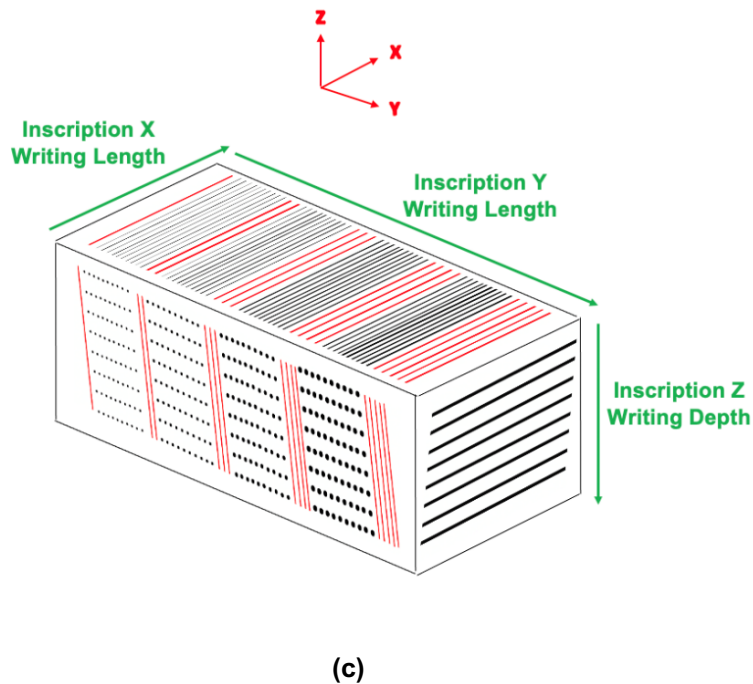
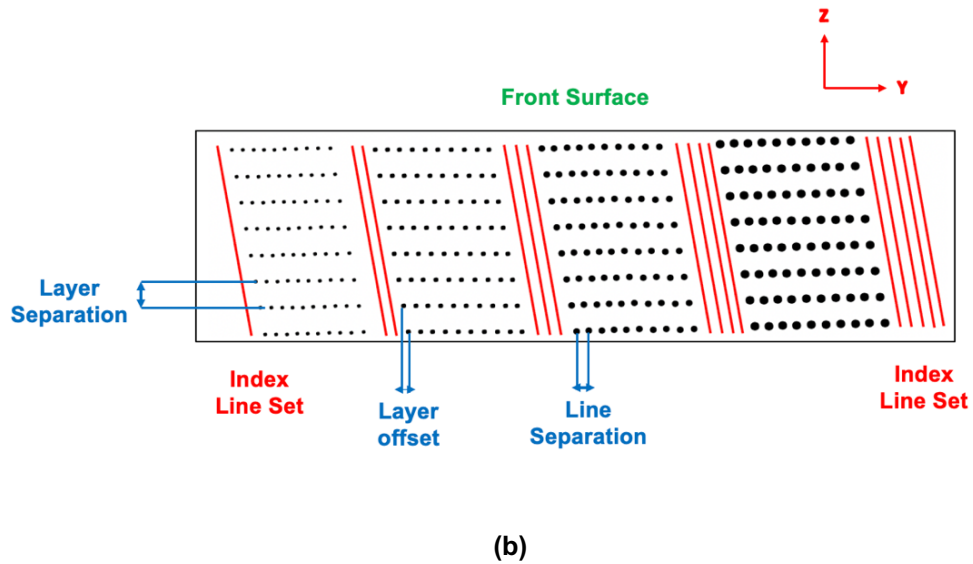


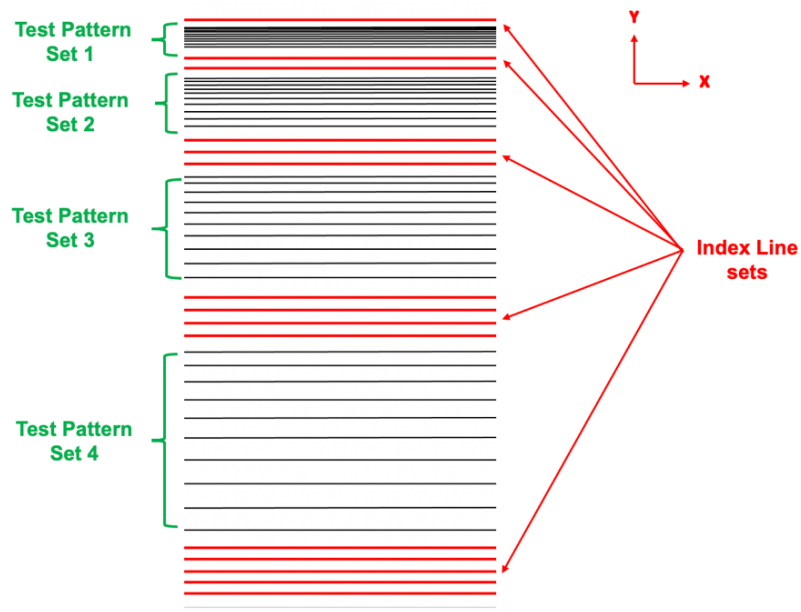
Figure 5-5. Patten design structure of the sensitivity phantom: (a) the layer pattern showing the first 4 test sets on the X-Y plane with index lines and test pattern area indicated; (b) cross-sectional profile of the phantom pattern of the first 4 test sets showing the parameter settings; (c) 3D pattern structure of the first 4 test sets showing every dimension of the pattern. Please note, there were 6 sets included in the real design and the fabrication.

5.2.3 Lateral resolution phantom

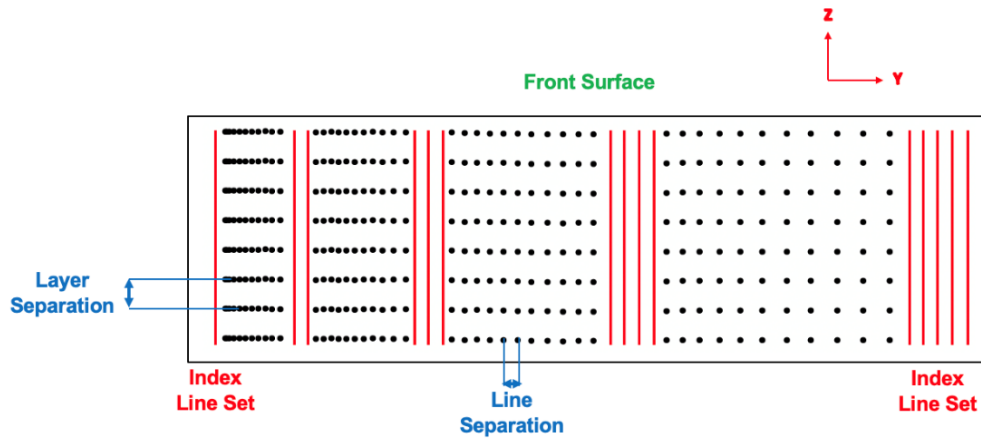
The Lateral resolution phantom was designed to assess the ability of the OCT system to distinguish the objects that are closely located [194]. At each layer, the phantom pattern consists of a series of inscription lines that are spaced with various line separations. There are 10 test sets included in this pattern with 11 lines (i.e. 10 line separations) in a set. The line separation was increased by $1\mu\text{m}$ between each test line with the first line separation started from $1\mu\text{m}$. For set 1, the variation of the range on the line separation was set to $1\text{-}10\mu\text{m}$, $11\text{-}20\mu\text{m}$ for set 2, $21\text{-}30\mu\text{m}$ for set 3 and so on until the last set (i.e. for set 10, it was $91\text{-}100\mu\text{m}$ for the line separation variation range). The layer separation was set to $150\mu\text{m}$ (in AD). There was no layer offset for this pattern. The pulse energy was applied to each layer was presented in Table 5-1.

The test set was separated by the index lines. There were 10 index line sets sitting between the test lines in a similar way to the sensitivity pattern such that the set n was located between the index line set n and the index line set $n+1$. The conceptual diagram of the pattern is shown in Figure 5-6(a) and the cross-sectional profile of the pattern is shown in Figure 5-6(b) and illustrates the parameter settings such as the layer separation, the line separation. In Figure 5-6(c), a 3D pattern structure was presented to show every dimension of the phantom.

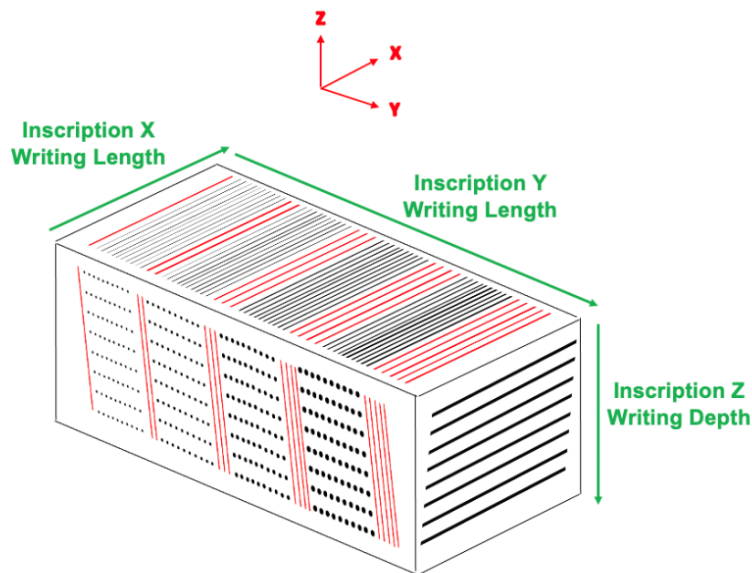
For the fabrication of this phantom pattern, firstly, the first index line was inscribed and then the test pattern of set 1 for each layer was fabricated for all eight layers and then the second index line set were inscribed afterwards followed by the set 2 of the test pattern was inscribed for all the layers. The process was repeated until the last test pattern set and the last index line set were inscribed. For this pattern structure, the pulse energies used for inscribing each layer test pattern were varied, which was the same as PSF phantom. After inscribing each layer of each test set, the pulse energy was quickly set to a new energy level through varying the attenuator position. The index line set is inscribed first followed by the pattern to minimise backtracking in the fabrication process. However, all test pattern layers can be inscribed at first, then add the index line sets to be in between the test pattern sets, which could introduce additional travel time.



(a)



(b)



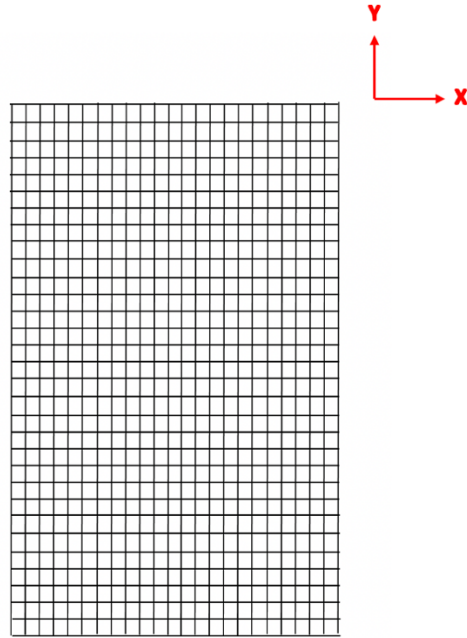
(c)

Figure 5-6. Patten design structure of the lateral resolution phantom: (a) the layer pattern showing the first 4 test sets on the X-Y plane with index lines and test pattern area indicated; (b) cross-sectional profile of the phantom pattern of the first 4 test sets showing the parameter settings; (c) 3D pattern structure of the first 4 test sets showing every dimension of the pattern. Please note, there were 10 sets included in the real design and the fabrication.

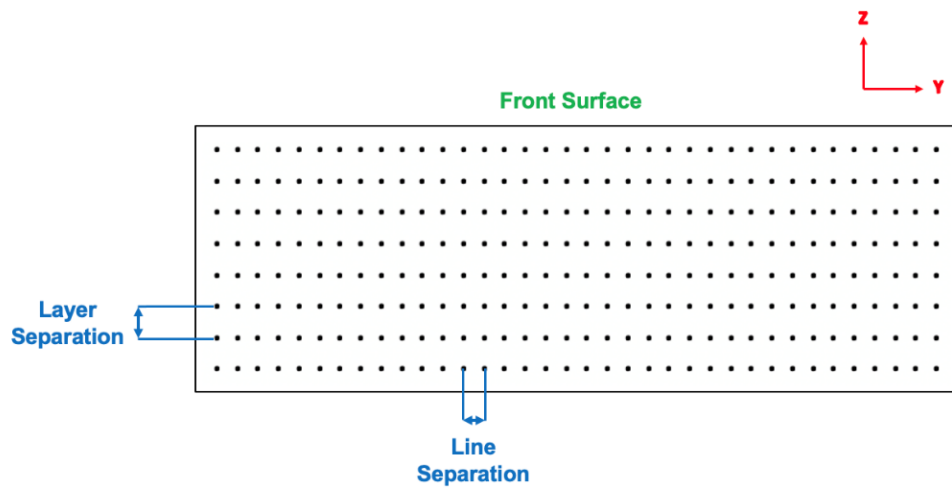
5.2.4 Distortion phantom

The distortion pattern was designed to assess the OCT system's distortion which is caused either by the material under test or issues with the scanning stages of the OCT measurement system [173]. The pattern consists of grid cells which have a dimension of $100\mu\text{m} \times 100\mu\text{m}$. The layer separation was set to $150\mu\text{m}$ (in AD) and there was no layer offset for this pattern structure. The pulse energy applied to inscribe each layer is presented in Table 5-1. Each layer pattern is shown in Figure 5-7(a), the cross-sectional view of the phantom structure is shown in Figure 5-7(b) and the 3D phantom structure was shown in Figure 5-7(c).

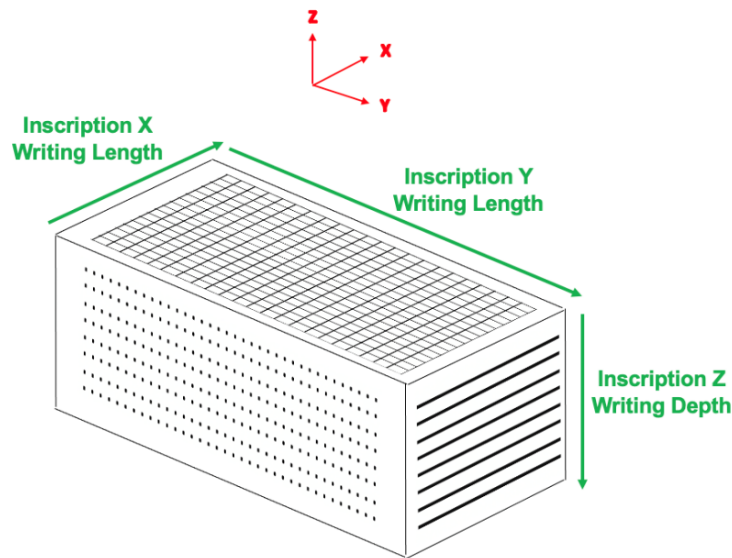
For the fabrication of this phantom structure, the layer-by-layer method was again used. For each layer pattern, the horizontal lines were inscribed first, and then vertical lines were inscribed. The inscription started from the bottom layer to the top layer. When one layer pattern was completed, the pulse energy would set to a new energy level for the next layer inscription.



(a)



(b)



(c)

Figure 5-7. Patten design structure of the distortion/grid phantom: (a) the layer pattern showing the grid pattern on the X-Y plane; (b) cross-sectional profile of the phantom pattern showing the parameter settings; (c) 3D pattern structure showing every dimension of the pattern.

5.3 Results and discussions

For the phantom characterisation, after the fabrication, the phantom was characterised by an optical microscope (Axioscope 2 MOT Plus, Zeiss) and OCT systems. The comparison was made between the previous phantom and this present phantom in order to see the difference. Both 5x objective lens and 20x objectives lens were used to observe and measure the sample for the characterisation. The SD-OCT system (Optimec is830) operating at a central wavelength of 830nm, which has an axial resolution in air of $\sim 12\mu\text{m}$ and a lateral resolution of $\sim 30\mu\text{m}$ [154] was mainly used to characterise the phantom.

5.3.1 Point spread function (PSF) phantom

5.3.1.1 Microscope characterisation

Figure 5-8 shows the microscope image using a 5x objective lens shows the overall pattern of point spread function (PSF) phantom. The line separation of $\sim 150.13\mu\text{m}$ is indicated in the image which matches to the parameter setting of $150\mu\text{m}$ for the line separation in the program, which can indicate the high accuracy and smooth finish of the

fabrication process using a femtosecond laser. The reading of the measurement can be slightly varied which has been previously discussed in section 3.6.3.5 for details of the measurement errors.

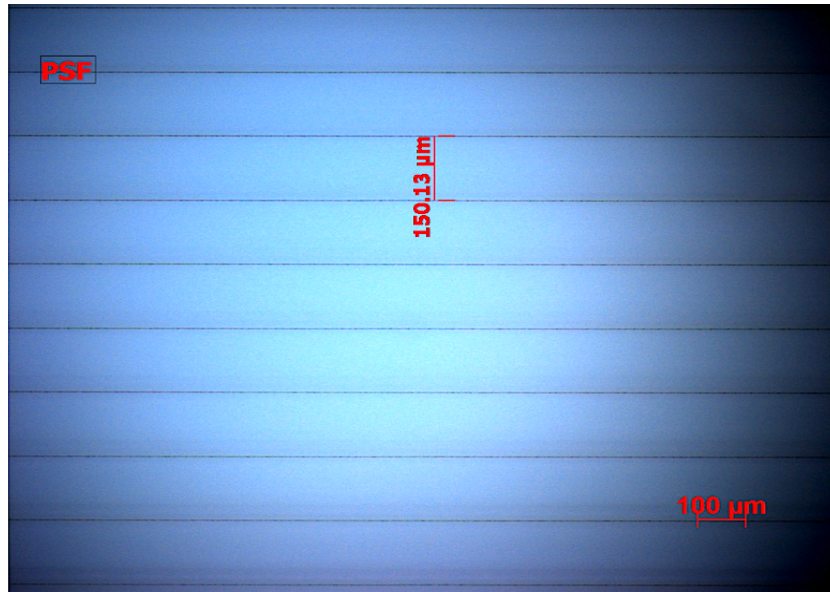
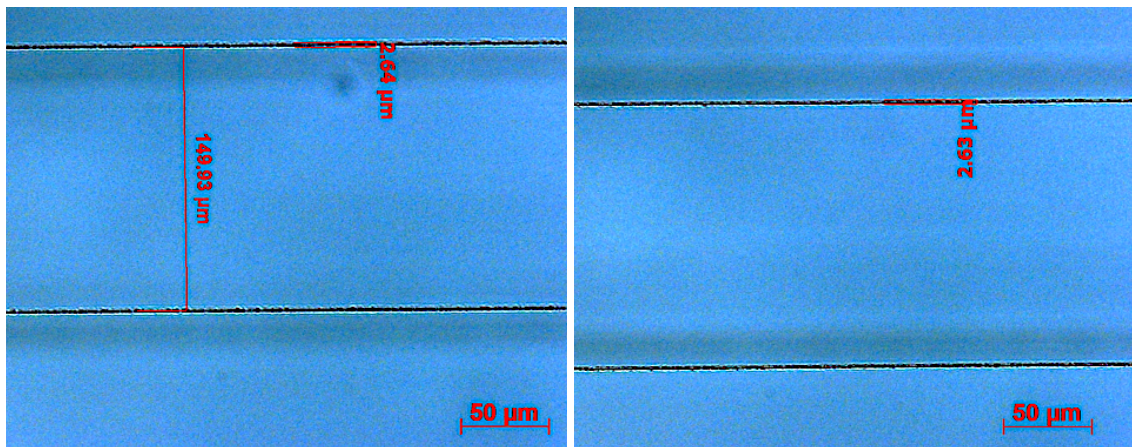


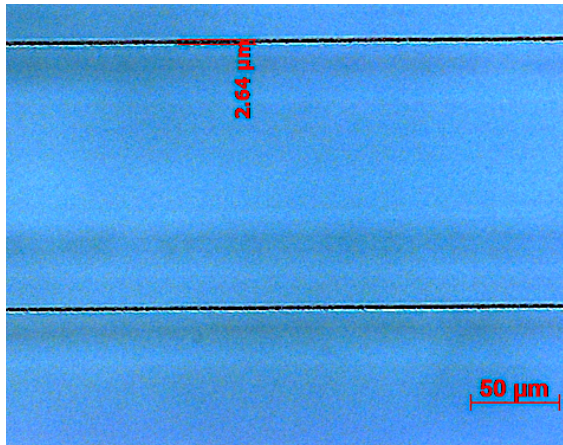
Figure 5-8. The microscope image using a 5x objective lens showing the overall pattern of PSF phantom. The line separation of $150.13\mu\text{m}$ is indicated.

Figure 5-9(a)-(h) show microscope images of PSF phantom with the linewidths for all eight layers measured using a 20x objective lens for a close-up view. It can be seen that with the pulse energy varied at different depths, similar linewidths can be achieved. The measurements for the linewidths of all eight layers are around $2.6\mu\text{m}$ which indicates a consistency of the linewidth across all the layers by adopting various pulse energies to different depths in order to compensate the power loss. In Figure 5-9(a) also shows the measurement of line separation is $149.93\mu\text{m}$ which matches to the designed parameter of $150\mu\text{m}$ setting in the fabrication program.

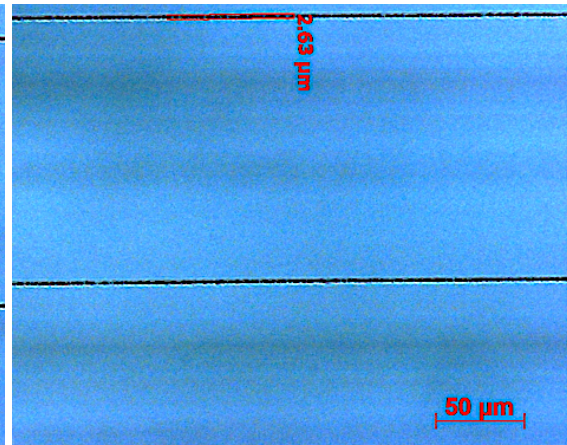


(a) 1st layer at $100.164\mu\text{m}$

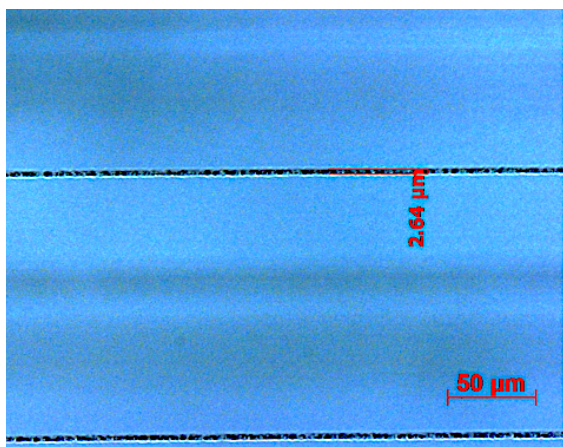
(b) 2nd layer at $250.716\mu\text{m}$



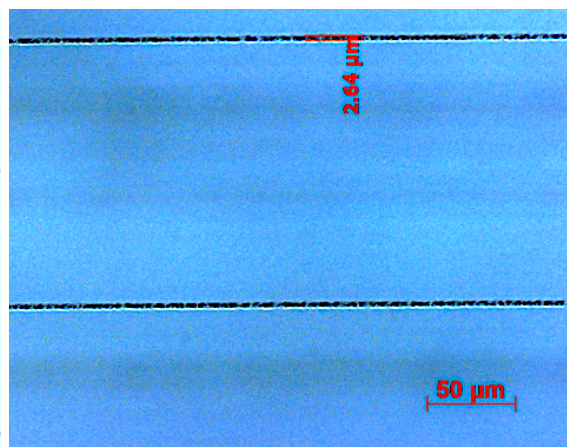
(c) 3rd layer at 400.962μm



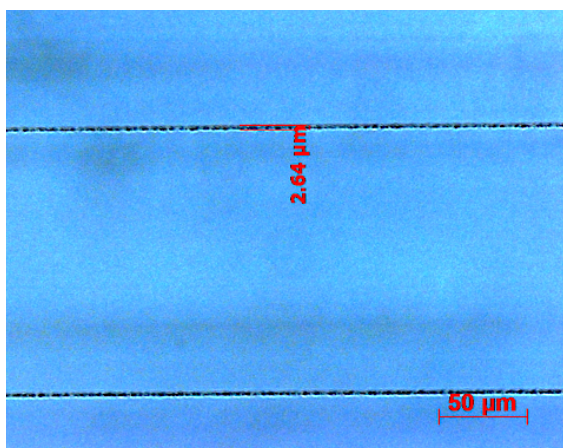
(d) 4th layer at 551.208μm



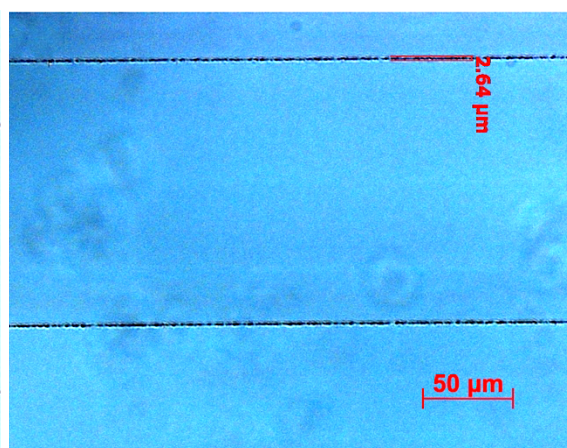
(e) 5th layer at 704.004μm



(f) 6th layer at 860.421μm



(g) 7th layer at 1011.228μm



(h) 8th layer at 1162.678μm

Figure 5-9. Microscope images using a 20x objective lens showing the linewidth measurement for all eight layers (from (a) to (h)) of the PSF phantom with layer depth and the linewidth indicated. With the varied laser power, the linewidth can be kept consistently for all the layer depths, measured as 2.64μm.

In order to better understand the changes to the design and the parameter settings, the cross-sectional profile of the phantom was inspected. A comparison between the

previous design and the present design shown in Figure 5-10 has also been presented in order to clearly see the difference. It can be seen with the current design, a total layer separation measured as $\sim 1534.07\mu\text{m}$ (in RD) has been reached with a single layer separation measured as $\sim 219.84\mu\text{m}$ in real depth (RD). For the cross-sectional profile, a real depth (RD) is used as the depth is no longer affected by the refractive index.

Moreover, as the designed parameter is known, the refractive index can be worked out by using the ratio of the layer separation in real depth (i.e. $\sim 219.84\mu\text{m}$ shown in Figure 5-10(a)) and the designed layer separation of $150\mu\text{m}$ which is $219.84\mu\text{m}/150\mu\text{m} = 1.465$. Compared with the previous design, a total layer separation of $\sim 510.72\mu\text{m}$ (in RD) has been reached with a single layer separation of $\sim 72.03\mu\text{m}$ (in RD). The setting parameter of the layer separation for this design was set to $50\mu\text{m}$, therefore the ratio for the refractive index can be calculated as 1.458. The measurement error and the scaling limit of the imaging software can also affect the accuracy of the measurement and the final results. Therefore, the error tolerance has to be considered when discussing the accuracy of the results.

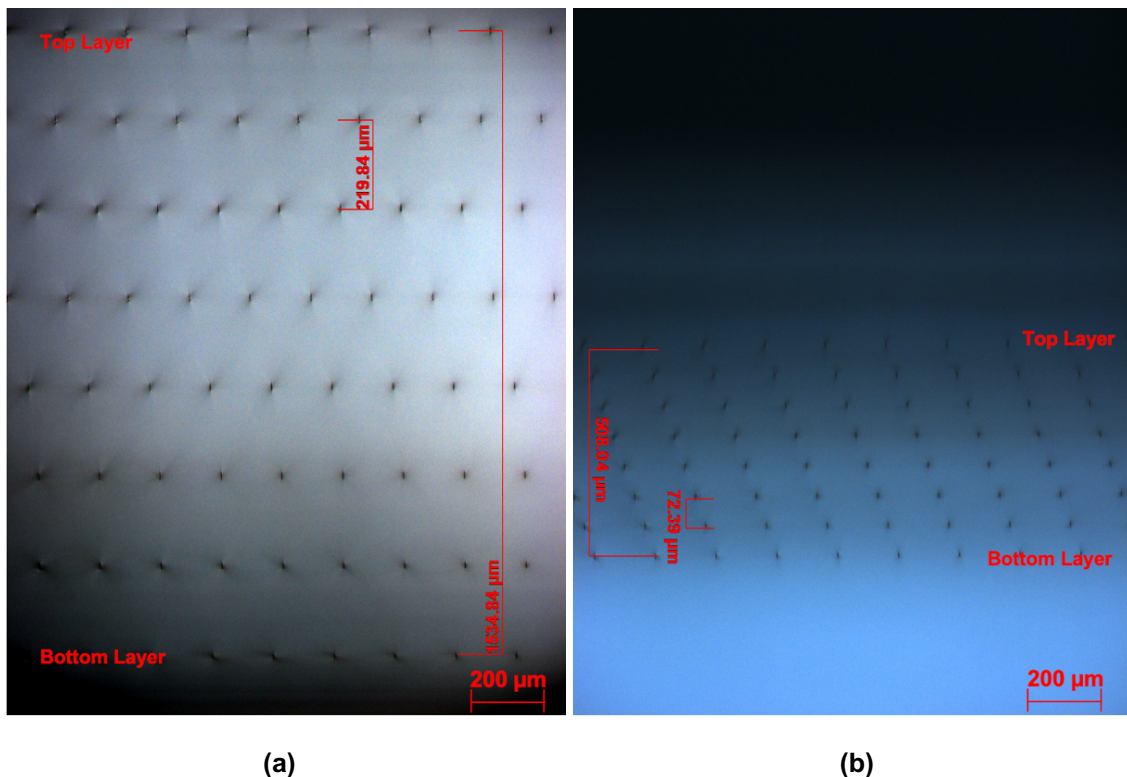
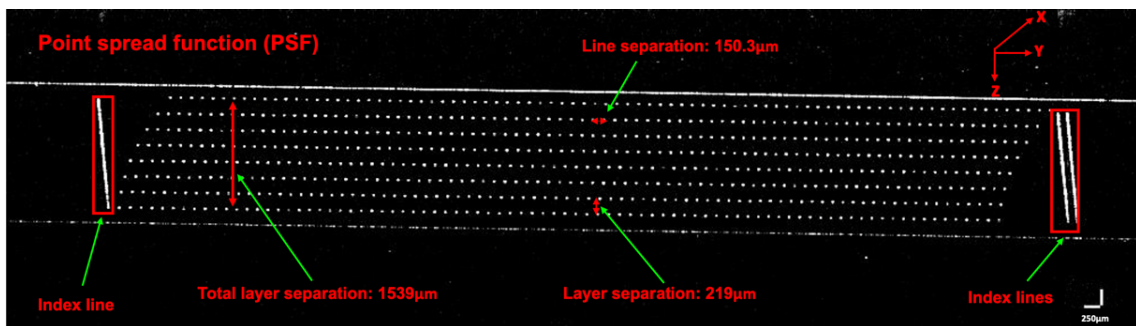


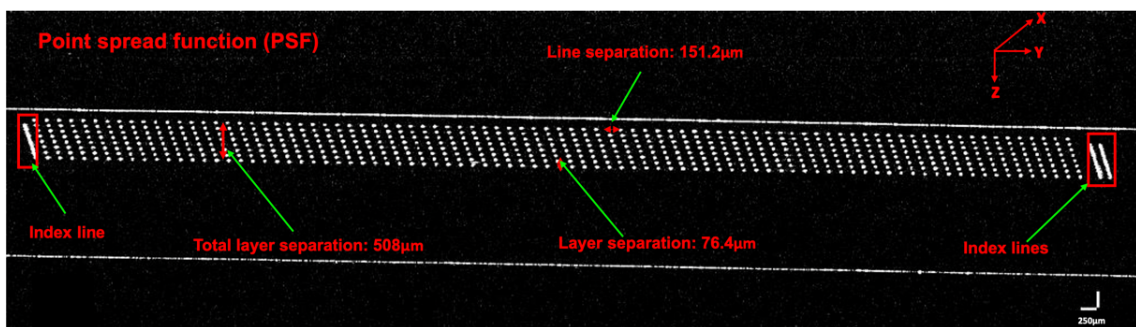
Figure 5-10. The microscope image using a 5x objective lens showing the cross-sectional profile of the PSF phantom: (a) the new phantom design has a larger layer depth of $150\mu\text{m}$ in apparent depth (AD), with the layer separation measured in real depth (RD) as $219.84\mu\text{m}$ and a total inscription depth of $1534.84\mu\text{m}$; (b) the previous phantom design with a smaller layer depth of $50\mu\text{m}$ (in AD), with the layer separation measured in real depth (RD) as $72.39\mu\text{m}$ and a total inscription depth of $508.04\mu\text{m}$.

5.3.1.2 OCT characterisation

After the microscope characterisation, the phantom then was characterised by an OCT system, which provided a cross-sectional information of the phantom structure. Moreover, it can also be used to check the OCT performance as a calibration phantom. In order to compare between two designs (i.e. the previous design and the current design), both OCT images were presented in Figure 5-11 to show the difference and the change in design. It can be seen from Figure 5-11(a), under the OCT system, the point size seems to be uniform and consistent across all the inscription layers. Compared with the previous design, the inscription area has been expanded more than three times in the Z-axis (inscription depth). The measurements presented in the OCT image for each parameter show the agreement between the designed and fabricated parameter values.



(a) The OCT image of PSF phantom with a greater layer separation (new design) with a scan size of $\sim 16\text{mm} \times 6.6\text{mm}$. The OCT measurement shows the layer separation of $219\mu\text{m}$, the line separation of $150.3\mu\text{m}$ and a total layer depth of $1539\mu\text{m}$.



(b) The OCT image of PSF phantom with a smaller layer separation (previous design) with a scan size of $\sim 14\text{mm} \times 4.53\text{mm}$. The OCT measurement shows the layer separation of $76.4\mu\text{m}$, the line separation of $151.2\mu\text{m}$ and a total layer depth of $508\mu\text{m}$.

Figure 5-11. OCT images for the point spread function (PSF) phantom showing both (a) the current design with a greater layer separation and (b) the previous design with smaller layer separation in order to make a comparison and present the change in design. Both the OCT images were taken by Optimec is830 SD-OCT system. The measurement values indicated in the image are showing in real depth (RD).

Figure 5-12 provides a close-up view of the fabricated OCT phantom. It can be seen clearly that the fabricated phantom structure has a consistent point size and line spacing. The PSF of the system can only be directly measured when the target size is smaller than the resolution, in which case the PSF of the sample can be treated as a delta function. However, based on the OCT image information shown in Figure 5-12, the measured point size is almost a pixel size which the pixel size for X-axis is $10\mu\text{m}$ and the pixel size for Z-axis is $12.89\mu\text{m}$ (i.e. the axial resolution of the OCT system), therefore the cross-sectional size of the line is of a similar size or less. Therefore, the current PSF phantom might not be suitable for direct measurement of OCT system PSF as the point size is fairly large on the Z-axis.

However, the size on the X-axis might allow for PSF to be closely measured as it is much smaller than lateral resolution of typical OCT systems (i.e. $20\text{-}30\mu\text{m}$). One thing that previous research suggested to obtain the PSF of the OCT system is to use a larger, well characterised, target to deconvolve their known shapes from the OCT signal [155]. The PSF phantom can be used as a target as it is well characterised. Moreover, as the PSF phantom was identically inscribed, it enables consistent and uniform reflection from the structure which can help to check the sensitivity and linearity of the OCT system. Also, the spatial variation of the system resolution can be measured by measuring the PSF phantom each point which can be used to improve the resolution of the OCT system [177].

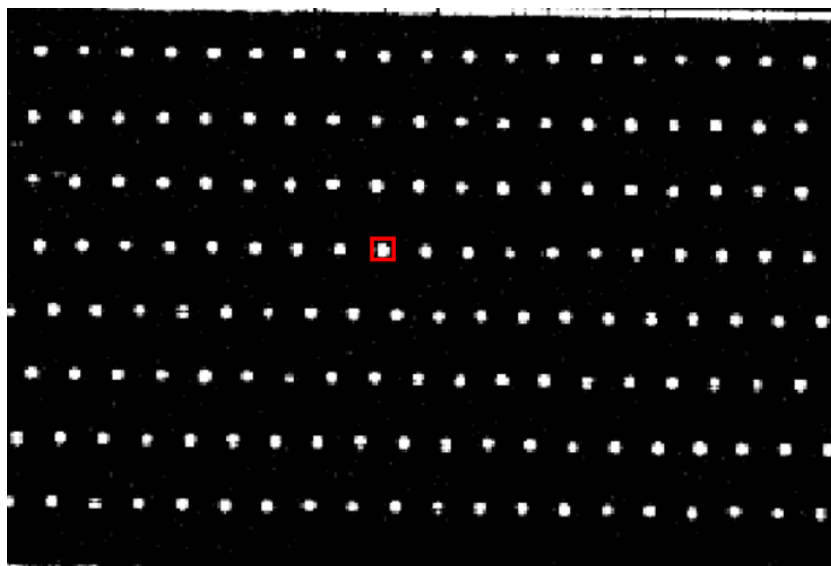


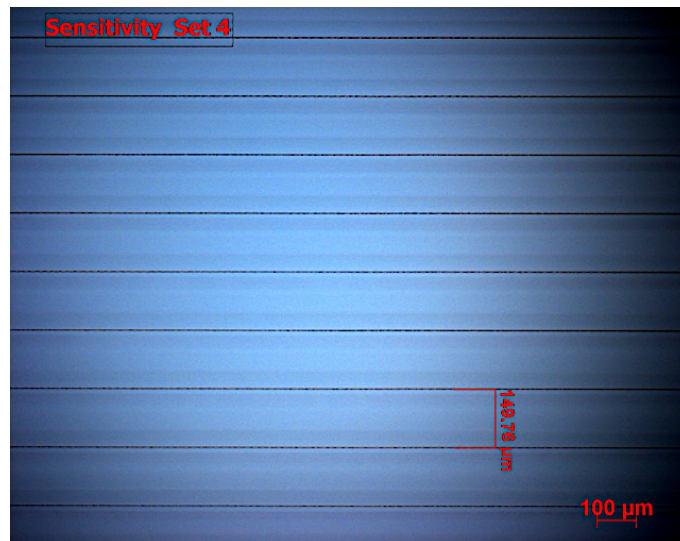
Figure 5-12. The OCT image showing the pixel size (labelled in red square) compared with the point size of the PSF phantom. This image also provides a close-up look for the fabrication.

5.3.2 Sensitivity phantom

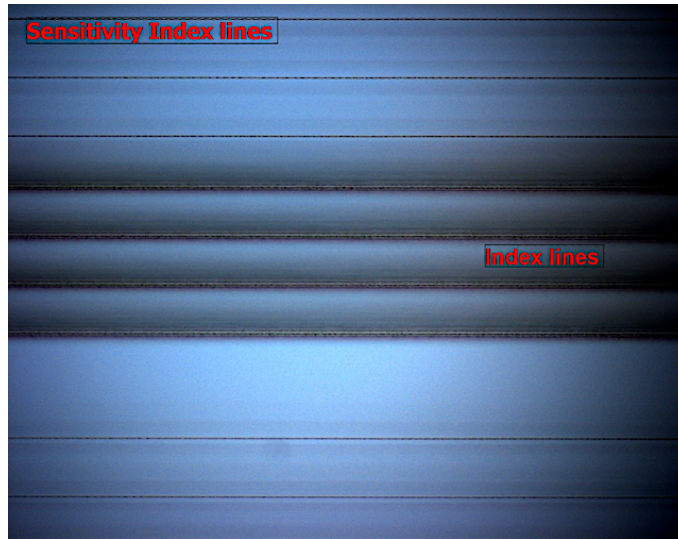
5.3.2.1 Microscope characterisation

The sensitivity phantom can be used to assess the sensitivity of an OCT system to see the weakest signal which can be detected. The phantom consists of a series of inscription lines inscribed with various laser energy levels, which provides a dynamic inscription size with various refractive index changes in the fused silica structure.

Figure 5-13 shows the microscope images using a 5x objective lens to overview the phantom structure for both the test pattern and the index lines. It can be seen that the test pattern was divided into different sets by placing the index lines in between. The line separation of $\sim 149.7\mu\text{m}$ was measured in Figure 5-13(a) which matches to the laser parameter for the line separation of $150\mu\text{m}$.



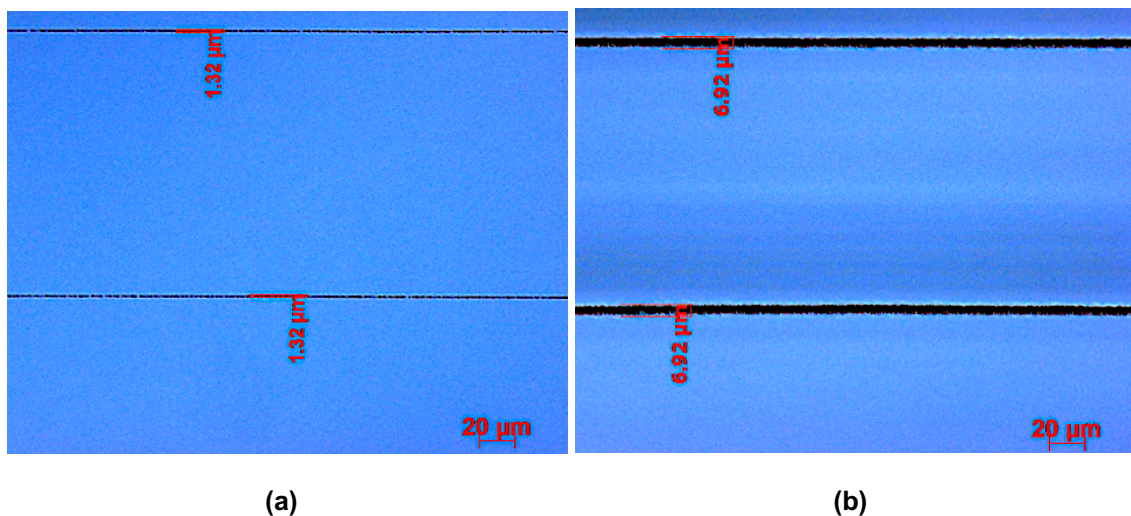
(a)



(b)

Figure 5-13. The microscope images using a 5x objective lens showing the overall pattern of the sensitivity phantom structure: (a) one of the test sets (Set 4); (b) one of the index line sets (Set 4).

After using a 5x objective lens to check the overall pattern, a 20x objective lens was then used to check the linewidth of the inscription as shown in Figure 5-14. The energy level pair of E3 (i.e. the third energy level pair) was chosen to present the linewidth for one of the lower energy level pairs (i.e. 11.6% of the laser average output power). The energy level pair of E30, the highest of the energy levels, was chosen to show the difference in the linewidth (i.e. 100% of the laser average output power). The linewidth for E3 was measured as $\sim 1.3\mu\text{m}$ and the linewidth for E30 was measured as $\sim 6.9\mu\text{m}$.



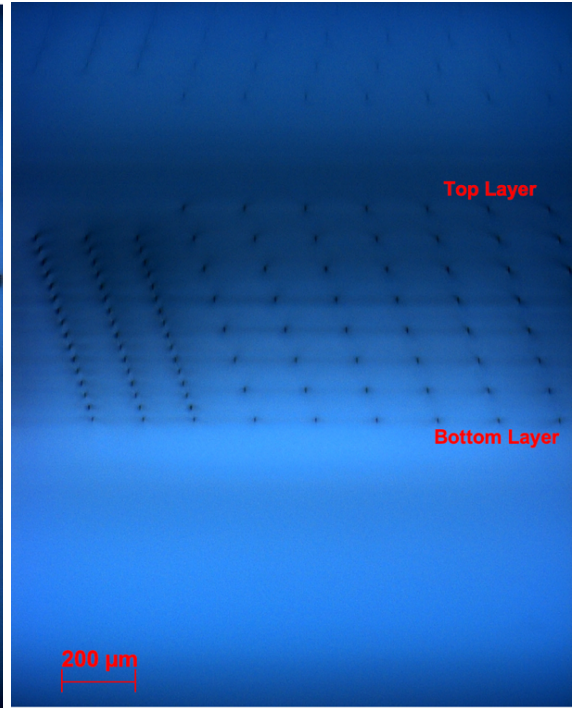
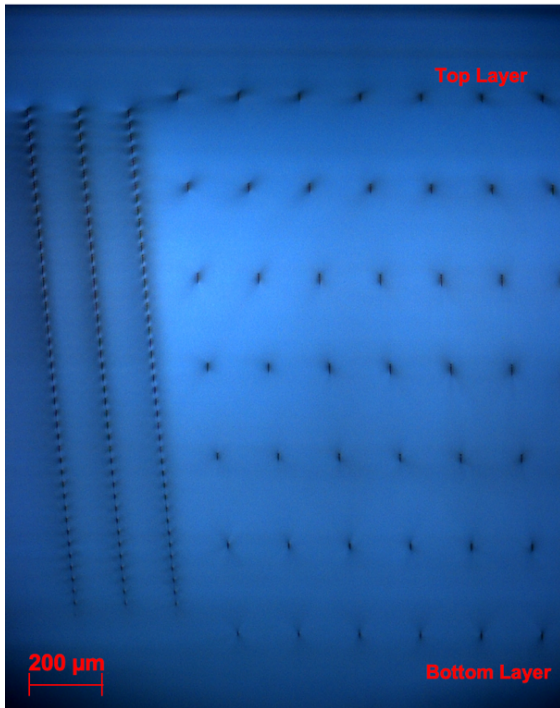
(a)

(b)

Figure 5-14. The microscope images using a 20x objective lens showing the linewidth of the inscription: (a) the linewidth of the third energy level pair (i.e. 11.6% of the laser average output power) measured as $1.32\mu\text{m}$; (b) the linewidth of the highest energy level pair (i.e. 100% of the laser average output power) measured as $6.92\mu\text{m}$.

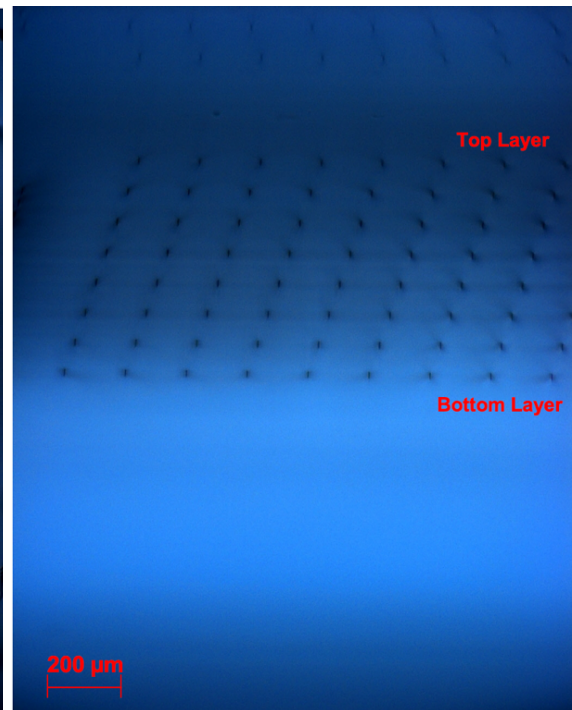
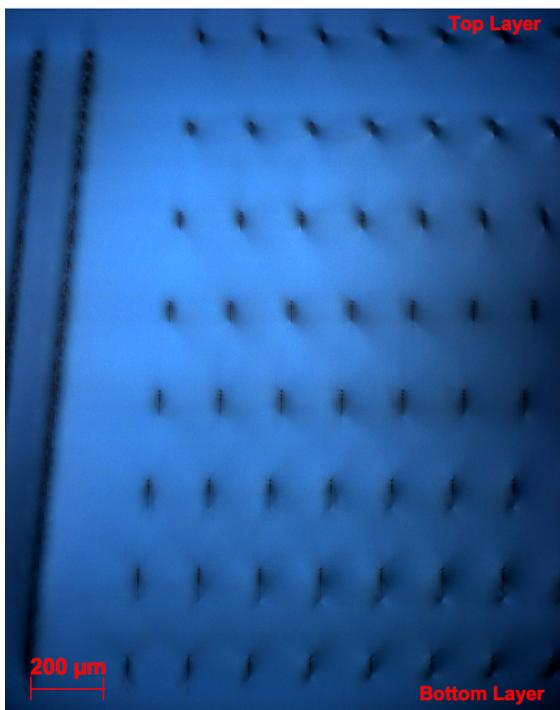
After measuring the linewidth in the X-Y plane, a 5x objective lens was again used to view the cross-sectional profile shown in Figure 5-15. Both set 3 and set 6 were chosen to do the comparison between the present phantom structure with a larger layer separation of 150 μm and the previous phantom structure with a smaller layer separation of 50 μm . The index line showing 3 lines means it is in set 3. It can be seen in Figure 5-15 that the sensitivity pattern inscribed with various pulse energies, the point size tends to become larger with increasing pulse energy.

As the inscription depth is increased, Figure 5-15(a) and (c), the elongation of the inscription tends to be more obvious at the deeper depths due to the presence of the spherical aberration and the self-focusing induced at higher energy sets (i.e. above the self-focusing threshold). However, in Figure 5-15(b) and (d), as the inscription was close to the surface and the lower range of energy levels (i.e. the previous phantom design parameter is discussed in Section 3.6) were used to fabricate this phantom, therefore optical distortion was not clearly observed in those images. To ensure a fine quality of fabrication, a lower pulse energy below the critical peak power for the self-focusing should be chosen when inscribing deeper depths to avoid the optical distortion. However, in order to provide a full range of sensitivity assessment for the OCT system, the energy levels setting for the sensitivity phantom was adopting a wider range of the laser pulse energy (i.e. from 5%-100% of the laser power). A full study of the linewidth variation with respect to the laser pulse energy and the inscription depth has been presented in Section 4.3. As with the pulse energy increased, the linewidth is increased proportional to the change in the pulse energy.



(a) Set 3 with larger layer separation

(b) Set 3 with smaller layer separation



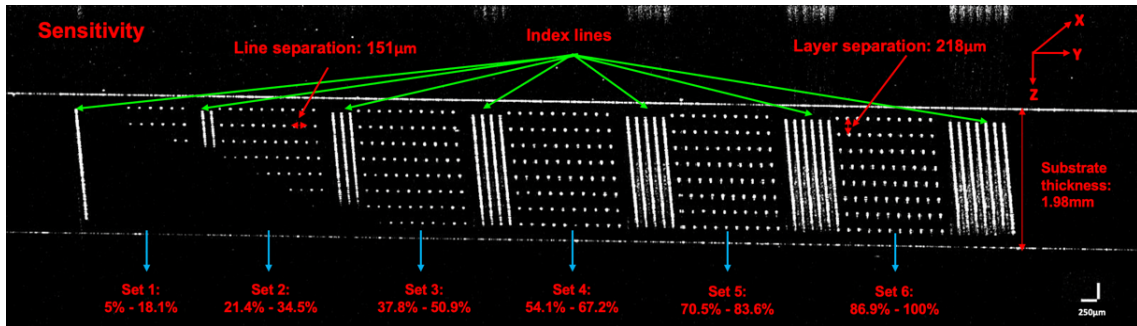
(c) Set 6 with larger layer separation

(d) Set 6 with smaller layer separation

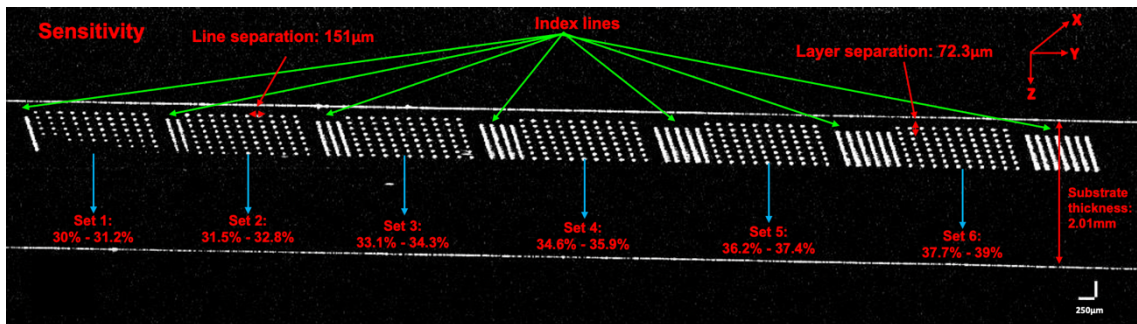
Figure 5-15. The microscope image using a 5x objective lens showing the cross-sectional profile of the sensitivity phantom: (a) the phantom design with a larger layer depth (150 μ m setting for the layer separation) for set 3; (b) the phantom design with a smaller layer depth (50 μ m setting for the layer separation) for set 3; (c) the phantom design with a larger layer depth (150 μ m setting for the layer separation) for set 6; (d) the phantom design with a smaller layer depth (50 μ m setting for the layer separation) for set 6.

5.3.2.2 OCT characterisation

Figure 5-16 shows the OCT images for both the current design with a greater layer separation of $\sim 218\mu\text{m}$ and the previous design which has a smaller layer separation of $\sim 72.3\mu\text{m}$. It can be seen that as the layer separation expanded, the lower pulse energy is no longer strong enough to reach to the deeper layer, for example, the majority of the first two sets of the test pattern shown in Figure 5-16(a).



(a) The OCT image of sensitivity phantom with a greater layer separation (new design) with a scan size of $\sim 16\text{mm} \times 6.6\text{mm}$. The OCT measurement shows the layer separation of $218\mu\text{m}$ and the line separation of $151\mu\text{m}$.



(b) The OCT image of sensitivity phantom with a smaller layer separation (previous design) with a scan size of $\sim 14\text{mm} \times 4.53\text{mm}$. The OCT measurement shows the layer separation of $72.3\mu\text{m}$ and the line separation of $151\mu\text{m}$.

Figure 5-16. OCT images for the sensitivity phantom showing both (a) the current design with a greater layer separation and (b) the previous design with smaller layer separation in order to make a comparison and present the change in design. Both the OCT images were taken by Optimec is830 SD-OCT system. The measurement values indicated in the image are showing in real depth (RD).

However, when the pulse energy is increased, the inscription size and intensity of the reflection light become stronger so that the pattern looks brighter. With the presence of the spherical aberration and the self-focusing, the elongation appears and becomes more obvious at deeper layers (i.e. the last three layers for higher energy levels such as the set 5 and the set 6) which is located beyond 1mm from the front surface. As it can be seen from Figure 5-16(b), with the original phantom design, the total inscription depth

was below 700 μm and the range of the laser energy level was controlled at a very low level, therefore, the point size looks more uniform not elongated. The sensitivity phantom is not only used to provide qualitative check for the sensitivity of an OCT system to see where in the pattern the point cannot be detected but also can use a reference for improving the system sensitivity at a later time.

5.3.3 Lateral resolution phantom

5.3.3.1 Microscope characterisation

The lateral resolution phantom was designed to assess the lateral resolution of an OCT system to determine the minimum line separation that the system can resolve. For each layer, the line was inscribed by the pulse energy but with a varied line separation setting from 1 μm to 100 μm . In Figure 5-17, the microscope image using a 5x objective lens shows the overall inscribed pattern for the first layer, which the first and the last line separation for both set 3 and 4 is indicated. Set 3 and set 4 have a line separation range of 21-30 μm and 31-40 μm correspondingly, which the measured values showing an agreement to the setting value, the index lines can be seen between the two sets.

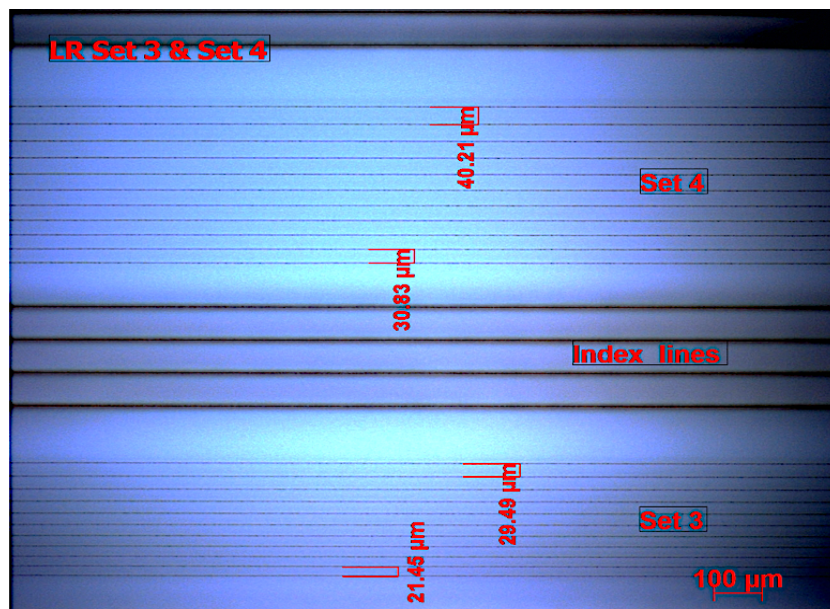


Figure 5-17. The microscope image of the lateral resolution phantom using a 5x objective lens shows the overall pattern and the line separation variation for the set 3 and the set 4 of the pattern.

Figure 5-18 presents a close-up view on one of the test pattern set (i.e. set 3) which has a line separation varied from 21 μm to 30 μm . It can be seen from the measured value of each line separation are a good match to the designed parameter values. It has to be

noted that the difference of $1\mu\text{m}$ shown in the measurement in Figure 5-17 and Figure 5-18 for the last line separation for the set 3 is due to a different microscope objective lens being used to observe the inscription. The accuracy can be slight differ as the 20x objective gives a more accurate measurement as the scaling become smaller.

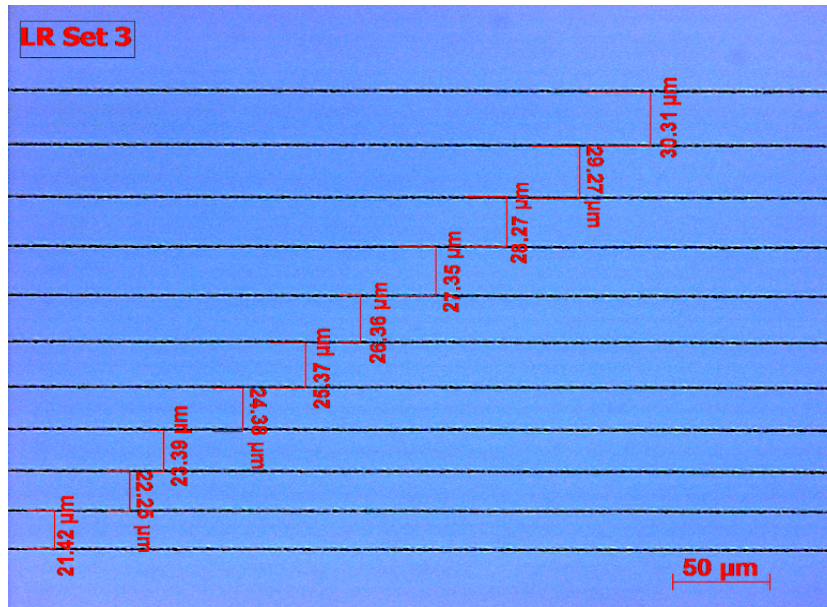


Figure 5-18. The microscope image of the lateral resolution phantom using a 20x objective lens to show the line separation variation (i.e. range from $21\text{-}30\mu\text{m}$) for set 3 with the measurement values labelled in the image.

Figure 5-19 shows a side-by-side comparison between the current new design shown in Figure 5-19(a) and the previous design shown in Figure 5-19(b) for set 2 and set 3. It can be seen that the total inscription depth has been increased around 3 times than the previous design. As the linewidth measured under the microscope is around $2.6\mu\text{m}$, therefore, the line should be separated above $2.6\mu\text{m}$.

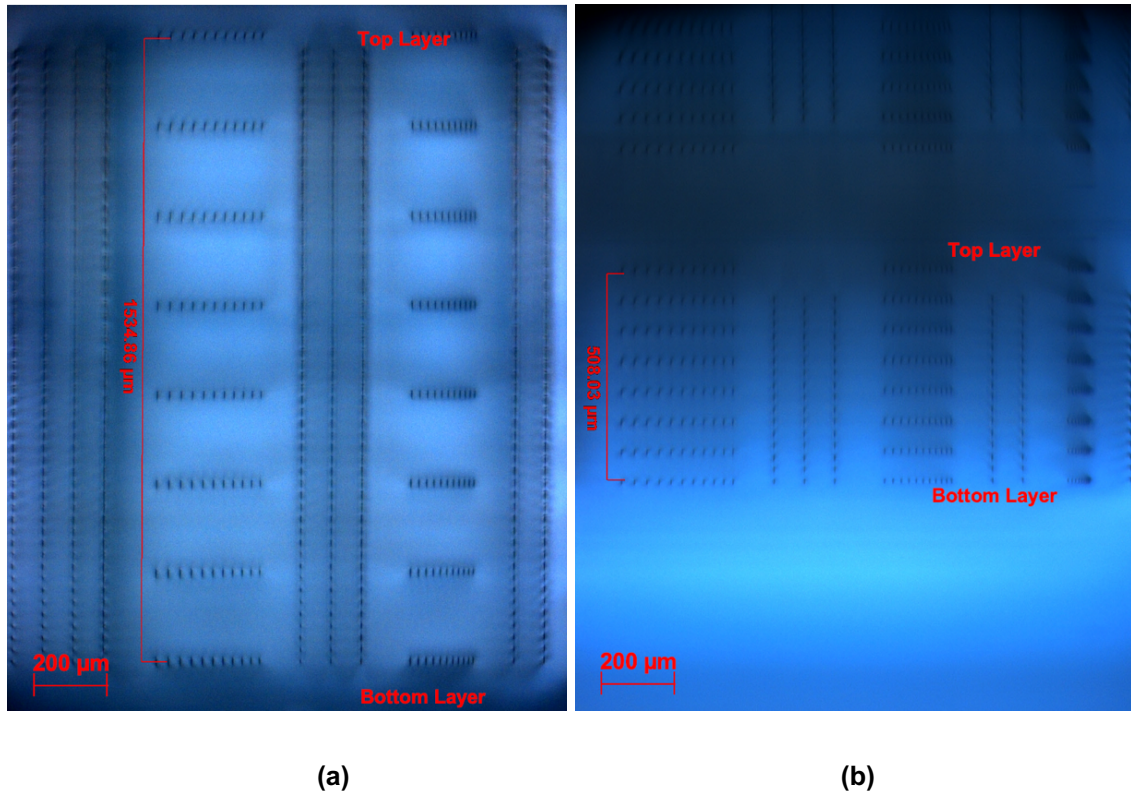
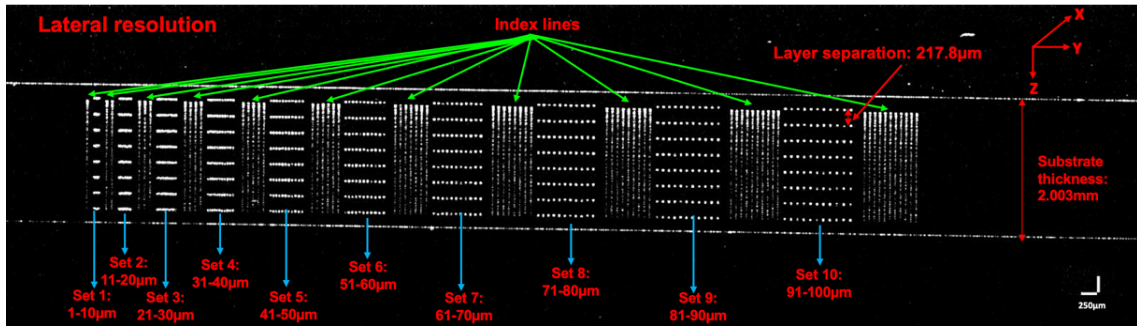


Figure 5-19. The microscope image of the lateral resolution phantom using a 5x objective lens to show the cross-sectional view of the pattern structure of set 2 and set 3: (a) the current phantom design with a larger layer depth (150 μm in AD setting for the layer separation) for both set 2 and set 3 with a total inscription depth of 1534.86 μm in RD; (b) the previous phantom design with a smaller layer depth (50 μm in AD setting for the layer separation) for both set 2 and set 3 with a total inscription depth of 508.03 μm in RD.

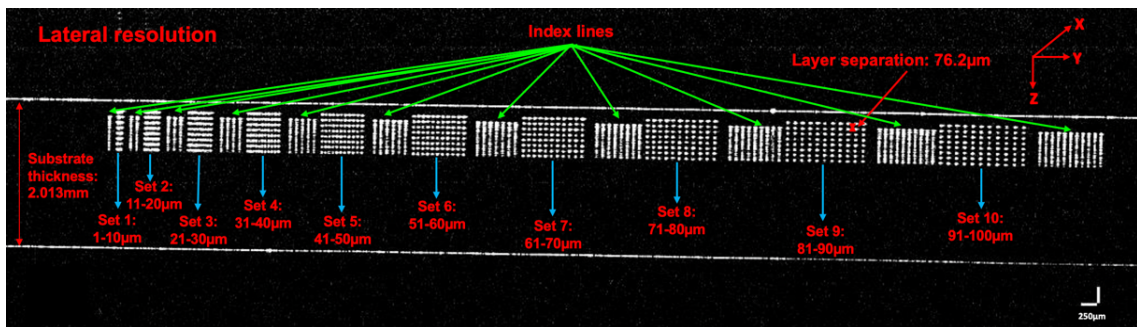
5.3.3.2 OCT characterisation

Figure 5-20 shows the OCT images for both the new design shown in Figure 5-20(a) and original design in Figure 5-20(b) for a comparison. The OCT system used to produce the images has a lateral resolution of $\sim 30\mu\text{m}$, although the linewidth was measured as $\sim 2.6\mu\text{m}$.

Subject to this resolution limit, for the first three sets, the lines are merged together as the system cannot resolve them. The lines appear to be separated from set 4 onwards, where set 4 has a line separation variation range of 31-40 μm , which matches to the lateral resolution of the OCT system.



(a) The OCT image of the lateral resolution phantom with a greater layer separation (new design) with a scan size of $\sim 16\text{mm} \times 6.6\text{mm}$. The OCT measurement shows the layer separation of $217.8\mu\text{m}$.



(b) The OCT image of the lateral resolution phantom with a smaller layer separation (previous design) with a scan size of $\sim 14\text{mm} \times 4.53\text{mm}$. The OCT measurement shows the layer separation of $76.2\mu\text{m}$.

Figure 5-20. OCT images for the lateral resolution phantom showing both (a) the current design with a greater layer separation and (b) the previous design with smaller layer separation in order to make a comparison and present the change in design. Both OCT images were taken by Optimec is830 SD-OCT system. The measurement values indicated in the image are showing in real depth (RD).

5.3.4 Distortion phantom

5.3.4.1 Microscope characterisation

The distortion phantom was designed to mainly measure the geometrical distortion of an OCT system but can also be used to assess the system resolution and any de-bending software algorithms. It consists of 8 layers of the grid pattern with a cell size of $\sim 100\mu\text{m} \times 100\mu\text{m}$. Figure 5-21 shows an overall phantom pattern using a 5x objective lens while Figure 5-22 presents a detailed view of the pattern using a 20x objective lens. The measured cell size shows a slightly different value which is due to the resolution and scaling limit of the microscope objective lens used. However, both measurements show a good agreement to the designed cell size.

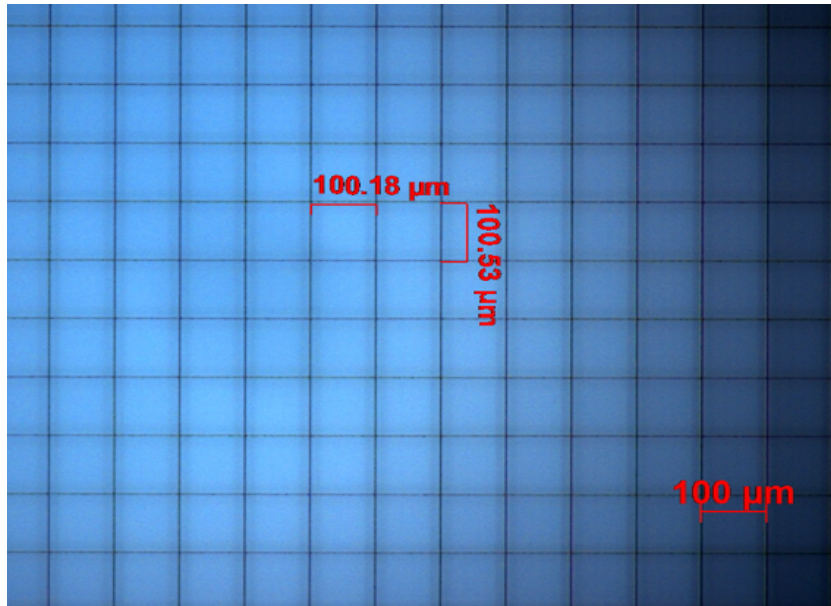


Figure 5-21. The microscope image of the distortion/grid phantom using a 5x objective lens to show the overall pattern with the measured cell size of $100.18\mu\text{m} \times 100.53\mu\text{m}$, as indicated in the image.

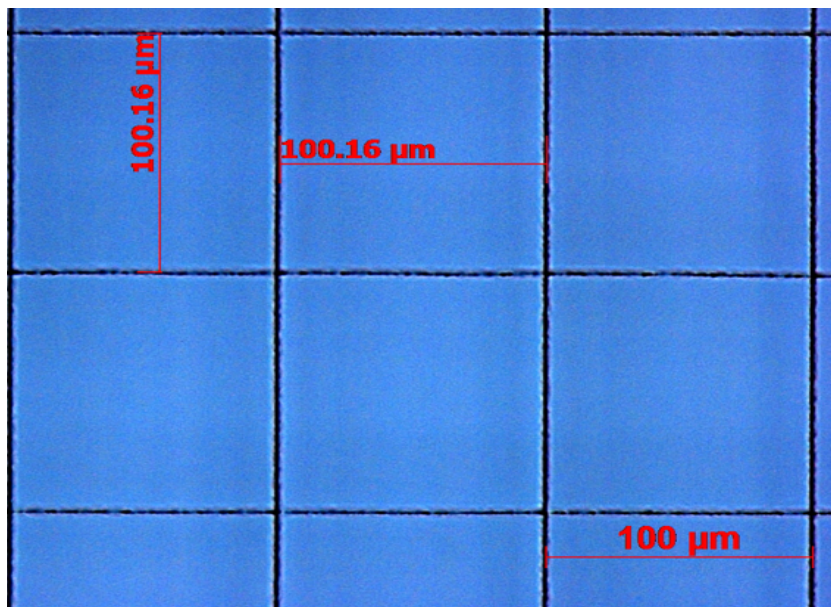


Figure 5-22. The microscope image of the distortion/grid phantom using a 20x objective lens to show the detailed pattern with the measured cell size of $100.16\mu\text{m} \times 100.16\mu\text{m}$, as indicated in the image.

Figure 5-23 shows a cross-sectional view of the pattern structure, which Figure 5-23(a) showing the current new design that has a greater layer separation of $150\mu\text{m}$ (in AD) and Figure 5-23(b) shows the previous design that has a smaller layer separation of $50\mu\text{m}$ (in AD). As the distortion/grid pattern was inscribed in both the horizontal and the vertical direction, the cross-sectional view can also show the joined parts where two lines cross each other under the microscope.

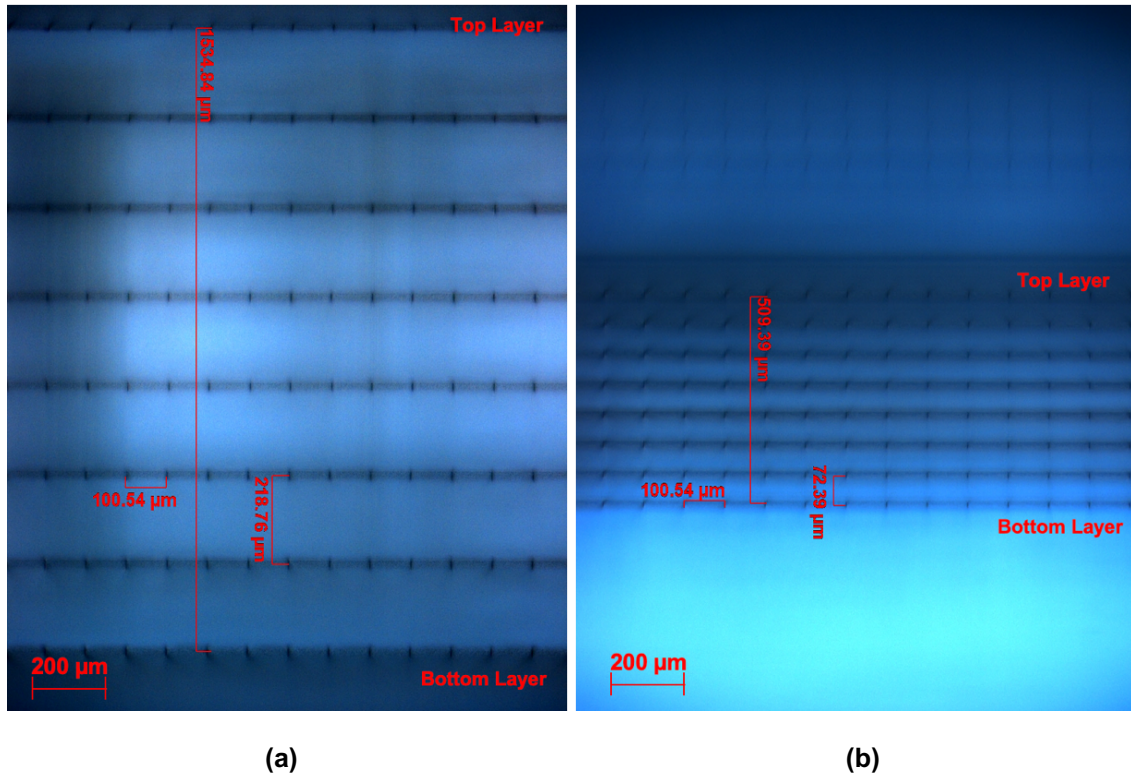
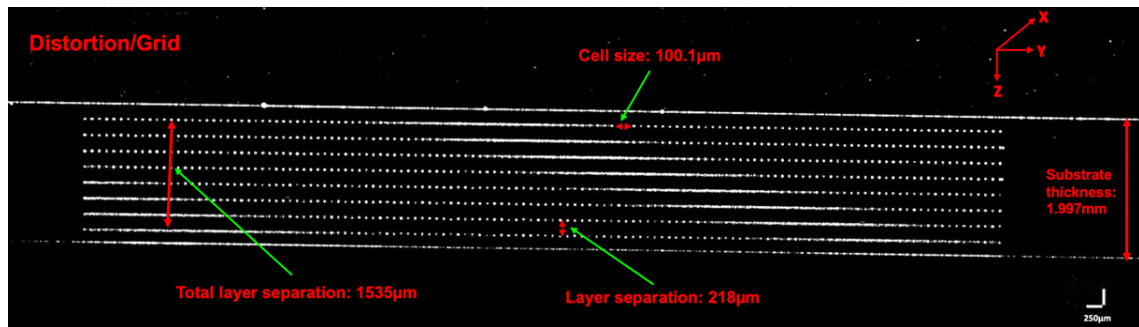


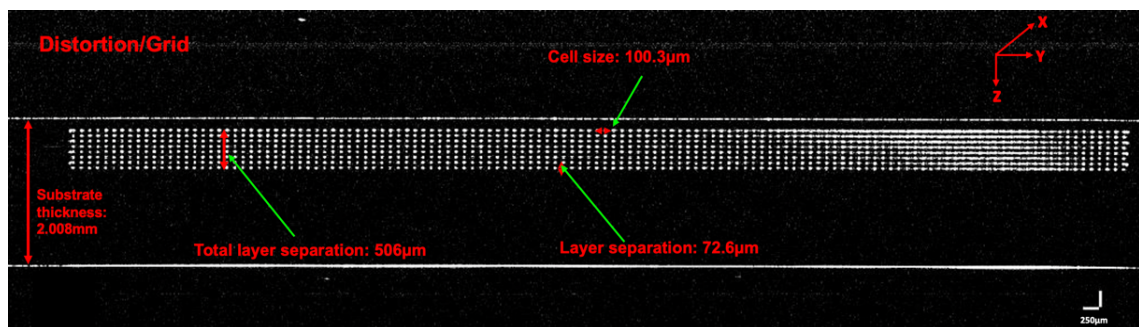
Figure 5-23. The microscope image using a 5x objective lens showing the cross-sectional profile of the distortion/grid phantom: (a) the current phantom design with a larger layer depth (i.e. 150 μm in AD setting for the layer separation) with the cell size measured as 100.54 μm , the layer separation measured as 218.76 μm in RD and a total inscription depth measured as 1534.84 μm ; (b) the previous phantom design with a smaller layer depth (i.e. 50 μm in AD setting for the layer separation) with the cell size measured as 100.54 μm , the layer separation measured as 72.39 μm and a total inscription depth measured as 509.39 μm .

5.3.4.2 OCT characterisation

Figure 5-24 shows the OCT scan image for both the new design shown in Figure 5-24(a) and the original design shown in Figure 5-24(b). It can be seen that as the distortion/grid pattern was similar to the PSF phantom apart from having the inscription in both the vertical and horizontal direction. However, as the phantom structure, it tends to be more difficult to align the phantom without getting interference and back reflection (i.e. those solid lines showing in both images). The distortion of an OCT system can be measured by analysing and comparing with the current image to a standard non-distorted image. Here, as the design parameter is known, it can be compared with the measured data to identify whether the OCT image is distorted or not. For example, if all the gaps between the dots are similar or identical, it means the OCT system is not distorted.



(a) The OCT image of the distortion/grid phantom with a greater layer separation (new design) with a scan size of $\sim 16\text{mm} \times 6.6\text{mm}$. The OCT measurement shows the cell size of $100.1\mu\text{m}$, the layer separation of $218\mu\text{m}$ and a total layer separation depth of $1535\mu\text{m}$.



(b) The OCT image of the distortion/grid phantom with a smaller layer separation (previous design) with a scan size of $\sim 14\text{mm} \times 4.53\text{mm}$. The OCT measurement shows the cell size of $100.3\mu\text{m}$, the layer separation of $72.6\mu\text{m}$ and a total layer separation depth of $506\mu\text{m}$.

Figure 5-24. OCT images for the distortion/grid phantom showing both (a) the current design with a greater layer separation and (b) the previous design with smaller layer separation in order to make a comparison and present the change in design. Both the OCT images were taken by Optimec is830 SD-OCT system. The measurement values indicated in the image are showing in real depth (RD).

5.3.5 Further discussions

The phantom inscription size has been optimised to ensure a consistency of the structure by using different laser pulse energies at different desired depths to compensate the loss of the laser power when travelling to a deeper depth inside of a material. For the current design, the starting laser attenuator position was set to 20% for the first layer and 55% for the deepest layer for all PSF, lateral resolution and the distortion/grid phantom.

The sensitivity pattern was inscribed from 5% to 100% of the total average laser output power. However, one thing should be noted is that when the pulse energy was at very low levels (i.e at 10% or below based on the present power measurement as the laser power might be varied over time), the energy level can only be sufficient to do the surface inscription. The laser energy is not able to make a visible inscription or modify the local

refractive index, therefore, it cannot be seen under both the microscope and the OCT system.

5.4 Chapter conclusions

In conclusion, the optimised OCT phantom has been presented with a new fabrication/inscription method, the total inscription depth has expanded by over 3 times with the total inscription depth reaching to almost 2mm. With varying the laser power for different depths, the inscription dimension can be well controlled so that even at a deeper depth, it can still be consistent and uniform. The optimised fabrication process also enables a highly repeatable and accurate finish so that it can be easily manufactured. This work can significantly benefit the future phantom fabrication.

Chapter 6

Non-planar OCT calibration phantom

This chapter presents the research work on the development of a novel non-planar OCT calibration phantom, which includes two published conference papers on the first two non-planar OCT phantoms that were proposed to be used as a potential multipurpose OCT system calibration tool. The first non-planar phantom (Section 6.2) was fabricated and later reported at the 2018 at Photonics West conference, where the design was based on a grid pattern to test the image distortion and was the first phantom demonstrated in a non-planar (i.e. plano-convex) lens to prove the idea that a curved phantom can be used as a self-referencing and comparison tool for OCT systems. The second non-planar phantom (Section 6.3) was designed, fabricated and later reported at the 2020 at Photonics West conference, which addressed alignment issues seen with the initial phantom due to the grid patterns require high level of alignment to the nearest 90° angle. The third non-planar phantom (Section 6.4) was an upgraded version based on the same pattern design but with the layer energy setting refined so that the inscription would exhibit a consistent layer thicknesses for every single layer, and it also reduces the effect of the laser beam filamentation. In addition, the results of an inscription attempted from the curved surface are given in Section 6.5 to illustrate the fabrication challenges with non-planar substrates and the resulting distortion caused by the curvature of the lens.

Some of the work presented in this chapter (Section 6.2 & Section 6.3) was undertaken in collaboration with Dr. Neil Gordon, Mr. David Robinson, Dr. Benjamin Coldrick, Dr. Vladimir Mezentsev, Dr. Francesco Menduni, Dr. Izzati Ibrahim, Dr. Antonio Fratini and Prof. Kate Sugden. The design, writing the CNC code and the phantom fabrication were undertaken by the thesis author under the supervision from Prof. Kate Sugden and the consultation from Dr. Neil Gordon. The OCT data was taken by Dr. Francesco Menduni who contributed to the first conference paper and Dr. Benjamin Coldrick who contributed to the second conference paper and the newer version of the OCT phantom. The co-authors got involved with the characterisation and results analysis for the fabricated phantom. Some texts and images presented in this chapter have been reproduced from previous published conference papers [92] [93] with the publisher's permission.

6.1 Introduction

In recent years, OCT systems have been intensively used in the biomedical and medical fields to assist with the diagnosis of diseases such as glaucoma [195]. However, there is no ubiquitous standard that can be used to calibrate and assess the performance of different OCT systems and there is a requirement for multi-purpose OCT phantoms to act as a three-dimensional optical ruler.

Previously, various methods of making OCT phantoms have been presented to assess the OCT system such as nanoparticle-embedded PSF phantom [15]. However, all these fabrication methods result in planar phantoms that do not fulfil the requirements of those systems designed for measuring curved structures such as contact lenses. Coldrick et al. demonstrated the measurement capability of using an OCT system (the Optimec is830 system) to measure and inspect curved surfaces (i.e. contact lenses), however, the system would further benefit from a large-area calibration method [154].

To address this and building on the previous work from [9], a novel OCT calibration phantom has been inscribed in a plano-convex lens using direct femtosecond laser writing technique. The phantom can simulate the curvature of a contact lens and be used to test the validity of post-processing techniques. The use of a plano-convex lens (rather than a convex lens) is important because it allows the calibration pattern to be written through the non-distorting flat face of the lens and then viewed/used through the distorting curved face.

Moreover, imaging distortion is also a big challenge for imaging systems (i.e. OCT systems). Having image distortion limits OCT system when used for quantitative

morphological imaging [172]. If there is a device/calibration tool that can be not only used to assess the performance of the OCT systems, but also to act as a diagnosis tool for validating the post-processing algorithms for correcting the image distortion, it will provide useful information for the OCT system developer and those OCT end users.

In this chapter, three versions of non-planar phantoms have been presented with each phantom has been characterised by the same optical microscope (Axioscope 2 MOT Plus, Zeiss) and OCT systems (Optimec is830 SD-OCT system). Two other OCT systems were used to compare the system performance (Thorlabs Ganymede OCT and Carl Zeiss Cirrus HD-OCT 5000) by using the same phantom. The femtosecond laser system was used to fabricate the phantom using a direct laser writing technique. All the phantoms presented in this chapter were inscribed with a 100x objective lens (Mititoyo Mplan Apo NIR) that has a NA of 0.5 which results of a spot size of $\sim 2\mu\text{m}$. The phantom was inscribed on a plano-convex lens (LA4380, Thorlabs) made of fused silica with a refractive index of 1.461 at the wavelength of 530nm. This lens has a central thickness of 3.8mm and 2mm for the edge thickness.

6.2 Non-planar grid-like OCT phantom

6.2.1 Phantom design and fabrication

A grid-like phantom was inscribed on a plano-convex lens as shown in Figure 6-1 using a direct femtosecond laser writing technique. A non-linear multi-photon absorption process occurs when there is an interaction between the focused laser beam and the material, which induces refractive index changes. The average power of the laser was set to 188mW (i.e. 20% of the total energy level) which results in 1880nJ per pulse and therefore, a peak pulse power of 3760kW.

The inscribed pattern consisted of a series of X and Y lines that make up a $100\mu\text{m}$ grid in a plane parallel to the flat surface of the lens. The size of the inscription was set to 25mm x 25mm in order to cover the entire lens area. The first grid is located at $150\mu\text{m}$ in apparent depth (AD) below the flat side of the lens which has a real depth (RD) of $219.15\mu\text{m}$ calculated as $150\mu\text{m} \times 1.461$ (fused silica refractive index at the wavelength of 532nm). The sample was then moved $50\mu\text{m}$ (in AD) in the Z direction and the grid pattern replicated and this process was repeated until there were 8 layers of $100\mu\text{m}$ grid patterns in total. To avoid scattering from pre-written lines, the inscription process starts from the lowest layer which is located at $500\mu\text{m}$ in the apparent depth (AD) below the

surface or $730\mu\text{m}$ below the surface in the real depth (RD). This process enables each layer to be clearly inscribed.

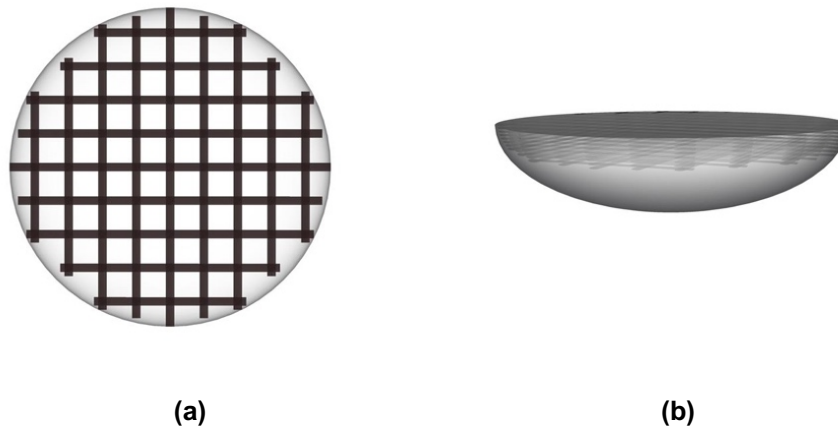
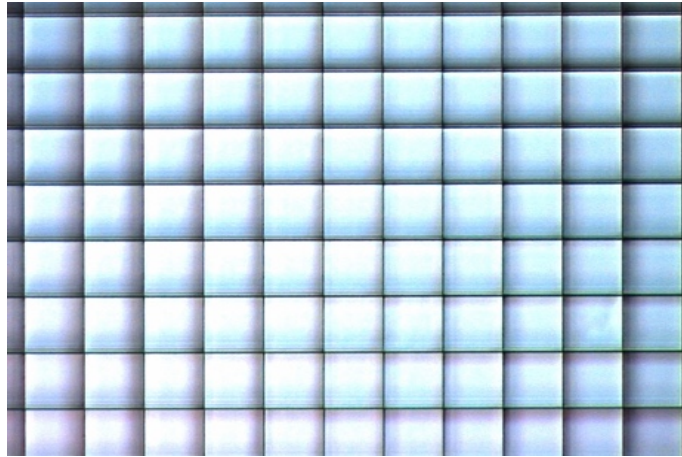


Figure 6-1. Conceptual drawings of the OCT phantom pattern: (a) the view from the top; (b) the view from the side.

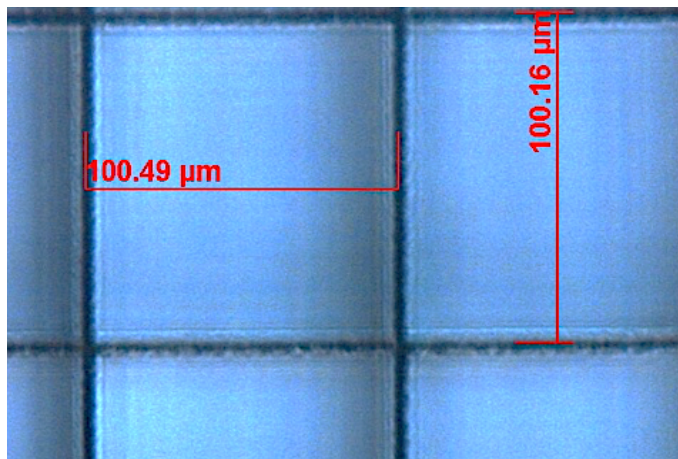
Alignment is a big challenge when placing the plano-convex lens on the CNC stage of the laser system, due to the difficulty in determining whether the planar side of the lens was parallel to the CNC stage. To overcome this challenge, three equidistant points close to the edge of the lens were focused upon to ensure the lens was flat. An alignment validation program performed a series of inscriptions to verify the alignment, ensuring that the flat side of the lens was parallel to the XY axis of the translation stage. Minor adjustments were then made on the sample's alignment using both software control and the manual adjustments of a goniometer stage. The process was repeated until the surface was suitably flat.

6.2.2 Results and discussions

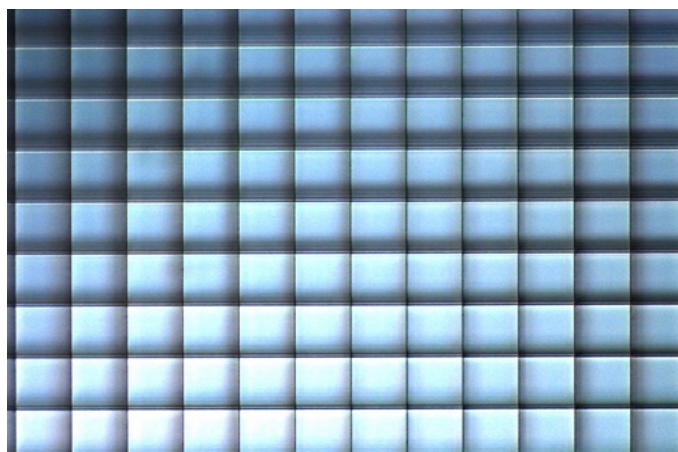
The phantom was characterised first using an optical microscope (Axioscope 2 MOT Plus, Zeiss). Example microscope images are shown in Figure 6-2. Figure 6-2(a) shows an image taken with a 5x objective lens from the planar side of the phantom, and Figure 6-2(b) is a close-up of this using a 20x objective lens and gives the dimensions of the cell under inspection showing a cell size of $\sim 100\mu\text{m} \times 100\mu\text{m}$. Figure 6-2(c) shows the image taken from the curved surface which shows the defocusing of the grid towards the outer edges of the image due to the effect of the lens curvature.



(a)



(b)



(c)

Figure 6-2. (a) Microscope image using a 5x objective lens from the planar side of the phantom, (b) the OCT phantom grid pattern cell size measurement using a 20x objective lens and giving the cell size of $\sim 100\mu\text{m} \times 100\mu\text{m}$, (c) the view from the curved side of the phantom.

Figure 6-3 shows that 5 points (labelled as point 1-5) were selected around 4 edges and 1 central point at the flat side of the plano-convex lens by using the 20x objective lens. The design parameters and the measured values (shown in Table 6-1) closely match each other, which verifies the accuracy of fabrication process.

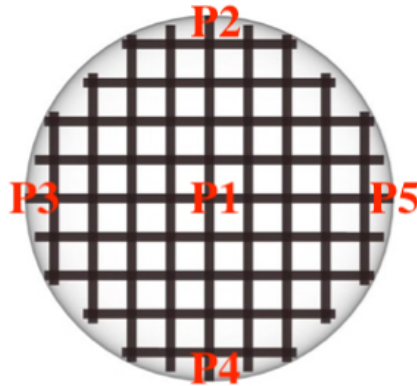


Figure 6-3. Microscope measurement points on the plano-convex lens.

Layer No.	Point 1	Point 2	Point 3	Point 4	Point 5	Measured Values (Average of 5 points)	Design Parameters
1	152.133	142.953	152.439	156.111	146.625	150.052	150
2	207.57	199.563	206.958	207.57	196.095	203.551	200
3	261.324	250.002	264.027	266.883	246.789	257.805	250
4	312.12	300.084	315.078	317.016	296.055	308.071	300
5	362.916	352.257	364.191	368.73	348.126	359.244	350
6	411.264	400.146	418.149	417.282	399.177	409.204	400
7	460.377	447.474	463.998	464.763	448.239	456.97	450
8	508.674	495.006	511.785	511.071	494.904	504.288	500

Table 6-1. Microscope measurement (measured in μm) datasheet for the OCT phantom to show the alignment and the flatness of the surface when fabricating the sample.

A comparison between design parameters and measured values is given in Figure 6-4, it can be seen that with the error tolerance considered, those two lines of the design parameter and measured value almost overlap each other, which demonstrates a high accuracy for the fabrication process and the characterisation process after the phantom has been fabricated.

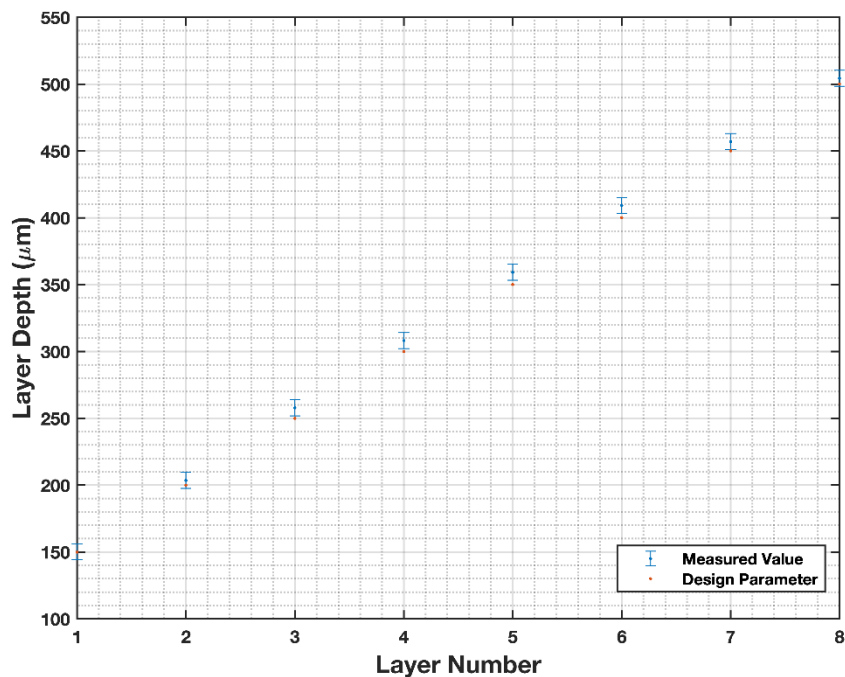
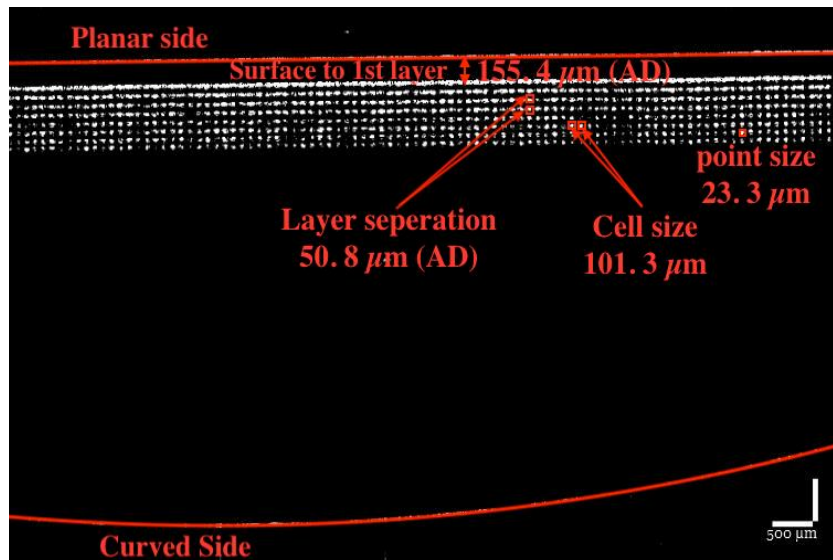
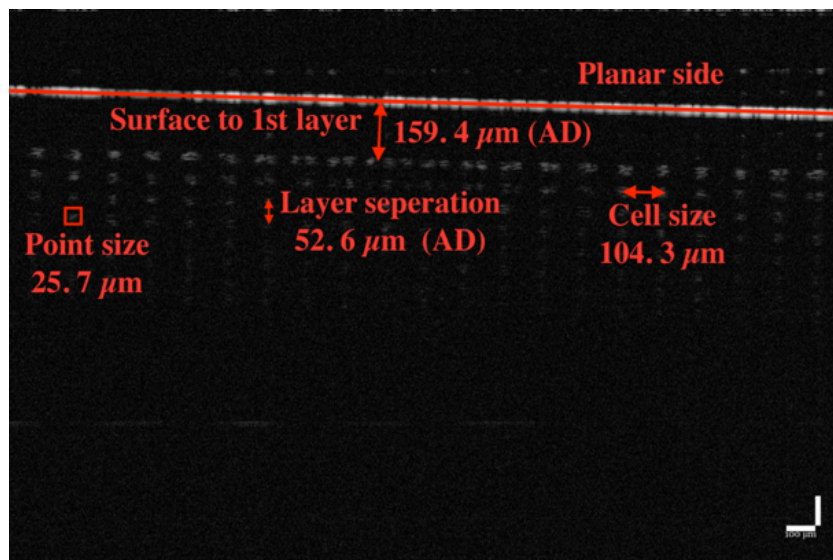


Figure 6-4. Comparison of design parameters and measured values from the optical microscope of the OCT phantom design. Measurements are all based on apparent depth (AD).

Subsequent to microscope-based measurements, the phantom was characterised using the two SD-OCT systems. The images taken from those two OCT systems are shown in Figure 6-5(a) and (b). Both OCT images consistently match the design parameters and microscope measurements (the OCT image data was measured in pixels and converted back to a micrometre scale). The Thorlabs Ganymede OCT system has a better axial resolution of $5.8\mu\text{m}$ (in air) (the image scaling bar in Figure 6-5(b) is $100\mu\text{m}$) and yields a more precise measurement than the Optimec is830 OCT system, which has an axial resolution of $12\mu\text{m}$ (in air) (the image scaling bar in Figure 6-5(a) is $500\mu\text{m}$). However, the Optimec is830 provides a larger field of view and has a better sensitivity which could provide a higher contrast image.



(a)



(b)

Figure 6-5. OCT images obtained from (a) the Optimec is830 system with a scan size of $\sim 12\text{mm} \times 5.6\text{mm}$ and (b) Thorlabs Ganymede SD-OCT system with a scan size of $\sim 4\text{mm} \times 1.9\text{mm}$ for comparison with design parameters and between OCT systems with annotations.

The summarised measurements from both OCT systems are listed in Table 6-2. These images were taken from the planar side of the OCT phantom.

OCT system model	Optimec is830 SD-OCT	Thorlabs Ganymede SD-OCT
Image scaling	500 μm	100 μm
Surface to 1st layer (AD)	155.4 μm	159.4 μm
Layer separation (AD)	50.8 μm	52.6 μm
Grid cell size	101.3 μm	104.3 μm

Table 6-2. OCT system characterization and comparison of OCT systems results.

Figure 6-6 and Figure 6-7 show the OCT images of the phantom taken from the curved side of the lens. It can be seen that cross-section of the grid lines looks wider. Images from both sides of the lens could be used to confirm the validity of the post-processing algorithms since the pattern should look the same in both directions after correction. Figure 6-6 was acquired using the Thorlabs Ganymede OCT system. The cross-section of the grid pattern is expanded due to the curvature of the lens, and the point size measured in this distorted image appears to be $\sim 47.8\mu\text{m}$. This is approximately 2 times as large as the non-distorted image which was determined from Figure 6-5(a) to be $\sim 23.3\mu\text{m}$.

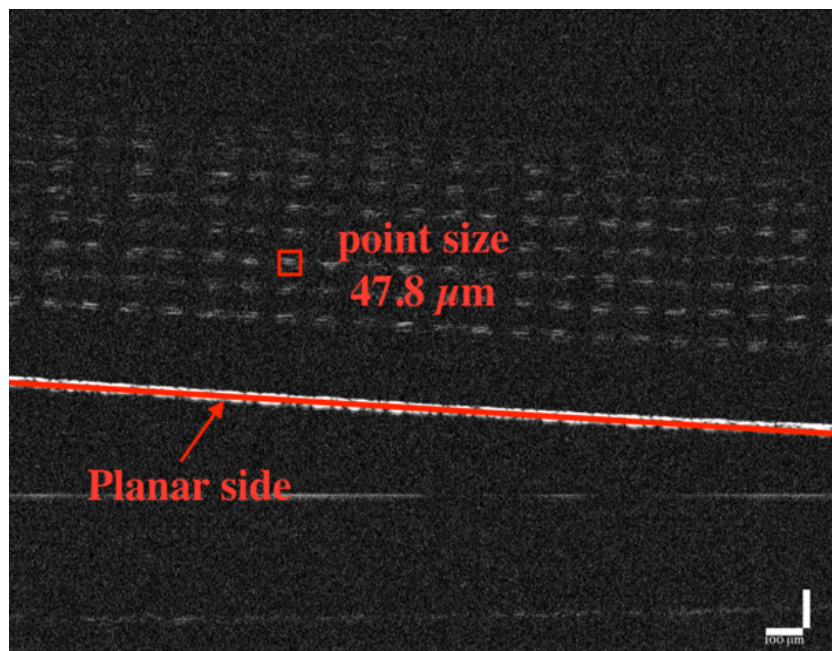


Figure 6-6. OCT image taken from the curved side (by using the Thorlabs Ganymede SD-OCT with a central wavelength of 930nm and an axial resolution of 5.8 μm).

In Figure 6-7, taken with the Optimec is830 system, it can be seen that the cross section of the grid and the planar surface at the bottom of the image appears to be bending. This shows that the distortion from the curved surface is present and therefore suitable post processing of the image is required to correct for such distortion.

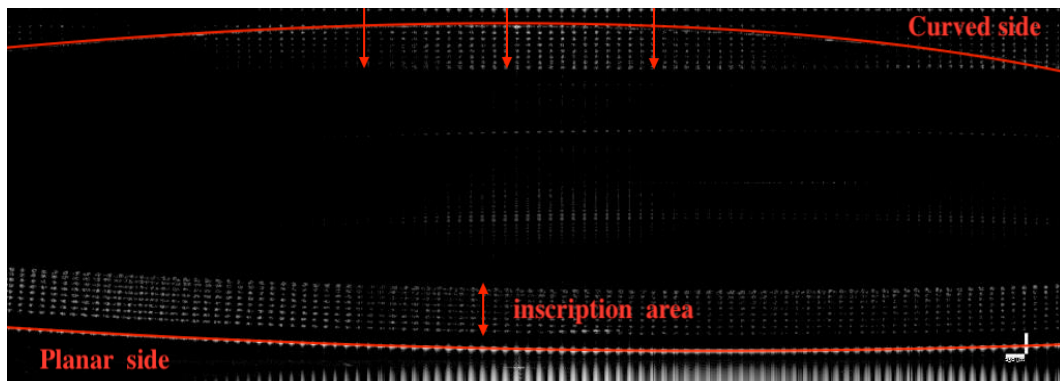


Figure 6-7. OCT image taken from the curved side (by using the Optimec is830 system with a central wavelength of 830 nm and an axial resolution of 12 μ m).

6.2.3 Further discussions

The grid cell size was set to 100 μ m x 100 μ m for the phantom pattern. Under the optical microscope, the fabricated structure can be clearly seen under both a 5x and 20x objective lens. However, under both OCT systems for the same phantom, the images are quite different. In Figure 6-5(a) the OCT image taken by the Optimec is830 system, the first layer of the pattern appeared as a line rather than the individual dots. When imaging the phantom under a higher resolution OCT system, although the dots are no longer jointed together, it seems that there is a misalignment in the centre of the OCT image shown in Figure 6-5(b) taken by Thorlabs Ganymede SD-OCT that the separation between dots are not identical. This demonstrates how the phantom can not only calibrate the individual OCT system but also can be used to compare performance across different OCT systems by being used as a reference target.

6.2.4 Section conclusions

In this section, a multifunctional non-planar OCT calibration phantom was inscribed in a plano-convex shape substrate. With using a planar-convex lens, the phantom can be used for multiple purposes. With the planar side, a non-distorted standard phantom can be used to calibrate the OCT system while with the non-planar side, the phantom can be used to assess and validate the post-processing algorithm for the image distortion correction. It can benefit for both the researcher and end-user to calibrate their systems.

Most importantly, the phantom can be easily reproduced with a highly repeatable and accurate fabrication method as an optical calibration device by using a femtosecond laser system.

6.3 Non-planar circle-like OCT phantom

6.3.1 Introduction

Previously, a non-planar grid-like OCT phantom inscribed in a plano-convex lens was successfully used to demonstrate a multi-purpose calibration phantom. However, there were some issues with the design relating to the angular alignment when imaging under an OCT system. The grid-like phantom requires a higher degree of alignment in terms of the angle of the sample when placing under the OCT system. It can be seen in Figure 6-8(a) that the grid phantom requires either a perfect horizontal or vertical scanning position such that the separation between dots can be identical. However, if the phantom is misaligned (shown in Figure 6-8(b)), the test results can be significantly affected as the separation between dots are no longer identical so that it will be difficult to assess the OCT system performance. Moreover, without the guideline, it will be difficult to guide the user with the test location. Therefore, a new phantom pattern is needed to overcome this angular issue with a landmark layer designed to guide the test location that can be potentially used to quantitatively correct the distortion.

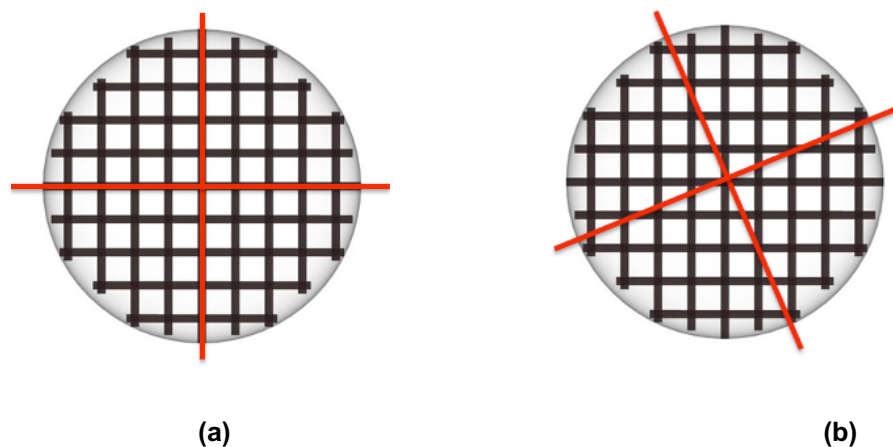


Figure 6-8. The alignment requirement for the grid-like phantom: (a) Top-view of the grid pattern phantom with red lines indicating aligned scanning position; (b) Top-view of the grid pattern phantom with red lines indicating misaligned scanning position.

6.3.2 Phantom design and fabrication

To resolve the issues described above, a new circle-like pattern was designed. The circular phantom pattern conceptual diagram is shown in Figure 6-9, which consists of one landmark layer located at $50\mu\text{m}$ (in apparent depth (AD)) below the surface and 8 layers of the test pattern where the first layer is located at $150\mu\text{m}$ (in AD) below the surface and each layer has a separation of $150\mu\text{m}$ so that in total the inscribed depth reaches $1200\mu\text{m}$ (in AD, so that the real depth (RD) is $\sim 1753.2\mu\text{m}$ ($1200\mu\text{m} \times 1.461$ (the refractive index of fused silica at the wavelength of 532nm) = $1753.2\mu\text{m}$). A set of radial lines is inscribed in the landmark layer that have an angular separation of 45 degrees. This design enables the end user to easily control the location of the phantom relative to the field of view of the OCT system and overcome the orientation challenges observed with the previous grid pattern.

The circular pattern is inscribed on each layer in this phantom design. Each layer includes a set of 40 circles with increasing radius (i.e. a radius difference of $254\mu\text{m}$), where the radius range varies from 0.254mm to 10.16mm . Due to the power loss when penetrating to deeper layers, each layer is inscribed with different laser powers between 40% and 100% of the total laser output power, where 40% of the laser power was used to inscribe the top layer and 100% of the laser power was used to inscribe the deepest layer. The laser power difference for each layer is identical, with the aim of obtaining a consistent linewidth for each layer. The pattern was inscribed on a planar-convex fused silica lens which has a central thickness of 3.8mm and an edge thickness of 2mm . The moving speed for the stage was set to 4mm/s and the writing speed was set to 1mm/s .

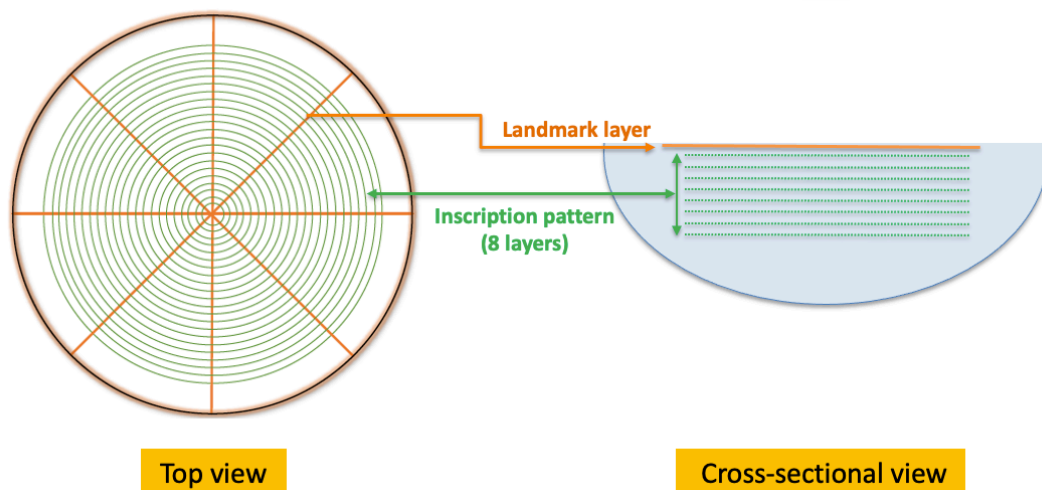


Figure 6-9. Conceptual diagram for the non-planar circle-like phantom with the top view and the cross-sectional view showed.

Alignment is always a challenge when placing a sample on the CNC stage to ensure its flatness, especially for a non-planar substrate which increases the difficulty. Four equidistant points on the planar side of the substrate were chosen to assist the alignment. A CCD camera was used in this alignment process to determine the focus position along with the adjustment through both software control of the CNC stage and the manual adjustment of a goniometer base. To ensure a high degree of alignment of the sample, a software program was designed to inscribe various minor marks to verify the surface and the alignment. The alignment is adjusted until at least three points on the edge were focused at the same position, at which point the alignment process is completed and the fourth point can be used to verify the alignment. The program was set to start at the center of the surface. The laser inscription was started from the lowest layer (i.e. the deepest layer) to avoid scattering caused by modified regions.

The phantom design was initially tested and fabricated in a planar substrate shown in Figure 6-10(a) and then extended to a non-planar phantom shown in Figure 6-10 (b). This illustrates that a highly simple and repeatable one-step fabrication process can be employed by using a femtosecond laser system.

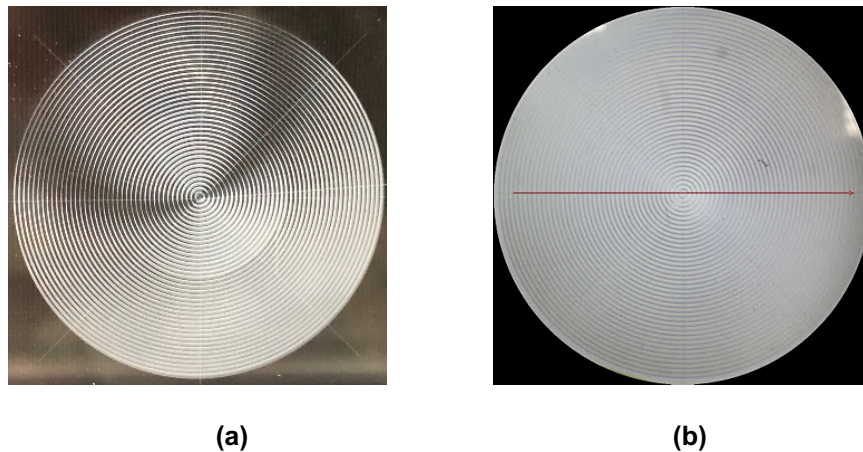


Figure 6-10. Phantom design pattern: (a) the pattern initially tested and fabricated in a planar substrate; (b) the pattern fabricated in a curved lens (LA4380, Thorlabs) viewed under an OCT system (Optimec is830 SD-OCT system).

6.3.3 Results and discussions

Both an optical microscope (Axioscope 2 MOT Plus, Zeiss) and an OCT system (Optimec is830) were used to characterise the OCT phantom. The microscope measurement provided information on the linewidth of the inscription in the XY plane which is parallel to the translation stage, and the layer depth for the Z-axis while the OCT system provided a cross-sectional image or a depth profile of the phantom. The

comparisons between the setting parameters and the measured parameters of the layer depth are presented in Figure 6-11 to show the accuracy of the laser fabrication.

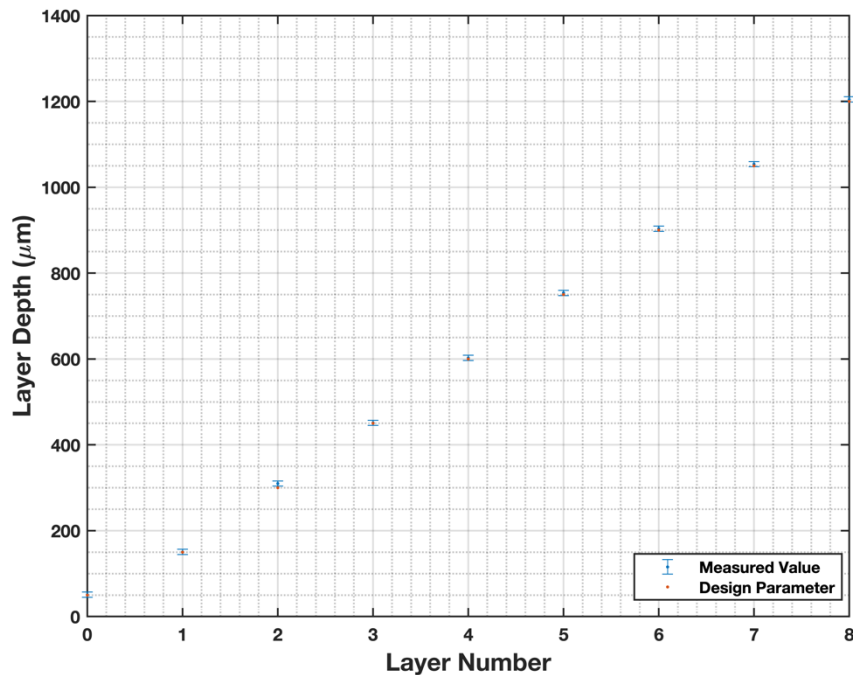
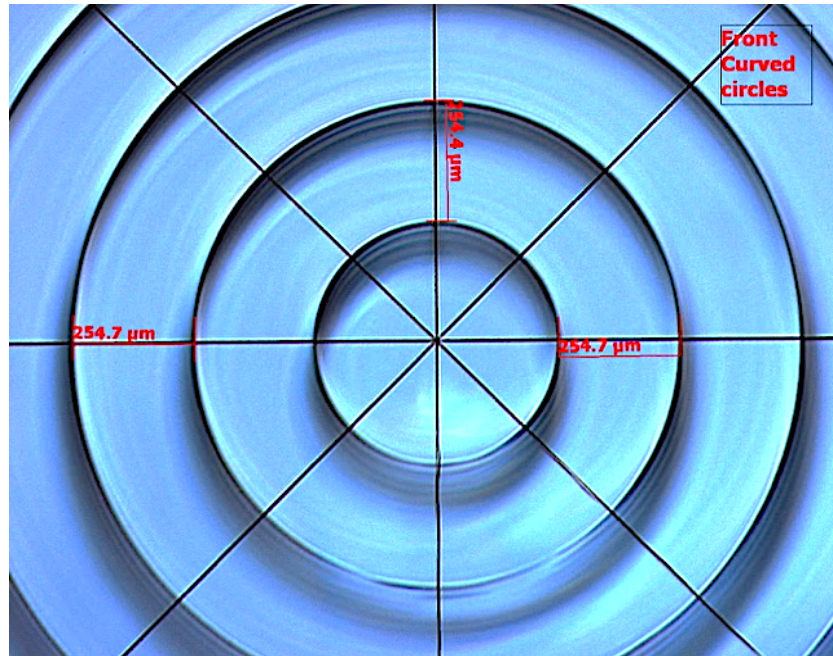


Figure 6-11. The comparison of design parameter values and measured values from the microscope measurement of the OCT phantom by using a 20x objective lens. The layer depth is in apparent (measured) depth (AD).

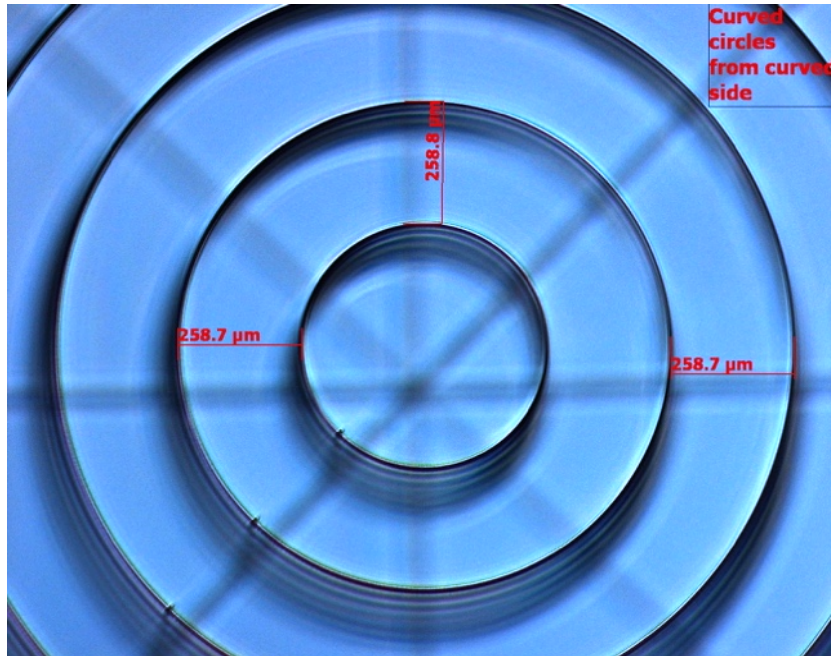
It can be seen that there is a high degree of alignment accuracy so that the measured values are almost identical to the designed value (with $\pm 2\mu\text{m}$ error tolerance) (i.e. the landmark layer was set to $50\mu\text{m}$ below the planar surface and the measured value of the landmark layer depth was $\sim 50.945\mu\text{m}$).

The microscope images taken using a 5x objective lens are shown in Figure 6-12(a) and (b) which Figure 6-12(a) was taken from a planar surface and Figure 6-12(b) was taken from a curved surface of the phantom. Figure 6-12(a) shows that there is high degree of agreement between the design value (i.e. $254\mu\text{m}$ between each circle) and the measured value for the spherical radius (i.e. $\sim 254 \pm 1\mu\text{m}$ between each circle). Figure 6-12(b) shows a microscope image when viewing the phantom from the curved surface. It can be seen that the radius difference between each circle is $\sim 258\mu\text{m} \pm 1\mu\text{m}$, a $4\mu\text{m}$ difference to the measurement taken from the planar surface. This may be due to the curvature of the lens distorting the image slightly, however, the separation is consistent for each circle indicating that the sample is not misaligned.

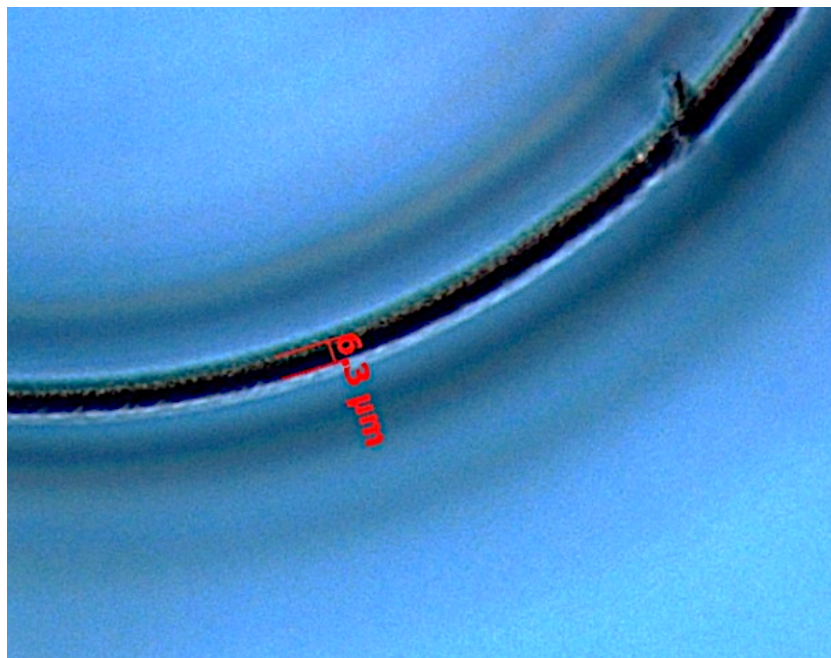
Figure 6-12(c) and (d) show the linewidth in the XY plane via an optical microscope was measured. The microscope image was acquired using a 20x objective lens taken from the planar side at the 5th layer (at 752.485 μm in AD below the planar surface) showing a linewidth of 6.3 μm . Figure 6-12(d), the microscope image was captured by using a 20x objective lens taken from the planar side at the 7th layer (at 1054.252 μm in AD below the planar surface) showing a linewidth of 6.3 μm . Therefore, varying the laser power was successful in ensuring that the linewidth of the inscription is consistent for each layer.



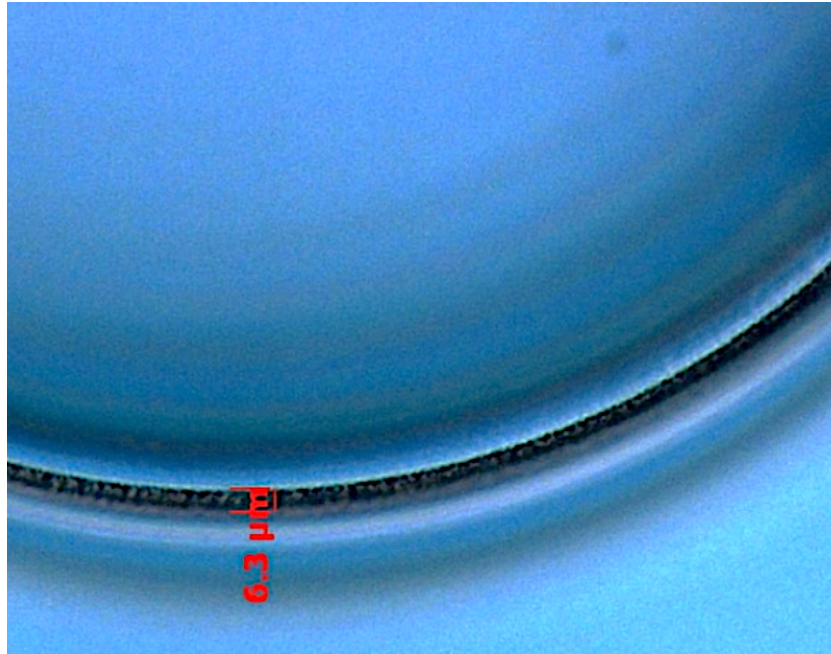
(a)



(b)



(c)



(d)

Figure 6-12. (a) Microscope image using a 5x objective lens taken from the planar side of the phantom; (b) microscope image using a 5x objective lens taken from the curved side of the phantom; (c) microscope image using a 20x objective lens taken from the planar side at the 5th layer (at 752.485μm in AD below the planar surface) showing a linewidth of 6.3μm; (d) microscope image using a 20x objective lens taken from the planar side at the 7th layer (at 1054.252μm in AD below the planar surface) showing a linewidth of 6.3μm.

Subsequent to the microscope characterisation, the phantom was then characterised using an OCT system (Optimec is830 system). Example images taken by this system are shown in Figure 6-13 and Figure 6-14 that verify the phantom design and illustrate its potential use as a calibration phantom. A solid line for the landmark layer (shown in yellow) indicates that the scan position went through the central point and parallel to a landmark line, this is helpful if using this phantom to correct the image distortion since it gives a known cross-sectional position. Figure 6-13 shows the view from the planar side of the phantom which is a non-distorted image. It be seen that the landmark layer and all eight layers of the pattern are clearly visible in the OCT image. The parameter measurement on the OCT image matches the designed parameters and the microscope measurements.

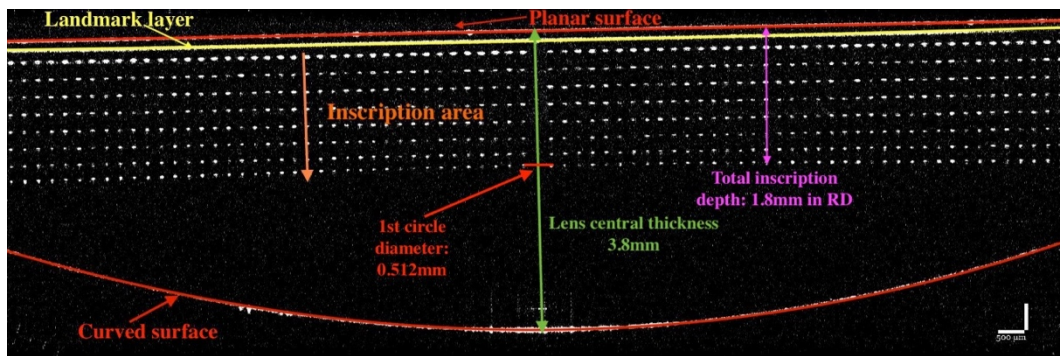


Figure 6-13. OCT image taken from the planar surface of the phantom. The scan pattern FOV is 19.00mm x 5.42mm. The scale bar is 500 μ m. The value indicated on this image is in real depth as the refractive index is applied.

Figure 6-14 shows an image taken from the curved surface of the OCT system. The pattern is distorted because of the curvature of the lens. For example, an ophthalmic application measuring a patient's eye, the OCT system would use a post-processing algorithm to correct the distortion, but this assumes a given curvature and refractive index of the lens. Moreover, the central area of this OCT image is much weaker compared with the image taken from the planar surface and the spot seems to be expanded vertically.

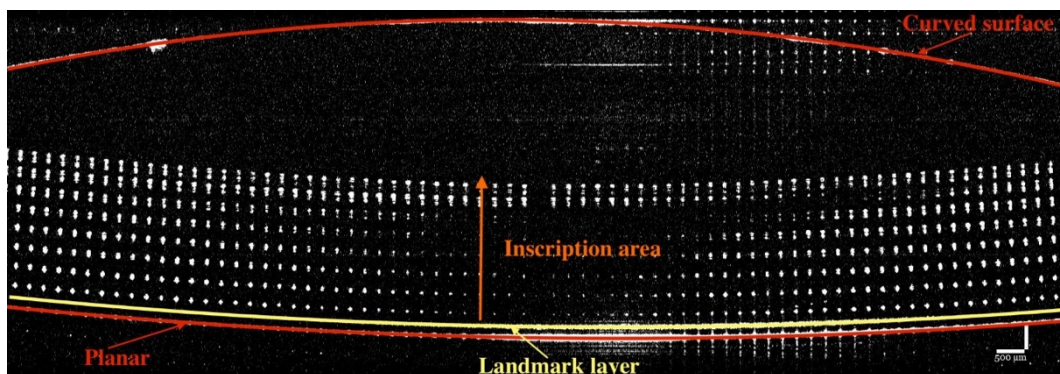


Figure 6-14. OCT image taken from the curved surface of the phantom. The scan pattern FOV size is 19.00mm x 5.42mm. The scale bar is 500 μ m.

6.3.4 Further discussions

A circle-like non-planar phantom has been developed to act as a multi-purpose calibration phantom. With the circular pattern, the angular issues that the grid-like phantom presented have been overcome and this improved the ease of the alignment process for scanning. Moreover, the landmark layer is designed and used to guide the scanning position. Although the laser energy was varied at every depth, at this time when developing this phantom, the focus was on the linewidth on the X-Y plane as with varied

laser pulse energy, the linewidth for each layer is fairly consistent. However, it can be noticed that the spot size showing under the OCT system is not consistent with the first layer showing a larger spot size but smaller size spots showing at deeper depths. This would affect the measurement of the separation between each spot as the separation between each spot needs to be used into the quantitative method to correct the distortion. Therefore, in order to keep the spot size consistency for both the linewidth and the inscription height for all the depth, a further optimisation on the fabrication will be beneficial for the quantitative method development.

6.3.5 Section conclusions

In summary, a spherical pattern with a landmark layer is used in a new phantom design. This phantom can be used to assess, characterise and calibrate the OCT system that are designed to measure non-planar samples. The spherical pattern overcomes the issues previously observed that were caused by the unknown alignment angle of the phantom when measuring the phantom with the OCT system. With this new phantom design, the post-processing image distortion correction can be validated since the landmark layer can confirm the exact location and orientation. The planar side can then provide a standard reference when comparing to the curved side. This phantom can be effectively applied to detect and potentially quantitatively correct the distortion based on a self-comparison method. By using the planar side as a standard reference (i.e. non-distorted image) and comparing it with the distorted image, any post-processing algorithms can be validated to ensure optimum system performance.

6.4 Optimised non-planar OCT phantom

6.4.1 Introduction

A non-planar circle-like OCT phantom was presented previously and demonstrated as a multi-purpose phantom. A quantitative method can be potentially developed based on the phantom. However, the consistency of the spot size is essential to the development of a universal calibration phantom as it could affect the measurement distance between each spot. After a detailed study on the laser power and the inscription size (discussed in Chapter 4), an optimised fabrication process has been proposed and applied to improve the phantom fabrication.

6.4.2 Phantom design and fabrication

The third phantom design is based on the optimised previous circular phantom where, in order to keep the consistency of the inscription size, the laser pulse energy settings have been further optimised based on the findings presented and verified in Section 4.5.

The phantom comprised of 8 test pattern layers and one landmark layer inscribed in total. The laser power range was set between 20%-55% of the total average output power with 20% was used to inscribe both the landmark layer and the first layer pattern. The inscription power was increased in 5% power steps as the depth increased, so that 25% of the laser power was applied to inscribe the second layer, then 30% for the third layer, 35% for the fourth layer and so on. The layer separation was the same as the previous circular phantom. The landmark layer was located 50 μm (in AD) below the planar surface with the first layer located at 150 μm (in AD) below the planar surface. There was a 150 μm (in AD) layer separation set between each test pattern layer. At each test pattern layer comprised of 40 circles with a separation set to 254 μm . The design was firstly tested on a planar fused silica substrate (shown in Figure 6-15(a) to inspect both the linewidth and the inscription height and then inscribed on a non-planar substrate (shown Figure 6-15(b)). The edge of the plano-convex lens (LA4380, Thorlabs) was coated therefore, it cannot be seen through to inspect the cross-sectional profile directly.

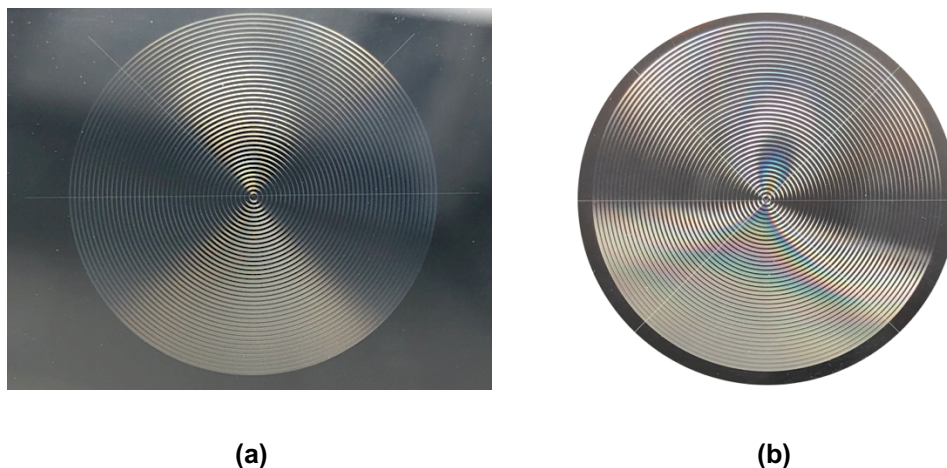


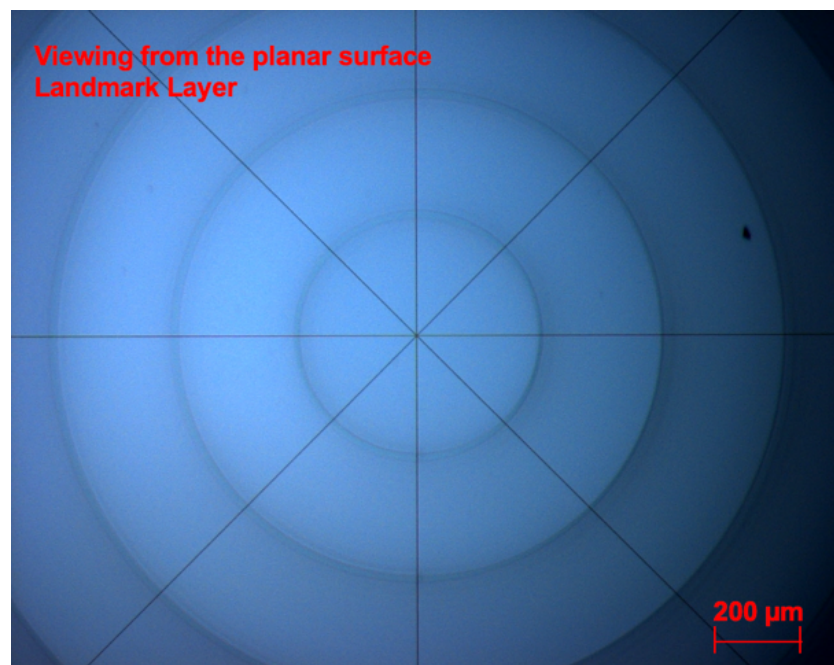
Figure 6-15. Femtosecond laser inscribed phantom: (a) the phantom design was initially tested on a planar substrate; (b) the phantom was then inscribed on a non-planar substrate.

6.4.3 Results and discussions

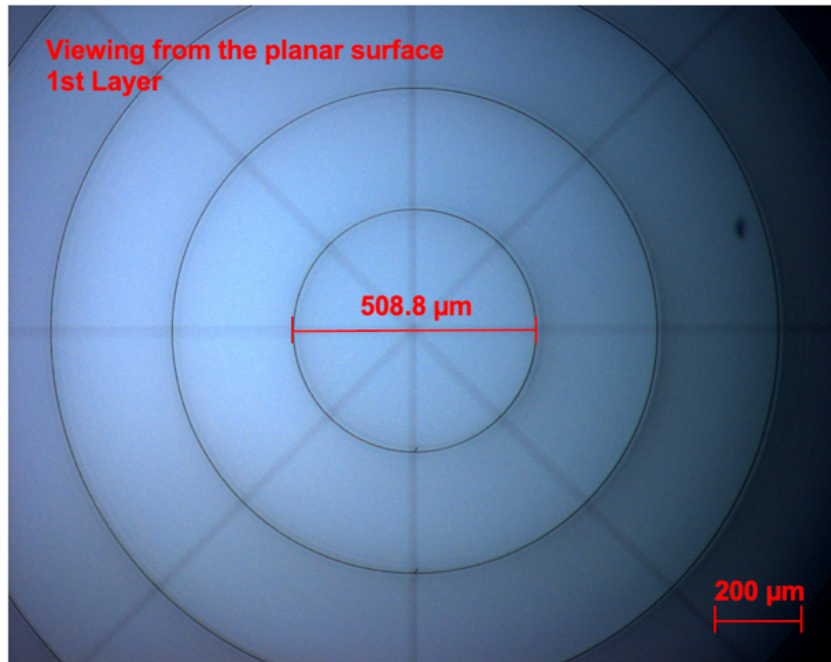
After the fabrication, the phantom was then characterised with an optical microscope (Axioskop 2 MOT Plus, Zeiss) and an OCT system (Optimec is830 system). A commercial OCT system (Carl Zeiss Cirrus HD-OCT 5000) was used to validate the

phantom and compared the performance with the other OCT system. For the microscope, both a 5x objective lens and a 20x objective lens were used. The 5x objective lens was used to inspect the overall inscribed pattern and the cross-sectional profile. The 20x objective lens was used to measure the linewidth and the distance between each circle. Both OCT systems were used to inspect the cross-sectional profile of the phantom.

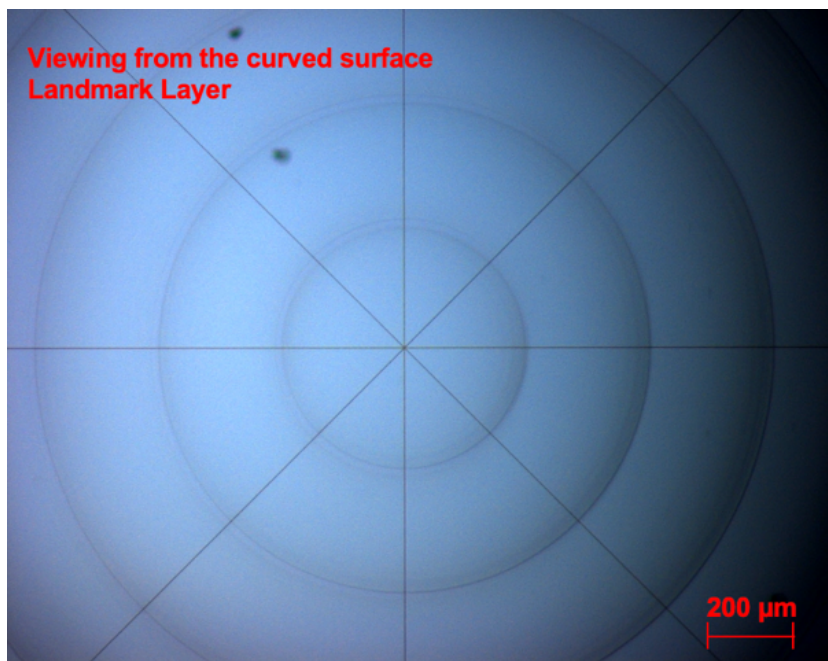
Both the planar surface and the curved surface were inspected under a 5x microscope objective lens to show the landmark layer and the first pattern layer. Figure 6-16(a) and (b) were viewed from the planar surface while Figure 6-16(c) and (d) were viewed from the curved surface. The diameter for the first circle was measured as $\sim 508.8\mu\text{m}$ viewed from the planar surface (a non-distorted image) and $\sim 521.44\mu\text{m}$ viewed from the curved surface (a distorted image due to the curvature of the lens). It can be seen there is a difference of $\sim 12.6\mu\text{m}$ presented for the diameter, although the same pattern layer was inspected. Therefore, it illustrates the impact of the image distortion when measuring through a non-planar surface.



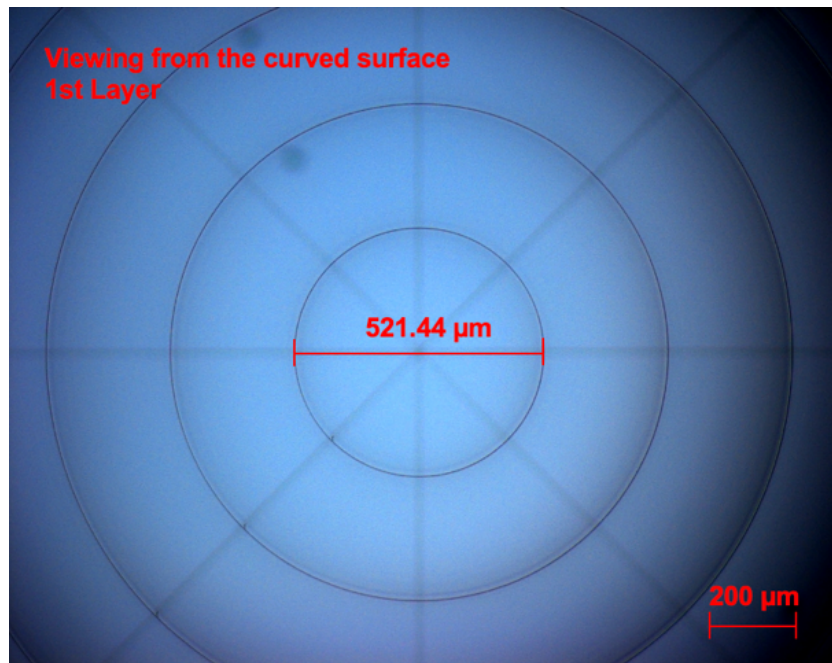
(a)



(b)



(c)



(d)

Figure 6-16. Microscope images using a 5x objective lens showing the landmark layer and the first test pattern layer: (a) the landmark layer viewing from the planar surface; (b) the first test pattern layer viewing from the planar surface with the diameter of the 1st circle measured as 508.8μm; (c) the landmark layer viewing from the curved surface; (d) the first test pattern layer viewing from the curved surface with the diameter of the 1st circle measured as 521.44μm.

Figure 6-17 shows a microscope image of the landmark layer using a 20x objective lens. The landmark consists of radial lines with angular spacing of 45-degree. Figure 6-18 show the microscope images of the linewidth measurement at different depths. It can be seen from Figure 6-18(a) to (d) that the linewidth for different depths is consistent, which were measured as $\sim 2.6 \pm 0.3 \mu\text{m}$ across all the depths.

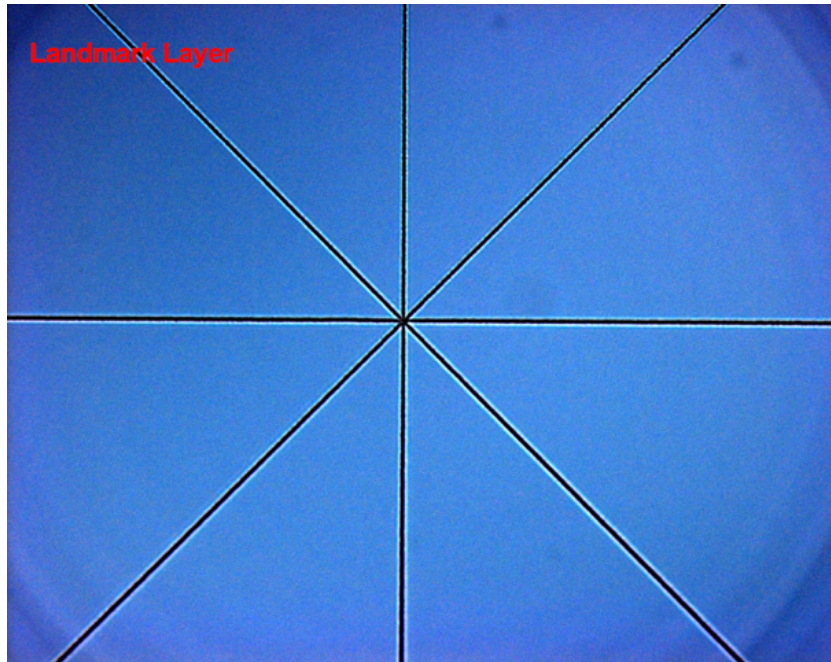
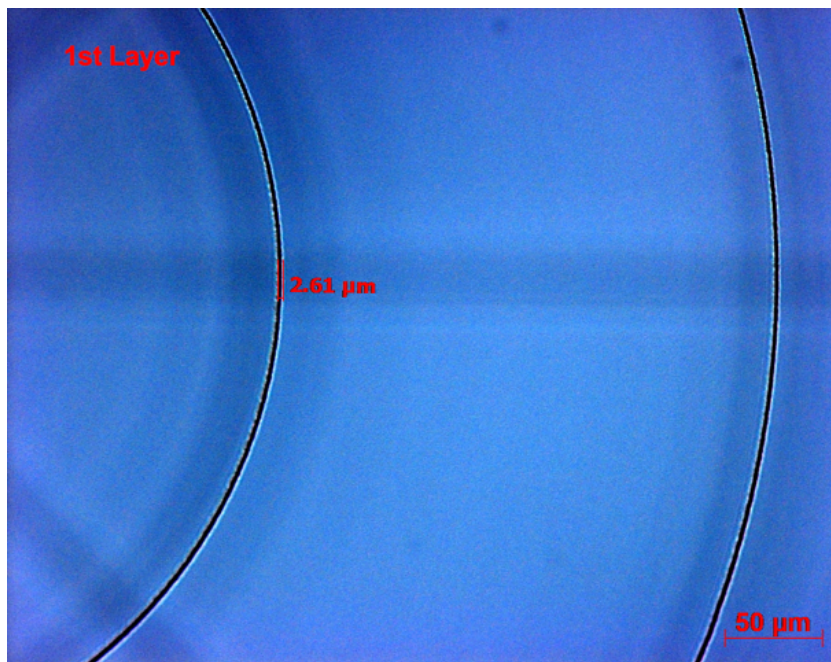
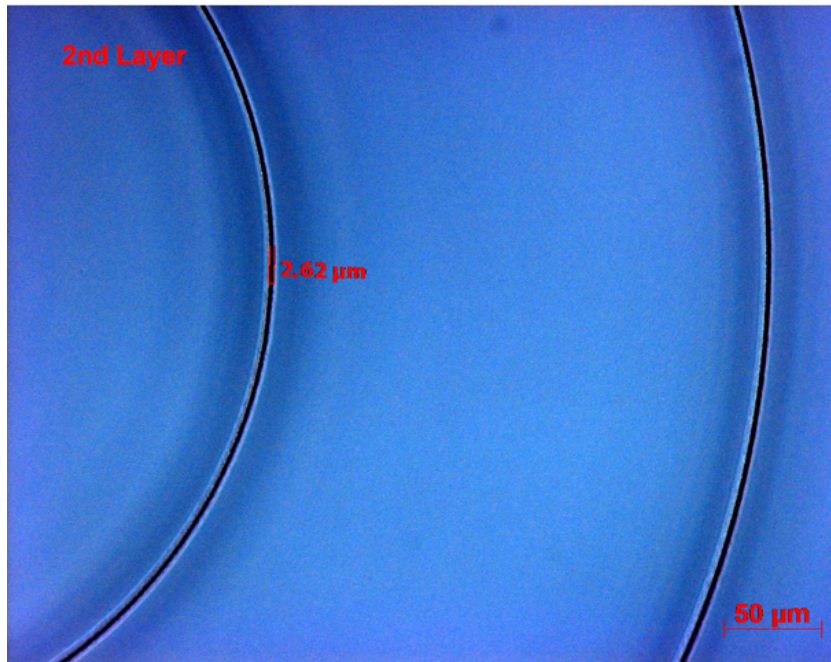


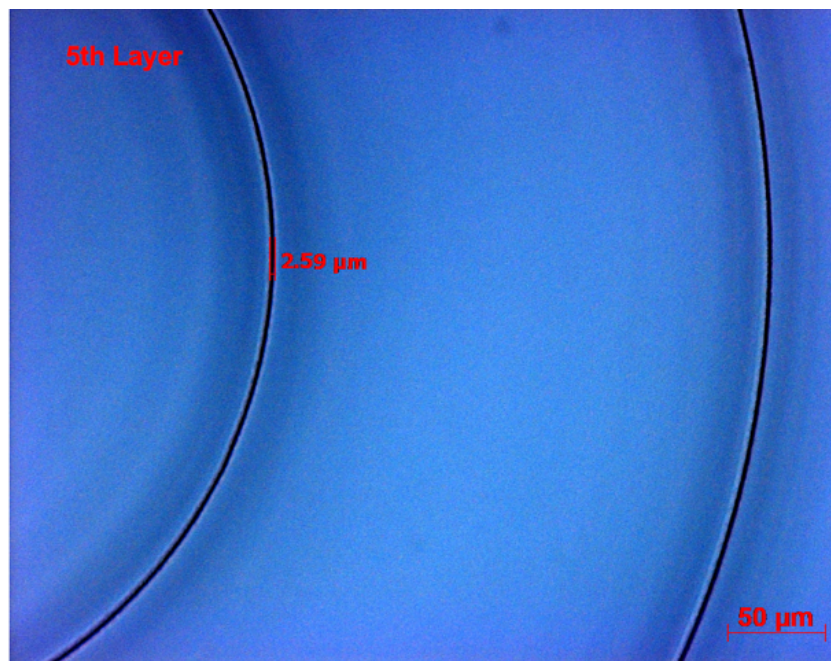
Figure 6-17. The microscope image using a 20x objective lens showing the landmark layer.



(a)



(b)



(c)



(d)

Figure 6-18. Microscope images using a 20x objective lens showing the linewidth measurement for different depths: (a) the linewidth measured as $2.61\mu\text{m}$ for the 1st layer located at depth of $150.603\mu\text{m}$ (in AD); (b) the linewidth measured as $2.62\mu\text{m}$ for the 2nd layer located at depth of $301.002\mu\text{m}$ (in AD); (c) the linewidth measured as $2.59\mu\text{m}$ for the 5th layer located at depth of $753.831\mu\text{m}$ (in AD); (d) the linewidth measured as $2.64\mu\text{m}$ for the 8th layer located at depth of $1204.62\mu\text{m}$ (in AD).

Figure 6-19 shows a microscope image of the cross-sectional view of the phantom that was inscribed in a planar substrate and fabricated using the same parameter settings. The layer separation was measured as $\sim 219.84\mu\text{m}$ (in real depth (RD)) and the circle separation measured as $\sim 254.69\mu\text{m}$ which matches the designed value and the measurement shown in Figure 6-16(b). As previously mentioned, the edge of the non-planar lens is coated, hence, it is not possible to view the cross section of the lens with microscope. Therefore, the planar substrate is used for a reference. With the optimised power setting, both the linewidth and the inscription height can be kept consistent with similar sizes across all the layers. A summary for all the key parameters is presented in Table 6-3.

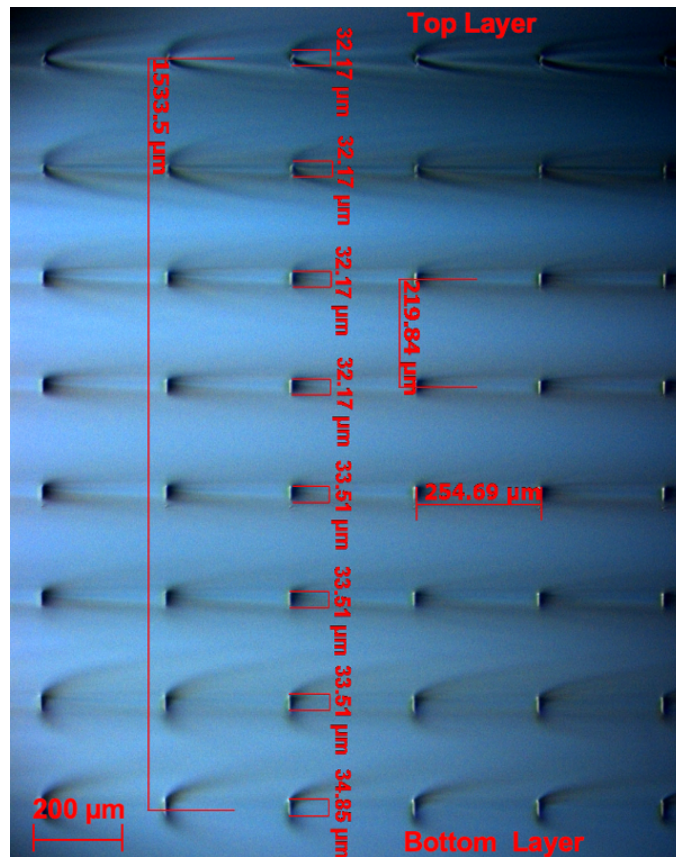


Figure 6-19. The microscope image showing the cross-sectional view of the circular phantom inscribed in a planar substrate fabricated using the same parameter settings with the inscription height measured. The layer separation was also measured as 219.84 μm (in real depth (RD)) and a circle separation measured as 254.69 μm .

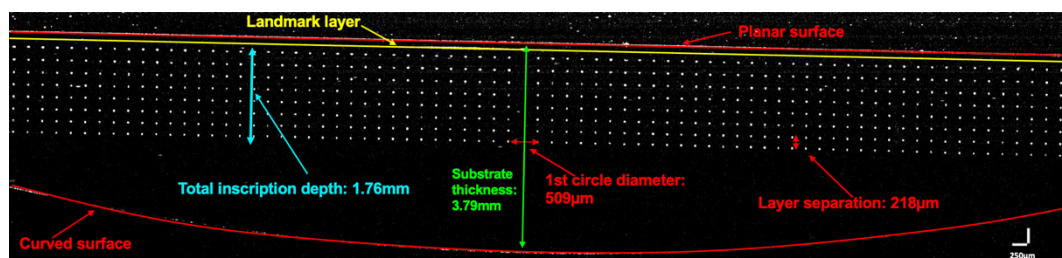
Layer No.	Design Parameters (μm)	Measured Values (μm)	Inscription Linewidth (μm)	Inscription Height (μm)
1	150	150.603	2.6	32.17
2	300	301.002	2.6	32.17
3	450	451.197	2.6	32.17
4	600	602.514	2.6	33.51
5	750	753.831	2.6	33.51
6	900	903.414	2.6	33.51
7	1050	1053.813	2.6	33.51
8	1200	1204.62	2.6	34.85

Table 6-3. Microscope measurement showing the comparison between the designed values and the measured value for the depth with the inscription linewidth and inscription height measured to show the consistency of the inscription size.

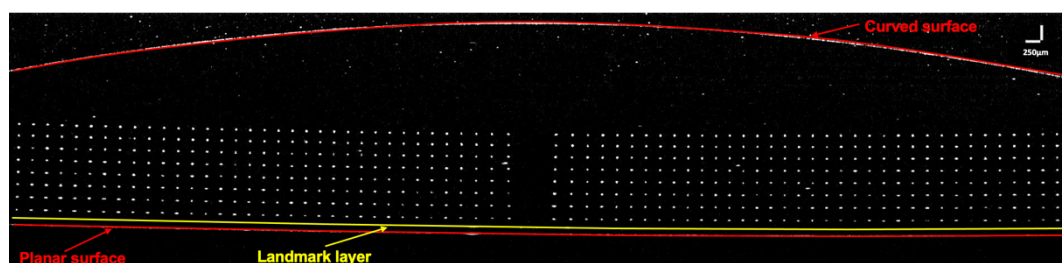
After the microscope characterisation, an OCT system (Optimec is830 system) was used to characterise and validate the phantom. In Figure 6-20, OCT images show the cross-sectional profile of the pattern with one image viewing from the planar surface (shown in Figure 6-20 (a)) and one image viewing from the curved surface (shown in Figure

6-20(b)). In Figure 6-20 (a), the central thickness was measured as $\sim 3.79\text{mm}$ which matches to the lens specification data of 3.8mm . The first circle diameter was measured as $\sim 509\mu\text{m}$ which is also showing agreement to the designed value of $508\mu\text{m}$. Therefore, the OCT measurement shows a strong agreement to microscope measurement and the designed parameter values. It can be seen from Figure 6-20 (b), due to the curvature of the lens, the inscription pattern was slightly bent compared with the image showing in Figure 6-20 (a), which means that the image is distorted, and the system has not corrected it.

In both images, all surfaces are marked in red with the landmark layer being marked in yellow. A solid landmark line indicates that the scanning position went through the centre of the phantom and it was parallel to the landmark line. However, either a solid line or a single dot in the centre can indicate that the scanning position goes through the centre. Moreover, with the laser power further optimised, the spot size is more consistent and uniform across all layers compared to the OCT image shown in both Figure 6-13 and Figure 6-14 for the previous version of the circle-like phantom.



(a)

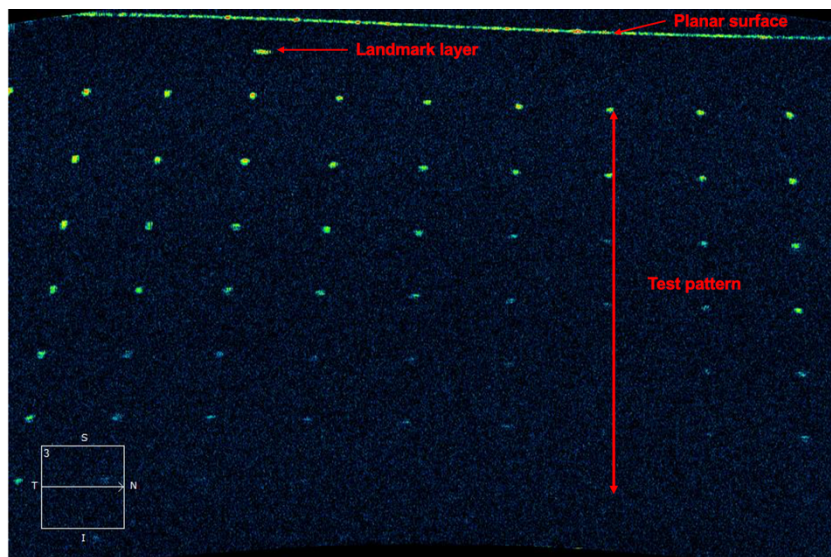


(b)

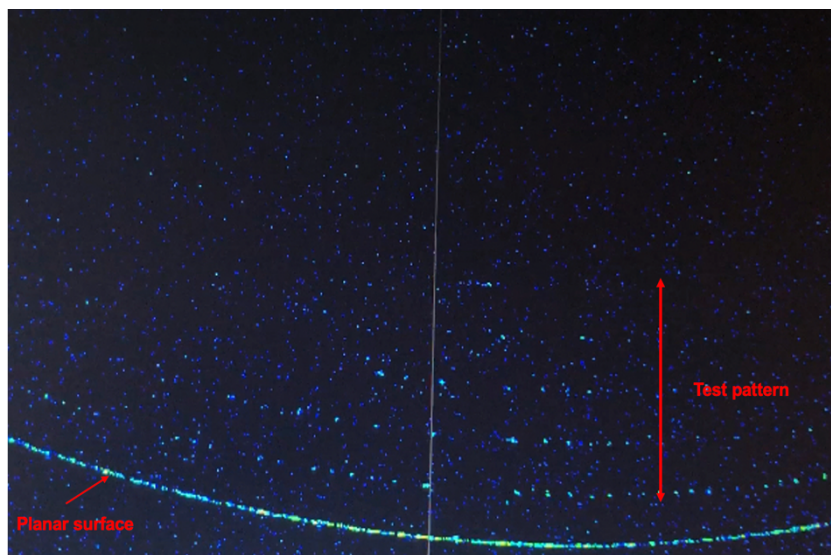
Figure 6-20. OCT Image taken by Optimec is830 SD-OCT system from both the planar surface (a) and the curved surface (b). The scan size is $19.00\text{mm} \times 4.55\text{mm}$ and the pixels size is 1900×512 pixel. The scale bar is $250\mu\text{m}$. The value indicated is in the real depth as the refractive index of 1.45 (at 830nm wavelength) is applied to the image.

After the OCT characterisation, the phantom was imaged under a commercial OCT system (Carl Zeiss Cirrus HD-OCT) to make a comparison. In Figure 6-21, OCT images are shown viewing from both surfaces, where Figure 6-21(a) presents the image viewing

from the planar surface and Figure 6-21(b) presents the image viewing from the curved surface. However, it can be seen that even viewing from a planar surface, the image shows that the pattern is bent compared with Figure 6-20(a) which shows as a straight line. This is because that most commercial OCT systems have pre-processing algorithm embedded to fit a curve (shown in Figure 6-22) such as mimicking the scleral curvature to the OCT system and correct for instrument-related optical distortion [123].



(a)



(b)

Figure 6-21. OCT images taken by a commercial OCT system (Carl Zeiss Cirrus HD-OCT): (a) viewing from the planar surface; (b) viewing from the curved surface.

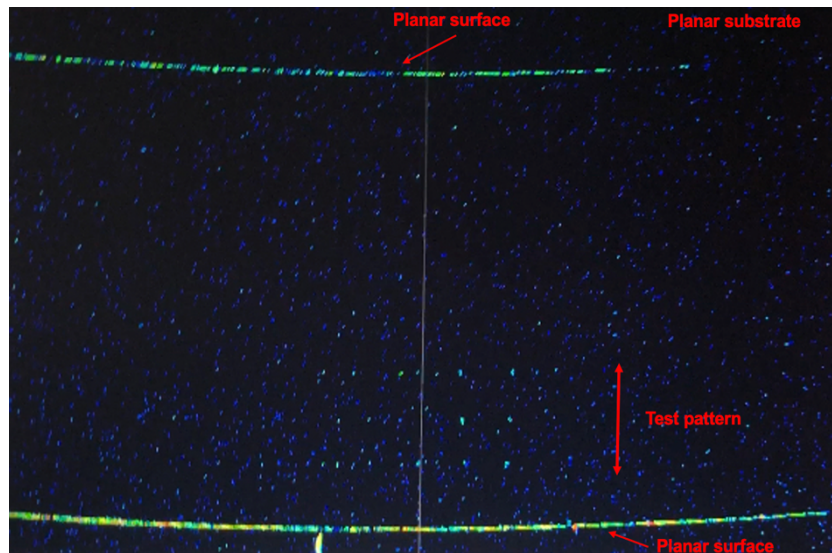


Figure 6-22. OCT image taken by Carl Zeiss Cirrus HD-OCT to show the pre-processing algorithm to fit a curve to the phantom.

6.4.4 Further discussions

For this optimised OCT phantom, the spot size is shown to be more consistent and uniform under the Optimec is830 OCT system. However, when imaging with a Carl Zeiss Cirrus HD-OCT system, there are few challenges seen. First of all, the system does not have a face-down stage that the sample can be placed like under a microscope. All the images taken was either hand-held or temporary positioned by a 3D printed holder. A customised phantom holder would help to capture a clear and still OCT image that can be used to perform further image analysis. However, for commercial OCT systems, they are usually fitted with a headrest that can limit the dimension of the holder. It was quite difficult to find the focus position and also the sample was tilted at a certain angle to avoid the interference. Those factors could affect the OCT image quality and the accuracy of the measurement results.

6.4.5 Section conclusions

In this section, an optimised non-planar circle-like OCT phantom has been developed that can potentially become a multi-purpose calibration phantom. With the consistent and uniform spot size, it would largely increase the measurement accuracy for analysing the OCT image. Moreover, it can be potentially used to develop the quantitative method that can be used to correct the distortion caused from the nature of curvature of a non-planar surface.

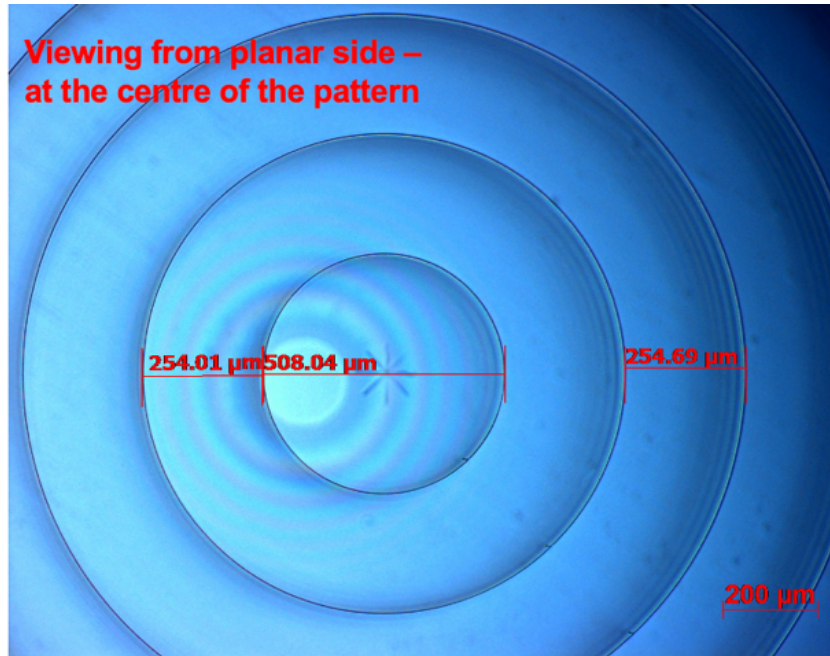
6.5 Inscription from a curved surface

After the inscription from a planar side, an inscription has been attempted from a curved surface to illustrate how significantly a curvature of a non-planar surface can affect both the fabrication and the imaging. The same fabrication process and parameter setting was used to fabricate this sample.

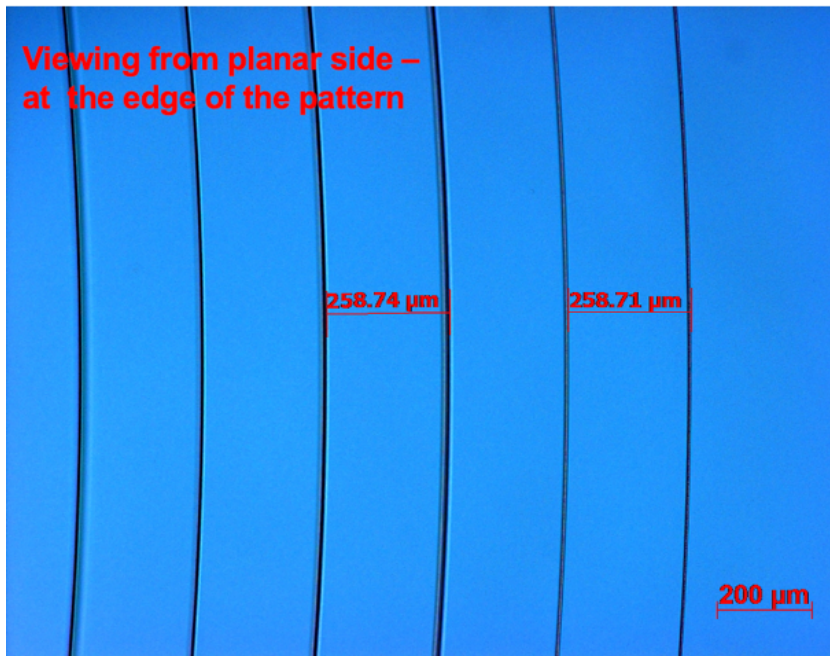
With regards to the lens alignment, as before, the central of the lens was marked and four orthogonal points on the edges were selected to be used for the flatness alignment. When three of the edge points was in focus, the fourth point was used to check. After that, the lens was fabricated and characterised using both the microscope (shown in Figure 6-23) and the OCT system (shown in Figure 6-24).

Figure 6-23(a) and (b) show the microscope image using a 5x objective lens viewing the inscription pattern from the planar surface, where Figure 6-23(a) shows the centre of the pattern and Figure 6-23(b) shows the edge of the pattern. It can be seen that the curvature doesn't have a significant effect to the fabrication compared with the edge of the lens where the curvature of the lens changed more sharply. The radius measurements of the first few circles were $254 \pm 1\mu\text{m}$, which matches to the designed parameter value. However, at the edge of the pattern, the radius tends to be slightly bigger measured as around $258 \pm 1\mu\text{m}$. Moreover, the inscription quality has been affected due to the curvature of the lens.

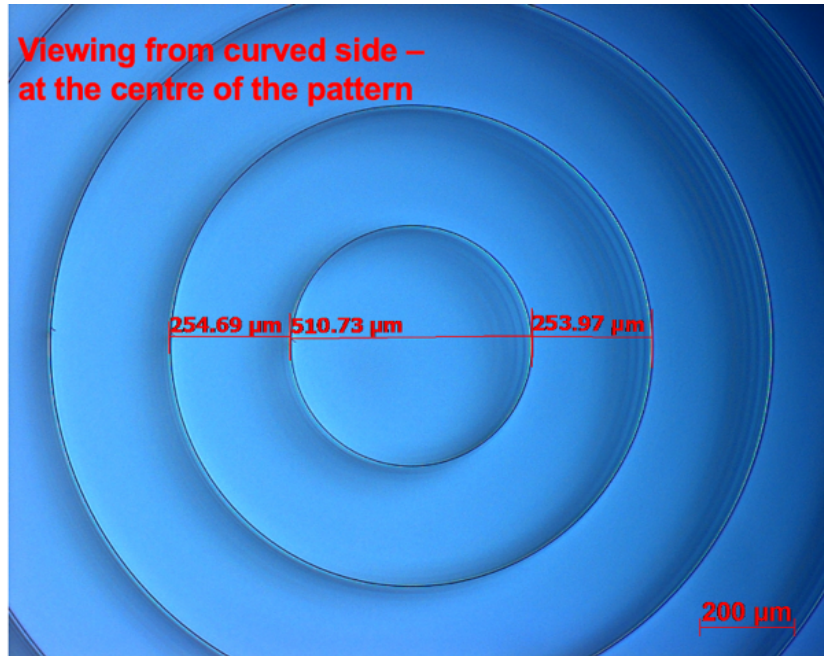
Figure 6-23(c) and (d) show the microscope image using a 5x objective lens viewing the inscription pattern from the curved surface, where Figure 6-23(c) showing the centre of the pattern and Figure 6-23(d) showing the edge of the pattern. It seems that the centre of the pattern is less distorted compared with the edge of the lens. However, as the laser inscribed from a curved surface, the optical path and the laser geometrical focus have been affected by the curvature of the lens. With the depth increasing, the spherical aberration would distort the inscription more significantly (as discussed in Section 4.4). A more distorted image would be therefore resulted if viewing from a curved surface.



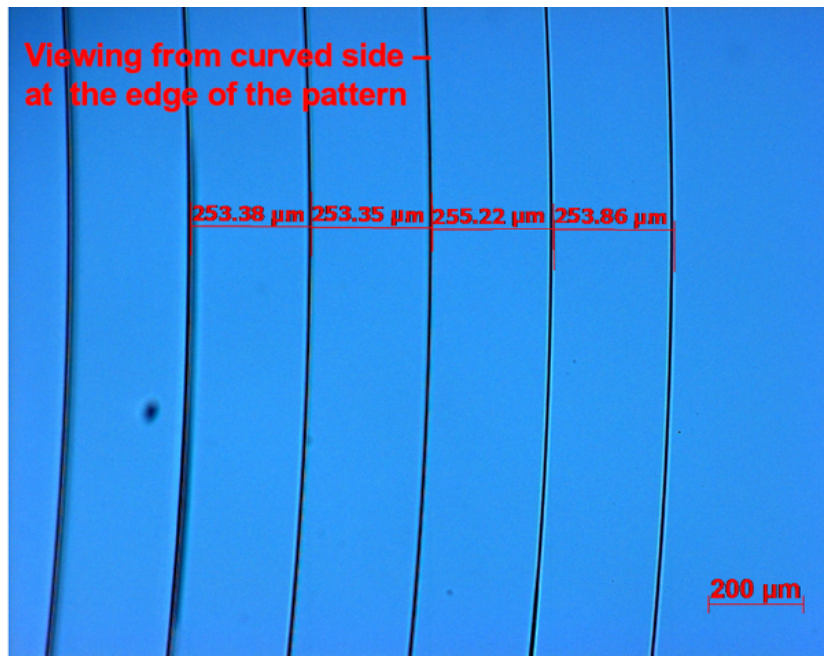
(a)



(b)



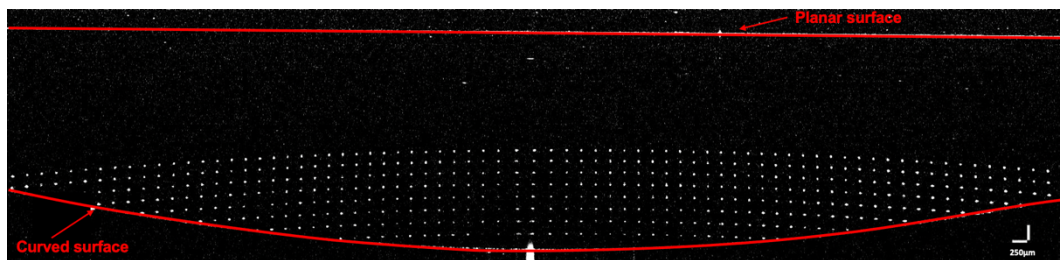
(c)



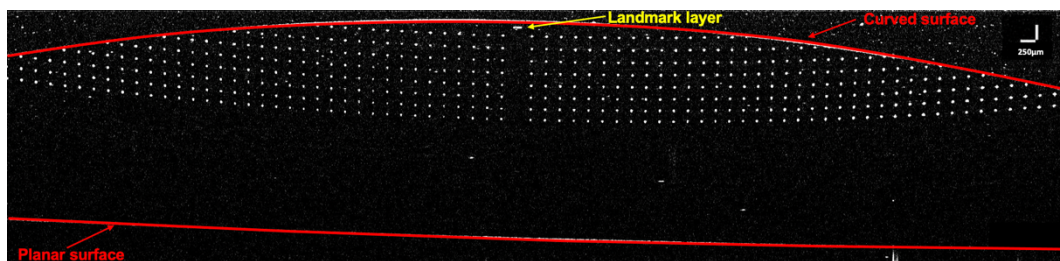
(d)

Figure 6-23. Microscope images using a 5x objective lens showing the inscription from a curved surface: (a) at the centre of the pattern viewing from the planar side with the measurement of the radius of $\sim 254 \pm 1 \mu\text{m}$; (b) at the edge of the pattern viewing from the planar side with the measurement of the radius of $\sim 258 \pm 1 \mu\text{m}$; (c) at the centre of the pattern viewing from the curved side with the measurement of the radius of $\sim 254 \pm 1 \mu\text{m}$; (d) at the edge of the pattern viewing from the curved side with the measurement of the radius of $\sim 254 \pm 1 \mu\text{m}$.

Figure 6-24 shows the OCT images taken by Optimec is830 system presenting the cross-sectional view of the inscription pattern. Figure 6-24(a) shows the image taking from the planar surface and Figure 6-24(b) shows the image taking from the curved surface. It can be seen that the pattern was bent due to the curvature of the lens, even viewing from the planar surface, which is due to the laser geometrical focus distorted by the curvature of the lens when fabricating from a curved surface. In Figure 6-24(b), the image was more distorted as it was viewed from a curved surface. Therefore, the inscription from a curved surface should be avoided as the curvature of the lens would significantly affect the laser geometrical focus and result in a distorted inscription.



(a)



(b)

Figure 6-24. OCT images taken by Optimec is830 system showing the inscription from a curved surface: (a) imaging from the planar side; (b) imaging from the curved side. The scan size is 19.00mm x 4.55mm and the pixels size is 1900 x 512 pixel. The scale bar is 250µm. The value indicated is in the real depth as the refractive index of 1.45 (at 830nm wavelength) is applied to the image.

6.6 Chapter conclusions

This chapter has presented three versions of the non-planar OCT calibration phantom. The use of the plano-convex shape of substrate enables the fabricated phantom not only to calibrate and assess the system performance but also to detect the system distortion, which makes the phantom a multi-purposes optical device. The grid-like phantom was firstly presented to demonstrate the use of the non-planar lens with the grid pattern inscribed to detect the system distortion. However, the grid pattern required a high degree of alignment when imaging under the OCT system. Therefore, the circle-like

phantom was then proposed and fabricated as it can overcome the angular issue that the grid-like phantom presented. In addition, the inscription depth has been extended so that the total inscription can reach to 1.8mm below the surface. The laser power parameter has been optimised to ensure a consistent and uniform inscription size to be maintained for all layers of the pattern. Moreover, a landmark layer was added so that to help to guide the test location but also it can be further used to develop a quantitative method to correct the distortion. Furthermore, fabrication was attempted from a curved surface to demonstrate the fabrication challenge and presented the distorted inscription caused by the curvature of a non-planar lens. Currently, the quantitative method for the image distortion correction is still under the development.

Chapter 7

OCT phantom application

This chapter presents the OCT phantom application for detecting OCT system scanning errors and provides a phantom-based method to correct the distortion caused by such errors. In Section 7.2, the scanning mechanism of the OCT system is briefly introduced. The phantom design, fabrication and characterisation is presented in Section 7.3. The image analysis and correction methods are described in Section 7.4 to indicate the use of the OCT phantom to detect the system scanning error and acting as a reference point to correct the image.

The content presented in this chapter is currently under collaborative preparation for a journal submission. The work has been carried out with Dr. Izzati Ibrahim, who developed the image processing algorithms, and Dr. Benjamin Coldrick, who collected the OCT data. Firstly, the phantom was designed, fabricated and characterised by the thesis author and then the phantom was sent to Optimec Systemes (Malvern, UK) to be validated under the Optimec is830 OCT system for the OCT images by Dr. Benjamin Coldrick and Dr. Izzati Ibrahim. Then the OCT images were analysed by Dr. Izzati Ibrahim with my help to understand the phantom design and parameter settings. After that, the correction method was discussed and carried out with Dr. Izzati Ibrahim for the image distortion correction. The work has been under the supervision from Prof. Kate Sugden and Dr. Antonio Fratini.

7.1 Introduction

For OCT imaging systems, there are two types of scanning system normally used that are galvanometer-based scanners [196] and microelectromechanical systems (MEMS) [197, 198] to scan across the sample. A galvanometer scanning system provides high resolution scanning at a very modest rate, but the size is quite large for compact OCT imaging systems. MEMS based scanning systems are smaller, lower in weight and able to provide higher rate of scanning than a galvanometer. Despite their advantages in enabling such imaging technology, all types of scanning systems can add distortion to the image due to irregularities in the scanning. The MEMS systems are usually driven with sinusoidal functions which can introduce significant distortion of images [196, 198]. The Optimec is830 OCT system equipped with a MEMS scanning system to capture the OCT image for the research study presented in this chapter. Work showing how a phantom can be used to capture an image of an object of known dimensions and then used to characterise the distortion and then correct for MEMS scanning errors will be presented.

7.2 Scanning mechanism

For an imaging system using a MEMS mirror for scanning, the scanning angle (θ) is given by:

$$\theta = \arctan\left(\frac{L}{S}\right) - \arctan\left(\frac{L + \Delta x}{S}\right)$$

Equation 7-1

where L represents the maximum scanning length along X-axis, S is the distance between the scanning point and the sample and Δx is the displacement of the scanning length in X-axis. The schematic diagram used to illustrate the scanning position using a MEMS mirror is shown in Figure 7-1.

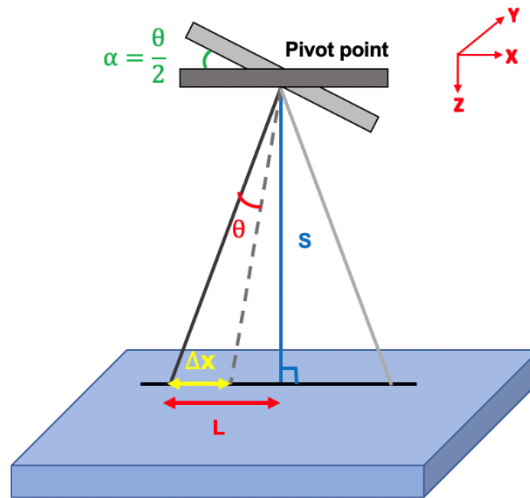


Figure 7-1. The schematic diagram showing the scanning position using a MEMS mirror.

The mirror is rotated at the pivot point, where the mechanical deflection angle (α) of the mirror is half of the optical scanning angle (θ). For a linear scanning system, the change in the X-axis (Δx) is linear with respect to the optical scanning angle (θ), therefore the Equation 7-1 can be rewritten as:

$$\theta = \frac{L}{S} - \left(\frac{L + \Delta x}{S} \right)$$

Equation 7-2

$$\theta = \frac{\Delta x}{S} \rightarrow \Delta x = S\theta$$

Equation 7-3

Errors in the scanning system will induce inaccuracies in Δx , leading to distortion on the OCT image [199, 200]. These errors may be caused by the non-uniformity of the driving force and the mismatch between the input current and the mirror-plate position and frequency [201]. During scanning, the mirror angle can be changed by controlling the input current that produces the torque that rotates the mirror [202-204]. The angular motion of the mirrors that deflect the light beam can be represented as continuous sinusoidal motion as shown in Figure 7-2.

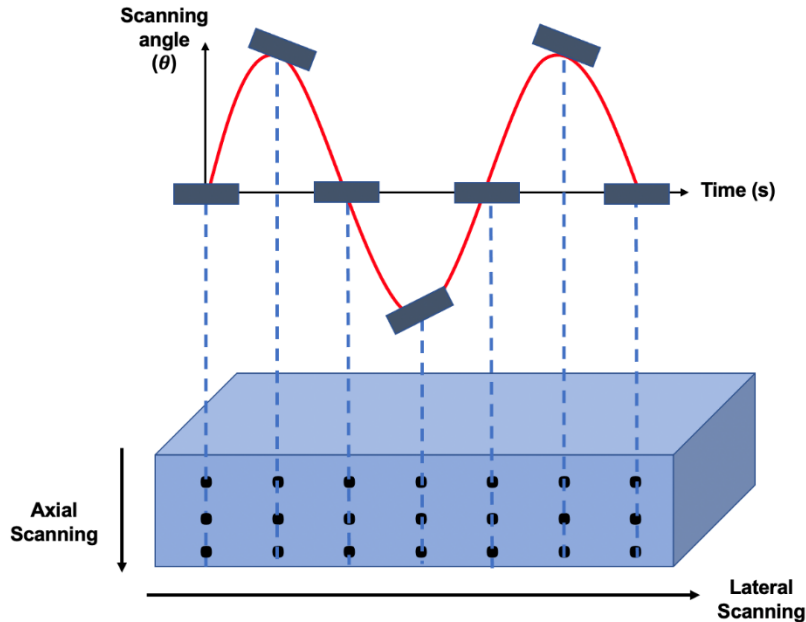


Figure 7-2. Schematic diagram showing the mirror movement for scanning the sample.

Due to this sinusoidal motion, the spacing between the pixels are non-uniform that leads to errors in the lateral scan, subsequently also causing errors in the axial scan. Although this error can be reduced by using a telecentric mirror, some applications require a non-telecentric scanning system, especially for imaging a non-planar sample [205, 206].

7.3 Phantom design and characterisation

The phantom pattern is inscribed inside a planar fused silica substrate (Ibsen Photonics, Denmark). The pattern has a total of 9 layers, including a top landmark layer which located at $50\mu\text{m}$ in apparent depth (AD) underneath of the planar surface and the other 8 layers of circular calibration patterns where the first layer is located at $150\mu\text{m}$ below the planar surface. There are 40 circles with a fixed increment of the radius for each layer where the smallest circle has a radius of $254\mu\text{m}$. The layer separation is $120\mu\text{m}$ (in AD) so that a total inscription depth is $\sim 960\mu\text{m}$ in apparent depth so that $\sim 1402\mu\text{m}$ in real depth (i.e. the refractive index of the fused silica at the wavelength of 532nm is 1.461). Each layer is applied with different laser powers to compensate a laser power loss when travelling to a deeper depth. The average linewidth for each layer of the circular pattern is around $6\mu\text{m}$. The circular pattern is used to overcome the angle limitation of the OCT imaging. The top view image of the fabricated phantom is shown in Figure 7-3.

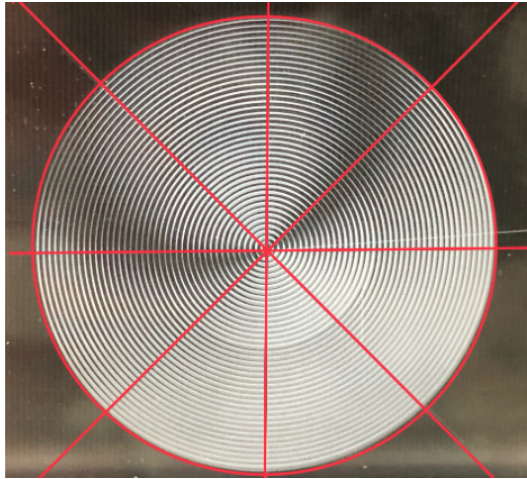
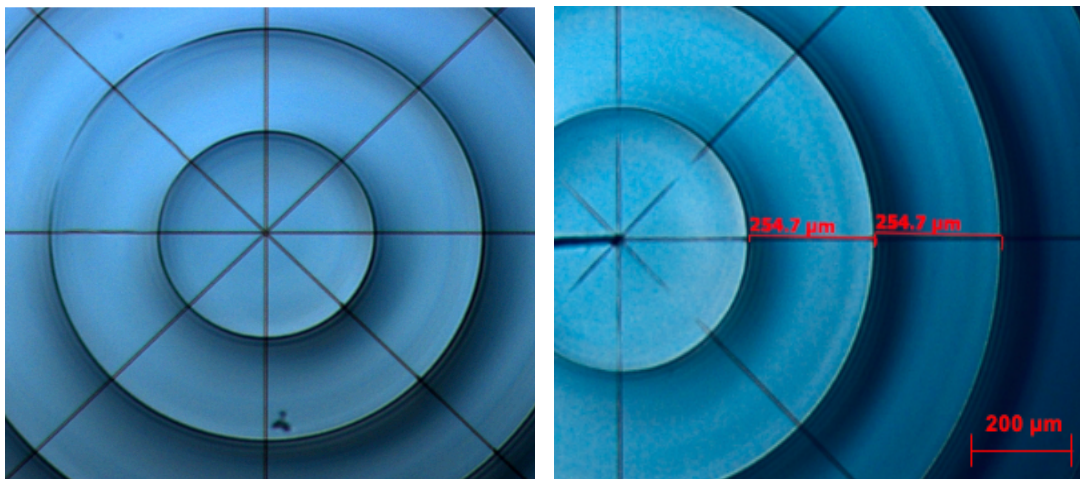


Figure 7-3. The image showing the phantom fabricated using a femtosecond laser with 8 layers of circular patterns inside the substrate. The landmark layer pattern is highlighted in red. The phantom was designed and fabricated by the thesis author.

An optical microscopy (Axioscope 2 MOT Plus, Zeiss) was used to characterise the phantom after the fabrication shown in Figure 7-4. The objective lens of 5x and 20x were used for the measurements. OCT systems were used to validate the phantom after the microscope characterisation process. In Figure 7-5, the graph shows the comparison between the designed parameter values and the measured parameter values for the fabrication of the OCT phantom to indicate the highly precise fabrication of the OCT phantom using a femtosecond laser.



(a)

(b)

Figure 7-4. The microscope image showing the inscribed pattern: (a) The overview image taken by the microscope using 5x objective magnification lens; (b) the microscope image showing the circular radius by using a 20x objective magnification lens. This microscope images were captured and measured by the thesis author.

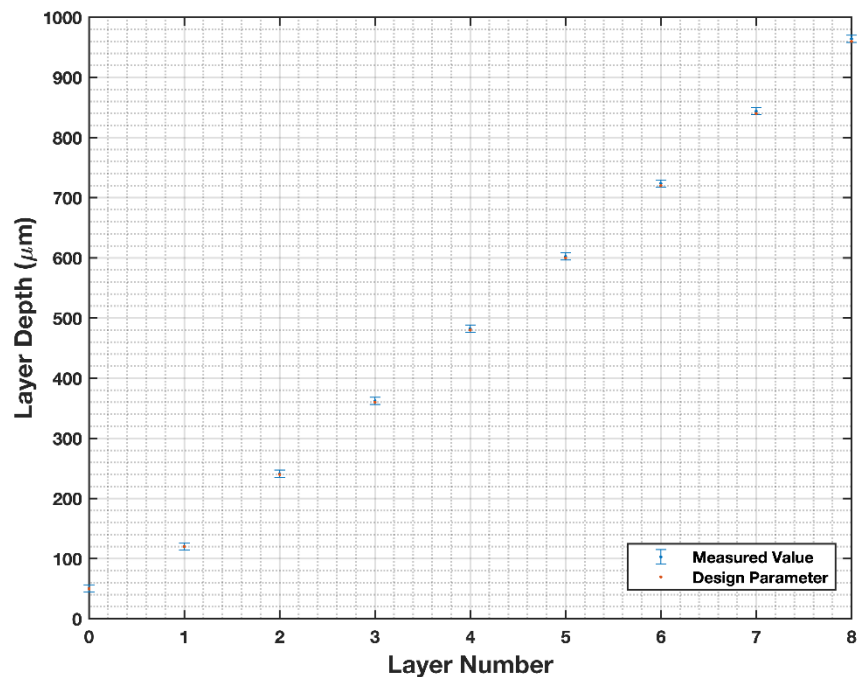


Figure 7-5. Comparison between the designed parameter values and the measured parameter values for the fabrication of the OCT phantom. This graph was plotted by the thesis author.

7.4 OCT image distortion detection and correction

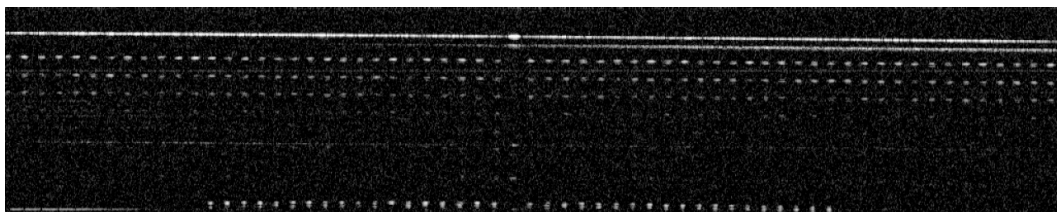
7.4.1 OCT system configuration

The OCT image was taken by the Optimec is830 SD-OCT system with a centre wavelength of 830 nm. The axial and lateral resolution of the system in air are 12 μm and 30 μm respectively. In addition, the sensitivity of the system is 107 dB at 1.2 kHz. The system employs a MEMS mirror system to scan the light across the sample. The systems capture A-scans of 512 pixels that represent the depth of the sample. The lateral scans (B-scan) are comprised of 1024 A-scans and the meridian to be captured can be controlled. For this research, the scan meridian was set at 90° while the scan width to 16 mm to allow an appropriate number of points on the circular pattern of the calibration sample to be detected (approximately 63 points). The sample holder height can be adjusted to ensure that the best quality OCT image is achieved by ensuring the measurement layer is in the OCT focus position. The focus position of the OCT is also dependant on the angle of the measurement probe and the type of the sample that is imaged.

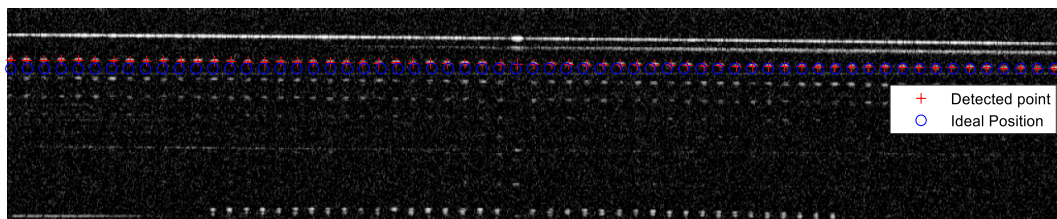
7.4.2 OCT image analysis

As the phantom is well characterised with known design parameters, a comparison can be performed between the real measurement and the designed parameter. The original OCT image is shown in Figure 7-6 (a) and the marked OCT image with both the detected real-time point and ideal true position are highlighted in Figure 7-6 (b). As this research is assessing the lateral scanning errors, only the first layer of the B-scan OCT pattern is analysed.

It can be seen from the comparison in Figure 7-6 (b), the position of the detected spot (taken from left to right in the lateral direction) is ahead of the true position at the beginning of the scan, then lags behind, in a repeating pattern. This error may be generated by the sinusoidal movement of the mirror during the scanning process.



(a)



(b)

Figure 7-6. The OCT image taken by Optimec is830 SD-OCT systems: (a) the original OCT system; (b) Plot of detected real-time position and ideal true position on the OCT image. The OCT image was captured by Dr. Izzati Ibrahim and Dr. Benjamin Coldrick and analysed by Dr. Izzati Ibrahim with the thesis author's help to understand the phantom parameters.

7.4.3 OCT image correction

7.4.3.1 Methods

In order to correct the image distortion, a phantom-based method is developed. A geometrical transformation was computed to correct the scanning error which resulted to the distortion of the OCT image. The following procedures shown in Figure 7-7 are followed for the data collection and analysis in order to correct the distorted image.

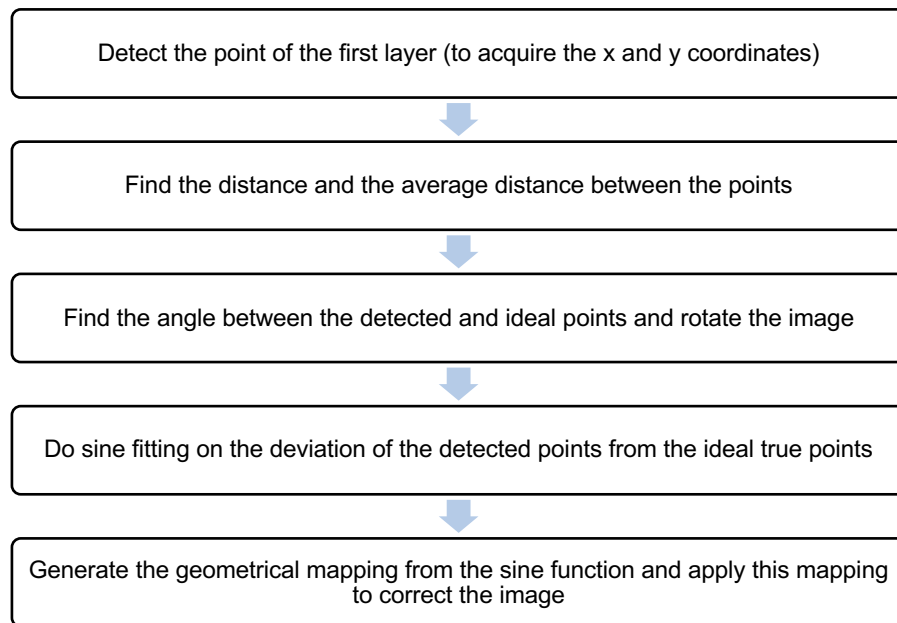


Figure 7-7. The procedures used for the data collection and analysis for correcting the distortion.

The deviation of the position of detected point (X_D) from the true position (X_C) can be calculated as:

$$\Delta X = X_D - X_C$$

Equation 7-4

The error of scan spacing depends on the distance from the probe to the sample (S) and the optical scanning angle (θ). As the distance from the probe is not changing, the spacing error is dependent on the scan angle. Plotting the scan spacing ΔX with respect to the detected points (presented in Figure 7-8) shows a good match of the sinusoidal variation to the sinusoidal fitting equation given below:

$$\Delta X = X_D - X_C = a_1 * \sin(b_1 * X_D + c_1)$$

Equation 7-5

where a_1 is the amplitude, b_1 is the frequency and c_1 is the phase shift for the sinusoidal fitting curve.

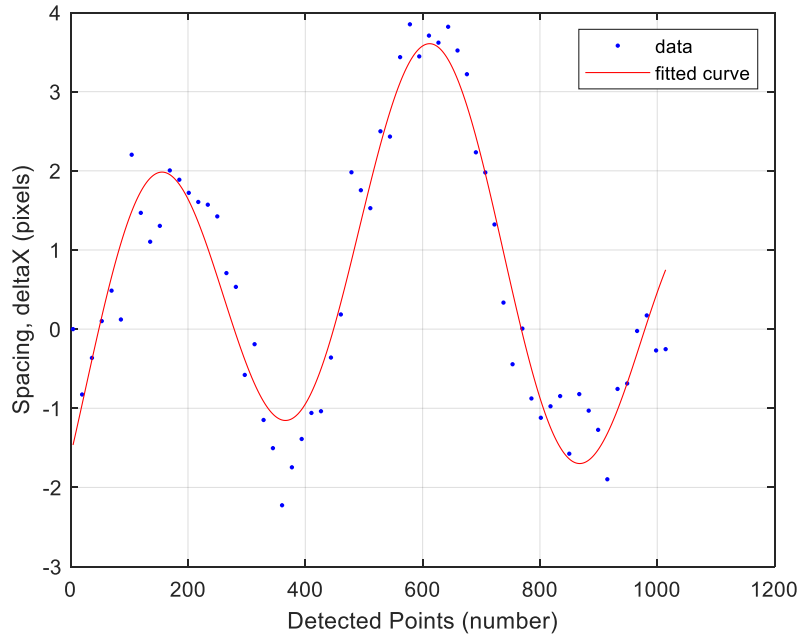


Figure 7-8. The plot showing the sinusoidal fitting of a distance between the consecutive points that might be due to the sinusoidal movement of the scanning mirror in projecting the location of the pixels. This graph was plotted by Dr. Izzati Ibrahim.

Before correcting for any scan spacing distortion, the image undergoes rotation correction to overcome the non-linearity in scanning. Given that a detected point from the calibration phantom is denoted as P with Cartesian coordinates of (x, y) and the ideal true position is P' with (x', y') coordinates, the scanning correction applied depends on the distance of the detected position P, and ideal true position P', from the centre of the image $P_0(x_c, y_c)$. The image rotation maps the original pixels onto a new position by rotating the image through an angle $(\Delta\theta)$ calculated by using the equation defined as:

$$\Delta\theta = \cos^{-1} \left[\frac{r_D \cdot r_i}{\left[(\sum r_D^2)^{\frac{1}{2}} \right] \left[(\sum r_i^2)^{\frac{1}{2}} \right]} \right]$$

Equation 7-6

where r_D and r_i are the radial distance of the detected point P (x, y) and the ideal true point P' (x', y') respectively, which is calculated using:

$$r_{D,i} = \frac{\sqrt{(x - x_c)^2 + (y - y_c)^2}}{\sqrt{(x_c)^2 + (y_c)^2}}$$

Equation 7-7

As the lateral scan spacing is affected predominantly on the X-axis, the spacing correction is applied only on the X-coordinate of the detected point. The scan spacing correction is performed by applying image transformation process on the image that has been rotated with the geometrical transformation mapping function. The correction is given in Equation 7-8:

$$x_{maps} = P(x) + A \sin(2\pi(P(x)))$$

Equation 7-8

where A is the distortion coefficient due to the non-uniformity of the scanning process and is given by the value of a_1 , acquired from the graph fitting from Figure 7-8 and it determines the scale of the distortion. High values of A indicates that the image has a high degree of scan spacing error. The mapping function x_{maps} acts as a function to transform or move the distorted pixel at coordinates (x, y) to a new position (x', y') by following the equation:

$$G(x', y') = T\{F(x, y)\}$$

where G is the output image, F is the input image and T is the transformation function. To ensure the accuracy of the mapping function, an image transformation is applied on the calibration phantom image first to assess the spacing of point after the transformation. In transforming the detected point to the corrected position, the red cross in Figure 7-9 is expecting to be moved to the blue circle, i.e. the spacing between each point should be uniform.

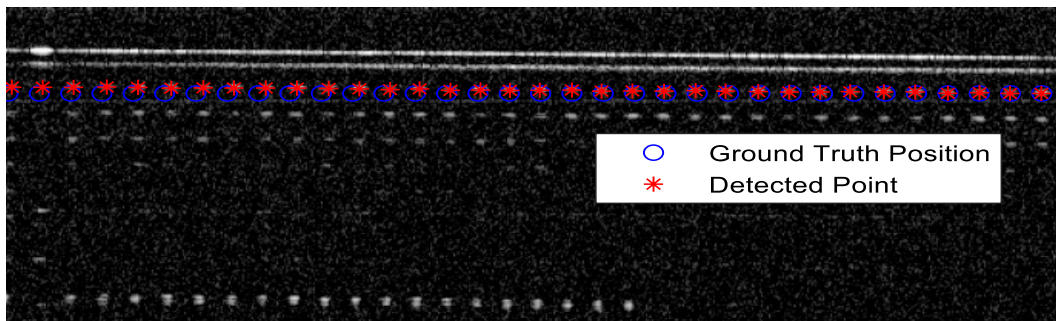


Figure 7-9: Plot of the true position and the detected position on the OCT image. This image was analysed by Dr. Izzati Ibrahim.

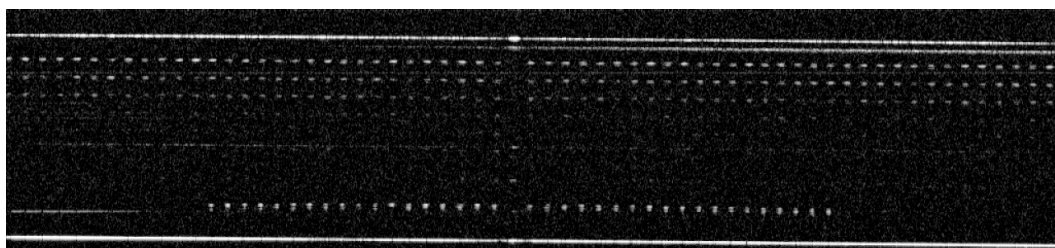
To assess the effectiveness of the transformation, the root mean square error (RMSE) is used to calculate error of spacing between the corrected point is P_C and the ideal true spacing \tilde{P} given in Equation 7-9.

$$RMSE = \sqrt{\frac{1}{N} \sum_{i=1}^n (P_{ci} - \tilde{P}_i)^2}$$

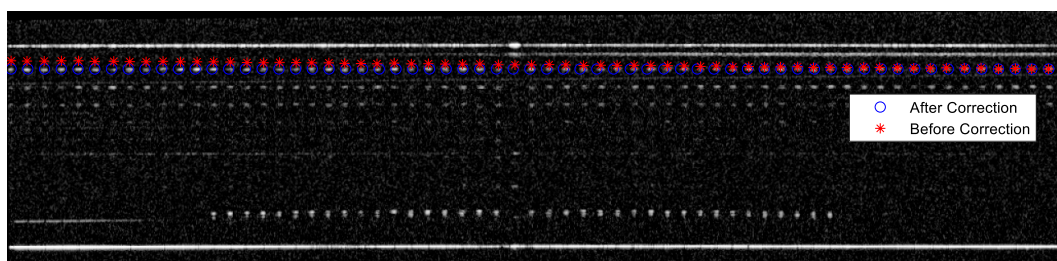
Equation 7-9

7.4.3.2 Results

The error of the point spacing on the calibration phantom image due to the scanning error has been corrected using a geometrical transformation based on the angle of rotation and sinusoidal transformation, with results shown in Figure 7-10. Figure 7-10(a) shows the image before the correction with the RMSE spacing errors between the points is 3.098. After implementing the image transform with the mapping function x_{maps} , the gaps between the points have moved and the error has been reduced to 1.046 (Figure 7-10 (b)). The overlay image of before and after correction is shown in Figure 7-11 to give a clear comparison. The uncorrected positions of the points (labelled in red) have been moved to the ideal position (labelled in green) to compensate for sinusoidal effect of the scanning system. This method has shown reduction of the scan spacing error by 82% after performing the image correction.



(a)



(b)

Figure 7-10. The OCT images showing the comparison between the original image and the transformed corrected image: (a) Image of OCT phantom before correction of scan spacing (RMSE spacing = 3.098) and (b) after correction (RMSE spacing = 1.046). This image was analysed by Dr. Izzati Ibrahim.

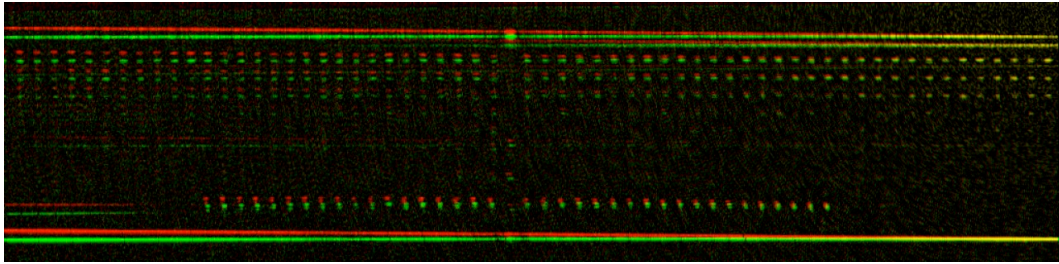


Figure 7-11: Overlap original image (before correction (in red)) on corrected image (in green). This image was analysed by Dr. Izzati Ibrahim.

7.4.4 Discussions

The results demonstrate that OCT geometrical distortion can be corrected using image post-processing technique based on a known calibration phantom, allowing for better metrology measurement of the sample. This novel approach can help to overcome these OCT intrinsic limitations without prior information of the scanning system. It is worth noting that the calibration phantom design should match the sensitivity of the system under analysis to ensure appropriate detection. In detail, accurate correction can only be achieved if the space between the points on the phantom is within the sensitivity of the imaging system. It needs to be considered that the position of the sample during the scanning process as this method assesses the spacing between the points, distortion due to misaligning the scan position to the sample may also induce errors. Accurate image rotation is essential to ensure that the image of the sample is perpendicular to the line of sight of the OCT system. This will minimise the error of spacing due to the nonparallel sample to the FOV of the camera.

Currently, only the planar phantom has been used to detect the OCT system distortion, the non-planar phantom can be used for the further expansion of this method to correct the distortion caused by the curvature of the lens. The work for the non-planar phantom is still under investigation.

7.5 Conclusions

This chapter has presented the OCT phantom application for detecting the OCT system scanning errors and being used as a reference point to correct the image distortion caused by the errors. These errors cause significant problems in metrology for obtaining accurate size and depth measurements for samples via an OCT imaging system. A phantom-based image post-processing method has been introduced by employing an OCT calibration phantom to measure the deviation of the point position with regards to

the idea true position. The mapping function was established based on this deviation to correct for the scan spacing of the OCT system, thus reducing the error of the pixels location on OCT images. The phantom-based distortion correction methods showing the potential of the OCT phantom being a multi-purpose calibration device.

Chapter 8

Conclusion and future works

8.1 Conclusion

This work has extensively explored the use of a femtosecond laser to fabricate highly precise microstructures for developing multipurpose 3D OCT calibration phantoms. The use of the direct femtosecond laser writing technique enabled a single-step fabrication procedure that can be easily implemented to make the OCT phantoms with a high level of accuracy and repeatability.

The motivation of the work was based on the fact that there is no standard available to calibrate and compare the performance between different OCT systems. With rapid development and extensive applications of the OCT system as clinical diagnosis devices, there was a need to develop an optical device (so called OCT phantom) that can be used as a calibration tool and to act as a 3D optical ruler to assess and compare the performance between different OCT systems which aimed to be universally accepted as a measurement standard.

A comprehensive literature review on different phantom fabrication methods was undertaken. The approaches have been compared to highlight the benefits of using a femtosecond laser to fabricate the phantom over other fabrication methods. Previously reported fabrication methods include nanoparticle doped into a clear epoxy resin to measure the 3D point spread function (PSF) of OCT system and tissue-mimicking OCT phantoms. However, the nanoparticle-dope method indicated the issue on the reliability and accuracy as the uncertainty can be caused by occasional aggregation of the particles and imperfection of the silicones. Tissue-mimicking OCT phantoms are compatible with both organic and inorganic optical scatters and mimic the properties of human tissue. However, the phantom had a very short lifetime (i.e. two years maximum) with multiple fabrication processes required. A femtosecond laser inscribed OCT phantom with four test patterns (i.e. PSF, sensitivity, lateral resolution and distortion) included inside a fused silica was presented by researchers at Aston University in 2012 to show the potential possibility of fabricating OCT calibration phantoms. By using this approach, a high accuracy and long lifetime (i.e. more than 8 years based on recent tests) can be achieved with a high repeatability for the fabrication process. However, the inscription method needed to be optimised as the previous method did not allow the

consistency and uniformity of the inscription for all the depths due to limitations in the writing algorithms. Therefore, one aim of the work was to optimise the inscription method.

Prior to the fabrication optimisation work, a detailed in-depth study was performed on investigating the correlation between laser power and the inscription size. A series of lines were inscribed with different laser pulse energies. Both the linewidth in the X-Y plane and the cross-sectional inscription height in the Y-Z plane were measured and characterised with an optical microscope and an OCT system (i.e. the Optimec is830 system). The results showed that with increased laser pulse energy, both the linewidth and the cross-inscription height were increased. A linear correlation was apparent between the laser power and the linewidth. A non-linear correlation was observed between the laser power and the cross-sectional inscription height associated with non-linear effects such as spherical aberration and the Kerr self-focusing which elongated the inscription in the axial direction. The critical power of self-focusing exceeded when the laser power was around 63% of the total laser average output power. It can be seen that a dramatic change in the size of the inscription height appeared after this critical point which matches the theoretical calculation. As the non-linear effect caused made it difficult to control the inscription size along the axial direction, a laser power range below the self-focusing threshold (i.e. 20% - 55%) was selected to inscribe the phantom which was still enough to reach to a greater depth (i.e. 1.8mm deep in real depth (RD) from the front surface) whilst allowing control of the inscription size.

The phantom fabrication optimisation process concluded with a redesigned layer-by-layer inscription method which allowed inscription at a greater depth and enabled the inscription size to be uniform and consistent for all the depths. This required the laser power to be reset at beginning of the inscription for each layer. The power selected was based on the results of the characterisation tests. Post-fabrication characterisation showed the cross-sectional inscription to be consistent and uniform under the OCT system with this optimised method.

In order to extend the use of OCT phantoms, a multipurpose non-planar phantom was initially proposed with grid pattern inscribed inside a plano-convex lens as the planar side provided a standard non-distorted image and the curved side provided a distorted image which can be used to detect the scanning errors and the post-processing algorithms of the OCT system for the distortion correction. However, the grid pattern required a high degree of alignment control under the OCT system since it required the sample to be centred and the scan to be parallel to the pattern. After discussions with OCT system users, a circular pattern was proposed to overcome this alignment issue.

An alternative circular pattern was developed that also included a landmark layer inscribed at the top of the test pattern to guide the location. An inscription attempt from a curved surface was made to illustrate how significant the affect induced by the curvature of the lens can be as the inscribed pattern was bent over along the curved surface which caused distortion of the inscription.

In addition, the OCT phantom was screened under a commercial OCT system (i.e. Carl Zeiss Cirrus HD-OCT 5000) to validate the application. Since the commercial OCT system was designed to inspect the human eyes and includes an embedded pre-processing algorithm to adjust for curvature, it emphasised distortion effects that can occur from the software. Even imaging from the planar surface generated a distorted image. It has to be noted that the alignment of the sample was challenging as a special holder to hold the sample upright was required for the OCT setup and uncertainty also caused by the tilted angle to avoid strong backscattering interference.

To validate the use of a phantom to correct for OCT system distortion, a planar phantom was designed and used as a reference point to correct the distorted image due to the scanning errors caused by the OCT system (in this case the Optimec is830 system). As the scanning errors were associated with lateral scanning, only the first layer of the inscribed pattern was selected for detailed investigation. All the point separations were measured and used to calculate the difference compared with the designed data. The results demonstrated how a known phantom-based distortion correction method can be used.

8.2 Future works

The non-planar OCT phantom which has been successfully demonstrated as a multipurpose optical device in this thesis, can be further extended to correct the image distortion caused by the nature of the curvature of the lens based on a phantom-based self-referencing/self-comparison method. However, to establish this method, OCT data from different OCT systems are required to be collected and tested to validate the method. Moreover, commercial OCT systems require further investigation in order to validate the OCT phantom to enable the OCT phantom to become universally accepted as a calibration device across different types of OCT systems. It is worth developing a specific holder for the calibration sample to be mounted to the commercial OCT systems in a reliable and repeatable manner.

In addition to this, different transparent materials and different curvatures of the plano-convex lens can also be tested to explore how well OCT systems cope under varying degrees of lens like distortion. Phantoms comprised of composite materials could also be explored as a means of simulating the varying tissues with various refractive indices and structures which may be experienced in biomedical imaging.

Further work should also focus on the work undertaken on the image processing of OCT systems. For example, a software package could be created to measure and analyse the distortion created by the phantom given a measured B-scan or C-scan and the known parameters of the phantom. This would allow for performance of the OCT system to be measured in addition to the required transformation to correct for OCT system introduced distortion, which is similar to the post-processing correction algorithms presented and discussed in chapter 7. The phantoms developed in this work and such a software package could potentially be commercialised as the first complete OCT performance measurement, distortion measurement and correction solution.

REFERENCES

- [1] D. Huang, E. A. Swanson, C. P. Lin *et al.*, "Optical Coherence Tomography," *Science*, vol. 254, no. 5035, pp. 1178-1181, Nov 22, 1991.
- [2] J. G. Fujimoto, C. Pitris, S. A. Boppart *et al.*, "Optical coherence tomography: An emerging technology for biomedical imaging and optical biopsy," *Neoplasia*, vol. 2, no. 1-2, pp. 9-25, Jan-Apr, 2000.
- [3] M. Adhi, and J. S. Duker, "Optical coherence tomography – current and future applications," *Current opinion in ophthalmology*, vol. 24, no. 3, pp. 213-221, 2013.
- [4] L. Pierro, E. Zampedri, P. Milani *et al.*, "Spectral domain OCT versus time domain OCT in the evaluation of macular features related to wet age-related macular degeneration," *Clinical Ophthalmology (Auckland, N.Z.)*, vol. 6, pp. 219-223, 02/09, 2012.
- [5] J. Welzel, "Optical coherence tomography in dermatology: a review," *Skin Research and Technology*, vol. 7, no. 1, pp. 1--9, 2001.
- [6] E. C. Sattler, R. Kästle, and J. Welzel, "Optical coherence tomography in dermatology," *Journal of Biomedical Optics*, vol. 18, pp. 18 - 18 - 7, 2013.
- [7] M. Ulrich, L. Themstrup, N. de Carvalho *et al.*, "Dynamic Optical Coherence Tomography in Dermatology," *Dermatology*, vol. 232, no. 3, pp. 298-311, 2016.
- [8] O. Babalola, A. Mamalis, H. Lev-Tov *et al.*, "Optical coherence tomography (OCT) of collagen in normal skin and skin fibrosis," *Archives of dermatological research*, vol. 306, no. 1, pp. 1-9, 2014.
- [9] P. H. Tomlins, G. N. Smith, P. D. Woolliams *et al.*, "Femtosecond laser micro-inscription of optical coherence tomography resolution test artifacts," *Biomedical Optics Express*, vol. 2, no. 5, pp. 1319-1327, 2011.
- [10] J. Rasakanthan, G. C. B. Lee, P. D. Woolliams *et al.*, "Parametric study of femtosecond inscription of microstructures for OCT artefact fabrication." pp. 82133N-82133N-11.
- [11] J. Pfefer, A. Fouad, C.-W. Chen *et al.*, "Multi-system comparison of optical coherence tomography performance with point spread function phantoms." pp. 85730C-85730C-10.
- [12] A. Fouad, T. J. Pfefer, C. W. Chen *et al.*, "Variations in optical coherence tomography resolution and uniformity: a multi-system performance comparison," *Biomedical Optics Express*, vol. 5, no. 7, pp. 2066-2081, 2014.

- [13] M. R. N. Avanaki, A. G. Podoleanu, M. C. Price *et al.*, "Phantoms for performance assessment of optical coherence tomography systems." pp. 82290W-82290W-9.
- [14] P. H. Tomlins, R. A. Ferguson, C. Hart *et al.*, "Point-spread function phantoms for optical coherence tomography," 2009.
- [15] A. Agrawal, T. J. Pfefer, N. Gilani *et al.*, "Three-dimensional characterization of optical coherence tomography point spread functions with a nanoparticle-embedded phantom," *Optics Letters*, vol. 35, no. 13, pp. 2269-2271, 2010/07/01, 2010.
- [16] A. V. Bykov, A. P. Popov, M. Kinnunen *et al.*, "Skin phantoms with realistic vessel structure for OCT measurements." pp. 73760F-73760F-7.
- [17] B. F. Kennedy, S. Loitsch, R. A. McLaughlin *et al.*, "Fibrin phantom for use in optical coherence tomography," *Journal of Biomedical Optics*, vol. 15, no. 3, pp. 030507-030507-3, 2010.
- [18] A. Curatolo, B. F. Kennedy, and D. D. Sampson, "Structured three-dimensional optical phantom for optical coherence tomography," *Optics Express*, vol. 19, no. 20, pp. 19480-19485, 2011/09/26, 2011.
- [19] J. Baxi, W. Calhoun, Y. J. Sepah *et al.*, "Retina-simulating phantom for optical coherence tomography," *Journal of Biomedical Optics*, vol. 19, no. 2, pp. 021106-021106, 2013.
- [20] A. Corcoran, G. Muyo, J. van Hemert *et al.*, "Application of a wide-field phantom eye for optical coherence tomography and reflectance imaging," *Journal of Modern Optics*, vol. 62, no. 21, pp. 1828-1838, 2015/12/15, 2015.
- [21] G. C. B. Lee, J. Rasakanthan, P. D. Woolliams *et al.*, "Fabrication of high quality optical coherence tomography (OCT) calibration artefacts using femtosecond inscription," *Biophotonics: Photonic Solutions for Better Health Care Iii*, vol. 8427, 2012.
- [22] M. G. Sandrian, P. Tomlins, P. Woolliams *et al.*, "Three-dimensional calibration targets for optical coherence tomography," *Proceedings of SPIE*, 2012.
- [23] K. Sugioka, and Y. Cheng, "Femtosecond laser three-dimensional micro- and nanofabrication," *Applied Physics Reviews*, vol. 1, no. 4, pp. 041303, 2014/12/01, 2014.
- [24] K. Sugioka, J. Xu, D. Wu *et al.*, "Femtosecond laser 3D micromachining: a powerful tool for the fabrication of microfluidic, optofluidic, and electrofluidic devices based on glass," *Lab on a Chip*, vol. 14, no. 18, pp. 3447-3458, 2014.
- [25] B. Guo, J. Sun, Y. Hua *et al.*, "Femtosecond Laser Micro/Nano-manufacturing: Theories, Measurements, Methods, and Applications," *Nanomanufacturing and Metrology*, vol. 3, no. 1, pp. 26-67, 2020/03/01, 2020.

- [26] K. Sugioka, and Y. Cheng, "Ultrafast lasers—reliable tools for advanced materials processing," *Light: Science & Applications*, vol. 3, no. 4, pp. e149-e149, 2014/04/01, 2014.
- [27] R. R. Gattass, and E. Mazur, "Femtosecond laser micromachining in transparent materials," *Nature Photonics*, vol. 2, no. 4, pp. 219-225, 2008/04/01, 2008.
- [28] M. Malinauskas, A. Žukauskas, S. Hasegawa *et al.*, "Ultrafast laser processing of materials: from science to industry," *Light: Science & Applications*, vol. 5, no. 8, pp. e16133-e16133, 2016/08/01, 2016.
- [29] K. M. Davis, K. Miura, N. Sugimoto *et al.*, "Writing waveguides in glass with a femtosecond laser," *Optics Letters*, vol. 21, no. 21, pp. 1729-1731, 1996/11/01, 1996.
- [30] K. Miura, J. Qiu, H. Inouye *et al.*, "Photowritten optical waveguides in various glasses with ultrashort pulse laser," *Applied Physics Letters*, vol. 71, no. 23, pp. 3329-3331, 1997/12/08, 1997.
- [31] M. Ams, P. Dekker, G. D. Marshall *et al.*, "Monolithic 100 mW Yb waveguide laser fabricated using the femtosecond-laser direct-write technique," *Optics Letters*, vol. 34, no. 3, pp. 247-249, 2009/02/01, 2009.
- [32] E. N. Glezer, M. Milosavljevic, L. Huang *et al.*, "Three-dimensional optical storage inside transparent materials," *Optics Letters*, vol. 21, no. 24, pp. 2023-2025, 1996/12/15, 1996.
- [33] M. H. Hong, B. Luk'yanchuk, S. M. Huang *et al.*, "Femtosecond laser application for high capacity optical data storage," *Applied Physics A*, vol. 79, no. 4, pp. 791-794, 2004/09/01, 2004.
- [34] C.-H. Park, Y. Petit, L. Canioni *et al.*, "Five-Dimensional Optical Data Storage Based on Ellipse Orientation and Fluorescence Intensity in a Silver-Sensitized Commercial Glass," *Micromachines*, vol. 11, no. 12, 2020.
- [35] D. Wu, Q.-D. Chen, L.-G. Niu *et al.*, "Femtosecond laser rapid prototyping of nanoshells and suspending components towards microfluidic devices," *Lab on a Chip*, vol. 9, no. 16, pp. 2391-2394, 2009.
- [36] J. Yong, Z. Zhan, S. C. Singh *et al.*, "Microfluidic Channels Fabrication Based on Underwater Superhydrophobic Microgrooves Produced by Femtosecond Laser Direct Writing," *ACS Applied Polymer Materials*, vol. 1, no. 11, pp. 2819-2825, 2019/11/08, 2019.
- [37] F. Sima, K. Sugioka, R. M. Vázquez *et al.*, "Three-dimensional femtosecond laser processing for lab-on-a-chip applications," *Nanophotonics*, vol. 7, no. 3, pp. 613-634, 2018.

- [38] R. Martínez Vázquez, G. Trotta, A. Volpe *et al.*, “Rapid Prototyping of Plastic Lab-on-a-Chip by Femtosecond Laser Micromachining and Removable Insert Microinjection Molding,” *Micromachines*, vol. 8, no. 11, 2017.
- [39] S. H. Chung, and E. Mazur, “Surgical applications of femtosecond lasers,” *Journal of Biophotonics*, vol. 2, no. 10, pp. 557-572, 2009/10/01, 2009.
- [40] N. Shen, D. Datta, C. B. Schaffer *et al.*, “Ablation of cytoskeletal filaments and mitochondria in live cells using a femtosecond laser nanoscissor,” *Molecular & Cellular Biomechanics*, vol. 2, no. 1, pp. 17, 2005.
- [41] J. Qiu, K. Miura, and K. Hirao, “Femtosecond laser-induced microfeatures in glasses and their applications,” *Journal of Non-Crystalline Solids*, vol. 354, no. 12, pp. 1100-1111, 2008/02/15/, 2008.
- [42] B. Zhang, L. Wang, and F. Chen, “Recent Advances in Femtosecond Laser Processing of LiNbO₃ Crystals for Photonic Applications,” *Laser & Photonics Reviews*, vol. 14, no. 8, pp. 1900407, 2020/08/01, 2020.
- [43] A. G. Okhrimchuk, A. V. Shestakov, I. Khrushchev *et al.*, “Depressed cladding, buried waveguide laser formed in a YAG:Nd³⁺ crystal by femtosecond laser writing,” *Optics Letters*, vol. 30, no. 17, pp. 2248-2250, 2005/09/01, 2005.
- [44] X. Sun, S. Sun, C. Romero *et al.*, “Femtosecond laser direct writing of depressed cladding waveguides in Nd:YAG with “ear-like” structures: fabrication and laser generation,” *Optics Express*, vol. 29, no. 3, pp. 4296-4307, 2021/02/01, 2021.
- [45] D. Sola, and R. Cases, “High-Repetition-Rate Femtosecond Laser Processing of Acrylic Intra-Ocular Lenses,” *Polymers*, vol. 12, no. 1, pp. 242, 2020.
- [46] B. Stępak, M. Gazińska, M. Nejbauer *et al.*, “Diverse nature of femtosecond laser ablation of poly(L-lactide) and the influence of filamentation on the polymer crystallization behaviour,” *Scientific Reports*, vol. 9, no. 1, pp. 3069, 2019/02/28, 2019.
- [47] D. Du, X. Liu, G. Korn *et al.*, “Laser - induced breakdown by impact ionization in SiO₂ with pulse widths from 7 ns to 150 fs,” *Applied Physics Letters*, vol. 64, no. 23, pp. 3071-3073, 1994/06/06, 1994.
- [48] P. P. Pronko, S. K. Dutta, J. Squier *et al.*, “Machining of sub-micron holes using a femtosecond laser at 800 nm,” *Optics Communications*, vol. 114, no. 1, pp. 106-110, 1995/01/15/, 1995.
- [49] J. S. Yahng, B. H. Chon, C. H. Kim *et al.*, “Nonlinear enhancement of femtosecond laser ablation efficiency by hybridization with nanosecond laser,” *Optics Express*, vol. 14, no. 20, pp. 9544-9550, 2006/10/02, 2006.
- [50] M. Ams, G. D. Marshall, P. Dekker *et al.*, “Investigation of Ultrafast Laser--Photonic Material Interactions: Challenges for Directly Written Glass Photonics,”

IEEE Journal of Selected Topics in Quantum Electronics, vol. 14, no. 5, pp. 1370-1381, 2008.

- [51] H. D. Jones, and H. R. Reiss, "Intense-field effects in solids," *Physical Review B*, vol. 16, no. 6, pp. 2466-2473, 09/15/, 1977.
- [52] L. V. Keldysh, "Ionization in the field of a strong electromagnetic wave," *Sov. Phys. JETP*, vol. 20, no. 5, pp. 1307-1314, 1965.
- [53] B. Rethfeld, "Unified Model for the Free-Electron Avalanche in Laser-Irradiated Dielectrics," *Physical Review Letters*, vol. 92, no. 18, pp. 187401, 05/06/, 2004.
- [54] C. B. Schaffer, A. Brodeur, and E. Mazur, "Laser-induced breakdown and damage in bulk transparent materials induced by tightly focused femtosecond laser pulses," *Measurement Science and Technology*, vol. 12, no. 11, pp. 1784-1794, Nov, 2001.
- [55] S. Leyder, D. Grojo, P. Delaporte *et al.*, "Multiphoton-avalanche absorption yields with femtosecond laser pulses in the wavelength range 1300–2200nm." pp. 1-1.
- [56] C. J. Scott, B. Peter, R. T. Casper *et al.*, "Recent Progress On Laser-Induced Modifications And Intrinsic Bulk Damage Of Wide-Gap Optical Materials," *Optical Engineering*, vol. 28, no. 10, pp. 1039-1068, 10/1, 1989.
- [57] L. Jiang, and H. L. Tsai, "Energy transport and material removal in wide bandgap materials by a femtosecond laser pulse," *International Journal of Heat and Mass Transfer*, vol. 48, no. 3, pp. 487-499, 2005/01/01/, 2005.
- [58] R. Mary, D. Choudhury, and A. K. Kar, "Applications of Fiber Lasers for the Development of Compact Photonic Devices," *IEEE Journal of Selected Topics in Quantum Electronics*, vol. 20, no. 5, pp. 72-84, 2014.
- [59] Amina, J. Lingfei, Y. Tianyang *et al.*, "Ionization behavior and dynamics of picosecond laser filamentation in sapphire," *Opto-Electronic Advances*, vol. 2, no. 8, pp. 190003, 2019/08/08, 2019.
- [60] G. C. B. Lee, "Femtosecond Laser Micromachining and Inscription of Novel Planar and Fibre Devices," Aston University, 2014.
- [61] B. C. Stuart, M. D. Feit, S. Herman *et al.*, "Nanosecond-to-femtosecond laser-induced breakdown in dielectrics," *Physical Review B*, vol. 53, no. 4, pp. 1749-1761, 01/15/, 1996.
- [62] A. Kaiser, B. Rethfeld, M. Vicanek *et al.*, "Microscopic processes in dielectrics under irradiation by subpicosecond laser pulses," *Physical Review B*, vol. 61, no. 17, pp. 11437-11450, 05/01/, 2000.

- [63] C. Hnatovsky, R. S. Taylor, P. P. Rajeev *et al.*, "Pulse duration dependence of femtosecond-laser-fabricated nanogratings in fused silica," *Applied Physics Letters*, vol. 87, no. 1, pp. 014104, 2005/07/04, 2005.
- [64] Y. Shimotsuma, P. G. Kazansky, J. Qiu *et al.*, "Self-Organized Nanogratings in Glass Irradiated by Ultrashort Light Pulses," *Physical Review Letters*, vol. 91, no. 24, pp. 247405, 12/11/, 2003.
- [65] C. Hnatovsky, R. S. Taylor, E. Simova *et al.*, "Fabrication of microchannels in glass using focused femtosecond laser radiation and selective chemical etching," *Applied Physics A*, vol. 84, no. 1, pp. 47-61, 2006/07/01, 2006.
- [66] V. R. Bhardwaj, E. Simova, P. P. Rajeev *et al.*, "Optically Produced Arrays of Planar Nanostructures inside Fused Silica," *Physical Review Letters*, vol. 96, no. 5, pp. 057404, 02/07/, 2006.
- [67] D. Tan, K. N. Sharafudeen, Y. Yue *et al.*, "Femtosecond laser induced phenomena in transparent solid materials: Fundamentals and applications," *Progress in Materials Science*, vol. 76, pp. 154-228, 2016/03/01/, 2016.
- [68] K. Itoh, W. Watanabe, S. Nolte *et al.*, "Ultrafast Processes for Bulk Modification of Transparent Materials," *MRS Bulletin*, vol. 31, no. 8, pp. 620-625, 2006.
- [69] S. M. Eaton, G. Cerullo, and R. Osellame, "11 - Thermal writing of photonic devices in glass and polymers by femtosecond lasers," *Laser Growth and Processing of Photonic Devices*, N. A. Vainos, ed., pp. 333-373: Woodhead Publishing, 2012.
- [70] M. Kamata, and M. Obara, "Control of the refractive index change in fused silica glasses induced by a loosely focused femtosecond laser," *Applied Physics A*, vol. 78, no. 1, pp. 85-88, 2004/01/01, 2004.
- [71] R. R. Thomson, N. D. Psaila, H. T. Bookey *et al.*, "Controlling the Cross-section of Ultrafast Laser Inscribed Optical Waveguides," *Femtosecond Laser Micromachining: Photonic and Microfluidic Devices in Transparent Materials*, R. Osellame, G. Cerullo and R. Ramponi, eds., pp. 93-125, Berlin, Heidelberg: Springer Berlin Heidelberg, 2012.
- [72] M. Will, S. Nolte, B. N. Chichkov *et al.*, "Optical properties of waveguides fabricated in fused silica by femtosecond laser pulses," *Applied Optics*, vol. 41, no. 21, pp. 4360-4364, 2002/07/20, 2002.
- [73] I.-B. Sohn, M.-S. Lee, J.-S. Woo *et al.*, "Fabrication of photonic devices directly written within glass using a femtosecond laser," *Optics Express*, vol. 13, no. 11, pp. 4224-4229, 2005/05/30, 2005.
- [74] J. W. Chan, T. Huser, S. Risbud *et al.*, "Structural changes in fused silica after exposure to focused femtosecond laser pulses," *Optics Letters*, vol. 26, no. 21, pp. 1726-1728, 2001/11/01, 2001.

- [75] U. Haken, O. Humbach, S. Ortner *et al.*, "Refractive index of silica glass: influence of fictive temperature," *Journal of Non-Crystalline Solids*, vol. 265, no. 1, pp. 9-18, 2000/03/02/, 2000.
- [76] Y. Bellouard, A. Champion, B. McMillen *et al.*, "Stress-state manipulation in fused silica via femtosecond laser irradiation," *Optica*, vol. 3, no. 12, pp. 1285-1293, 2016/12/20, 2016.
- [77] Q. Sun, T. Lee, M. Beresna *et al.*, "Control of Laser Induced Cumulative Stress for Efficient Processing of Fused Silica," *Scientific Reports*, vol. 10, no. 1, pp. 3819, 2020/03/02, 2020.
- [78] M. Montecchi, R. M. Montereali, and E. Nichelatti, "Refractive index modification from colour centres in dielectric confining structures," *Optical Materials*, vol. 17, no. 1, pp. 347-350, 2001/06/01/, 2001.
- [79] Q.-Z. Zhao, J.-R. Qiu, X.-W. Jiang *et al.*, "Mechanisms of the refractive index change in femtosecond laser-irradiated Au³⁺-doped silicate glasses," *Journal of Applied Physics*, vol. 96, no. 12, pp. 7122-7125, 2004/12/15, 2004.
- [80] A. Saliminia, J.-P. Bérubé, and R. Vallée, "Refractive index-modified structures in glass written by 266nm fs laser pulses," *Optics Express*, vol. 20, no. 25, pp. 27410-27419, 2012/12/03, 2012.
- [81] A. Kubota, M. J. Caturla, J. S. Stölken *et al.*, "Densification of fused silica due to shock waves and its implications for 351 nm laser induced damage," *Optics Express*, vol. 8, no. 11, pp. 611-616, 2001/05/21, 2001.
- [82] B. Pommellec, M. Lancry, A. Chahid-Erraji *et al.*, "Modification thresholds in femtosecond laser processing of pure silica: review of dependencies on laser parameters [Invited]," *Optical Materials Express*, vol. 1, no. 4, pp. 766-782, 2011/08/01, 2011.
- [83] B. McMillen, O. Uteza, R. Clady *et al.*, "Laser-induced densification of fused silica using spatially overlapping sub-30 fs pulses," *Journal of Applied Physics*, vol. 128, no. 8, pp. 083107, 2020/08/28, 2020.
- [84] B. McMillen, Y. Bellouard, O. Uteza *et al.*, "Quantification of bulk densification in fused silica induced by femtosecond laser exposure in the sub-50 fs regime." pp. 1-2.
- [85] K. Hirao, and K. Miura, "Writing waveguides and gratings in silica and related materials by a femtosecond laser," *Journal of Non-Crystalline Solids*, vol. 239, no. 1, pp. 91-95, 1998/10/01/, 1998.
- [86] A. Saliminia, R. Vallée, and S. L. Chin, "Waveguide writing in silica glass with femtosecond pulses from an optical parametric amplifier at 1.5 μ m," *Optics Communications*, vol. 256, no. 4, pp. 422-427, 2005/12/15/, 2005.

- [87] L. Sudrie, M. Franco, B. Prade *et al.*, "Writing of permanent birefringent microlayers in bulk fused silica with femtosecond laser pulses," *Optics Communications*, vol. 171, no. 4, pp. 279-284, 1999/12/01/, 1999.
- [88] H. Wang, J. Song, Q. Li *et al.*, "Formation of nanograting in fused silica by temporally delayed femtosecond double-pulse irradiation," *Journal of Physics D: Applied Physics*, vol. 51, no. 15, pp. 155101, 2018/03/20, 2018.
- [89] D. A. Yashunin, Y. A. Malkov, L. A. Mochalov *et al.*, "Fabrication of microchannels in fused silica using femtosecond Bessel beams," *Journal of Applied Physics*, vol. 118, no. 9, pp. 093106, 2015/09/07, 2015.
- [90] S. J. Mihailov, D. Grobnic, C. Hnatovsky *et al.*, "Extreme Environment Sensing Using Femtosecond Laser-Inscribed Fiber Bragg Gratings," *Sensors (Basel, Switzerland)*, vol. 17, no. 12, pp. 2909, 2017.
- [91] H. Ma, R. A. Zakoldaev, A. Rudenko *et al.*, "Well-controlled femtosecond laser inscription of periodic void structures in porous glass for photonic applications," *Optics Express*, vol. 25, no. 26, pp. 33261-33270, 2017/12/25, 2017.
- [92] Y. Lu, N. Gordon, D. Robinson *et al.*, "Non-planar calibration phantoms for optical coherence tomography," *Proc.SPIE*, vol. 10544, pp. 10544 - 10544 - 7, 2018.
- [93] Y. Lu, N. Gordon, B. Coldrick *et al.*, "Femtosecond laser inscribed advanced calibration phantom for optical coherence tomography (OCT)," *Proc.SPIE*, vol. 11292, 2020.
- [94] D. Ehrt, T. Kittel, M. Will *et al.*, "Femtosecond-laser-writing in various glasses," *Journal of Non-Crystalline Solids*, vol. 345, pp. 332-337, 2004/10/15/, 2004.
- [95] M. Beresna, M. Gecevičius, and P. G. Kazansky, "Ultrafast laser direct writing and nanostructuring in transparent materials," *Advances in Optics and Photonics*, vol. 6, no. 3, pp. 293-339, 2014/09/30, 2014.
- [96] P. A. Dmitriev, S. V. Makarov, V. A. Milichko *et al.*, "Direct Femtosecond Laser Writing of Optical Nanoresonators," *Journal of Physics: Conference Series*, vol. 690, no. 1, pp. 012021, 2016.
- [97] L. J. Jiang, S. Maruo, R. Osellame *et al.*, "Femtosecond laser direct writing in transparent materials based on nonlinear absorption," *MRS Bulletin*, vol. 41, no. 12, pp. 975-983, 2016/12/01, 2016.
- [98] D. J. Little, M. Ams, P. Dekker *et al.*, "Femtosecond laser modification of fused silica: the effect of writing polarization on Si-O ring structure," *Optics Express*, vol. 16, no. 24, pp. 20029-20037, 2008/11/24, 2008.
- [99] D. Liu, Y. Li, M. Liu *et al.*, "The polarization-dependence of femtosecond laser damage threshold inside fused silica," *Applied Physics B*, vol. 91, no. 3, pp. 597, 2008/05/07, 2008.

- [100] K. Gaudfrin, J. Lopez, K. Mishchik *et al.*, "Fused silica ablation by double femtosecond laser pulses: influence of polarization state," *Optics Express*, vol. 28, no. 10, pp. 15189-15206, 2020/05/11, 2020.
- [101] V. Stankevič, G. Račiukaitis, F. Bragheri *et al.*, "Laser printed nano-gratings: orientation and period peculiarities," *Scientific Reports*, vol. 7, no. 1, pp. 39989, 2017/01/09, 2017.
- [102] S. Richter, M. Heinrich, S. Döring *et al.*, "Nanogratings in fused silica: Formation, control, and applications," *Journal of Laser Applications*, vol. 24, no. 4, pp. 042008, 2012/09/01, 2012.
- [103] R. Osellame, N. Chiodo, G. Della Valle *et al.*, "Optical waveguide writing with a diode-pumped femtosecond oscillator," *Optics Letters*, vol. 29, no. 16, pp. 1900-1902, 2004/08/13, 2004.
- [104] S. M. Eaton, H. Zhang, M. L. Ng *et al.*, "Transition from thermal diffusion to heat accumulation in high repetition rate femtosecond laser writing of buried optical waveguides," *Optics Express*, vol. 16, no. 13, pp. 9443-9458, 2008/06/23, 2008.
- [105] J. Bovatsek, A. Arai, and C. B. Schaffer, "Three-dimensional micromachining inside transparent materials using femtosecond laser pulses: New applications." pp. 1-2.
- [106] Q. Sun, H. Asahi, Y. Nishijima *et al.*, "Pulse duration dependent nonlinear propagation of a focused femtosecond laser pulse in fused silica," *Optics Express*, vol. 18, no. 24, pp. 24495-24503, 2010/11/22, 2010.
- [107] B. C. Stuart, M. D. Feit, A. M. Rubenchik *et al.*, "Laser-Induced Damage in Dielectrics with Nanosecond to Subpicosecond Pulses," *Physical Review Letters*, vol. 74, no. 12, pp. 2248-2251, 03/20/, 1995.
- [108] N. Huot, R. Stoian, A. Mermillod-Blondin *et al.*, "Analysis of the effects of spherical aberration on ultrafast laser-induced refractive index variation in glass," *Optics Express*, vol. 15, no. 19, pp. 12395-12408, 2007/09/17, 2007.
- [109] C. Mauclair, A. Mermillod-Blondin, N. Huot *et al.*, "Ultrafast laser writing of homogeneous longitudinal waveguides in glasses using dynamic wavefront correction," *Optics Express*, vol. 16, no. 8, pp. 5481-5492, 2008/04/14, 2008.
- [110] L. Huang, P. S. Salter, F. Payne *et al.*, "Aberration correction for direct laser written waveguides in a transverse geometry," *Optics Express*, vol. 24, no. 10, pp. 10565-10574, 2016/05/16, 2016.
- [111] N. Bisch, J. Guan, M. J. Booth *et al.*, "Adaptive optics aberration correction for deep direct laser written waveguides in the heating regime," *Applied Physics A*, vol. 125, no. 5, pp. 364, 2019/04/26, 2019.

- [112] M. J. Booth, M. A. A. Neil, and T. Wilson, "Aberration correction for confocal imaging in refractive-index-mismatched media," *Journal of Microscopy*, vol. 192, no. 2, pp. 90-98, 1998/11/01, 1998.
- [113] C. Hnatovsky, R. S. Taylor, E. Simova *et al.*, "High-resolution study of photoinduced modification in fused silica produced by a tightly focused femtosecond laser beam in the presence of aberrations," *Journal of Applied Physics*, vol. 98, no. 1, pp. 013517, 2005/07/01, 2005.
- [114] T. F. Johnston, "Beam propagation (M2) measurement made as easy as it gets: the four-cuts method," *Applied Optics*, vol. 37, no. 21, pp. 4840-4850, 1998/07/20, 1998.
- [115] A. Couairon, and A. Mysyrowicz, "Femtosecond filamentation in transparent media," *Physics Reports*, vol. 441, no. 2, pp. 47-189, 2007/03/01/, 2007.
- [116] E. L. Kerr, "Filamentary Tracks Formed in Transparent Optical Glass by Laser Beam Self-Focusing. II. Theoretical Analysis," *Physical Review A*, vol. 4, no. 3, pp. 1195-1218, 09/01/, 1971.
- [117] A. Brodeur, and S. L. Chin, "Ultrafast white-light continuum generation and self-focusing in transparent condensed media," *Journal of the Optical Society of America B*, vol. 16, no. 4, pp. 637-650, 1999/04/01, 1999.
- [118] A. Saliminia, N. T. Nguyen, S. L. Chin *et al.*, "The influence of self-focusing and filamentation on refractive index modifications in fused silica using intense femtosecond pulses," *Optics Communications*, vol. 241, no. 4, pp. 529-538, 2004/11/16/, 2004.
- [119] J. H. Marburger, "Self-focusing: Theory," *Progress in Quantum Electronics*, vol. 4, pp. 35-110, 1975/04/01/, 1975.
- [120] Z. Wu, H. Jiang, H. Yang *et al.*, "The refocusing behaviour of a focused femtosecond laser pulse in fused silica," *Journal of Optics A: Pure and Applied Optics*, vol. 5, pp. 102-107, 2003.
- [121] N. Naseri, G. Dupras, and L. Ramunno, "Mechanism of laser induced filamentation in dielectrics," *Optics Express*, vol. 28, no. 18, pp. 26977-26988, 2020/08/31, 2020.
- [122] A. V. Dostovalov, A. A. Wolf, V. K. Mezentsev *et al.*, "Quantitative characterization of energy absorption in femtosecond laser micro-modification of fused silica," *Optics Express*, vol. 23, no. 25, pp. 32541-32547, 2015/12/14, 2015.
- [123] S. J. Vincent, D. Alonso-Caneiro, and M. J. Collins, "Optical coherence tomography and scleral contact lenses: clinical and research applications," *Clinical and Experimental Optometry*, vol. 102, no. 3, pp. 224-241, 2019/05/01, 2019.

- [124] A. Al-Mujaini, U. K. Wali, and S. Azeem, "Optical coherence tomography: clinical applications in medical practice," *Oman medical journal*, vol. 28, no. 2, pp. 86, 2013.
- [125] G. Song, K. K. Chu, S. Kim *et al.*, "First Clinical Application of Low-Cost OCT," *Translational Vision Science & Technology*, vol. 8, no. 3, pp. 61-61, 2019.
- [126] J. de Moura, J. Novo, J. Rouco *et al.*, "Retinal vasculature identification and characterization using oct imaging," *OCT-Applications in Ophthalmology*: IntechOpen, 2018.
- [127] D. R. Reyes-Hernandez, M. W. Halter, and J. Hwang, "Optical Coherence Tomography for Dimensional Metrology of Lab-on-a-chip devices," 2013.
- [128] P. Meemon, J. Yao, K.-S. Lee *et al.*, "Optical Coherence Tomography Enabling Non Destructive Metrology of Layered Polymeric GRIN Material," *Scientific Reports*, vol. 3, no. 1, pp. 1709, 2013/04/23, 2013.
- [129] D. Stifter, "Beyond biomedicine: a review of alternative applications and developments for optical coherence tomography," *Applied Physics B*, vol. 88, no. 3, pp. 337-357, 2007/08/01, 2007.
- [130] N. A. Russo, E. N. Morel, J. R. Torga *et al.*, "OCT in Applications That Involve the Measurement of Large Dimensions," *Optical Coherence Tomography and Its Non-medical Applications*, p. 53: IntechOpen, 2020.
- [131] P. Targowski, M. Kowalska, M. Sylwestrzak *et al.*, "OCT for examination of cultural heritage objects," *Optical Coherence Tomography and Its Non-Medical Applications; Wang, MR, Ed*, pp. 147-164, 2020.
- [132] J. Fujimoto, and E. Swanson, "The Development, Commercialization, and Impact of Optical Coherence Tomography," *Investigative ophthalmology & visual science*, vol. 57, no. 9, pp. OCT1-OCT13, 2016.
- [133] J. J. Wild, and J. M. Reid, "Application of Echo-Ranging Techniques to the Determination of Structure of Biological Tissues," *Science*, vol. 115, no. 2983, pp. 226-230, 1952.
- [134] J. G. Fujimoto, "Optical Coherence Tomography: Principles and Applications," vol. 31, no. 10, pp. 635-642, 2003.
- [135] R. Leitgeb, C. K. Hitzenberger, and A. F. Fercher, "Performance of fourier domain vs. time domain optical coherence tomography," *Optics Express*, vol. 11, no. 8, pp. 889-894, Apr 21, 2003.
- [136] D. P. Popescu, L.-P. i. Choo-Smith, C. Flueraru *et al.*, "Optical coherence tomography: fundamental principles, instrumental designs and biomedical applications," *Biophysical reviews*, vol. 3, no. 3, pp. 155-155, 2011.

- [137] Z. Yaqoob, J. Wu, and C. Yang, "Spectral domain optical coherence tomography: a better OCT imaging strategy," *Biotechniques*, vol. 39, no. 6 Suppl, pp. S6-13, Dec, 2005.
- [138] P. H. Tomlins, and R. K. Wang, "Theory, developments and applications of optical coherence tomography," *Journal of Physics D, Applied Physics*, vol. 38, no. 15, pp. 2519-2535, 2005.
- [139] A. G. Podoleanu, "Optical coherence tomography," *Journal of Microscopy*, vol. 247, no. 3, pp. 209--219, 2012.
- [140] W. Wieser, B. R. Biedermann, T. Klein *et al.*, "Multi-Megahertz OCT: High quality 3D imaging at 20 million A-scans and 4.5 GVoxels per second," *Optics Express*, vol. 18, no. 14, pp. 14685-14704, 2010/07/05, 2010.
- [141] M. A. Choma, M. V. Sarunic, C. Yang *et al.*, "Sensitivity advantage of swept source and Fourier domain optical coherence tomography," *Opt. Express*, vol. 11, no. 18, pp. 2183--2189, 2003.
- [142] S. H. Yun, G. J. Tearney, B. E. Bouma *et al.*, "High-speed spectral-domain optical coherence tomography at 1.3 μm wavelength," *Opt. Express*, vol. 11, no. 26, pp. 3598--3604, 2003.
- [143] W. Drexler, U. Morgner, F. X. Kartner *et al.*, "In vivo ultrahigh-resolution optical coherence tomography," *Opt. Lett.*, vol. 24, no. 17, pp. 1221--1223, 1999.
- [144] B. Cense, N. A. Nassif, T. C. Chen *et al.*, "Ultrahigh-resolution high-speed retinal imaging using spectral-domain optical coherence tomography," *Opt. Express*, vol. 12, no. 11, pp. 2435--2447, 2004.
- [145] A. F. Fercher, C. K. Hitzenberger, G. Kamp *et al.*, "Measurement of intraocular distances by backscattering spectral interferometry," vol. 117, no. 1, pp. 43-48, 1995.
- [146] A. Agrawal, T. J. Pfefer, P. D. Woolliams *et al.*, "Methods to assess sensitivity of optical coherence tomography systems," *Biomedical Optics Express*, vol. 8, no. 2, pp. 902-917, 2017.
- [147] S. Aumann, S. Donner, J. Fischer *et al.*, "Optical Coherence Tomography (OCT): Principle and Technical Realization," *High Resolution Imaging in Microscopy and Ophthalmology: New Frontiers in Biomedical Optics*, J. F. Bille, ed., pp. 59-85, Cham: Springer International Publishing, 2019.
- [148] M. Wojtkowski, V. Srinivasan, J. G. Fujimoto *et al.*, "Three-dimensional Retinal Imaging with High-Speed Ultrahigh-Resolution Optical Coherence Tomography," *Ophthalmology*, vol. 112, no. 10, pp. 1734-1746, 2005.
- [149] D. Wolfgang, "Ultrahigh-resolution optical coherence tomography," *Journal of Biomedical Optics*, vol. 9, no. 1, pp. 47-74, 1/1, 2004.

- [150] L. Ge, Y. Yuan, M. Shen *et al.*, "The Role of Axial Resolution of Optical Coherence Tomography on the Measurement of Corneal and Epithelial Thicknesses," *Investigative Ophthalmology & Visual Science*, vol. 54, no. 1, pp. 746-755, 2013.
- [151] R. M. Werkmeister, S. Sapeta, D. Schmidl *et al.*, "Ultrahigh-resolution OCT imaging of the human cornea," *Biomedical Optics Express*, vol. 8, no. 2, pp. 1221-1239, 2017/02/01, 2017.
- [152] P. D. Woolliams, R. A. Ferguson, C. Hart *et al.*, "Spatially deconvolved optical coherence tomography," *Applied Optics*, vol. 49, no. 11, pp. 2014-2021, 2010/04/10, 2010.
- [153] J. Holmes, S. Hattersley, N. Stone *et al.*, "Multi-channel Fourier domain OCT system with superior lateral resolution for biomedical applications."
- [154] B. J. Coldrick, C. Richards, K. Sugden *et al.*, "Developments in contact lens measurement: A comparative study of industry standard geometric inspection and optical coherence tomography," *Contact Lens and Anterior Eye*, vol. 39, no. 4, pp. 270-276, 2016.
- [155] H. T. Peter, W. Peter, T. Matthew *et al.*, "Measurement of the three-dimensional point-spread function in an optical coherence tomography imaging system."
- [156] B. E. Rapp, "Chapter 3 - Engineering Mathematics," *Microfluidics: Modelling, Mechanics and Mathematics*, B. E. Rapp, ed., pp. 21-50, Oxford: Elsevier, 2017.
- [157] A. F. Fercher, W. Drexler, C. K. Hitzenberger *et al.*, "Optical coherence tomography - principles and applications," *Reports on Progress in Physics*, vol. 66, no. 2, pp. 239, 2003.
- [158] J. Rasakanthan, "Advances in Characterisation, Calibration and Data Processing Speed of Optical Coherence Tomography Systems," Aston University, 2014.
- [159] A. G. Podoleanu, M. Seeger, G. M. Dobre *et al.*, "Transversal and longitudinal images from the retina of the living eye using low-coherence reflectometry," *Journal of Biomedical Optics*, vol. 3, pp. 3 - 3 - 9, 1998.
- [160] S. P. K. Karri, N. Garai, D. Nawn *et al.*, "Simultaneous reconstruction and restoration of sparsely sampled optical coherence tomography image through learning separable filters for deep architectures." pp. 52-55.
- [161] J. Cheng, D. Tao, Y. Quan *et al.*, "Speckle Reduction in 3D Optical Coherence Tomography of Retina by A-Scan Reconstruction," *IEEE Transactions on Medical Imaging*, vol. 35, no. 10, pp. 2270-2279, 2016.
- [162] P. Hunziker, O. V. Morozov, O. V. Volosyuk *et al.*, "Improved method of Optical Coherence Tomography imaging." pp. 421-424.

- [163] A. Ahmad, S. G. Adie, E. J. Chaney *et al.*, "Cross-correlation-based image acquisition technique for manually-scanned optical coherence tomography," *Opt. Express*, vol. 17, no. 10, pp. 8125--8136, 2009.
- [164] E. Aukorius, and A. C. Boccara, "Fast subsurface fingerprint imaging with full-field optical coherence tomography system equipped with a silicon camera," *Journal of Biomedical Optics*, vol. 22, pp. 22 - 22 - 8, 2017.
- [165] T. S. Ralston, J. A. Mayen, D. L. Marks *et al.*, "Real-time digital design for an optical coherence tomography acquisition and processing system," *Proc.SPIE*, vol. 5324, pp. 5324 - 5324 - 12, 2004.
- [166] D. Alonso-Caneiro, S. A. Read, and M. J. Collins, "Optical Coherence Tomography Image Enhancement By Automatic B-scan Alignment And Registration," *Investigative Ophthalmology & Visual Science*, vol. 52, no. 14, pp. 1314-1314, 2011.
- [167] R. D. Ferguson, D. X. Hamme, L. A. Paunescu *et al.*, "Tracking optical coherence tomography," *Opt. Lett.*, vol. 29, no. 18, pp. 2139--2141, 2004.
- [168] E. Lebed, P. J. Mackenzie, M. V. Sarunic *et al.*, "Rapid volumetric OCT image acquisition using Compressive Sampling," *Optics Express*, vol. 18, no. 20, pp. 21003-21012, 2010/09/27, 2010.
- [169] R. Su, P. Ekberg, M. Leitner *et al.*, "Accurate and automated image segmentation of 3D optical coherence tomography data suffering from low signal-to-noise levels," *J. Opt. Soc. Am. A*, vol. 31, no. 12, pp. 2551--2560, 2014.
- [170] P. R. T. Munro, A. Curatolo, and D. D. Sampson, "A model of optical coherence tomography image formation based on Maxwell's equations." pp. 134-135.
- [171] A. Podoleanu, I. Charalambous, L. Plesea *et al.*, "Correction of distortions in optical coherence tomography imaging of the eye," *Physics in Medicine & Biology*, vol. 49, no. 7, pp. 1277, 2004.
- [172] V. Westphal, A. M. Rollins, S. Radhakrishnan *et al.*, "Correction of geometric and refractive image distortions in optical coherence tomography applying Fermat's principle," *Optics Express*, vol. 10, no. 9, pp. 397-404, 2002/05/06, 2002.
- [173] S. Ortiz, D. Siedlecki, I. Grulkowski *et al.*, "Optical distortion correction in Optical Coherence Tomography for quantitative ocular anterior segment by three-dimensional imaging," *Optics Express*, vol. 18, no. 3, pp. 2782-2796, 2010/02/01, 2010.
- [174] J. D. Díaz, M. Rahlves, O. Majdani *et al.*, "Towards a one step geometric calibration of an optical coherence tomography." pp. 85630J-85630J-12.
- [175] J. D. Díaz, M. Rahlves, O. Majdani *et al.*, "A one step vs. a multi step geometric calibration of an optical coherence tomography." pp. 85730D-85730D-12.

- [176] J. D. Díaz, J. Stritzel, M. Rahlves *et al.*, “One step geometrical calibration method for optical coherence tomography,” *Journal of Optics*, vol. 18, no. 1, pp. 015301, 2016.
- [177] G. C. B. Lee, “Femtosecond Laser Micromachining and Inscription of Novel Planar and FibreDevices,” Aston University, 2014.
- [178] C. E. Cook, “Pulse Compression-Key to More Efficient Radar Transmission,” *Proceedings of the IRE*, vol. 48, no. 3, pp. 310-316, 1960.
- [179] D. Strickland, and G. Mourou, “Compression of amplified chirped optical pulses,” *Optics Communications*, vol. 55, no. 6, pp. 447-449, 1985/10/15/, 1985.
- [180] O. L. Ltd., *J-1030-4-ATH1-OA System Operation Manual*, Oxford, UK: Oxford Laser Ltd., 2007.
- [181] J. Nees, S. Biswas, F. Droun *et al.*, “Ensuring compactness, reliability, and scalability for the next generation of high-field lasers,” *IEEE Journal of Selected Topics in Quantum Electronics*, vol. 4, no. 2, pp. 376-384, 1998.
- [182] U. Keller, K. J. Weingarten, F. X. Kartner *et al.*, “Semiconductor saturable absorber mirrors (SESAM's) for femtosecond to nanosecond pulse generation in solid-state lasers,” *IEEE Journal of Selected Topics in Quantum Electronics*, vol. 2, no. 3, pp. 435-453, 1996.
- [183] F. X. Kartner, I. D. Jung, and U. Keller, “Soliton mode-locking with saturable absorbers,” *IEEE Journal of Selected Topics in Quantum Electronics*, vol. 2, no. 3, pp. 540-556, 1996.
- [184] I. H. Malitson, “Interspecimen Comparison of the Refractive Index of Fused Silica*,†,” *Journal of the Optical Society of America*, vol. 55, no. 10, pp. 1205-1209, 1965/10/01, 1965.
- [185] U. Sharma, E. W. Chang, and S. H. Yun, “Long-wavelength optical coherence tomography at 1.7 microm for enhanced imaging depth,” *Optics express*, vol. 16, no. 24, pp. 19712-19723, 2008.
- [186] T. A. Tun, M. Baskaran, S. S. Tan *et al.*, “Evaluation of the Anterior Segment Angle-to-Angle Scan of Cirrus High-Definition Optical Coherence Tomography and Comparison With Gonioscopy and With the Visante OCT,” *Investigative Ophthalmology & Visual Science*, vol. 58, no. 1, pp. 59-64, 2017.
- [187] P. J. Rosenfeld, M. K. Durbin, L. Roisman *et al.*, “ZEISS Angioplex™ Spectral Domain Optical Coherence Tomography Angiography: Technical Aspects,” *Developments in Ophthalmology*, vol. 56, pp. 18-29, 2016.
- [188] J. Lapointe, and R. Kashyap, “A simple technique to overcome self-focusing, filamentation, supercontinuum generation, aberrations, depth dependence and waveguide interface roughness using fs laser processing,” *Scientific Reports*, vol. 7, no. 1, pp. 499, 2017/03/29, 2017.

- [189] X. Wang, X. Yu, H. Shi *et al.*, "Characterization and control of laser induced modification inside silicon," *Journal of Laser Applications*, vol. 31, no. 2, pp. 022601, 2019/05/01, 2019.
- [190] Y. Dogan, and C. K. Madsen, "Optimization of ultrafast laser parameters for 3D micromachining of fused silica," *Optics & Laser Technology*, vol. 123, pp. 105933, 2020/03/01/, 2020.
- [191] X. Wang, H. Ye, Z. Su *et al.*, "Observation of two-times self-focusing of femtosecond laser beam in ZnO crystal by two-photon luminescence," *Science Bulletin*, vol. 63, no. 21, pp. 1392-1396, 2018/11/15/, 2018.
- [192] E. Ohmura, "Analyses of Self-Focusing Phenomenon and Temperature Rise in Fused Silica by Ultrashort Pulse Laser Irradiation," *Procedia CIRP*, vol. 5, pp. 7-12, 2013/01/01/, 2013.
- [193] A. Agrawal, M. Connors, A. Beylin *et al.*, "Characterizing the point spread function of retinal OCT devices with a model eye-based phantom," *Biomedical optics express*, vol. 3, no. 5, pp. 1116-1126, 2012.
- [194] K. Shen, H. Lu, S. Baig *et al.*, "Improving lateral resolution and image quality of optical coherence tomography by the multi-frame superresolution technique for 3D tissue imaging," *Biomedical optics express*, vol. 8, no. 11, pp. 4887-4918, 2017.
- [195] I. I. Bussel, G. Wollstein, and J. S. Schuman, "OCT for glaucoma diagnosis, screening and detection of glaucoma progression," *British Journal of Ophthalmology*, vol. 98, no. Suppl 2, pp. ii15, 2014.
- [196] V.-F. Duma, P. Tankam, J. Huang *et al.*, "Optimization of galvanometer scanning for optical coherence tomography," *Applied Optics*, vol. 54, no. 17, pp. 5495-5507, 2015/06/10, 2015.
- [197] J. Sun, and H. Xie, "MEMS-Based Endoscopic Optical Coherence Tomography," *International Journal of Optics*, vol. 2011, pp. 825629, 2011/06/09, 2011.
- [198] C. D. Lu, M. F. Kraus, B. Potsaid *et al.*, "Handheld ultrahigh speed swept source optical coherence tomography instrument using a MEMS scanning mirror," *Biomedical Optics Express*, vol. 5, no. 1, pp. 293-311, 2014/01/01, 2014.
- [199] S. Ortiz, D. Siedlecki, L. Remon *et al.*, "Optical coherence tomography for quantitative surface topography," *Applied Optics*, vol. 48, no. 35, pp. 6708-6715, 2009/12/10, 2009.
- [200] D. Wang, P. Liang, S. Samuelson *et al.*, "Correction of image distortions in endoscopic optical coherence tomography based on two-axis scanning MEMS mirrors," *Biomedical Optics Express*, vol. 4, no. 10, pp. 2066-2077, 2013/10/01, 2013.

- [201] T. Izawa, T. Sasaki, and K. Hane, "Scanning Micro-Mirror with an Electrostatic Spring for Compensation of Hard-Spring Nonlinearity," *Micromachines*, vol. 8, no. 8, 2017.
- [202] P. J. Brosens, "Dynamic Mirror Distortions in Optical Scanning," *Applied Optics*, vol. 11, no. 12, pp. 2987-2989, 1972/12/01, 1972.
- [203] R. A. Conant, J. T. Nee, K. Y. Lau *et al.*, "Dynamic deformation of scanning mirrors." pp. 49-50.
- [204] A. Isheil, J. P. Gonnet, D. Joannic *et al.*, "Systematic error correction of a 3D laser scanning measurement device," *Optics and Lasers in Engineering*, vol. 49, no. 1, pp. 16-24, 2011/01/01/, 2011.
- [205] D. Xu, R. Chaudhuri, and J. P. Rolland, "Telecentric broadband objective lenses for optical coherence tomography (OCT) in the context of low uncertainty metrology of freeform optical components: from design to testing for wavefront and telecentricity," *Optics Express*, vol. 27, no. 5, pp. 6184-6200, 2019/03/04, 2019.
- [206] R. P. McNabb, J. Polans, B. Keller *et al.*, "Wide-field whole eye OCT system with demonstration of quantitative retinal curvature estimation," *Biomedical optics express*, vol. 10, no. 1, pp. 338-355, 2018.

List of publications

[1] Lu, Y., Gordon, N., Robinson, D., Coldrick, B., Mezentsev, V., Menduni, F., Fratini, A. and Sugden, K., "Non-planar calibration phantoms for optical coherence tomography," *In Advanced Fabrication Technologies for Micro/Nano Optics and Photonics XI*, Vol. 10544, 2018.

[2] Lu, Y., Gordon, N., Coldrick, B., Ibrahim, I., Mezentsev, V., Robinson, D. and Sugden, K., "Femtosecond laser inscribed advanced calibration phantom for optical coherence tomography (OCT)," *In Advanced Fabrication Technologies for Micro/Nano Optics and Photonics XIII*, Vol. 11292, 2020.

[3] Nock, R.W., Ai, X., Lu, Y., Dahnoun, N. and Rarity, J.G., "FPGA based time-to-digital converters," *In Quantum Technologies 2020*, Vol. 11347, 2020.

[4] Sadik, M., Ai, X., Lu, Y. and Nock, R., "Real-time time correlated photon counters for photon number resolving detectors," *In Optical Sensing and Detection VI*, Vol. 11354, 2020.

[5] Nock, R.W., Sadik, M. and Lu, Y., "Improved FPGA time-to-digital converter architecture to improve precision, converter linearity and reduce dead-time," *In Advanced Photon Counting Techniques XIV*, Vol. 11386, 2020.

Oral presentation:

Lu, Y., Gordon, N., Webb, D. J., Robinson, D., and Sugden, K. "A review of calibration phantom fabrication methods for optical coherence tomography (OCT)," ISROS, Toulouse, 2019.

Poster presentation:

Lu, Y., Gordon, N., Robinson, D., Coldrick, B., Mezentsev, V., Menduni, F., Fratini, A. and Sugden, K., "Calibration phantoms for optical coherence tomography," Photon 2018, IOP, Birmingham, 2018.

Currently writing:

Lu, Y., Ibrahim, I., Coldrick, B., Robinson, D., Fratini, A. and Sugden, K. "Femtosecond laser inscribed calibration phantom for optical coherence tomography and its application for the image distortion correction." *Biomedical Optics Express*, 2021.

Appendices

Appendix A

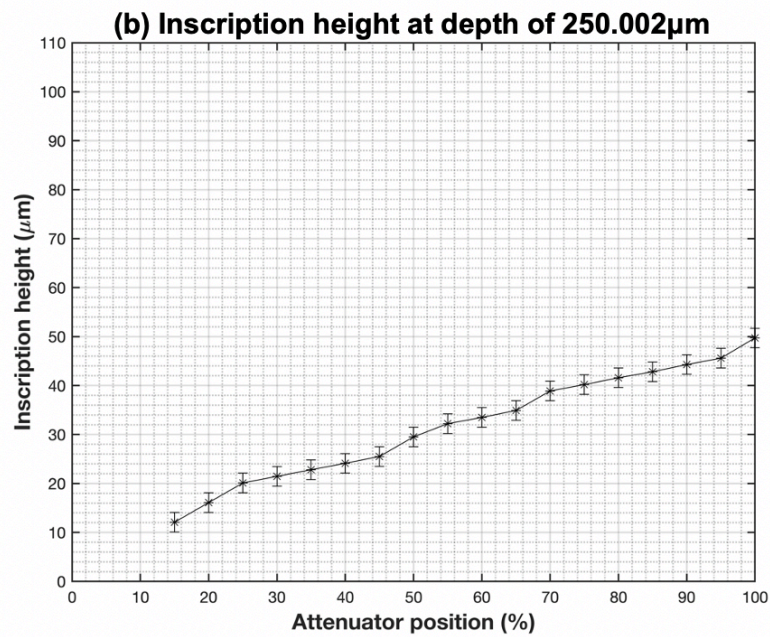
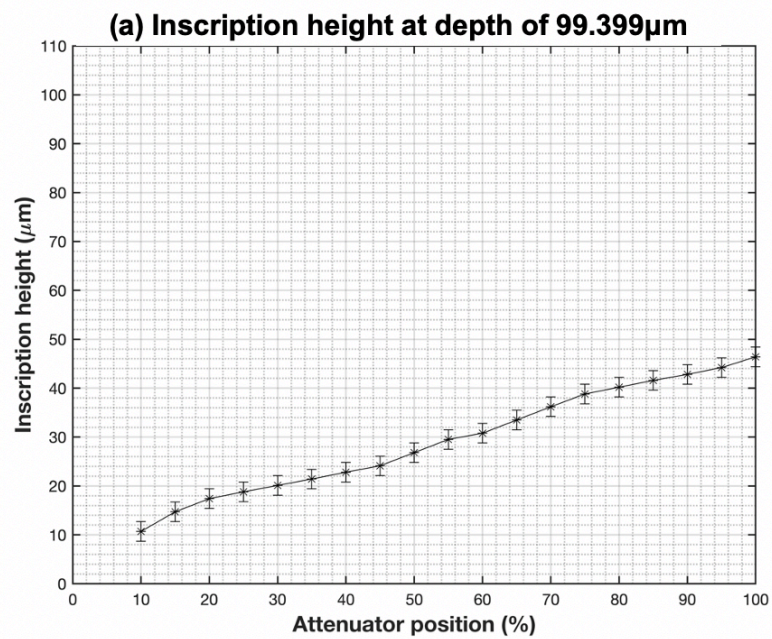
Measurement on thicknesses of the fused silica substrate

Here listed the physical substrate thickness measurement for 14 sample substrates which were tested by using a micrometre:

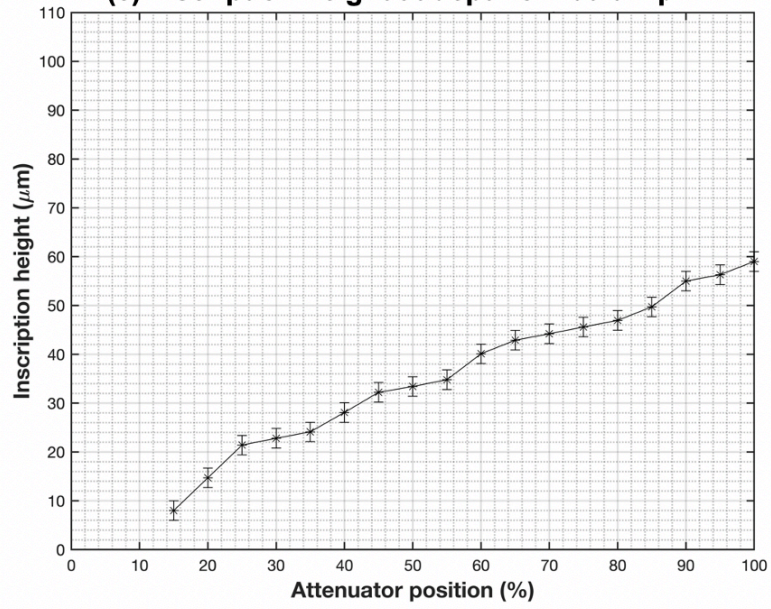
Sample No.	Thickness (mm)
1	2.04
2	2.06
3	2.06
4	2.06
5	2.06
6	2.07
7	2.07
8	2.04
9	2.06
10	2.07
11	2.07
12	2.04
13	2.03
14	2.08

Appendix B

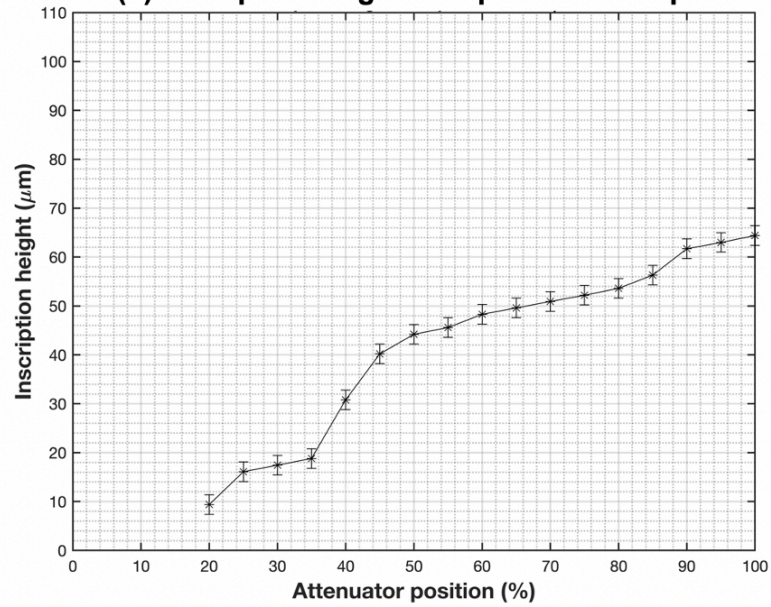
Line plots for the correlation between the inscription height (in μm) and the laser power (% of the total output power).



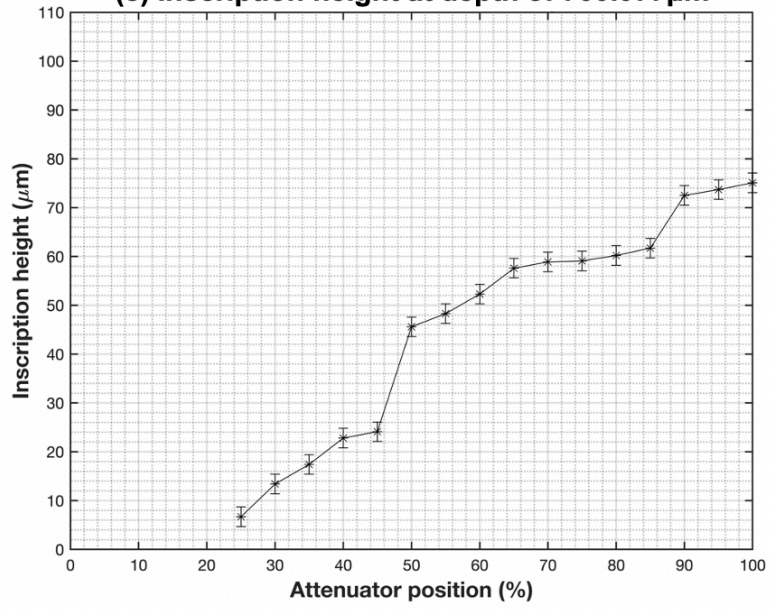
(c) Inscription height at depth of 400.044 μm



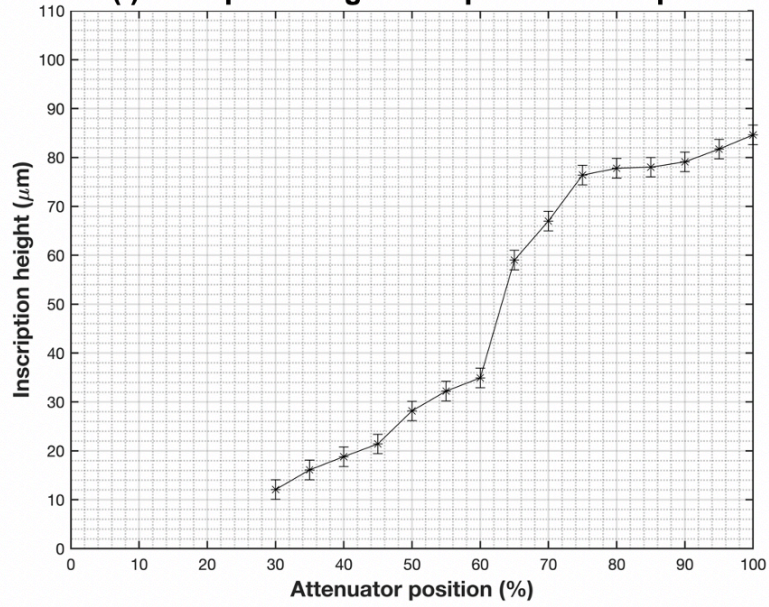
(d) Inscription height at depth of 550.137 μm



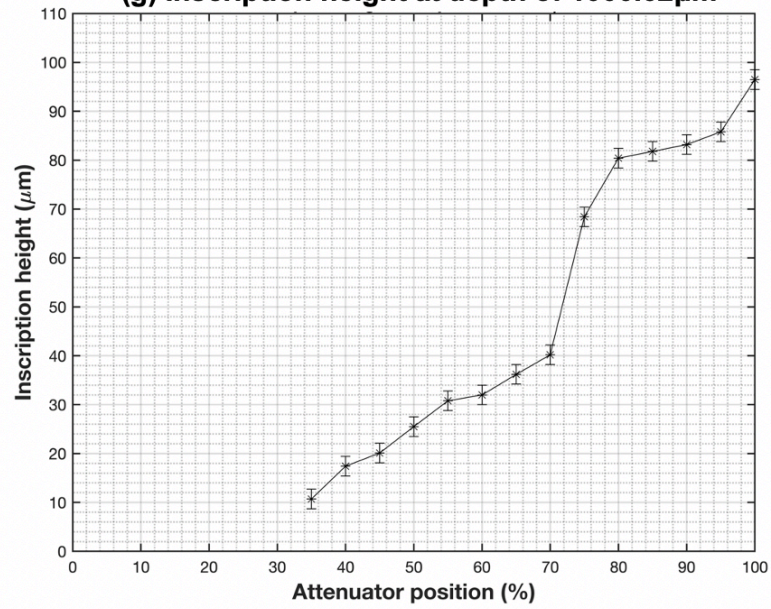
(e) Inscription height at depth of 700.077 μm



(f) Inscription height at depth of 850.068 μm



(g) Inscription height at depth of 1000.62 μm



(h) Inscription height at depth of 1150.05 μm

